A microwave-assisted synthesis of nitrogen-doped TiO2/graphene oxide for use in visible-light-activated photocatalytic processes

Sánchez Tobón, Camilo

Doctoral thesis / Disertacija

2024

Degree Grantor / Ustanova koja je dodijelila akademski / stručni stupanj: **University of Zagreb, Faculty of Mechanical Engineering and Naval Architecture / Sveučilište u Zagrebu, Fakultet strojarstva i brodogradnje**

Permanent link / Trajna poveznica: https://urn.nsk.hr/urn:nbn:hr:235:020046

Rights / Prava: In copyright / Zaštićeno autorskim pravom.

Download date / Datum preuzimanja: **2024-07-18**

Repository / Repozitorij:

Repository of Faculty of Mechanical Engineering and Naval Architecture University of Zagreb

FACULTY OF MECHANICAL ENGINEERING AND NAVAL ARCHITECTURE

CATALAN INSTITUTE FOR WATER RESEARCH

FACULTY OF SCIENCE

Camilo Sánchez Tobón

A MICROWAVE-ASSISTED SYNTHESIS OF NITROGEN-DOPED TiO_2/GRAPHENE OXIDE FOR USE IN VISIBLE-LIGHT-ACTIVATED PHOTOCATALYTIC PROCESSES

INTERNATIONAL DUAL DOCTORATE

Zagreb, 2024

FACULTY OF MECHANICAL ENGINEERING AND NAVAL ARCHITECTURE

CATALAN INSTITUTE FOR WATER RESEARCH

FACULTY OF SCIENCE

Camilo Sánchez Tobón

A MICROWAVE-ASSISTED SYNTHESIS OF NITROGEN-DOPED TiO_2/GRAPHENE OXIDE FOR USE IN VISIBLE-LIGHT-ACTIVATED PHOTOCATALYTIC PROCESSES

INTERNATIONAL DUAL DOCTORATE

Supervisors:

Prof. Lidija Ćurković, PhD

Prof. Jelena Radjenovic, PhD

Prof. Davor Ljubas, PhD

Zagreb, 2024

University of Zagreb

FACULTY OF MECHANICAL ENGINEERING AND NAVAL ARCHITECTURE

CATALAN INSTITUTE FOR WATER RESEARCH

FACULTY OF SCIENCE

Camilo Sánchez Tobón

MIKROVALNO POTPOMOGNUTA SINTEZA DUŠIKOM DOPIRANOGA TiO_2/GRAFENOVA OKSIDA ZA PRIMJENU U FOTOKATALITIČKIM PROCESIMA AKTIVIRANIMA VIDLJIVIM ZRAČENJEM

MEĐUNARODNI DVOJNI DOKTORAT

Mentori:

Prof. dr. sc. Lidija Ćurković,

Prof. dr. sc. Jelena Radjenovic

Prof. dr. sc. Davor Ljubas

Zagreb, 2024

FACULTY OF MECHANICAL ENGINEERING AND NAVAL ARCHITECTURE

CATALAN INSTITUTE FOR WATER RESEARCH

FACULTY OF SCIENCE

Camilo Sánchez Tobón

SÍNTESIS ASISTIDA POR MICROONDAS DE TiO_2/ÓXIDO DE GRAFENO DOPADOS CON NITRÓGENO PARA SU USO EN PROCESOS FOTOCATALÍTICOS ACTIVADOS POR LUZ VISIBLE

DOCTORADO DUAL INTERNACIONAL

Supervisores:

Prof.ª Dr. ª Lidija Ćurković

Prof.ª Dr. ª Jelena Radjenovic

Prof. Dr. Davor Ljubas

Zagreb, 2024

Bibliographic page

- UDK: 544.526:549.514.6:628(043.3)=111
- Scientific area: Technical Sciences
- Scientific field: Mechanical engineering
- Scientific branch: Production engineering
- Institutions:

  University of Zagreb, Faculty of Mechanical Engineering and Naval Architecture, Zagreb, Croatia

  University of Girona, Girona, Spain

  Catalan Institute for Water Research, Girona, Spain
- Supervisors: Prof. Lidija Ćurković, PhD; Prof. Jelena Radjenovic, PhD and Prof. Davor Ljubas, PhD
- Number of pages: 141 (with Appendix)
- Number of figures: 61
- Number of tables: 18
- Number of appendices: 32
- Number of references: 183
- Date of defense: March 11, 2024
- Defense Committee:

  Assoc. Prof. Hrvoje Juretić, PhD, University of Zagreb, Faculty of Mechanical Engineering and Naval Architecture, Croatia – Committee Chair

  Prof. Slaven Dobrović, PhD, University of Zagreb, Faculty of Mechanical Engineering and Naval Architecture, Croatia – Committee Member

  Prof. Mira Petrović, PhD, Catalan Institute for Water Research (ICRA), Spain – Committee Member

  Dr. Gianluigi Buttiglieri, PhD Catalan Institute for Water Research (ICRA), Spain – Committee Member

  Prof. Sandra Babić, PhD, University of Zagreb, Faculty of Chemical Engineering and Technology, Croatia – Committee Member

- The thesis is stored at:

  National and University Library in Zagreb, Hrvatske bratske zajednice bb;

  Library of Faculty of Mechanical Engineering and Naval Architecture, University of Zagreb,

Jacobo,

en los momentos de duda y/o angustia,
cierra tus ojos,

respira lento y conscientemente,

y escucha la voz de tu corazón.

Te amo

ACKNOWLEDGEMENTS

I would like to express my profound gratitude and heartfelt appreciation to all who have contributed to the successful completion of my doctoral thesis. This journey has been an incredible learning experience, and I am indebted to numerous individuals and institutions who have supported me along the way. Special thanks to the European Commission for funding the Nowelties project and everyone involved in its creation and development.

First and foremost, I would like to thank my supervisors Prof. Dr. Lidija Ćurković, Prof. Dr. Davor Ljubas and Prof. Dr. Jelena Radjenovic for giving the opportunity to be part of this amazing project, for their guidance, wisdom, and patience throughout this research endeavor. Their expertise, dedication, and mentorship have been invaluable, and I am truly grateful for their belief in me and this research.

I would like to acknowledge everyone who has assisted me to develop my research during the time at the University of Zagreb. Thanks to Prof. Dr. Hrvoje Juretić, and Dr. Maja Zebić Avdičević for their advice and feedback, to Marko Skozrit for helping in the laboratory making experimental setups, to Goran Smoljanić for his comradeship, to Ivana Gabelica and Martina Kocijan for supporting me with administrative matters, to Zrinka Švagelj for sharing her knowledge and providing some materials for the research. Also, I would like to thank the people that contributed to this research at the Catalan Institute for Water Research (ICRA). Thanks to Dr. Maria José Farré and Dr. Elisabeth Cuervo Lumbaque for their guidance and support for detection and elucidation of byproducts transformation in the Orbitrap device.

I am also grateful to friends for their unwavering encouragement, love, and understanding during the ups and downs of this journey. Special thanks to Nikoletta Tsiarta, Silvia Morović, Nevena Milčić, Roko Blažic and Marko Racar for the unforgettable moments shared during this journey.

Thank you to my mother Marta, my father Nelson, and my siblings Julian, Jose, Kelly and Daniel for their encouragement and continued support over the years and their enthusiasm as I neared my goal. Finally, but most importantly, I wish to thank my wife Sandra for her patience, assistance, support and faith in me. She has been a light on my way and gave me the biggest gift of life, my son Jacobo.

I could not have completed my research without the support of all these wonderful people!

This work is supported by the European Union's Horizon 2020 research and innovation program under the Marie Sklodowska-Curie grant agreement N° 81288 – Nowelties ITN-EJD project.

ABSTRACT

This research was mainly focused on the synthesis by microwave-assisted method to produce a low bandgap energy N/TiO_2/rGO nanocomposite photocatalyst used to remove organic micropollutants (OMPs) under different irradiation sources. Initially, the influence of temperature and reaction time in the microwave (MW) oven on the final properties of N/TiO_2 was investigated. Also, the effect of nitrogen doping was researched using urea as a nitrogen source. It also explored the effect of reduced graphene oxide (rGO) and its synergy with nitrogen doping. All synthesized materials were characterized by X-ray diffraction (XRD), Raman spectroscopy (RS), infrared spectroscopy (FTIR), diffuse reflectance spectroscopy (DRS), electron microscopy (SEM-EDS), nitrogen adsorption/desorption isotherms (BET), while the most photoactive materials were additionally characterized by photoelectron spectroscopy (XPS). The synthesized materials were tested in the degradation of ciprofloxacin (CIP), while the most photoactive material (N/TiO_2/rGO) was further evaluated in the degradation of diclofenac (DCF) and salicylic acid (SA) under different irradiation sources. Immobilization of the photocatalyst on a suitable support is crucial for practical application in the water treatment process. Therefore, the most photoactive N/TiO_2/rGO nanocomposite was immobilized over an alumina (Al_2O_3) ceramic foam to evaluate the photocatalyst stability and reusability.

Results revealed that it is possible to obtain crystalline TiO_2 (anatase phase) by the microwave-assisted method in a short period (up to 10 minutes) without subsequent thermal treatment. It was found that the reaction temperature is the most critical parameter in comparison to the reaction time. On the other hand, although nitrogen content does not affect morphological properties of the photocatalyst, it influences the photocatalytic performance, especially under visible irradiation sources. Additionally, the rGO incorporation increased the specific surface area of the photocatalyst and improved the photocatalytic activity, specifically under solar irradiation, due to hindering the recombination phenomenon. The photocatalytic evaluation showed that CIP and SA removal were achieved by a synergistic effect of adsorption and photocatalysis, while DCF removal was done solely by photocatalysis. Regarding the irradiation source, the results suggested that the photocatalytic mechanism and kinetic model rely mainly on the type of pollutant rather than the irradiation source. It was found that although the irradiation source does not influence either the photocatalytic mechanism or the kinetic model, it impacts the degradation rate. The immobilized photocatalyst showed that the material is stable after 19 consecutive photocatalytic cycles without losing photoactivity.

Key words: Microwave-assisted synthesis; photocatalysis; N/TiO_2/rGO; irradiation sources; organic micropollutants; transformation products; water treatment.

PROŠIRENI SAŽETAK NA HRVATSKOM

Voda je jedan od bitnih elemenata života jer se na njoj temelje gotovo sve ljudske aktivnosti, a Opća skupština Ujedinjenih naroda je 2010. g. pristup vodi proglasila ljudskim pravom. Međutim, brzi porast stanovništva i globalno zatopljenje doveli su do globalne vodne krize. U nedavnim istraživanjima procjenjuje se da se polovica svjetske populacije suočava s ozbiljnom nestašicom vode barem jedan mjesec godišnje, dok gotovo 1,5 milijardi ljudi živi u područjima s visokim ili iznimno visokim rizikom od nestašice vode. Osim problema s nedostatkom vode, stalni razvoj novih kemijskih proizvoda za različite primjene i kasnije njihovo ispuštanje u vodne tokove bez odgovarajuće obrade, ili čak i bez obrade, još je jedan izazov koji pojačava krizu s vodom. U posljednjih 20 godina značajna pozornost usmjerena je na takozvana organska mikrozagađivala (OMZ), integrirana uglavnom u farmaceutske proizvode, proizvode za osobnu njegu, dezinfekcijske nusprodukte, endokrine modulatore i sve njihove nusprodukte transformacije, a zbog njihova mogućeg negativnog utjecaja na okoliš. Nekoliko je studija pokazalo da, osim činjenice da OMZ-ove nije lako ukloniti konvencionalnim postrojenjima za pročišćavanje otpadnih voda, neki od njih vrlo su postojani u okolišu i mogu se bioakumulirati, štetno djeluju na vodne sustave i mogu ugroziti zdravlje ljudi. S obzirom na nestašicu vode i kontinuirani porast nedostatka vode u mnogim regijama diljem svijeta, ponovna uporaba vode postaje najpraktičnije rješenje za prevladavanje krize s vodom. Međutim, kako bi se zajamčilo potpuno uklanjanje OMZ-ova i sigurnost ponovne upotrebe vode, moraju se implementirati nove tehnologije pročišćavanja zajedno s postojećim uređajima za pročišćavanje otpadnih voda.

Napredni oksidacijski procesi (engl. *advanced oxidation processes,* AOP) smatraju se zanimljivim alternativama za uklanjanje OMZ-ova iz otpadne vode s visokom učinkovitošću oksidacije i bez sekundarnog onečišćenja. Među različitim AOP-ima, heterogena fotokataliza korištenjem TiO_2 aktivno se proučava zbog izvanredne fotokatalitičke aktivnosti, niske cijene, izvrsne kemijske stabilnosti i netoksičnosti. TiO_2 se aktivira svjetlosnom energijom koja proizvodi reaktivne kisikove vrste (RKV), koje potom mogu neselektivno oksidirati OMZ-ove. Međutim, zbog širokog energijskog procjepa (3,2 eV), fotoaktivacija TiO_2 odvija se samo ultraljubičastim (UV) svjetlom, smanjujući njegov potencijal za korištenje Sunčeva zračenja (4% UV, 48% vidljivo). Dodatno, učinak brze rekombinacije fotogeneriranih parova elektron/šupljina (e^-/h^+) koji proizvode RKV može umanjiti fotokatalitičku aktivnost TiO_2. Stoga, kako bi se prevladala ova dva glavna nedostatka, dopiranje TiO_2 jedna je od najistraživanijih strategija za sprječavanje procesa rekombinacije ili proširenje fotokatalitičke

aktivnosti TiO_2 u vidljivom dijelu zračenja kako bi se povećala fotokatalitička učinkovitost uz Sunčevo zračenje.

Dopiranje metalima, kao što su Pd, Pt, Au, Cu, Fe itd., utjecalo je na poboljšanje fotokatalitičke aktivnost u vidljivom području; međutim, visoki troškovi i moguće eluiranje metala zbog niske toplinske stabilnosti mogu biti zdravstveni rizik, smanjujući njegovu primjenjivost. Stoga je dopiranje nemetalima, kao što su N, P, S i C, praktičniji i jeftiniji način za poboljšanje fotoaktivnosti Sunčevim zračenjem. Dopiranje dušikom istražuje se zbog sličnosti njegova atomskog radijusa s kisikovim. TiO_2 dopiran dušikom pokazao je fotokatalitičku aktivnost djelovanjem vidljivog zračenja, što se može pripisati formiranju novih energetskih razina koje smanjuju energijski procjep. Nadalje, neke studije ukazuju da dušik pogoduje formiranju anatas TiO_2 faze koja ima najveću fotokatalitičku aktivnost u odnosu na ostale TiO_2 polimorfe. S druge strane, reducirani grafenov oksid (rGO) privukao je značajnu pozornost kao materijal za pripravu kompozita na bazi TiO_2 zbog svoje velike specifične površine i dobre toplinske i elektronske vodljivosti koji bi mogli pridonijeti poboljšanju fotoaktivnosti TiO_2. Nedavne studije pokazale su da spajanje rGO s TiO_2 može poboljšati fotokatalitičku aktivnost jer rGO djeluje kao ponor elektrona, odvajajući fotogenerirane naboje i smanjujući učinak rekombinacije. Stoga bi integracija dušika i rGO u TiO_2 mogla biti zanimljiv pristup za rješavanje dva glavna, prije spomenuta, nedostatka TiO_2.

Uz dopiranje, metoda sinteze TiO_2 ima važnu ulogu zbog utjecaja na strukturna, morfološka i optička svojstva koja određuju ukupnu fotokatalitičku aktivnost. Neke uobičajene konvencionalne metode sinteze su sol-gel metoda, kemijsko taloženje iz parne faze, hidrotermalna sinteza, itd. Glavni nedostatak ovih metoda je dugo trajanje sinteze. Međutim, mikrovalno potpomognuta metoda pojavila se kao nekonvencionalna metoda zagrijavanja i nedavno je postala atraktivna alternativa konvencionalnim metodama sinteze zbog kraćeg trajanja sinteze i manje potrošnje energije. Ove prednosti mikrovalno potpomognute metode uglavnom su posljedica izravnog ("u jezgri") zagrijavanja reakcijske smjese mikrovalnim zračenjem, što je posljedica brze pretvorbe elektromagnetske energije u toplinsku energiju, smanjujući gradijent temperature unutar reakcijske posude doprinoseći proizvodnji materijala s homogenijim svojstvima.

Osim velikog energijskog procjepa i faktora rekombinacije, korištenje TiO_2 praha u obliku suspenzije predstavlja tehničke i ekonomske izazove vezano za separaciju i ponovnu uporabu fotokatalizatora u pročišćavanju otpadnih voda. Dakle, kako bi se izbjegao proces

separacije TiO_2 praha i pojednostavila daljnja ponovna uporaba fotokatalizatora, TiO_2 se imobilizira na različite supstrate kao što su staklo, polimeri, magnetske čestice, keramika itd. Imobilizacija TiO_2 na keramičku pjenu kao supstrat aktivno se proučava posljednjih godina jer ovaj supstrat pruža izvrsnu kemijsku inertnost, visoku otpornost na UV zračenje, mehaničku stabilnost i veliku specifičnu kontaktnu površina, što ga čini prikladnom opcijom za imobilizaciju fotokatalizatora.

Stoga se ovo istraživanje uglavnom usredotočuje na sintezu fotokatalizatora na bazi TiO_2 s niskim energijskim procjepom korištenjem nekonvencionalne tehnike poput mikrovalno potpomognute sinteze. Razvijeni fotokatalizator mogao bi se koristiti za uklanjanje OMZ-ova iz vode uz učinkovito korištenje Sunčeva zračenja. Prvo je procijenjena uloga temperature, vremena trajanja reakcije i sadržaja dušika na strukturna, morfološka i fotokatalitička svojstva TiO_2 dopiranog dušikom (N/TiO_2) za uklanjanje ciprofloksacina (CIP) uz UVA, Sunčevo i vidljivo zračenje. Rezultati su pokazali da se veća kristalnost i veća veličina kristalita postižu pri višoj temperaturi (200°C), dok vrijeme reakcije u mikrovalnom reaktoru ima zanemariv učinak na morfološka i fotokatalitička svojstva. Utvrđeno je da je temperatura ključni parametar u mikrovalno potpomognutoj sintezi TiO_2.

S druge strane, promjene količine dušika pokazale su da promjene u molarnom omjeru N/Ti imaju zanemariv utjecaj na morfološka i optička svojstva fotokatalizatora. Nasuprot tome, promjene količine dušika imale su značajan utjecaj na fotokatalitička svojstva, osobito uz vidljive izvore zračenja. Ovaj pozitivni učinak, uglavnom uz vidljivo zračenje, pripisan je novim energetskim razinama, a ne smanjenju energetskog procjepa, što je pridonijelo apsorpciji fotona u vidljivom spektru. Nadalje, primijećeno je da je s višim molarnim omjerom N/Ti poboljšana fotokatalitička aktivnost pri uklanjanju ciprofloksacina (CIP-a) uz različite izvore zračenja. Međutim, nakon povećanja koncentracije dušika, može se pojaviti nepovoljan učinak na brzinu razgradnje jer bi dušik mogao djelovati kao centar rekombinacije koji pogoduje rekombinaciji naboja.

Nakon što su uspostavljeni radni parametri u reaktoru za mikrovalnu sintezu i optimalna količina dopiranoga dušika, procijenjena je uloga sadržaja rGO (0,25 – 10 wt. % rGO) na morfološka svojstva i fotokatalitičku aktivnost N/TiO_2/rGO nanokompozita pri razgradnji tri različita OMZ-a (ciprofloksacin (CIP), diklofenak (DCF) i salicilna kiselina (SA)) uz različite izvore zračenja (UVA, Sunčevo i vidljivo zračenje). Utvrđeno je da unatoč optičkim svojstvima materijala koji je modificiran dodatkom rGO, gdje je energetski procjep smanjen, povećanje

količine rGO nije imalo pozitivan učinak na fotokatalitičke karakteristike, osobito pod vidljivim izvorima zračenja, povećana količina rGO sprječava apsorpciju svjetla, a mogla bi djelovati i kao rekombinacijski centar koji ometa fotokatalitičku aktivnost TiO_2. Fotokatalitičkim ispitivanjima ustanovljeno je da se s nižim sadržajem rGO postiže bolja fotoaktivnost. Dodatno, utvrđeno je da je glavni doprinos rGO na fotokatalizatoru smanjenje učinka rekombinacije, ukazujući da bi kombinacija dopiranja dušikom i ugradnje rGO mogla biti dobra strategija za prevladavanje ograničenja TiO_2 fotokatalize.

Za utvrđivanje mehanizma fotokatalitičke razgradnje s različitim izvorima zračenja korištene su tvari koje inhibiraju reaktivne vrste (engl. *scavengers*) koje se generiraju na površini fotokatalizatora. Provedene su dodatne studije o intenzitetu zračenja kako bi se istražila primjena prirodnoga Sunčeva zračenja. Rezultati su pokazali da su kinetički model i mehanizam razgradnje uglavnom vezani na vrstu organskog mikrozagađivala, a ne na izvor zračenja. Također, utvrđeno je da proces adsorpcije igra važnu ulogu, osobito kada se provodi razgradnja uz vidljivo zračenje. Međutim, iako izvor zračenja, tj. intenzitet ozračenja, ne određuje mehanizam razgradnje, on značajno utječe na brzinu razgradnje za uklanjanje OMZ-a. Također, utvrđeno je da je uz prirodno Sunčevo zračenje proces fotolize značajno sporiji, dok je TiO_2 fotokataliza pokazala dobru učinkovitost uklanjanja CIP-a, što ukazuje da bi razvijeni N/TiO_2/rGO fotokatalizator mogao učinkovito koristiti Sunčevo zračenje pri uklanjanju OMZ-ova iz vode.

Imobilizacija fotokatalizatora na odgovarajuću podlogu ključna je za praktičnu primjenu u procesu obrade vode. Stoga je N/TiO_2/rGO nanokompozit s najvećom fotoaktivnošću pokazanom u praškastom obliku imobiliziran na Al_2O_3 keramičku pjenu metodom uranjanja i niskom toplinskom obradom, korištenjem SiO_2 kao veziva za bolju adheziju na supstrat Al_2O_3 pjene (stabilnost) i mogućnost ponovne upotrebe. Stabilnost i mogućnost ponovne upotrebe imobiliziranog N/TiO_2/rGO procijenjene su uzastopnom razgradnjom u nekoliko ciklusa za tri različita OMZ-a. Nakon nekoliko ponavljajućih fotokatalitičkih ciklusa (19 ciklusa), fotokatalizatori nisu izgubili fotoaktivnost, čime je potvrđena dobra stabilnost i mogućnost ponovne upotrebe. Također, utvrđeno je da se keramička pjena s otvorenim ćelijama pokazala dobrom alternativom za imobilizaciju fotokatalizatora zato što se time smanjuje ograničenje masenog transfera zagađivala do aktivnih mjesta na fotokatalizatoru uz postizanje veće aktivne površine za ozračivanje i naknadne reakcije.

Konačno, primjenom vezanog sustava tekućinske kromatografije (LC) i spektrometrije masa visoke razlučivosti (Orbitrap) identificirani su razgradni produkti dvaju OMZ-a (CIP i DCF) nastali fotokatalitičkom razgradnjom uz primjenu različitih izvora zračenja. Rezultati su pokazali da je uz vidljive izvore zračenja većina detektiranih razgradnih produkata nastalih tijekom razgradnje početnog OMZ-a ostala prisutna u otopini nakon dva sata zračenja (tj. nije došlo do njihove potpune razgradnje).

Ključne riječi: Mikrovalno potpomognuta sinteza; fotokataliza; N/TiO_2/rGO; izvori zračenja; organska mikrozagađivala; razgradni produkti; obrada vode.

RESUMEN EXTENDIDO EN CASTELLANO

El agua es uno de los elementos esenciales para la vida porque casi todas las actividades humanas se basan en ella, declarada un derecho humano en 2010 por la Asamblea General de las Naciones Unidas. Sin embargo, el rápido crecimiento demográfico y el calentamiento global han provocado una crisis mundial del agua. Estudios recientes estimaron que la mitad de la población mundial experimenta una grave escasez de agua al menos un mes al año, mientras que casi 1.500 millones de personas viven en zonas con un riesgo de escasez de agua alto o extremadamente alto. Además de los problemas de escasez de agua, el desarrollo continuo de nuevos productos químicos para diferentes aplicaciones y su posterior vertido en cuerpos de agua sin un tratamiento adecuado o incluso sin tratamiento es otro desafío que intensifica la crisis del agua. En los últimos 20 años se ha centrado una importante atención en los llamados microcontaminantes orgánicos (MCO), integrados principalmente por productos farmacéuticos, productos de cuidado personal, subproductos de la desinfección, disruptores endocrinos y todos sus subproductos de transformación, debido a su posible impacto negativo sobre el medio ambiente. Varios estudios han demostrado que, aparte del hecho de que las plantas de tratamiento de aguas residuales convencionales (PTAR) no eliminan fácilmente los MCO, algunas son persistentes y podrían bioacumularse, dañando el sistema acuático y amenazando la salud pública. Teniendo en cuenta la escasez de agua y el continuo aumento del estrés hídrico en muchas regiones del mundo, la reutilización del agua se está convirtiendo en la solución más práctica para superar la crisis del agua. Sin embargo, para garantizar la eliminación completa de los MCO y la seguridad del agua de reutilización, se deben implementar nuevas tecnologías de tratamiento acopladas a las PTAR existentes.

Los procesos de oxidación avanzada (POA) se han considerado alternativas interesantes para eliminar los MCO de las aguas residuales, con alta eficiencia de oxidación y sin contaminación secundaria. Entre los diferentes POA, la fotocatálisis heterogénea de TiO_2 se estudia activamente debido a su excelente actividad fotocatalítica, bajo costo, excelente estabilidad química y no toxicidad. El TiO_2 se activa mediante la energía luminosa que produce especies reactivas del oxígeno (ERO), que posteriormente pueden oxidar los MCO de forma no selectiva. Sin embargo, debido a su alta banda prohibida de energía (3,2 eV), la fotoactivación del TiO_2 se produce sólo por luz ultravioleta (UV), lo que dificulta su potencial uso con radiación solar (4% UV, 48% Visible). Además, el rápido efecto de recombinación de los pares fotogenerados electrón/hueco (e^-/h^+) que producen las ERO, puede reducir la actividad fotocatalítica del TiO_2. Por lo tanto, para superar estos dos inconvenientes principales, el dopaje

del TiO_2 es una de las estrategias más investigadas para prevenir el proceso de recombinación o cambiar la respuesta óptica del TiO_2 al rango de luz visible para aumentar la eficiencia fotocatalítica bajo la radiación solar.

El dopaje con metales, como Pd, Pt, Au, Cu, Fe, etc., ha mostrado una actividad fotocatalítica mejorada en el rango visible; sin embargo, los altos costos del metal y la probabilidad de lixiviación del metal debido a la baja estabilidad térmica, podrían ser un riesgo para la salud, reduciendo su aplicabilidad. Por lo tanto, el dopaje con no metales, como N, P, S y C, ha sido una forma más práctica y menos costosa de mejorar la fotoactividad bajo la irradiación del espectro solar. Entre los dopajes no metálicos, el nitrógeno es ampliamente estudiado debido a su similitud en radio atómico con el oxígeno, haciendo más probable la sustitución atómica. El TiO_2 dopado con nitrógeno ha mostrado una interesante respuesta fotoactiva bajo luz visible, que puede atribuirse a la formación de nuevos niveles energéticos que reducen la banda prohibida. Además, algunos estudios sugieren que el nitrógeno podría favorecer la formación de la fase anatasa del TiO_2, la polimorfa más fotoactiva del TiO_2. Por otro lado, el óxido de grafeno reducido (rGO) ha atraído mucha atención como material para producir compuestos de TiO_2 debido a su alta área superficial y buena conductividad térmica y electrónica que podría mejorar la fotoactividad del TiO_2. Estudios recientes han demostrado que acoplar rGO con TiO_2 puede mejorar la actividad fotocatalítica porque el rGO actúa como un sumidero de electrones, separando las cargas fotogeneradas y reduciendo el efecto de recombinación. Por lo tanto, integrar el nitrógeno y el rGO en el TiO_2 podría ser un enfoque interesante para abordar los dos principales inconvenientes del TiO_2 mencionados anteriormente.

Además de la estrategia de dopaje, el método de síntesis de TiO_2 juega un papel importante debido a su influencia en las propiedades estructurales, morfológicas y ópticas, que determinan la actividad fotocatalítica en general. Algunas estrategias de síntesis convencionales comunes son el método sol-gel, deposición química de vapor, método hidrotermal, etc. El principal inconveniente de estos métodos es el largo tiempo de síntesis. Sin embargo, el método asistido por microondas surgió por primera vez como un método de calentamiento no convencional y recientemente se ha convertido en una alternativa atractiva debido a su menor tiempo de síntesis y menor consumo de energía en comparación con los métodos de síntesis convencionales. Estas ventajas del método asistido por microondas se deben principalmente al calentamiento directo "en el núcleo" de la mezcla de reacción mediante la radiación de microondas, la cual se debe a la rápida conversión de energía electromagnética en energía

térmica, reduciendo el gradiente de temperatura dentro del recipiente de reacción y contribuyendo a la producción de un material con propiedades más homogéneas.

Además de la alta energía de la banda prohibida y el factor de recombinación, el uso de TiO_2 en polvo suspendido presenta desafíos técnicos y económicos para la recuperación y reutilización de fotocatalizadores en el tratamiento de aguas residuales. Así, para evitar el proceso de recuperación y simplificar la reutilización del fotocatalizador, se ha inmovilizado el TiO_2 sobre diferentes soportes tales como vidrio, polímeros, partículas magnéticas, cerámicas, etc. La inmovilización de TiO_2 sobre cerámica se ha estudiado activamente en los últimos años porque el soporte es inerte químicamente, tiene alta resistencia a la luz ultravioleta, buena estabilidad mecánica y una gran área superficial, lo que lo convierte en una opción adecuada para la inmovilización de fotocatalizadores.

Por lo tanto, esta investigación se centró en la síntesis de fotocatalizadores basados en TiO_2 de baja energía de banda prohibida utilizando una técnica no convencional como el método asistido por microondas. El fotocatalizador desarrollado podría utilizarse para eliminar microcontaminantes orgánicos (MCO) del agua utilizando energía solar de manera eficiente. Inicialmente, se evaluó el papel de la temperatura, el tiempo de reacción y el contenido de nitrógeno en las propiedades estructurales, morfológicas y fotocatalíticas del TiO_2 dopado con nitrógeno (N/TiO_2) para la eliminación de ciprofloxacina (CIP) con radiación UVA, solar y visible. Los resultados mostraron que se logra una mayor cristalinidad y un mayor tamaño de cristal a una temperatura más alta (200°C), mientras que el tiempo de reacción en el horno de microondas tiene un efecto insignificante sobre las propiedades morfológicas y fotocatalíticas. Se determinó que la temperatura es el parámetro crucial en la síntesis de TiO_2 mediante el método asistido por microondas.

Por otro lado, los cambios en el contenido de nitrógeno revelaron que los cambios en la relación molar N/Ti apenas influyeron en las propiedades morfológicas y ópticas. Por el contrario, la variación en el contenido de nitrógeno tuvo un impacto relevante en el rendimiento fotocatalítico, especialmente bajo fuentes de irradiación visible. Este efecto positivo, principalmente bajo la irradiación visible, se atribuyó a los nuevos niveles energéticos más que a la reducción de la banda prohibida de energía, lo que contribuyó a la adsorción de fotones en el espectro visible. Además, se observó que con una mayor relación molar N/Ti, se mejoraba la actividad fotocatalítica en la eliminación de CIP bajo diferentes fuentes de irradiación. Sin embargo, después de cierta concentración de nitrógeno, podría tener un efecto desfavorable en

la tasa de degradación porque el nitrógeno podría actuar como un centro de recombinación que favorece la recombinación de cargas.

Se evaluó el papel del contenido de rGO (0,25 – 10% en peso de rGO) en las propiedades morfológicas y la actividad fotocatalítica de N/TiO_2/rGO en la degradación de tres MCO diferentes (ciprofloxacina (CIP), diclofenaco (DCF) y ácido salicílico (AS)) bajo diferentes fuentes de radiación (UVA, solar y visible). Se encontró que a pesar de que la propiedad óptica del material se modificó mediante la adición de rGO, donde se reduce la banda prohibida de energía, el incremento en la cantidad de rGO no tuvo un impacto positivo en el rendimiento fotocatalítico, especialmente bajo fuentes de irradiación visible debido a un exceso de rGO, el cual tiene un efecto de apantallamiento para la absorción de luz y podría actuar como un centro de recombinación que dificulta la fotoactividad del TiO_2. El rendimiento fotocatalítico reveló que un menor contenido de rGO logra una mejor fotoactividad. Además, se determinó que la principal contribución de rGO sobre el fotocatalizador fue reducir el efecto de recombinación, demostrando que una combinación de dopaje con nitrógeno e incorporación de rGO podría ser una buena estrategia para superar las limitaciones de la fotocatálisis de TiO_2.

Se utilizaron especies carroñeras para determinar el mecanismo fotocatalítico bajo diferentes fuentes de irradiación. Se realizaron estudios adicionales sobre las intensidades de irradiación para investigar la viabilidad del uso de la luz solar natural. Los resultados mostraron que el modelo cinético y el mecanismo de degradación dependen principalmente del tipo de contaminante más que de la fuente de irradiación. Además, se encontró que el proceso de adsorción juega un papel importante, principalmente bajo fuentes de irradiación visible. Sin embargo, aunque la fuente de irradiación no determina el mecanismo de degradación, sí afecta significativamente la tasa de degradación para la eliminación de contaminantes. Además, se determinó que, bajo la irradiación solar natural, el proceso de fotólisis se redujo significativamente, mientras que la fotocatálisis de TiO_2 mostró una buena eficiencia de eliminación de CIP, lo que indica que el fotocatalizador N/TiO_2/rGO podría utilizar eficientemente la energía solar para la eliminación de MCO presentes en el agua.

El fotocatalizador N/TiO_2/rGO se inmovilizó sobre una espuma cerámica de Al_2O_3 aplicando el método de recubrimiento por inmersión y un tratamiento térmico suave, utilizando SiO_2 como aglutinante para mejorar la estabilidad y la reutilización. La estabilidad y reutilización del N/TiO_2/rGO inmovilizado se evaluaron varias veces mediante la degradación de tres MCO diferentes. Después de varios ciclos fotocatalíticos repetitivos (19 ciclos), el

fotocatalizador no perdió fotoactividad, lo que demuestra que tiene buena estabilidad y reutilización. Además, se encontró que la espuma cerámica de poros abiertos resultó ser una alternativa para la inmovilización de fotocatalizadores debido a la reducción de la limitación de transferencia de masa y al mismo tiempo proporciona una buena área para la irradiación.

Finalmente, los subproductos de transformación de la eliminación de CIP y DCF bajo diferentes fuentes de irradiación fueron seguidos por el espectrómetro de masas Orbitrap Exploris 120. Los resultados mostraron que, bajo fuentes de irradiación visibles, la mayoría de los subproductos de transformación detectados permanecían en la solución después de dos horas de irradiación, y algunos subproductos formados podrían ser potencialmente más tóxicos que los compuestos originales.

Palabras claves: Síntesis asistida por microondas; fotocatálisis, N/TiO_2/rGO; fuentes de irradiación; microcontaminantes orgánicos; productos de transformación; tratamiento de aguas.

RESUM AMPLIAT EN CATALÀ

L'aigua és un dels elements essencials per a la vida perquè gairebé totes les activitats humanes s'hi basen, i ha sigut declarada un dret humà el 2010 per l'Assemblea General de les Nacions Unides. Malgrat això, el ràpid creixement demogràfic i l'escalfament global han provocat una crisi mundial de l'aigua. Estudis recents han estimat que la meitat de la població mundial experimenta una greu escassetat d'aigua almenys un mes a l'any, mentre que gairebé 1.500 milions de persones viuen en zones amb un risc d'escassetat d'aigua alt o extremadament alt. A més dels problemes d'escassetat d'aigua, el desenvolupament continu de nous productes químics per a diferents aplicacions i el seu abocament posterior en cossos d'aigua sense un tractament adequat o, fins i tot, sense tractament, és un altre desafiament que intensifica la crisi de l'aigua. En els darrers 20 anys s'ha centrat una important atenció en els anomenats microcontaminants orgànics (MCO), integrats principalment en productes farmacèutics, productes de cura personal, subproductes de la desinfecció, disruptors endocrins i tots els seus subproductes de transformació, a causa del seu possible impacte negatiu sobre el medi ambient. Diversos estudis han demostrat que, a banda del fet que les plantes de tractament d'aigües residuals convencionals (PTAR) no eliminen fàcilment els MCO, algunes són persistents i es podrien bioacumular, fet que danya el sistema aquàtic i amenaça la salut pública. Tenint en compte l'escassetat d'aigua i el continu augment de l'estrès hídric a moltes regions del món, la reutilització de l'aigua s'està convertint en la solució més pràctica per a superar la crisi de l'aigua. Tot i això, per garantir l'eliminació completa dels MCO i la seguretat de l'aigua de reutilització, s'han d'implementar noves tecnologies de tractament juntament amb les PTAR existents.

Els processos d'oxidació avançada (POA) han estat considerats alternatives interessants per eliminar els MCO de les aigües residuals amb alta eficiència d'oxidació i sense contaminació secundària. Entre els diferents POA, la fotocatàlisi heterogènia de TiO_2 s'estudia activament a causa de la seva excel·lent activitat fotocatalítica, baix cost, excel·lent estabilitat química i no-toxicitat. El TiO_2 s'activa mitjançant l'energia lluminosa que produeix espècies reactives d'oxigen (ERO), que posteriorment poden oxidar els MCO de manera no selectiva. Amb tot, a causa de la seva alta banda prohibida d'energia (3,2 eV), la fotoactivació del TiO_2 es produeix només per llum ultraviolada (UV), la qual cosa en dificulta el potencial amb la radiació solar (4% UV, 48% Visible) . A més, el ràpid efecte de recombinació dels parells fotogenerats electró/buit (e^-/h^+) que produeixen les ERO pot reduir l'activitat fotocatalítica del TiO_2. Per tant, per superar aquests dos inconvenients principals, el dopatge amb TiO_2 és una de les estratègies més investigades per prevenir el procés de recombinació o per canviar la resposta

òptica del TiO_2 al rang de llum visible per augmentar l'eficiència fotocatalítica sota la radiació solar.

El dopatge amb metalls, com ara Pd, Pt, Au, Cu, Fe, etc., ha mostrat una activitat fotocatalítica millorada en el rang visible; no obstant això, els alts costos del metall i la probabilitat de lixiviació del metall degut a la baixa estabilitat tèrmica podrien ser un risc per a la salut, fet que en redueix l'aplicabilitat. Per tant, el dopatge amb no metalls, com ara N, P, S i C, ha estat una forma més pràctica i menys costosa de millorar la fotoactivitat sota la irradiació de l'espectre solar. Entre els dopatges no metàl·lics, el nitrogen és àmpliament estudiat a causa de la seva similitud en ràdio atòmica amb l'oxigen, per tant, fa més probable la substitució atòmica. El TiO_2 dopat amb nitrogen ha mostrat una interessant resposta fotoactiva sota llum visible, que es pot atribuir a la formació de nous nivells energètics que redueixen la banda prohibida. A més, alguns estudis suggereixen que el nitrogen podria afavorir la formació de la fase anatasa del TiO_2, la polimorfa més fotoactiva del TiO_2. D'altra banda, l'òxid de grafè reduït (rGO) ha atret molta atenció com a material per produir compostos de TiO_2 per la seva alta àrea superficial i bona conductivitat tèrmica i electrònica que podria millorar la fotoactivitat del TiO_2. Estudis recents han demostrat que acoblar rGO amb TiO_2 pot millorar l'activitat fotocatalítica perquè rGO actua com un embornal d'electrons, separa càrregues fotogenerades i redueix l'efecte de recombinació. Per tant, integrar el nitrogen i l'rGO al TiO_2 podria ser un enfocament interessant per abordar els dos principals inconvenients del TiO_2 esmentats anteriorment.

A més de l'estratègia de dopatge, el mètode de síntesi de TiO_2 hi juga un paper important a causa de la seva influència en les propietats estructurals, morfològiques i òptiques, que determinen l'activitat fotocatalítica en general. Algunes estratègies de síntesi convencionals comunes són el mètode sol-gel, la deposició química de vapor, o el mètode hidrotermal, entre d'altres. El principal inconvenient d'aquests mètodes és el llarg temps de síntesi. Tot i això, el mètode assistit per microones va sorgir per primera vegada com un mètode d'escalfament no convencional i recentment s'ha convertit en una alternativa atractiva a causa del menor temps de síntesi i menor consum d'energia en comparació dels mètodes de síntesi convencionals. Aquests avantatges del mètode assistit per microones es deuen principalment a l'escalfament directe "al nucli" de la barreja de reacció mitjançant la radiació de microones, que es deu a la ràpida conversió d'energia electromagnètica en energia tèrmica, fet que redueix el gradient de temperatura dins del recipient de reacció i contribueix a la producció d'un material amb propietats més homogènies.

A més de l'alta energia de la banda prohibida i el factor de recombinació, l'ús de TiO_2 en pols suspesa presenta desafiaments tècnics i econòmics per a la recuperació i la reutilització de fotocatalitzadors en el tractament d'aigües residuals. Així, per evitar el procés de recuperació i simplificar la reutilització del fotocatalitzador, s'ha immobilitzat TiO_2 sobre diferents suports com ara vidre, polímers, partícules magnètiques, ceràmiques, etc. La immobilització de TiO_2 sobre ceràmica s'ha estudiat activament en els darrers anys perquè el suport és inert químicament, té alta resistència a la llum ultraviolada, estabilitat mecànica i una gran àrea superficial, cosa que el converteix en una opció adequada per a la immobilització de fotocatalitzadors .

Per tant, aquesta investigació se centra en la síntesi de fotocatalitzadors basats en TiO_2 de baixa energia de banda prohibida, i s'utilitza una tècnica no convencional com el mètode assistit per microones. El fotocatalitzador desenvolupat es podria utilitzar per eliminar microcontaminants orgànics (MCO) de l'aigua utilitzant energia solar de manera eficient. Inicialment, es va avaluar el paper de la temperatura, el temps de reacció i el contingut de nitrogen a les propietats estructurals, morfològiques i fotocatalítiques del TiO_2 dopat amb nitrogen (N/ TiO_2) per a l'eliminació de ciprofloxacina (CIP) amb radiació UVA, solar i visible. Els resultats van mostrar que s'aconsegueix una cristal·linitat més gran i una mida més gran de vidre a una temperatura més alta (200°C), mentre que el temps de reacció al forn de microones té un efecte insignificant sobre les propietats morfològiques i fotocatalítiques. Es va descobrir que la temperatura és el paràmetre crucial a la síntesi de TiO_2 mitjançant el mètode assistit per microones.

D'altra banda, els canvis en el contingut de nitrogen van revelar que els canvis en la relació molar N/Ti gairebé no van influir en les propietats morfològiques i òptiques. Per contra, la variació del contingut de nitrogen va tenir un impacte rellevant en el rendiment fotocatalític, especialment sota fonts d'irradiació visible. Aquest efecte positiu, principalment sota la irradiació visible, es va atribuir als nous nivells energètics més que no pas a la reducció de la banda prohibida d'energia, cosa que va contribuir a l'adsorció de fotons a l'espectre visible. A més, es va observar que amb una relació molar N/Ti més gran, es millorava l'activitat fotocatalítica en l'eliminació de CIP sota diferents fonts d'irradiació. Tot i això, després de certa concentració de nitrogen, podria tenir un efecte desfavorable en la taxa de degradació perquè el nitrogen podria actuar com un centre de recombinació que afavoreix la recombinació de càrregues.

Es va avaluar el paper del contingut d'rGO (0,25 – 10% en pes d'rGO) a les propietats morfològiques i l'activitat fotocatalítica de N/ TiO_2/rGO a la degradació de tres MCO diferents (ciprofloxacina (CIP), diclofenac (DCF) i àcid salicílic (AS)) sota diferents fonts de radiació (UVA, solar i visible). Es va trobar que tot i que la propietat òptica del material es va modificar mitjançant l'addició d'rGO, on es redueix la banda prohibida d'energia, l'increment en la quantitat d'rGO no va tenir un impacte positiu en el rendiment fotocatalític, especialment sota fonts de irradiació visible a causa d'un excés d'rGO, que té un efecte d'apantallament per a l'absorció de llum i podria actuar com a centre de recombinació que dificulta la fotoactivitat del TiO_2. El rendiment fotocatalític va revelar que un menor contingut de rGO aconsegueix una millor fotoactivitat. A més, es va determinar que la principal contribució d'rGO sobre el fotocatalitzador va ser reduir l'efecte de recombinació, demostrant que una combinació de dopatge amb nitrogen i incorporació d'rGO podria ser una bona estratègia per superar les limitacions de la fotocatàlisi de TiO_2.

Es van utilitzar espècies carronyeres per determinar el mecanisme fotocatalític sota diferents fonts d'irradiació. Es van fer estudis addicionals sobre les intensitats d'irradiació per investigar la viabilitat de l'ús de la llum solar natural. Els resultats van mostrar que el model cinètic i el mecanisme de degradació depenen principalment del tipus de contaminant més que no pas de la font d'irradiació. A més, es va trobar que el procés d'adsorció hi juga un paper important, principalment sota fonts d'irradiació visible. Tot i això, encara que la font d'irradiació no determina el mecanisme de degradació, sí que afecta significativament a la taxa de degradació per a l'eliminació de contaminants. A més, es va descobrir que sota la irradiació solar natural, el procés de fotòlisi es va reduir significativament, mentre que la fotocatàlisi de TiO_2 va mostrar una bona eficiència d'eliminació de CIP, cosa que indica que el fotocatalitzador N/ TiO_2/rGO podria utilitzar eficientment l'energia solar per a l'eliminació de MCO de l'aigua.

El fotocatalitzador N/ TiO_2/rGO es va immobilitzar sobre una escuma ceràmica d'Al_2O_3 amb l'aplicació del mètode de recobriment per immersió i un tractament tèrmic suau, i amb l'ús de SiO_2 com a aglutinant per millorar l'estabilitat i la reutilització. L'estabilitat i la reutilització del N/TiO_2/rGO immobilitzat es van avaluar diverses vegades mitjançant la degradació de tres OMP diferents. Després de diversos cicles fotocatalítics repetitius (19 cicles), el fotocatalitzador no va perdre fotoactivitat, cosa que demostra que té bona estabilitat i reutilització. A més, es va trobar que l'escuma ceràmica de porus oberts va resultar ser una alternativa per a la immobilització de fotocatalitzadors a causa de la reducció de la limitació de transferència de massa i, alhora, proporciona una bona àrea per a la irradiació.

Finalment, els subproductes de transformació de l'eliminació de CIP i DCF sota diferents fonts d'irradiació van ser seguits per l'espectròmetre de masses Orbitrap Exploris 120. Els resultats van mostrar que, sota fonts d'irradiació visibles, la majoria dels subproductes de transformació detectats romanen en la solució després de dues hores d'irradiació, i que alguns subproductes formats podrien ser potencialment més tòxics que els compostos originals.

Paraules clau: Síntesi assistida per microones; fotocatàlisi; N/TiO$_2$/rGO; fonts d'irradiació; microcontaminants orgànics; productes de transformació; tractament d'aigües.

LIST OF ACRONYMS

AcAc	Acetylacetone
AMR	Antimicrobial Resistance
AOP	Advanced Oxidation Process
ATR	Attenuated Total Reflectance
BVL	Blue Visible Light
CB	Conduction Band
CIP	Ciprofloxacin
CVL	Cold Visible Light
DCF	Diclofenac
DRS	Diffuse Reflectance Spectroscopy
EDXS	Energy Dispersive X-ray Spectroscopy
***E*g**	Energy bandgap
EQSD	Environmental Quality Standards Directive
EtOH	Ethanol
EU	European Union
FTIR	Fourier-Transform InfraRed spectroscopy
GO	Graphene Oxide
HPLC	High-Performance Liquid Chromatography
HRMS	High Resolution Mass Spectrometry
MW	Microwave
NSAID	Non-Steroidal Anti-Inflammatory Drug
OMP	Organic Micropollutant
rGO	Reduced Graphene Oxide

ROS	Reactive Oxygen Species
SA	Salicylic Acid
SEM	Scanning Electron Microscopy
SLS	Solar Light Simulator
TTIP	Titanium (IV) isopropoxide
UVA	Ultraviolet-A
VB	Valence Band
WFD	Water Framework Directive
WWTPs	Wastewater Treatment Plants
XPS	X-ray Photoelectron Spectroscopy
XRD	X-Ray Diffraction

TABLE OF CONTENTS

LIST OF FIGURES

LIST OF TABLES

1. INTRODUCTION

Water is one of the essential elements of life because almost all human activities are based on it, declared a human right in 2010 by the United Nations General Assembly. However, the fast-growing population and global warming have led to a global water crisis. Recent studies estimated that half-global population is experiencing severe water scarcity at least one month per year, while nearly 1.5 billion people live in areas with high or extremely high-water scarcity risk [1, 2]. Due to the water scarcity and continuous increment of water stress in many regions worldwide, water reuse is becoming one of the most practical solutions to overcome the water crisis[3], especially for the agricultural sector, one of the most water-demanding sectors [4].

Apart from the water scarcity issues, the continuous development of society and technological processes brought about the use of new chemical products for different applications, which are released into water bodies without suitable treatment or even no treatment after performing their end goal. This is another challenge that intensifies the water crisis. [5]. In the last 20 years, significant attention has been focused on the anthropogenic contaminants in water, including the so-called organic micropollutants (OMPs), organic carbon based molecules that includes pharmaceuticals, personal care products, disinfection byproducts, endocrine disruptors, and all their transformation products (TPs). Among the different OMPs, pharmaceutical compounds are quite relevant due to their potential negative impact on the environment [6–8]. Several studies have shown that apart from the fact that OMPs are not easily removed by conventional wastewater treatment plants (WWTPs), some are persistent and could bioaccumulate, harming the aquatic system and threatening public health [9, 10]. Considering the water reuse scenario and the public health risk that involves the OMPs, new treatment technologies coupled with existing WWTPs must guarantee the complete removal of OMPs and the safety of reused water [11, 12].

Advanced oxidation processes (AOPs) such as ozonation, Fenton, photocatalysis, photoelectrocatalysis, ultrasound-assisted oxidation, etc., have been considered interesting alternatives for removing OMPs from wastewater with high oxidation efficiency and no secondary pollution [13–18]. Among different AOPs, TiO_2 heterogeneous photocatalysis is actively studied because of its outstanding photocatalytic activity, low cost, excellent chemical stability, and non-toxicity [19, 20]. TiO_2 is activated by the light energy that produces reactive oxygen species (ROS), which subsequently can oxidize OMPs non-selectively. However, due to its high energy bandgap (3.2 eV), photoactivation of TiO_2 occurs only by ultraviolet (UV)

light, hindering its potential under solar radiation (4% UV, 48% Visible) [21, 22]. Additionally, the fast recombination effect of the photogenerated electron/hole (e^-/h^+) pairs that produce ROS can reduce TiO_2 photocatalytic activity [23, 24]. Therefore, to overcome these two main drawbacks, TiO_2 doping is one of the most investigated strategies either for preventing the recombination process or for shifting the optical response of TiO_2 into the visible light range, aiming to boost photocatalytic efficiency under solar radiation.

Metal doping such as Pd, Pt, Au, Cu, Fe, etc., have shown improved photocatalytic activity in the visible range; however, the high costs of metal and the probability of metal leaching due to low thermal stability might be a health risk, reducing their applicability [25–27]. Therefore, non-metal dopants, such as N, P, S, and C, has been a more practical and less expensive way to enhance photoactivity under solar spectrum irradiation [28–30]. Among non-metal doping, nitrogen is widely studied due to its similarity in atomic radius with oxygen, making atomic substitution more probable [31]. Nitrogen-doped TiO_2 has shown an interesting photoactive response under visible light, which can be attributed to the formation of new energetic levels that reduce the energy bandgap [19, 32, 33]. Additionally, some studies suggest nitrogen could favor the TiO_2 anatase phase formation, the most photoactive TiO_2 polymorph [34].

On the other hand, reduced graphene oxide (rGO) has attracted significant attention as a material for producing composites rGO/TiO_2 due to its high surface area and good thermal and electronic conductivity that could improve the photoactivity of TiO_2 [35, 36]. Recent studies have shown that coupling rGO with TiO_2 can improve photocatalytic activity because rGO acts as a sink of electrons, separating photogenerated charges and reducing the recombination effect [37–39]. So, integrating nitrogen and rGO with TiO_2 could be an interesting approach for tackling the two main TiO_2 drawbacks mentioned before.

In addition to the doping strategy, the TiO_2 synthesis method plays an important role due to its influence on the structural, morphological, and optical properties, which determine the overall photocatalytic activity [31, 40]. Some common conventional synthesis strategies are the sol-gel method, chemical vapor deposition, hydrothermal, etc. The main drawbacks of these methods are the long synthesis time and higher energy consumption [41]. However, the microwave-assisted method first emerged as a non-conventional heating method and has recently become an attractive alternative because of its shorter synthesis time and lower energy consumption than conventional synthesis methods [42]. These advantages of the microwave-

assisted method are mainly due to the direct "in core" heating of the reaction mixture by the microwave radiation, which is due to the fast conversion of electromagnetic energy into heat energy[43], reducing the temperature gradient inside the reaction vessel and contributing to the production of a material with more homogeneous properties [41, 44].

Besides the high energy bandgap and the recombination factor, using TiO_2 in a suspended powder presents technical and economic challenges for photocatalyst recovery and reusability in wastewater treatment. Thus, to avoid the recovery process and simplify further reuse of the photocatalyst, TiO_2 has been immobilized over different supports such as glass, polymers, magnetic particles, ceramics, etc. [45–48]. TiO_2 immobilization over ceramics has been actively studied in recent years because this support provides excellent chemical inertness, high UV light resistance, mechanical stability, and a large specific surface area, making it a suitable option for photocatalyst immobilization [49, 50].

Therefore, this research focused on developing a N/TiO_2/rGO photocatalyst synthesized by microwave-assisted method for removing OMPs using different irradiation sources. Initially, the role of the temperature, reaction time, and nitrogen content was evaluated on the structural, morphological, and photocatalytic properties of nitrogen-doped TiO_2 (N/TiO_2) for the ciprofloxacin (CIP) removal under UVA, solar and visible lights sources. Once the operational parameters in the microwave oven and the optimal nitrogen doping load were established, the role of rGO content (0.25 – 10 wt. % of rGO) in the morphological properties and photocatalytic activity of N/TiO_2/rGO was evaluated in the degradation of three different OMPs (CIP, diclofenac (DCF), and salicylic acid (SA)) under different radiation sources (UVA light, solar light, and visible light).

Scavenging species were used to determine the photocatalytic mechanism under various irradiation sources after obtaining the most photoactive N/TiO_2/rGO nanocomposite among all synthesized and evaluated materials. Additional studies on irradiation intensities were performed to investigate natural solar light's feasibility. Subsequently, the N/TiO_2/rGO photocatalyst was immobilized over Al_2O_3 ceramic foam by applying the dip-coating method and mild thermal treatment, using SiO_2 as a binder to enhance stability and reusability. The stability and reusability of the immobilized N/TiO_2/rGO were evaluated several times through the degradation of three different OMPs. Finally, the TPs of CIP and DCF removal under different irradiation sources were identified by means of Orbitrap high resolution mass

spectrometry (HRMS). Salicylic acid was not considered as a model compound to make TPs analysis using HRMS due to the simplicity of this molecule compared to CIP or DCF.

As the model substances, aqueous solutions of CIP, DCF, and SA were used. The DCF and CIP were included in the first and second EU watch list of substances for union-wide monitoring in the field of water policy, respectively [51, 52]. Meanwhile, SA is a precursor and a transformation byproduct of acetylsalicylic acid, one of the most widely used analgesics and additives for several healthcare products [15].

All synthesized nanomaterials were characterized by X-ray diffraction (XRD) analysis, N_2 adsorption isotherms (BET), Raman spectroscopy, Fourier-transform infrared spectroscopy (FTIR), scanning electron microscopy with energy dispersive X-ray spectroscopy (SEM/EDS), and diffuse reflectance spectroscopy (DRS). The most photoactive materials (N/TiO_2 and N/TiO_2/rGO nanocomposites) were also characterized by X-ray photoelectron spectroscopy (XPS) analysis. OMP removal was followed-up by UV-VIS spectrophotometer and HPLC chromatography equipped with UV-Vis detector and diode array detector.

Apart from the contribution to photocatalyst development by the microwave-assisted method and the role played by the doping elements, this scientific work was performed to understand the photocatalyst behavior under different irradiation sources. Although there are plenty of scientific articles regarding TiO_2 doping and evaluation under solar or visible irradiation, there are scarce publications in which different irradiation sources and intensities are compared in the photocatalytic processes. Parts from this dissertation have already been included in peer reviewed journal articles with open access, published in journal Nanomaterials (Q1) and referenced as references 133 and 134.

2. WATER: LITERATURE REVIEW

2.1. Water related issues

2.1.1. Water distribution and water scarcity

Although around 70% of Earth's surface is covered by water, barely 2.5% is freshwater humans can use. However, most of the freshwater is locked up in ice and the ground, having available for human activities less than 2% of freshwater. On the other hand, water quantity has always been the same, and it is recycled and distributed through the water cycle. Due to global warming, the water cycle has been altered, with climate changes in which some regions are affected by severe droughts while others suffer heavy floods. In 2021, around 62% of registered internal displacement was caused by natural disasters, while more than 200 million people are expected to be displaced by 2050 [53].

On the other hand, prolonged and severe droughts have caused nearly half of the global population to experience water scarcity at least one month per year, and the number of people living in water-stressed areas has increased to 2.3 billion [54]. Considering the continuous and fast-growth population and the increasing demand for water, particularly in agriculture, where almost 72% of water withdrawal is for this purpose [4, 54], water resources must be managed sustainably. In this context, water reuse is one of the most feasible solutions to mitigate water shortages and contribute to a sustainable water supply for everyone.

2.1.2. Water pollution and organic micropollutants

Besides the lack of fresh water, water quality is another challenge in the worldwide water crisis. According to the United Nations, 80% of wastewater is discharged into the environment without any treatment, worsening the situation of 1.8 billion people that do not have access to safe drinking water [54]. In addition, the development of thousands of new chemicals for various applications and subsequent releases into the environment without any regulation contribute to the pollution of freshwater sources, mainly in low and middle-income countries [10, 55]. In the last two decades, significant attention has been paid to OMPs, organic carbon-based substances with an anthropogenic origin that could cause adverse environmental impacts. These OMPs, primarily composed of pharmaceuticals, personal care products,

disinfection byproducts, endocrine disruptors, and all their transformation byproducts, are usually found at very low concentrations on the order of micrograms (µg) or nanograms (ng) per liter [56, 57]. It has been observed that conventional WWTPs have problems removing some OMPs, allowing their entry into the environment. In the case of pharmaceutical molecules, principally antibiotic compounds such as ciprofloxacin (CIP), releasing this kind of compound could lead to persistence and bioaccumulation in the environment, promoting the appearance of antibiotic-resistant bacteria [6, 8, 58–60].

Due to the need to gather information regarding the effects and consequences of continuous exposure to OMPs, the European Union decided through its Water Framework Directive (WFD) 2000/60/EC and the Environmental Quality Standards Directive (EQSD) 2008/105/EC to establish a list of priority substances for monitoring. This list is to be revised every two years. In addition to the Priority List, in 2015, the Decision (EU) 2015/495 established the first Watch list, which initially listed ten substances to monitor [51]. Since then, the watch list has been continuously updated: in 2018 by the Decision (EU) 2018/840, in 2020 by the Decision (EU) 2020/1161, and in 2022 by the Decision (EU) 2022/1307 [52, 61, 62]. The inclusion of new substances in the list is based on the EU Strategic Approach to Pharmaceuticals in the Environment and the European One Health Action Plan against Antimicrobial Resistance (AMR). In contrast, excluding substances from the list depends on whether there is sufficient high-quality monitoring data about it or whether the substance has been continuously monitored for four years.

2.1.3. Target organic micropollutants in water

Taking into account some of the pollutants listed on the EU Watch list since 2015 and considering the most commonly consumed pharmaceuticals, the following target pollutants were selected to be studied in this research: CIP, DCF, and SA. Although SA has not been included in the EU Watch list, this pharmaceutical product is the precursor for aspirin, one of the most widely used painkillers without a medical prescription.

Ciprofloxacin

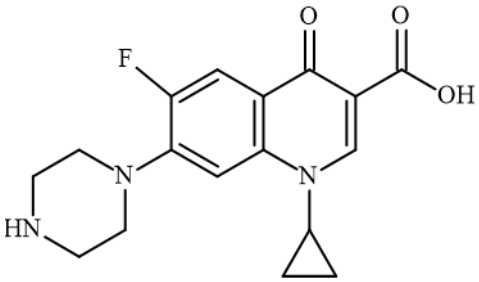

Figure 1. Chemical structure of ciprofloxacin.

The 1-cyclopropyl-6-fluoro-4-oxo-7-piperazin-1-ylquinoline-3-carboxylic acid (molecular formula: $C_{17}H_{18}FN_3O_3$, molecular weight: 331.34 g·mol^{-1}), also known as ciprofloxacin (CIP) is a fluoroquinolone antibacterial used to treat and prevent some urinary, lower respiratory tract, and skin infections. Figure 1 shows the molecular structure of ciprofloxacin. CIP is one of the most often found OMPs in the effluents of wastewater, surface waters, and drinking waters, with an average concentration of 6.0 μg·L^{-1} [63], and a maximum of up to 6.5 mg·L^{-1} [7, 64]. Due to the lack of its efficient removal by biological systems and due to inaccurate information about its toxicity and bioaccumulation, it was included in the second EU watch list of substances for union-wide monitoring in the field of water policy (Decision (EU) 2018/840 of 5 June 2018) and continued under monitoring in the third EU watch list (Decision (EU) 2020/1161 of 4 August 2020) [52, 61].

Diclofenac

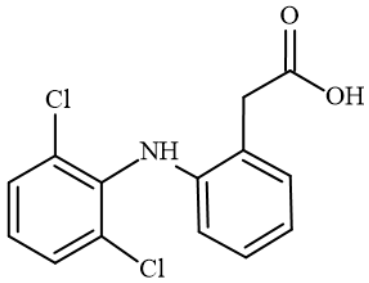

Figure 2. Chemical structure of diclofenac.

The 2-[2-(2,6-dichloroanilino) phenyl] acetic acid (molecular formula: $C_{14}H_{11}Cl_2NO_2$, molecular weight: 296.10 g·mol^{-1}), also known as diclofenac (DCF), is a nonsteroidal anti-inflammatory drug (NSAID). Figure 2 shows the molecular structure of diclofenac. DCF is widely used to treat chronic arthritis, inflammation, and mild-to-moderate pain. Due to its large production and consumption, DCF has been detected in wastewater, surface water, and drinking

waters in the range ng·L^{-1} to µg·L^{-1} [65–67]. Some toxicological studies have concluded that even at low concentrations, DCF negatively impacts aquatic organisms, mainly affecting liver, kidney, and gill cells [68–70]. Because of its toxicity to aquatic life, bioaccumulation, and ineffective removal by conventional WWTPs, it was included as one of the ten substances listed in the first EU watch list (Decision (EU) 2015/495 of 20 March 2015) [51].

Salicylic acid

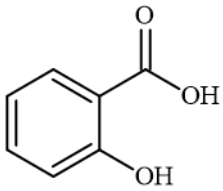

Figure 3. Chemical structure of salicylic acid.

The 2-hydroxybenzoic acid (molecular formula: $C_7H_6O_3$, molecular weight: 138,12 g·mol^{-1}), also known as salicylic acid (SA) and with chemical structure as shown in Figure 2, is the precursor and transformation byproduct of the most used analgesics worldwide, the aspirin [15]. Also, SA is widely used in the pharmaceutical industry as raw material for several healthcare products, such as creams and skin-care ointments [71, 72]. Although several studies have shown that SA could be removed in the conventional WWTPs, it is still found at low concentrations in wastewater-treated effluents, rivers, and drinking water [73, 74].

2.2. Water treatment

2.2.1. Water management and water reuse

Generally, in conventional water management, freshwater is taken from rivers, lakes, aquifers, etc., and treated in a water treatment plant (WTP) to make it potable or suitable according to industry needs; once it has been used, it is collected through the sewage system to the WWTPs, and finally disposed again into the environment, meeting water quality standards as per the regulations of each country. Figure 4 presents a schematic illustration of conventional water management. This water management model has been proven unsuitable for water scarcity scenarios due to its reliance on rain and the water cycle to replenish water reservoirs.

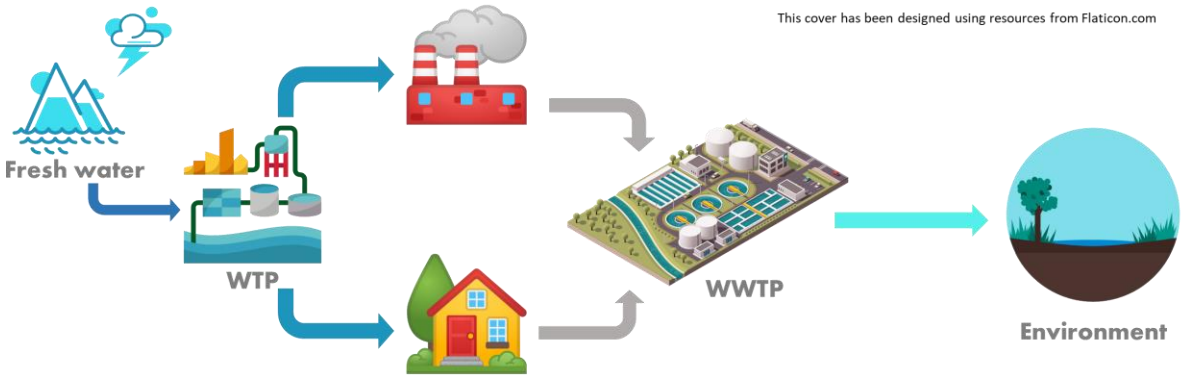

Figure 4. Conventional water management. (This schematic has been designed with resources from Flaticon.com)

Once the water has been used and collected in the sewage, it is treated in the WWTP, applying a combination of physical, physicochemical, and biological processes to remove principally suspended solids, organic and inorganic matter, and pathogens. However, due to the water scarcity crisis and the water supply needs for the growing population and agricultural purposes, a new water management approach, having water reuse as a primary objective, is proposed to be adopted to face the water crisis [75–77]. Figure 5 shows a schematic illustration of the new water management approach, framed on the circular economy and sustainability concept, in which reclaimed water can be used for different needs (e.g., agriculture or aquifer recharge). In this water management approach, it is necessary to implement new wastewater technologies linked to the existing WWTPs to ensure the complete removal of OMPs to safeguard public health and the environment [77].

Based on the water reuse concept, the EU recently established the minimum water reuse requirements for agricultural purposes by the regulation (EU) 2020/74 of 25 May 2020 [78]. Although this new regulation promotes water reuse and considers the development of risk assessment for the compounds of concern, the minimum water quality standards are based only on removing suspended solids, organic and inorganic matter, and pathogens, excluding any regulation regarding the OMPs. The lack of regulation regarding OMPs could be attributed mainly to two reasons. On one hand, although there are several techniques and methods to detect OMPs and their byproducts, economically, it still is not feasible to detect them at a large scale (such as municipal WWTPs). On the other hand, it is still in the research phase, and there are no general recommendations for the most feasible technologies for the efficient removal of OMPs.

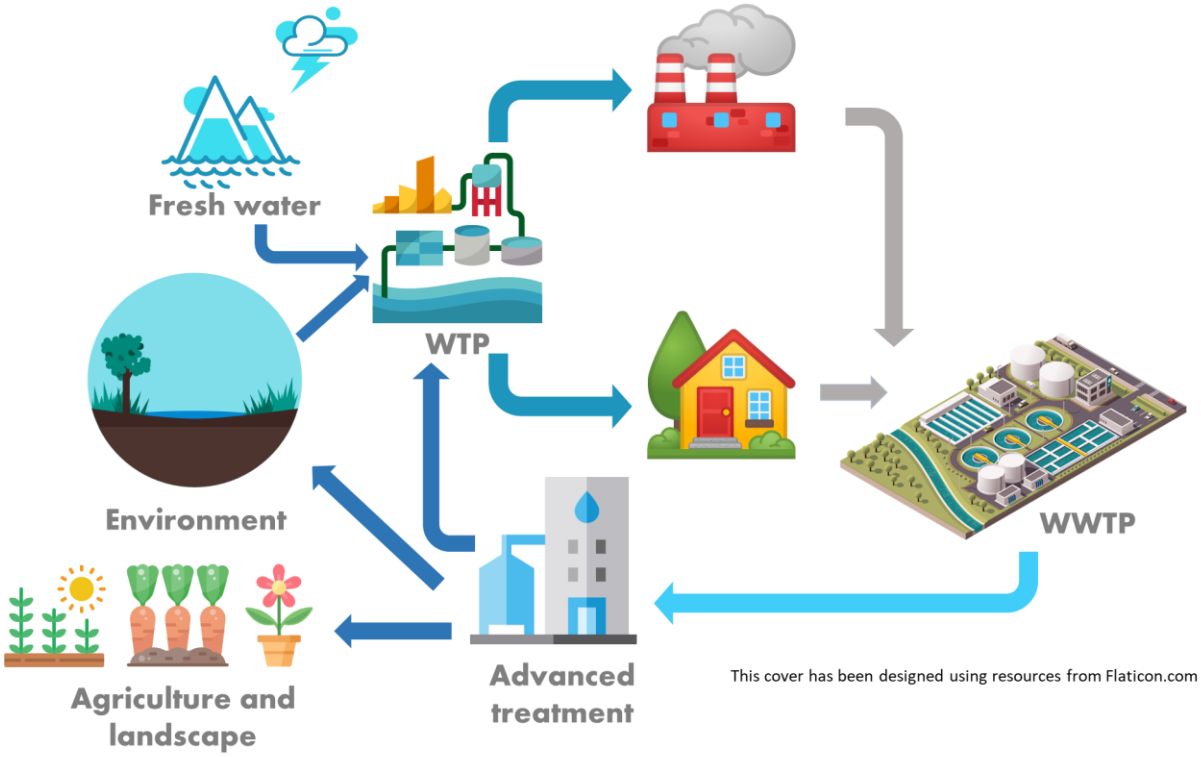

Figure 5. New water management approach. (This schematic has been designed with resources from Flaticon.com)

2.2.2. Advanced Oxidation Processes

Several technologies, such as adsorption, membrane separation, and advanced oxidation processes (AOPs), have been successfully applied to remove OMPs from wastewater [77, 79–81]. However, in the case of adsorption and membrane separation, these technologies do not eliminate the OMPs; they only move the contaminants from one phase to another or concentrate them, creating secondary pollution that needs further treatment. On the contrary, AOPs generate highly oxidizing species, including reactive oxygen species (ROS), that might transform OMPs into less toxic and more biodegradable molecules than their parent compounds or can even degrade them to carbon dioxide and water (mineralization) [79, 82, 83]. The main ROS commonly generated in most AOPs is the hydroxyl radical ($HO^{\bullet}$), which has the highest oxidative potential among all ROS (2.8 eV) and can non-selectively oxidize the OMPs [64, 84]. Other ROS that could be involved in AOPs are superoxide radical ($O_2^{\bullet-}$), singlet oxygen ($^1O_2$), and sulphate radical ($SO_4^{\bullet-}$), and their formation will depend on the type of AOPs and the target pollutant to be treated [18, 24, 85, 86].

AOPs can be classified into two main groups: photochemical and non-photochemical processes. Photochemical processes rely on light to generate ROS, such as Photo-Fenton, UV/O_3, heterogenous photocatalysis, UV/H_2O_2, and photolysis, while non-photochemical processes, such as ozonation, Fenton, sonolysis, and electrochemical oxidation use other forms of energy to produce ROS [14, 79, 83, 87, 88]. Also, AOPs could be divided into homogeneous or heterogeneous processes, depending on whether reactions occur in one or two phases. Table 1 describes some AOPs with their advantages and disadvantages.

Table 1. AOPs with their main advantages, and disadvantages [89, 90].

AOPs	**Advantages**	**Disadvantages**
UV/O_3	• Higher efficiency compared to UV or O_3 alone. • High biodegradability. • Effective for a wide range of OMPs. • Quickly scale up to WWTPs.	• Potential bromated byproduct formation. • High operation costs. • Not efficient with high turbidity. • Turbidity affects the efficiency of the process.
Fenton	• Inexpensive and non-hazard chemicals. • No energy input is required. • Effective for a wide range of OMPs, and high turbidity.	• Low pH operation (< 3) • Inorganic sludge production (Fe^{3+}). • Chemicals consumption.
Photo-Fenton	• High removal efficiency. • Efficiency is higher than Fenton. • Iron is regenerated by light.	• Low pH operation (< 3) • Chemicals consumption. • Turbidity affects the efficiency of the process.
Photocatalysis	• Reusability of catalyst. • Use of solar energy. • Mild operation conditions. • Mineralization of OMPs is possible.	• Catalyst recovery. • Difficult to scale up. • Turbidity affects the efficiency of the process.
UV/H_2O_2	• Quickly scale up to WWTPs. • Effective for a wide range of OMPs.	• Turbidity affects the efficiency of the process. • Chemicals consumption.

Sonolysis	• No chemicals are required. • Effective for a wide range of OMPs.	• High energy consumption. • A large amount of dissolved oxygen is required. • Difficult to scale up.

Among the different AOPs, heterogeneous photocatalysis is one of the most studied because of its potential to use an unlimited and free energy source, solar light. In heterogeneous photocatalysis, a semiconductor is irradiated with light to produce electron/hole (e^-/h^+) pairs that generate ROS, which can non-selectively oxidize different pollutants, including OMPs [15, 20]; also, the holes (h^+) on the photocatalyst's surface that are involved in the ROS generation can directly oxidize target pollutants. ZnO, WO_3, TiO_2, ZnS, and CdS are the most common semiconductors. However, TiO_2 is the most investigated photocatalyst because of its outstanding photocatalytic activity, low cost, excellent chemical stability, and non-toxicity.

2.2.3. TiO_2 photocatalysis

TiO_2 is a semiconductor with three different crystalline phases: anatase (tetragonal), rutile (tetragonal), and brookite (orthorhombic). However, anatase is the crystalline polymorphic form with the highest photocatalytic activity, while rutile is the most thermodynamically stable crystalline phase [24, 91]. TiO_2 is activated by the light energy producing reactive oxygen species (ROS), that can non-selectively oxidize OMPs (Figure 6). However, due to its high energy bandgap (3.2 eV), photoactivation of TiO_2 occurs only under UV light, hindering its potential under solar radiation (4 % UV, 48 % Visible). The fast recombination of photogenerated electron/hole (e^-/h^+) pairs that produce ROS can also reduce TiO_2 photocatalytic activity [23, 24]. Figure 6 shows the different mechanisms that can occur once a TiO_2 particle absorbs a photon.

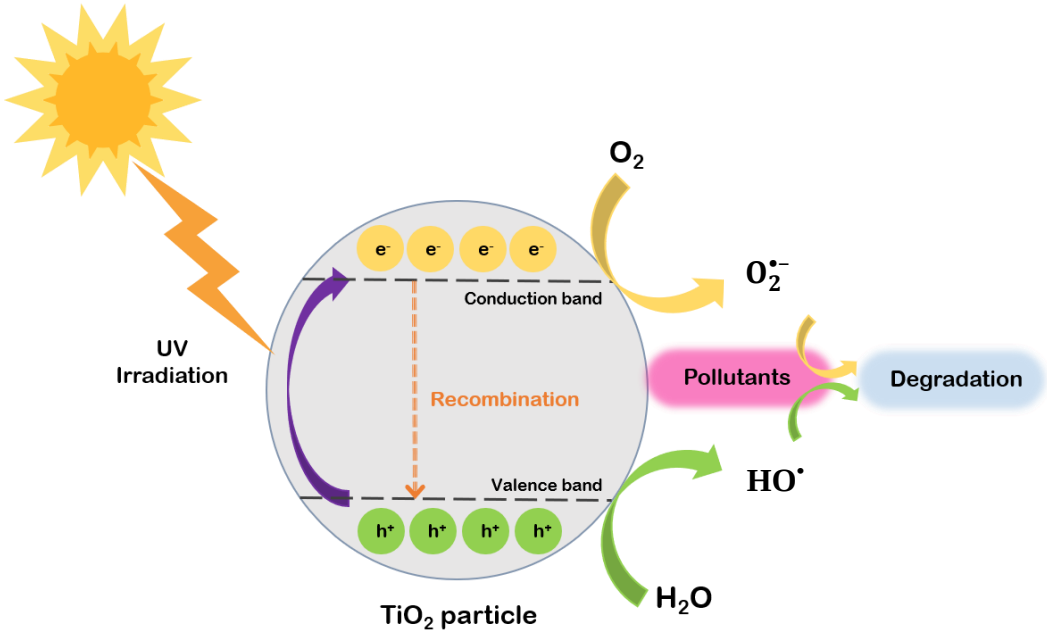

Figure 6. Mechanism of TiO_2 photocatalysis.

Once a photon is absorbed by the TiO_2, an electron (e^-) is transferred from the valence band (VB) to the conduction band (CB), leaving a hole (h^+) in the VB (eq. 1); after that, several reactions can take place. On one side, adsorbed water on the photocatalyst surface can react with the h^+ to form hydroxyl radical ($^{\bullet}OH$) (eq. 2), the ROS with the highest oxidation potential (2.8 V). Meanwhile, the absorbed oxygen can react with the e^- to form the superoxide radical ion ($O_2^{\bullet-}$) (eq. 4), another ROS. The pollutant can be degraded by the ROS or directly by the h^+/e^- charges when the photocatalyst adsorbs the contaminant [16, 92, 93]. If the h^+/e^- photo-formed charges do not participate in any of the possible mechanisms described before, in a short period, they recombine to release heat (recombination process, equation (9)). The following equations summarize the possible mechanisms during the photocatalysis process.

$$TiO_2 \xrightarrow{hv} h^+ + e^- \quad (1)$$

$$H_2O + h^+ \rightarrow {}^{\bullet}OH + e^- \quad (2)$$

$$OH^- + h^+ \rightarrow {}^{\bullet}OH \quad (3)$$

$$O_2 + e^- \rightarrow O_2^{\bullet-} \quad (4)$$

$$O_2^{\bullet-} + H^+ \rightarrow HO_2^{\bullet} \quad (5)$$

$$O_2^{\bullet-} + HO_2^{\bullet} \rightarrow {}^{\bullet}OH + O_2 + H_2O_2 \quad (6)$$

$$H_2O_2 + e^- \rightarrow {}^{\bullet}OH + OH^- \quad (7)$$

$$\text{Pollutant} \xrightarrow{TiO_2+hv} \text{intermediate} \xrightarrow{TiO_2+hv} CO_2 + H_2O \quad (8)$$

$$h^+ + e^- \rightarrow \text{heat (Recombination)} \quad (9)$$

2.2.4. TiO_2 synthesis method

The different pollutant removal mechanisms depend on several factors, including pollutant properties (p*Ka*) and photocatalyst properties (hydrophilicity, hydrophobicity, oxygen vacancies, doping element, composite, etc.) [94, 95]. Although pollutant removal somehow could be influenced by the pollutant properties, the photocatalytic activity performance is mainly defined by the photocatalyst properties, which are strongly influenced by the synthesis method [96, 97].

Multiple methods to obtain TiO_2 can be applied according to the final purpose (electronics, optics, energy storage, catalysis, etc.) [98–100]. However, the most common techniques for producing ceramics, photocatalysts, and thin films are the sol-gel method, hydrothermal and solvothermal because they allow controlling the morphological and textural properties of the TiO_2 [31, 96]. However, the long synthesis reaction time is the main drawback of the conventional synthesis method and consumes much energy. On the other hand, non-conventional synthesis methods like the microwave-assisted technique have appeared to be a promising alternative for material production due to their shorter reaction time and higher yield production, which could also significantly reduce the energy consumption used in material synthesis [44, 101, 102].

2.2.4.1. Sol-gel method

The sol-gel method is based on the principles of inorganic polymerization, in which hydrolysis and condensation reactions occur. This synthesis method allows controlling the particle size and shape based on the control of parameters such as pH, temperature, and precursor mixture [103, 104]. The main advantages of this technique are processing at low temperatures and ambient pressure, control of the size and shape of the particle, homogeneous material, and high purity [105, 106]. Figure 7 presents the different processing routes that derive from the sol-gel method. The main disadvantage of the sol-gel method is the long processing time, and for TiO_2 photocatalysis, the calcination step is required to obtain a crystalline material, which involves high energy consumption [93, 107].

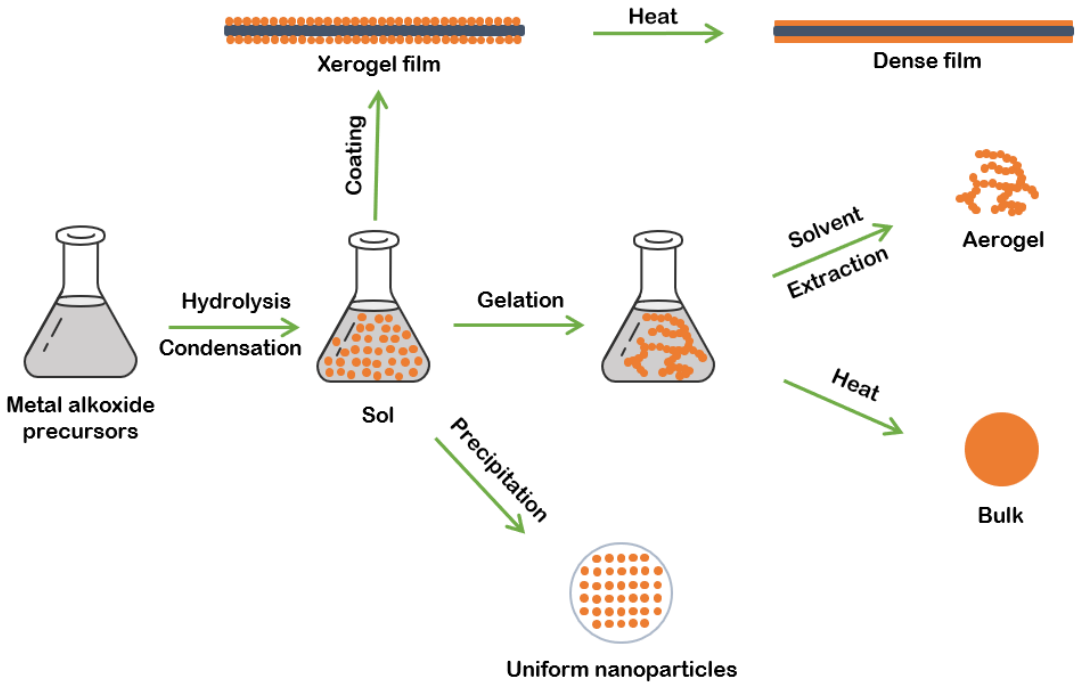

Figure 7. Material processing routes by sol-gel method.

2.2.4.2. Hydrothermal/Solvothermal method

Hydrothermal and solvothermal methods use the inner pressure created in a closed reaction vessel to produce crystalline materials under mild conditions (below 250°C and 40 bar) [31]. In these methods, particle size and shape can be controlled by modifying parameters such as temperature, pH, reaction vessel filling (inner pressure), and solvent [108]. The only difference between the hydrothermal and solvothermal methods is the solvent used for the synthesis; while the hydrothermal uses water, an organic solvent is employed in the solvothermal [96]. The hydrothermal/solvothermal method can produce materials in a shorter reaction time than the sol-gel method, and depending on the synthesis parameters, such as reaction vessel filling, a crystalline material can be obtained without requiring a further calcination step [86]. Although reaction time can be reduced to a few hours in this method, the main drawback of this synthesis method is that the homogeneity of material can be affected due to the temperature profile in the reaction vessel, as shown in Figure 8.

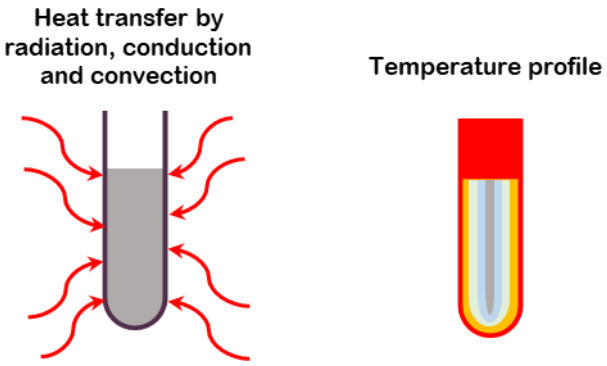

Figure 8. Temperature profile inside the reaction vessel during the material synthesis by hydrothermal/solvothermal method, produced by the conventional heat transfer.

2.2.4.3. Microwave-assisted method

The microwave-assisted method has been applied actively in the last two decades in different fields like organic chemistry, metal oxides, and nanoparticle synthesis because of its fast heating in the core of the reaction mixture by microwave radiation caused by dielectric heating effects [101, 109]. Dielectric heating occurs mainly by dipolar polarization and ionic conduction heat transfer mechanisms [31]. In one mechanism, dipoles of polar molecules oscillate synchronized with the oscillation of the electromagnetic field, causing friction and heat; this phenomenon is called dipolar polarization [110, 111]. On the other hand, ionic conduction heat occurs when dissolving charged particles also oscillate synchronized with the electromagnetic field, colliding them and releasing heat energy [108].

The high heating rate of reactants inside the reaction vessel is mainly caused by the rapid conversion of electromagnetic radiation into heat energy. Usually, materials with high dielectric loss absorb microwave radiation more efficiently and are heated quickly [35, 112]. Examples of these materials are some alcohols (methanol, ethanol, 1-propanol). Compared to the conventional heat transfer (Figure 8), hot spots inside the reaction vessel are formed, producing a more homogenous temperature distribution [101], as shown in Figure 9.

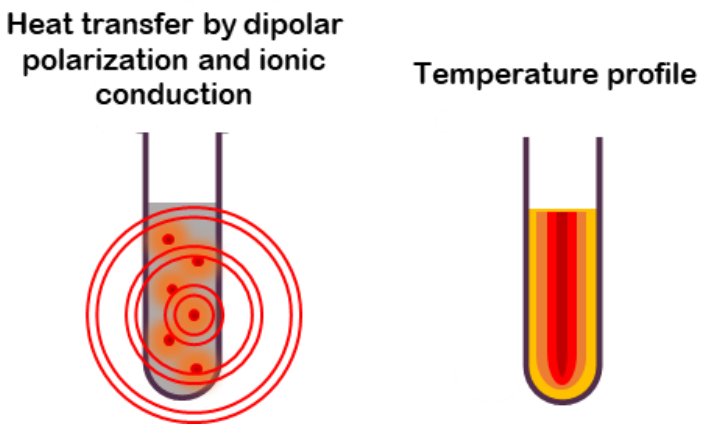

Figure 9. Hot spots are produced by dielectric heating and temperature profile inside the vessel.

When the microwave-assisted method is applied for material synthesis, the reaction time can be reduced to a few minutes. A homogeneous temperature distribution inside the vessel produces a high purity and yield material [110]. One of the microwave-assisted method's main drawbacks is the equipment cost and the limited size of reaction vessels (up to 1 L).

2.2.5. Doping elements

Apart from the synthesis method, the properties of the photocatalyst can be modified by introducing some elements that change the optical, electronic, and photoactivity properties of TiO_2. One of the most common strategies to change TiO_2 photoresponse to the visible light region has been the doping approach, in which metal and non-metal elements are incorporated [26, 113]. On the one hand, metal doping has been a promising approach for enhancing photocatalytic activity, either reducing recombination or shifting light absorption of TiO_2 to the visible light range. Metal dopants such as Fe, Pd, Pt, Au, etc., could act as an electron-trapping center that promotes the charge separation of photogenerated electron/hole pairs, and thus, charge recombination is reduced, improving the photocatalytic activity [25, 97, 114]. Also, it can reduce the energy band gap, as shown by Fe/TiO_2 materials [34, 87], or shift the photoactive response under visible light by the surface resonance plasmon effect that produces some elements like Au and Pt [115, 116]. However, metal stability and the high probability of leaching due to low thermal stability might represent a health risk that reduces their applicability [25, 26, 117]. Therefore, non-

metal doping, such as N, P, S, and C, seems more feasible and less expensive to enhance photoactivity under solar spectrum irradiation [28–30].

Although several non-metals have been used to dope TiO_2, nitrogen is one of the most studied doping elements because its atomic radius is quite similar to the oxygen atom, giving a higher probability of atomic substitution [31, 118]. Nitrogen incorporation into the TiO_2 lattice can significantly alter the electronic and optical properties of TiO_2 by creating new energy states within the TiO_2 bandgap, which could extend the absorption spectrum of the photocatalyst to the visible region [33, 119]. The photocatalytic performance of nitrogen-doped TiO_2 depends on several factors, such as the doping concentration, the type of nitrogen dopant, the type of doping (interstitial/substitutional), and the synthesis method [31, 86, 119]. Higher doping concentrations usually can lead to a higher concentration of oxygen vacancies and more efficient charge separation. However, excessive doping can also lead to the formation of recombination centers that can reduce the photocatalytic activity [118]. The type of nitrogen dopant can also affect the photocatalytic properties of the material, being ammonia and urea as the most used nitrogen-containing precursors in wet chemical synthesis, while high-temperature annealing process in the presence of a nitrogen-containing gas is widely used for doping synthesized TiO_2 [19, 32]. Interstitial or substitutional doping can occur depending on the synthesis method and the nitrogen precursor. Nitrogen is added to the TiO_2 lattice in interstitial doping, while substitutional doping involves oxygen replacement. Although nitrogen doping can occur interstitially or substitutionally, there is still no consensus on which type is most effective for light absorption shifting [19, 27, 29, 31].

On the other hand, carbon material has been extensively applied to create TiO_2 composites to improve charge separation, reduce the recombination process, and increase the photocatalytic activity of TiO_2 [99, 120, 121]. Among the different allotropic forms of carbon used for carbon-based TiO_2, graphene has attracted significant attention because of its exceptional properties, such as high specific surface area, great electronic and thermal conductivity, and excellent mechanical strength [35, 36, 100]. These properties make graphene a potential material for improving the photocatalytic properties of TiO_2. However, pristine graphene is typically not used to prepare TiO_2/carbon composites due to the cost involved in obtaining it. Instead, reduced graphene oxide (rGO) and graphene oxide (GO) are commonly used to prepare TiO_2 composites. GO is produced when graphite powder is oxidized by applying different harsh reagents, in which the improved Hummers method is

the most preferred technique because it allows a high conversion rate while avoiding producing toxic gases [35, 122]. Once GO is obtained, it can be reduced to remove most oxygen functional groups to produce rGO. The success of the removal of these oxygen functional groups is what defines the final properties of rGO [36, 123, 124]. The mechanism behind the carbon-based TiO_2 nanocomposites includes the synergetic effect between the TiO_2 and the carbon structure, in which rGO acts as a charge carrier to separate the photogenerated h^+/e^-, reducing the recombination rate. Additionally, rGO could serve as a sensitizer, shifting the light absorption to the visible range [22, 120, 125, 126].

2.2.6. Immobilization

Besides the high energy bandgap and the recombination factor, using TiO_2 in a suspension presents technical and economic challenges for photocatalyst application on wastewater treatment due to the difficulty of recovering and reusing the material. As an alternative for avoiding the recovery process and simplifying further re-usage of TiO_2, photocatalyst has been immobilized over different supports such as glass, polymers, magnetic particles, ceramics, etc. [41, 45, 46, 50, 127]. Several methods for immobilizing TiO_2 include the sol-gel method, immobilization via binding agents, coating techniques, encapsulation, etc. [50, 128–130]. The selection and combination of the various immobilization methods depend on the final application and the substrate material in which TiO_2 will be anchored. Usually, the sol-gel method is applied when the material synthesis process is involved because it allows easy dispersion of formed gel onto the supporting material, which is further dried and annealed to obtain a crystalline TiO_2 immobilized on the substrate.

On the other hand, using binding agents gives excellent stability to immobilized TiO_2 because binders create chemical bonds with the substrate. In order to achieve a successful anchoring of TiO_2, the substrate material should have most of the following properties: excellent chemical inertness, high UV light resistance, mechanical stability, and a large specific surface area. Most recent studies have selected ceramics as the substrate material because it offers all the properties described before[49, 50]. The main drawback of immobilized TiO_2 is that the mass transfer is reduced compared to the TiO_2 in suspension; therefore, the substrate's geometry and shape should be considered to reduce the mass transfer limitations.

2.2.7. Radiation source

The light wavelength is one of the most important factors in the photocatalytic activity of TiO_2 because it establishes whether the photoexcitation takes place or not. For photoexcitation of the TiO_2 particles, the light wavelength should have equal or higher energy than the energy bandgap to promote the charges' separation. In most cases, TiO_2 photoactivation occurs with a photon emitted at a wavelength of around 387 nm or lower (for the dominant crystal form, anatase); this means only UV light promotes the photogeneration h^+/e^- that starts the redox reactions. As explained before, introducing dopant elements like nitrogen shifts light absorption to the visible range, allowing photoactivation at wavelengths higher than 400 nm and offering the possibility to utilize solar energy. Besides the light wavelengths, light intensity is another critical aspect to consider because photocatalytic kinetics depends on it, too. When the light intensity is low, the reaction kinetic has a linear dependency, changing to square-root dependency when moderate light intensity is applied. Finally, when high light intensity is used, the photocatalytic reaction kinetic becomes independent of the light intensity [131, 132], as shown in Figure 10.

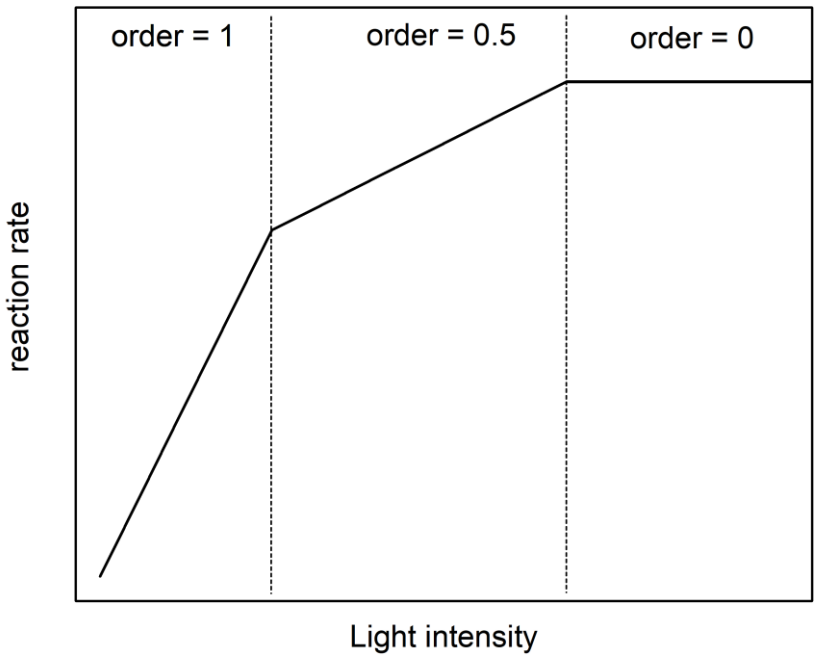

Figure 10. Reaction rate dependency of light intensity.

3. EXPERIMENTAL PART

3.1. Materials

Table 2 shows the list of chemicals used in this research.

Table 2. List of chemicals used in this research.

Substance	CAS	Purity	Supplier
Target OMPs			
Ciprofloxacin	85721-33-1	98 %	Acros Organics
Diclofenac sodium salt	15307-79-6	p.a.	Sigma-Aldrich
Salicylic acid	69-72-7	p.a.	Gram mol
Reagents for nanomaterials synthesis			
Titanium (IV) isopropoxide	546-68-9	97 %	Sigma-Aldrich
Acetylacetone	123-4-6	≥ 99%	Honeywell
Ethanol	64-17-5	p.a.	Gram mol
Urea	57-13-6	p.a.	Sigma-Aldrich
Graphene oxide water dispersion	Not applicable	Not applicable	Graphenea
Ascorbic acid	50-81-7	p.a.	Sigma-Aldrich
Scavengers			
p-Benzoquinone	106-51-4	≥ 99%	Sigma-Aldrich
Formic acid	4-18-6	≥ 95%	Sigma-Aldrich
Methanol	67-56-1	≥ 99%	Sigma-Aldrich
Chromatographic analysis			
Acetic acid	64-19-7	≥ 99. 7% ACS	Sigma-Aldrich
Acetonitrile	75-05-8	≥ 99. 9% HPLC	Sigma-Aldrich
Phosphoric acid	7664-38-2	85%	Sigma-Aldrich
Formic acid	4-18-6	≥ 98-100% HPLC	Sigma-Aldrich
Methanol	67-56-1	≥ 99. 9% HPLC	Sigma-Aldrich
Reagents for ceramic foam and coating			
Tetraethyl orthosilicate	78-10-4	99%	Merck
Hydrochloric acid	7647-01-0	37% ACS	Merck
Commercial Al_2O_3 powder CT 3000 SG	1344-28-1	Not applicable	Almatis

carbonic acid-based polyelectrolyte Dolapix CE 64	Not applicable	Not applicable	Zschimmer & Schwarz Chemie
polyvinyl alcohol	9002-89-5	99+% hydrolyzed	Sigma-Aldrich
antifoaming agent Contraspum K 1012	Not applicable	Not applicable	Zschimmer & Schwarz Chemie
Polyurethane foam	Not applicable	Not applicable	Rekord-tim
Others			
TiO_2 P-25	13463-67-7	Not applicable	Degussa-Hűls

3.2. Materials synthesis

3.2.1. Microwave-assisted synthesis of N/TiO_2 nanophotocatalysts: the effects of microwave temperature and microwave time

The initial molar ratios of reagents were kept invariable to determine the microwave oven parameters for the N/TiO_2 synthesis while the temperature and time in the microwave (MW) oven were varied. The sol-gel method was combined with the microwave-assisted approach, applying similar chemical reagents and ratios as described by Thapa et al. [38]. Briefly, titanium (IV) isopropoxide (TTIP) was mixed with acetylacetone (AcAc). Then, ethanol (EtOH) was added while stirring at room temperature. These reagents were mixed at a molar ratio of TTIP:AcAc:EtOH = 0.014:0.039:1.37 and labeled as solution A.

On the other hand, urea (N/Ti molar ratio equal to 2) was dissolved in 20 mL of deionized water and labeled as solution B. Solutions A and B were added dropwise to 80 mL of deionized water under continuous stirring at room temperature. The final solution was stirred for one hour at room temperature. Then, the solution was transferred to four Teflon vessels in the microwave (MW) oven (Microwave Reaction System SOLV, Multiwave PRO, Anton-Paar GmbH, Graz, Austria) for thermal treatment at a specific temperature and time. Inner pressure and temperature were monitored using a *p*/*T* sensor accessory during synthesis. The synthesized material was washed several times with ethanol and water, centrifuged, and dried at 65°C overnight. The molar ratio of nitrogen in N/TiO_2 was not evaluated. Instead, two different temperatures (150°C and 200°C) and three reaction times (10, 20, and 30 minutes) were considered critical parameters for the microwave-assisted method. The obtained materials were labeled as N/TiO_2 *T_t*, where *T* and *t* denote the temperatures and time, respectively. Table 3

shows the four materials synthesized based on temperature and time applied for the thermal treatment in the MW oven [133].

Table 3. Material labeling according to evaluated parameters.

Material Labeling	Parameters
N/TiO_2 150_10	Temperature: 150°C; time: 10 min
N/TiO_2 200_10	Temperature: 200°C; time: 10 min
N/TiO_2 200_20	Temperature: 200°C; time: 20 min
N/TiO_2 200_30	Temperature: 200°C; time: 30 min

3.2.2. Microwave-assisted synthesis of N/TiO_2 nanophotocatalysts: effect of nitrogen content

Once the critical microwave parameters were studied, the molar ratios of reagents were modified, while temperature (*T)* and time (*t*) in the MW oven were kept invariable. A similar procedure as described for microwave-assisted synthesis parameters for N/TiO_2 was used to determine the effect of nitrogen in N/TiO_2 synthesis. However, the N/Ti molar ratio was varied (0, 1, 2, 4, 12, and 24) to evaluate the effect of nitrogen on the photocatalytic and morphological properties. Therefore, different amounts of urea were dissolved in 20 mL of deionized water and labeled as solution B, while the other reagents were kept at the same molar ratio. Only one temperature and reaction time were used in the MW oven, based on the optimal parameters found from the microwave-assisted synthesis parameters for N/TiO_2 (200°C and 10 min). The obtained materials were labeled as N/TiO_2 *x*, where *x* is the N/Ti molar ratio used (Table 4). Commercial TiO_2 Degussa P25 was used as a benchmark material for morphological and photocatalytic properties comparison purposes.

Table 4. Material labeling according to nitrogen content.

Material Labeling	N/Ti molar ratio
N/TiO_2 0	0
N/TiO_2 1	1
N/TiO_2 2	2
N/TiO_2 4	4
N/TiO_2 12	12
N/TiO_2 24	24

3.2.3. Reduction of graphene oxide (GO)

Before incorporating reduced graphene oxide (rGO) into the N/TiO_2 photocatalyst, it was necessary to reduce graphene oxide (GO). Therefore, commercial GO was reduced by applying a similar procedure reported by Baptista-Pires et al. [31]. First, commercial GO water dispersion (0.4 wt. % concentration, 4 mg·mL^{-1}) was diluted in water to a final concentration of 1 mg·mL^{-1}. Then, an equal volume ratio of prepared GO solution was mixed with 1 mg·mL^{-1} ascorbic acid solution, followed by a thermal treatment in the MW oven at 125°C for 45 minutes. The material was collected in a 500 mL Erlenmeyer flask, filtered, and washed several times with deionized water. Finally, the material was dried overnight at 65°C and labeled as reduced graphene oxide (rGO).

3.2.4. Microwave-assisted synthesis of N/TiO_2/rGO nanocomposites: effect of rGO content

For evaluating the effect of rGO and its synergy with nitrogen, N/TiO_2/rGO nanocomposites were synthesized by applying a methodology similar to the N/TiO_2 synthesis. The sol-gel method was combined with the microwave-assisted approach, changing the amount of rGO (0.25 – 10 wt. %). Firstly, a certain amount of rGO was dispersed in ethanol and sonicated for 45 min at 35 Hz. Meanwhile, TTIP was mixed with AcAc and stirred for several minutes, then ethanol/rGO solution was added while stirring at room temperature; these reagents were mixed at a molar ratio of TTIP:AcAc:EtOH = 0.014:0.039:1.37 and labeled as solution A.

On the other hand, urea (N/Ti molar ratio equal to 12) was dissolved in 20 mL of deionized water and labeled as solution B. Solutions A and B then were added dropwise to 80 mL of deionized water while stirring at room temperature. This final solution was kept under stirring for one hour at room temperature. Then, the solution was transferred to four Teflon vessels in the MW oven for thermal treatment at 200°C for 10 min. Inner pressure and temperature were monitored using a *p*/*T* sensor accessory during synthesis. The synthesized material was washed several times with ethanol and water, centrifuged, and dried at 65°C overnight. The obtained materials were labeled as N/TiO_2/rGO *x* wt. %, where x is the amount of rGO added (Table 5). N/TiO_2 material and commercial TiO_2 Degussa P25 were used to compare morphological and photocatalytic properties [134].

Table 5. Material labeling according to rGO content.

Material labeling	wt. % rGO
N/TiO_2/rGO 0.25 wt. %	0
N/TiO_2/rGO 1 wt. %	1
N/TiO_2/rGO 3 wt. %	3
N/TiO_2/rGO 5 wt. %	5
N/TiO_2/rGO 10 wt. %	10

3.2.5. Preparation of Al_2O_3 ceramic foam substrate

N/TiO_2/rGO photocatalyst was immobilized on the surface of an open-cell alumina (Al_2O_3) ceramic foam. Alumina foam was prepared following the Schwarzwalder and Somers replica method [135]. The alumina foam was designed as a ring form, with outer and inner diameters of approximately 90 and 40 mm, respectively, and a thickness of 15 mm. For that purpose, a polyurethane (PU) sponge with a pore density of 17 pores per inch was impregnated with an aqueous ceramic suspension having alumina powder (α-Al_2O_3, CT 3000 SG), a dispersant (Dolapix CE 64), a binder (poly (vinyl alcohol)) and an antifoaming agent (Contraspum K 1012). The following amounts were used: 75, 0.4, 1.5, and 0.1 wt. %, respectively. After impregnation and overnight drying, the foam was thermally treated. First, a slow heating rate of 1°C·min^{-1} was applied until reaching 600°C, with a 1 hour holding period at 300°C and at 600°C to prevent the structure from collapsing during the burnout of the PU foam and other organic matter. After that, the temperature was increased to 1600°C at a rate of 5°C·min^{-1}. The foam was kept at the final sintering temperature for 2 hours before furnace cooling. More details about this procedure are published elsewhere [136].

3.2.6. Deposition of N/TiO_2/rGO nanocomposites on Al_2O_3 foam substrate

A binder solution was prepared before immobilizing N/TiO_2/rGO (with 0.25 wt.% of rGO material – selected based on results of photocatalytic properties) onto the Al_2O_3 foam substrate. Briefly, acidified deionized water (with 0.01 mol hydrochloric acid, HCl) was mixed with tetraethyl orthosilicate in a molar ratio of 100:1 and kept under stirring for 5 hours at room temperature to form a binder solution. Then, a coating solution was prepared using binder: EtOH:N/TiO_2/rGO in a weight ratio of 7.5:85:7.5 and sonicated for 30 minutes at 35 Hz. Meanwhile, the Al_2O_3 ceramic foam was placed in a vacuum chamber (CitoVac, Struers) at

− 0.16 bar for 20 minutes; then, the coating solution was injected slowly into the vacuum chamber until the ceramic foam was entirely covered, keeping the vacuum for another 20 minutes. After the coating time, the ceramic foam was removed from the coating solution and left to dry at room temperature for 30 minutes. Subsequently, it was thermally treated at 65°C for 3 hours, followed by another 3 hours at 90°C, and finally at 120°C overnight. The N/TiO_2/rGO nanocomposite immobilized on the Al_2O_3 foam was labeled Al_2O_3@N/TiO_2/rGO.

3.3. Materials characterization

Materials characterization is crucial because it allows to correlate changes in the photocatalytic activity of TiO_2-based materials with the morphological, structural, and optical properties of the synthesized nanostructured materials.

XRD analysis was performed to identify the crystalline phase and calculate crystal size under specific conditions such as temperature *(T*) and time (*t*) in the MW oven, nitrogen content, and rGO loading. For the XRD analysis, a Shimadzu XRD6000 (Shimadzu Corporation, Kyoto, Japan) X-ray diffractometer with CuKα radiation was used. The fixed step scans were collected in the 2θ range 20–60° with steps of 0.02° 2θ and counting time 0.6 s under an accelerating voltage of 40 kV and current of 30 mA.

To check the porosity, pore size distribution, and specific surface area of the synthesized materials, Brunauer–Emmett–Teller (BET) analysis was performed. The BET surface area, pore volumes, and pore size distribution were estimated from nitrogen adsorption and desorption isotherm data using an ASAP 2000 apparatus (Micromeritics Corporation, Norcross, GA, USA). Before the analysis, the material was degassed under a dynamic vacuum of 6.6 mPa at 150°C for 10 hours to remove any physically adsorbed species. The Barret–Joyner–Halenda model was used to determine the material's pore size distribution by using the data of the adsorption and desorption branches of the nitrogen isotherms.

Fourier Transform Infrared Spectroscopy (FTIR) is a technique that provides information about the surface chemistry of the materials, such as functional groups, chemical bonds, and the nature of the photocatalyst surface (hydrophilic/hydrophobic). FTIR spectra were recorded on an IRSpirit (Shimadzu, Kyoto, Japan) in the range of 400 – 4000 cm^{-1}, using an attenuated total reflection accessory.

Raman spectroscopy provides insight into how dopant incorporation affects the formation of oxygen vacancies, crystalline phases, and surface change. Raman measurements were performed by confocal micro-Raman spectroscopy using a T64000 (Horiba Jobin Yvone) equipped with a solid-state laser with a wavelength of 532.5 nm, a 50× magnification and large working distance objective in the range of 90 – 3000 cm^{-1}. Laser power at the sample was optimized to avoid heating and possible phase transition of TiO_2 during measurement.

The photocatalytic optical properties can be measured through diffuse reflectance spectroscopy (DRS), which helps to determine wavelength adsorption shifting by the dopant introduction. The energy bandgap (*E*g) was calculated through Tauc plots from DRS measurements. These measurements were performed on a QE Pro High-Performance Spectrometer (Ocean Insight, Orlando, FL, USA) equipped with an integrating sphere and a DH 2000 deuterium-halogen source in the analysis range 200 – 1000 nm with a resolution of 1 nm and integration time of 10 s.

Scanning Electron Microscopy (SEM) is a powerful tool that provides high-resolution imaging of the photocatalyst surface. When combined with Energy Dispersive Spectroscopy (EDS), it is possible to have a clue about surface chemical composition and element distribution. The elemental surface composition was determined by SEM using a Vega Easyprobe 3 device (Tescan, Brno, Czech Republic). EDS spectra were recorded with an XFlash 6|30 detector (Bruker, Billerica, MA, USA) at a working distance of 10 mm under an accelerating voltage of 20 keV.

On the other hand, X-ray photoelectron spectroscopy (XPS) is an essential technique that determines each element's chemical bonding and electronic states within the photocatalyst. Additionally, it provides accurate information about the type of doping (interstitial/substitutional). Therefore, the chemical composition and energy binding were determined by an XPS spectrometer equipped with a Phoibos MCD 100 electron analyzer (SPECS, Berlin, Germany) and a monochromatic source of Al Kα X-rays of 1486.74 eV. During analysis, the typical pressure in the UHV chamber was in the 10^{-7} Pa range. For the electron pass energy of the hemispherical electron energy analyzer of 10 eV used in the present study, the overall energy resolution was around 0.8 eV. All spectra were calibrated by the position of C 1s peak, placed at the binding energy of 284.5 eV. The XPS spectra were deconvoluted into several sets of mixed Gaussian-Lorentzian functions with Shirley background subtraction.

3.4. Photocatalyst evaluation

3.4.1. Adsorption test

The adsorption-desorption equilibrium was established before checking the photoactivity of any synthesized materials. For adsorption, 25 mg of the photocatalyst was dispersed in 100 mL of pollutant solution (CIP, DCF, or SA) (10 $mg \cdot L^{-1}$) and left in the dark for two hours. Samples were taken at different intervals, filtered using a 0.45 µm mixed cellulose ester membrane filter, and directly analyzed with a UV-Vis spectrophotometer (HEWLETT PACKARD, Model HP 8453, Palo Alto, CA, USA). For CIP, measurements were done at 273 nm (maximum absorption peak), while for DCF and SA, measurements were done at 276 nm and 297 nm, respectively. For every adsorption test, the pH value was measured at the beginning and at the end of each experiment using a pH-meter type SevenCompact pH/Ion S220 (Mettler-Toledo Co.)

In the case of Al_2O_3@N/TiO_2/rGO and Al_2O_3 foam, the adsorption-desorption equilibrium was determined by immerging the ceramic rings in 100 mL of pollutant solution (CIP, DCF or SA) (10 $mg \cdot L^{-1}$) and left in the dark for two hours. Sampling and measurements were done following the same procedure as described above.

3.4.2. Photolytic and photocatalytic tests

For the photocatalytic test, 25 mg of the photocatalyst was dispersed in 100 mL of pollutant solution (CIP, DCF or SA) (10 $mg \cdot L^{-1}$) and irradiated in each experiment from above with lamps 20 cm away from the reactor.

Four lamps with different wavelengths of emission were used as a radiation source to determine the dependence of photoactivity by the radiation wavelengths:

- UVA lamp, model UVAHAND LED (Dr. Hönle AG, UV-Technologie, Gilching, Germany) (peak on 365 nm, 70 W),
- solar light simulator (SLS) model SOL500 (Dr. Hönle AG, UV-Technologie, Gilching, Germany) (430 W),
- blue visible light (BVL) lamp, model UVAHAND LED (Dr. Hönle AG, UV-Technologie, Gilching, Germany) (peak on 405 nm, 70 W),

- cold visible light (CVL), model OSRAM Endura Flood 100W 840 GD (Ledvance GmbH, Osram, Munich, Germany) (450 nm and 600 nm, 100 W).

Before irradiation, the suspension was stirred for 30 minutes in the dark to ensure adsorption-desorption equilibrium, determined previously by the adsorption test. After that, the lamp was turned on and irradiated the suspension for 2 hours. Samples were taken from the reactor at intervals (0, 5, 10, 20, 30, 45, 60, 90, and 120 min), filtered using a 0.45 µm mixed cellulose ester membrane filter, and directly analyzed by high performance liquid chromatography (HPLC, SCL-10A, Shimadzu) equipped with a UV-Vis detector (SPD-10 AV, Shimadzu). For the target pollutant transformation and byproducts detection, photocatalytic degradation was followed at 273 nm, 276 nm, and 297 nm, respectively, for CIP, DCF, and SA. The separation was performed on a Shim-pack VP-ODS column (4.6×150.0 mm; 5 µm, Shimadzu). For CIP quantitative determination by the HPLC, the mobile phase was a mixture of 2% acetic acid/acetonitrile (*V*/*V*, 84:16) with a flow rate of 1 $mL \cdot min^{-1}$ in the isocratic mode. While for DCF and SA quantitative determination, the separation was achieved using a mobile phase composed of 2 % phosphoric acid/acetonitrile (*V*/*V*, 40:60) with a flow rate of 1 $mL \cdot min^{-1}$ in the isocratic mode. CIP, DCF and SA degradation tests were performed separately under each of the radiation sources mentioned above. During the photocatalytic experiments, the temperature was kept at 25°C by a thermostatic bath, while the pH value was measured at the beginning and the end of each experiment using a pH-meter type SevenCompact pH/Ion S220 (Mettler-Toledo Co.)

Once the most photoactive material ($N/TiO_2/rGO$) was selected from all the synthesized materials, a photocatalytic mechanism determination was implemented for each pollutant under the four radiation sources. To do that, a similar procedure as the photocatalytic test was executed, but by adding the scavenger agents such as methanol ($^{\bullet}OH$), *p*-benzoquinone ($O_2^{\bullet -}$), and formic acid (h^+) prior to the photocatalytic test. The molar ratio pollutant/scavenger was 1/100, except for *p*-benzoquinone, which was 1/10 due to its limitations on analytical determination.

In addition to the photocatalytic test, the photolysis test of each pollutant under the four radiation sources was carried out to identify the effects of pollutant degradation solely by light. For the photolysis process, 100 mL of pollutant solution (CIP, DCF, or SA) (10 $mg \cdot L^{-1}$) without a catalyst was irradiated for 2 hours, applying the same sampling and analysis procedures described above for the photocatalytic test.

For N/TiO_2/rGO-coated Al_2O_3 foam ring (Al_2O_3@N/TiO_2/rGO) photocatalytic test, the N/TiO_2/rGO-coated Al_2O_3 foam ring was placed in 100 mL of pollutant solution (CIP, DCF, or SA) (10 mg·L^{-1}) and left for 30 minutes in the dark to ensure adsorption-desorption equilibrium, followed by 2 hours of radiation. The sampling and analysis were the same as described for the photocatalytic test. For comparative purposes, Al_2O_3 foam was evaluated on the degradation of CIP, DCF, and SA, using the same conditions applied for Al_2O_3@N/TiO_2/rGO ceramic foam to determine the substrate contribution.

Finally, to determine the dependence of radiation intensity on the photocatalytic and photolytic processes, the irradiation intensities effect of each lamp in the degradation of CIP was evaluated, placing each lamp at two different heights from the photocatalytic reactor. For this analysis, DCF was not considered due to only showing photolysis under SLS irradiation, while SA did not exhibit any photolysis under the studied irradiation sources. Before this analysis, global and UV-A irradiation intensities of each lamp at different heights were measured. Global irradiation was measured using a pyranometer in the range 285 –2800 nm (Kipp & Zonen Co., model CMP11, Delft, Netherlands), while the UV-A irradiation was measured by a radiometer equipped with a UV-A sensor in the range 315 – 400 nm (Opsytec Dr. Gröbel Co., model RM 21, Ettlingen, Germany). Global and UV-A irradiation charts of each lamp and radiation spectra of the different lamps used are presented in Appendix (Figure S2).

3.5. Transformation products (TP) detection

Liquid chromatography coupled to high resolution mass spectrometry (LC-HRMS) was used to elucidate the potential transformation pathways for CIP and DCF under different irradiation sources. For this purpose, Orbitrap Exploris 120 (HRMS) instrument from Thermo Fisher Scientific was used.

Ciprofloxacin was chosen to follow its TPs because of its possible contribution to the emergence and spread of multi-resistant bacteria due to the excessive or inappropriate use of this pharmaceutical, which is known for its bactericidal effect against most strains of gram-negative bacteria and against certain gram-positive bacteria. The bactericidal effect of this molecule comes from its fluoroquinolone structure. Therefore, it is important to determine if the TPs retain this structure, indicating that they could still possess the bactericidal effect.

In the case of diclofenac, this nonsteroidal anti-inflammatory drug (NSAID) has been associated with renal failure as a side effect and demonstrated to be toxic for some fishes and birds. Therefore, identifying probable TPs of DCF will contribute to identifying how effective the degradation process of this pharmaceutical is under different irradiation sources.

On the contrary, salicylic acid was not considered as a model compound to make TPs analysis using HRMS due to the simplicity of this molecule compared to CIP or DCF.

The analysis of CIP transformation was performed using a heated electrospray ionization (H-ESI) system as an ionization source, in positive ion mode with ionization voltages of 3500 V. In comparison, negative and positive ion modes with ionization voltages of 2500 V and 3500 V, respectively, were applied for DCF. The mass spectra were acquired in full scan mode in the mass to charge ratio (*m/z*) range of *m/z* 40 to 5,000. A reverse-phase column (Hypersil GOLD-Selectivity C18, 3 µm, 2.1 mm × 50 mm) was used to separate each compound, setting the column temperature at 30 ºC. The injection volume and flow rates were 10 µL and 0.4 $mL \cdot min^{-1}$, respectively. For CIP, the mobile phase composition was HPLC water with 0.1% formic acid and acetonitrile. For DCF analysis in the positive ion mode, the mobile phase composition was HPLC water with 0.1% formic acid and methanol. For the negative ion mode, the mobile phase composition was HPLC water with 5 mM ammonium acetate and methanol. The results were processed using Compound Discoverer™ 3.0 Software (Thermo Fisher Scientific).

4. RESULTS AND DISCUSSION

4.1. Microwave-assisted synthesis of N/TiO_2 nanophotocatalysts: optimization of microwave temperature and microwave time

4.1.1. Characterization

The nitrogen adsorption/desorption isotherms of N/TiO_2 materials, synthetized at different microwave temperature and microwave time, were collected and described by the Brunauer, Emmett, and Teller (BET) and Barrett-Joyner-Halenda (BJH) models to derive specific surface area, pore volume, and pore size distribution values, as shown in Table 6.

Table 6. Specific surface area, pore-volume, and crystallite size of N/TiO_2 materials.

Material	S_{BET}, $m^2\ g^{-1}$	V_{pore}, $cm^3\ g^{-1}$	Average pore diameter, nm
N/TiO_2 150_10	172.4	0.260	5.46
N/TiO_2 200_10	185.3	0.326	6.68
N/TiO_2 200_20	187.8	0.342	6.91
N/TiO_2 200_30	179.2	0.330	7.02

It can be observed that N/TiO_2 materials synthesized at the same temperature, but a different reaction time in the MW, have a similar specific surface area, pore-volume, and average pore diameter, indicating that the reaction time on the MW oven does not play an important role on the porosity of the material. On the other hand, increasing the reaction temperature, while keeping constant the reaction time (N/TiO_2 150_10 and N/TiO_2 200_10), resulted in an increase in the specific surface area, pore volume, and average pore diameter.

The adsorption and desorption isotherms of synthesized materials and pore size distribution are shown in Figure 11. From Figure 11 it can be observed that all materials display type IV nitrogen adsorption-desorption isotherms, typical for mesoporous materials, with an H2 hysteresis type, indicating that the porosity is composed mainly of neck-like and wide body pores [36, 37].

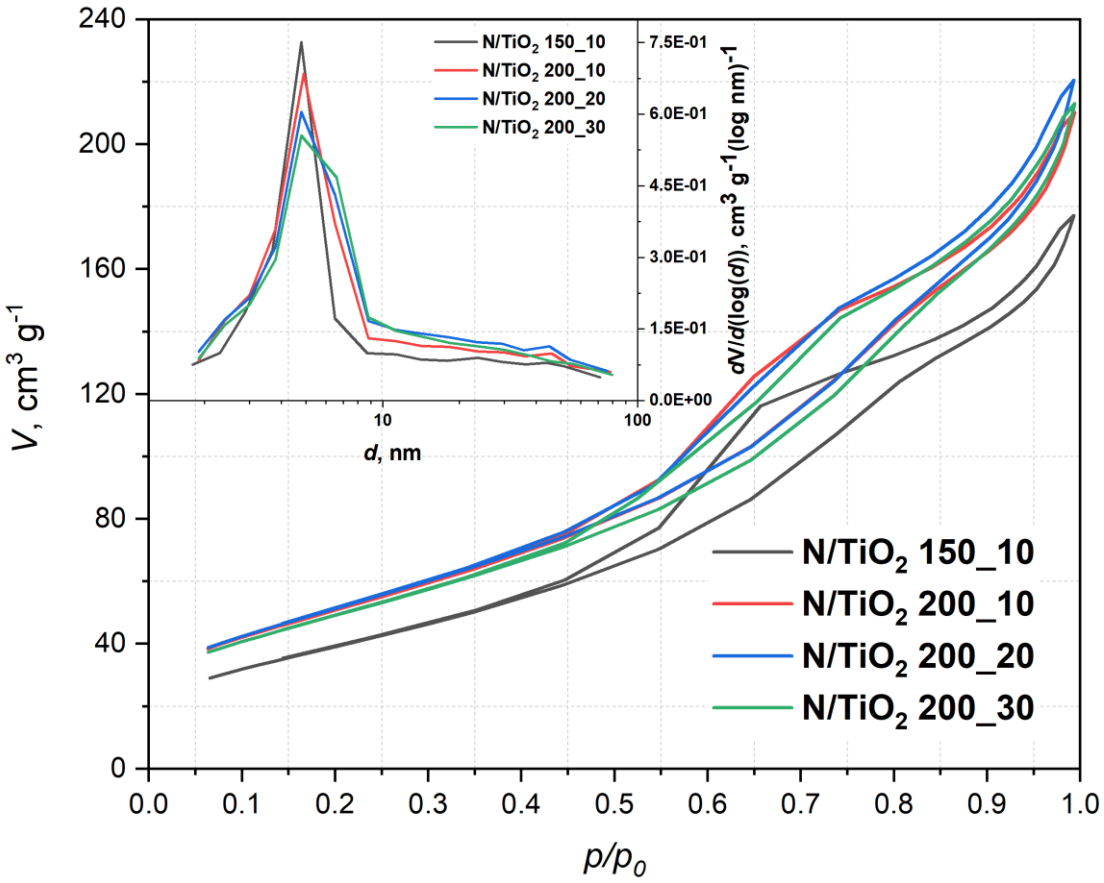

Figure 11. Adsorption-desorption isotherm, and pore size distribution of N/TiO_2 materials at different temperature and reaction time.

The FTIR spectra of the N/TiO_2 materials synthesized at different temperatures and reaction times are presented in Figure 12. All materials show a strong wide band between 400 and 800 cm^{-1}, which corresponds to the stretching vibrations of Ti–O–Ti bonds [137], whereas the broad band between 3,650 and 2,850 cm^{-1}, and the peak at 1,632 cm^{-1}, are attributed to stretching vibrations of O–H group [138]. However, N/TiO_2 150_10 has additional peaks at 1,590 cm^{-1}, 1,525 cm^{-1}, 1,443 cm^{-1}, and 1,372 cm^{-1}, which were ascribed to the stretching vibrations of N–H, C=O, and C–N groups, respectively, associated with the remaining urea in the material [139].

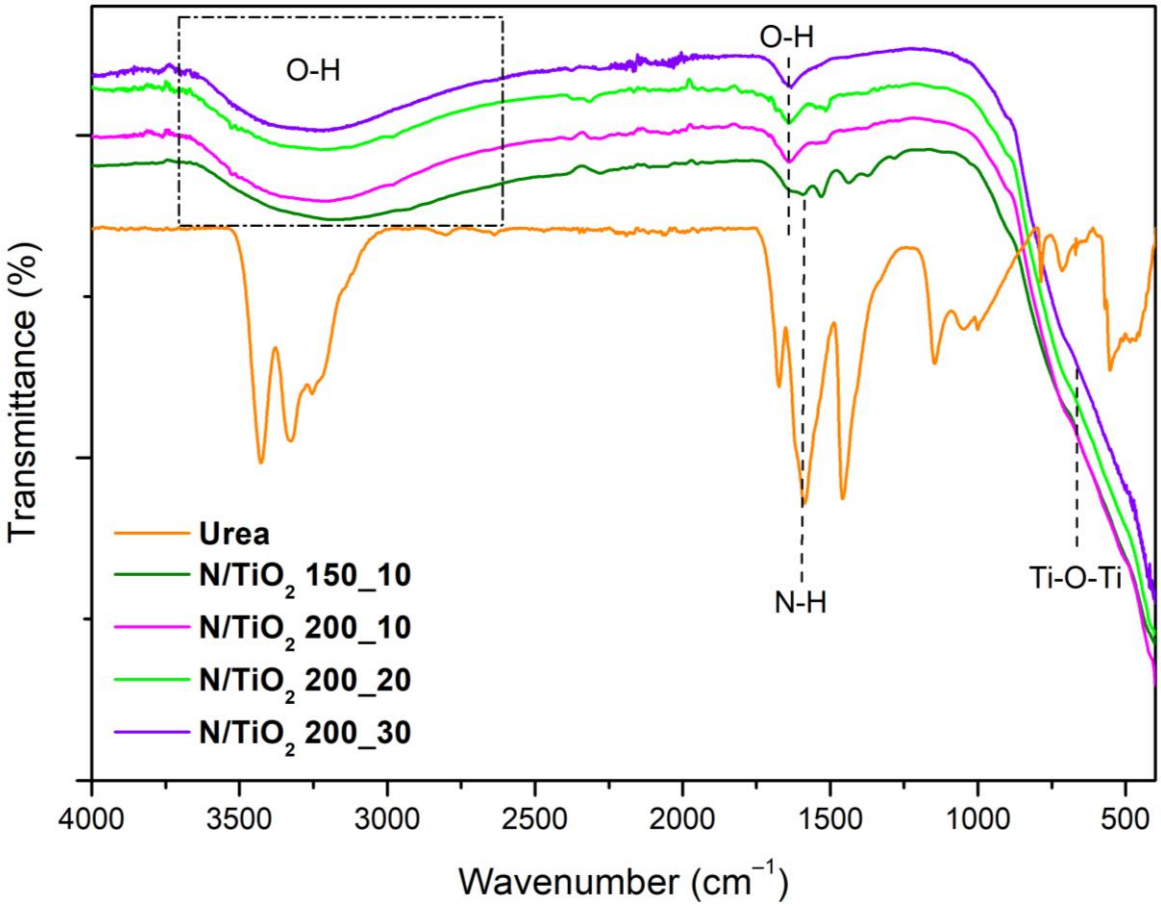

Figure 12. FTIR spectra of N/TiO_2 materials at different temperature and reaction time.

Figure 13 shows the X-ray diffraction patterns of N/TiO_2 materials synthesized at different temperatures and reaction times. All materials show diffraction peaks of TiO_2 anatase, assigned to the ICDD PDF#21–1272 [133]. It can be noticed that a higher treatment temperature is leading to narrower peaks, indicating larger crystallite size and more crystalline material. Similar results were reported by Kadam et al. [42]. However, in this study, the anatase crystal phase was formed even at low temperatures as 150°C. On the contrary, the reaction time does not have any effect on the crystal phase and crystallite size (inset). Based on the BET, XRD and FTIR analysis, it is observed that temperature is a crucial parameter in the microwave-assisted synthesis, while the reaction time is irrelevant for defining the morphological and superficial structure.

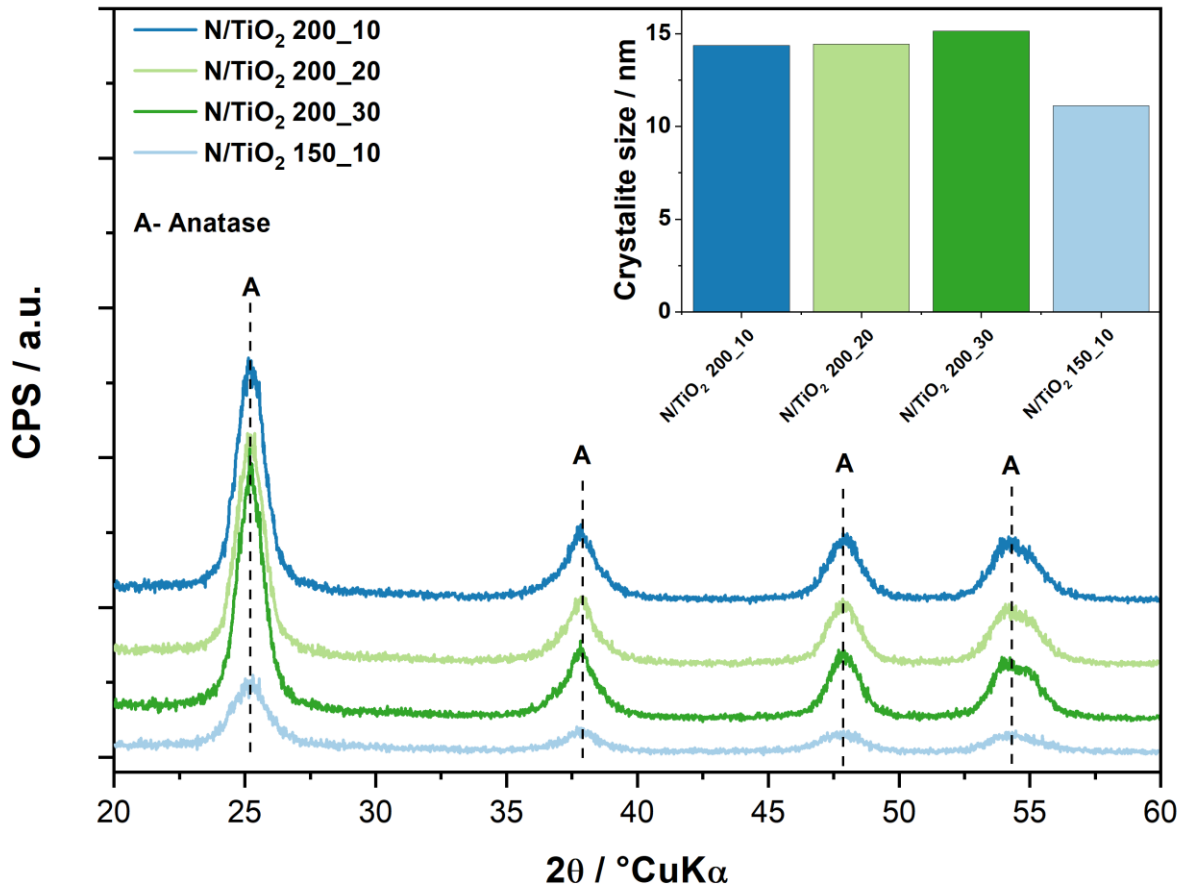

Figure 13. X-ray diffraction patterns and crystal size of N/TiO_2 materials at different temperature and reaction time.

4.1.2. Adsorption and photocatalytic test

Photocatalytic experiments using the N/TiO_2 materials synthesized at different temperatures and reaction time were subject to adsorption and photocatalytic test to correlate these parameters with the morphological properties. For these evaluations, CIP was used as a target pollutant (10 mg·L^{-1} = 30 µM). The results of the adsorption test, displayed in Figure 14, show that all synthesized materials have a larger adsorption capacity than the commercial TiO_2 P25 Degussa (TiO_2 P25, 50 $m^2 \cdot g^{-1}$) [129], which could be attributed to the larger specific surface area. Additionally, it is observed that materials synthesized at different reaction times, but at the same temperature, exhibit similar adsorption capacity. Although the N/TiO_2 150_10 material has the lower specific surface area, pore size and pore volume, it displays the highest adsorption capacity, which could be attributed to hydrogen bonding by the affinity between amino or carboxylic group present in the ciprofloxacin structure, and the urea remaining in the material synthesized at 150°C, as confirmed by the FTIR analysis.

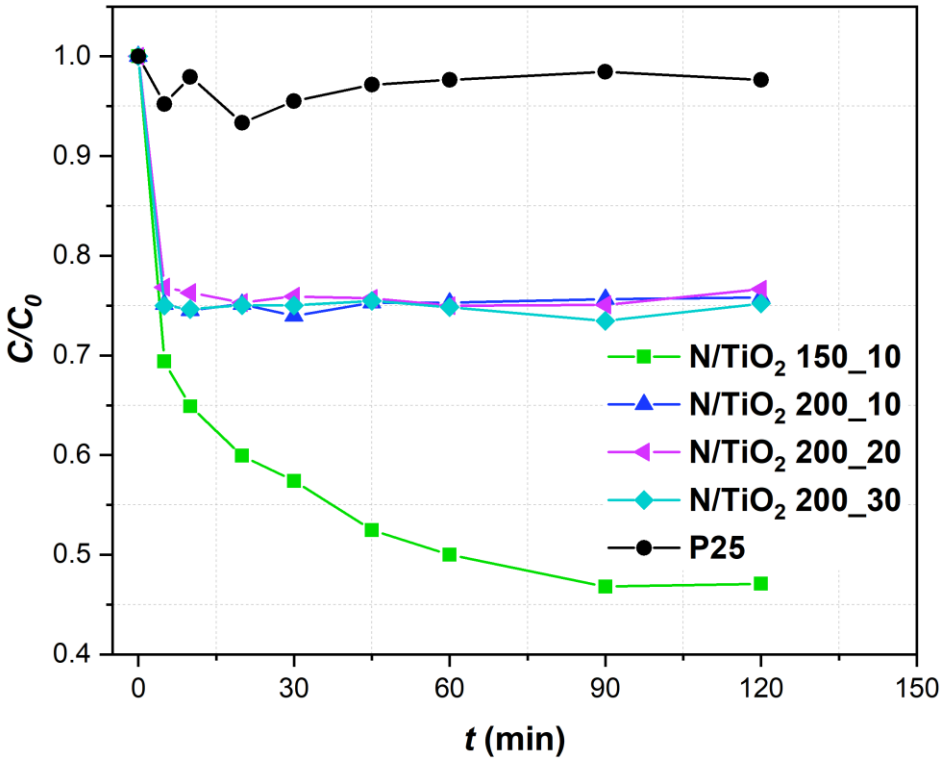

Figure 14. Adsorption test of ciprofloxacin (CIP) on Degussa P25 TiO_2 and N/TiO_2 materials synthesized at different temperatures and reaction time.

The photocatalytic activity of the N/TiO_2 materials synthesized at different temperatures and reaction times was evaluated for the degradation of CIP aqueous solution (10 mg·L^{-1} = 30 µM) under both UVA light and visible light. The results of the photocatalytic experiments under the UVA light, as shown in Figure 15, reveal that N/TiO_2 materials synthesized at 200°C degrade 90% of CIP in just 20 min of irradiation, while the material synthesized at 150°C achieves less than 90% of removal at the same period. Additionally, it is noticed that materials synthesized at 200 °C with different reaction times (10, 20, and 30 min of MW oven treatment) exhibit similar photoactivity, comparable to commercial Degussa P25 TiO_2, achieving more than 95% degradation of CIP in only 45 min under the UVA radiation. After 45 min, no significant changes in CIP degradation are observed for materials synthesized at 200°C, while the material synthesized at 150°C requires more than 90 min to reach a similar removal efficiency (Figure 15).

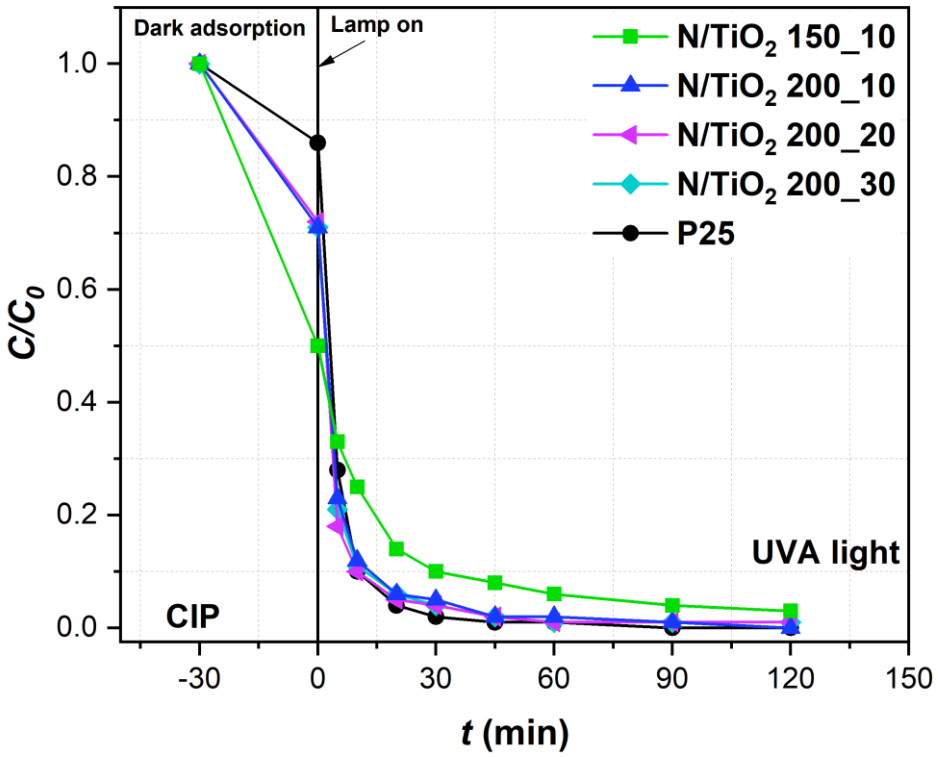

Figure 15. Photocatalytic degradation of ciprofloxacin (CIP) by Degussa P25 TiO_2 and N/TiO_2 materials under ultraviolet A (UVA) light.

Figure 16 presents the photoactivity of N/TiO_2 materials under cold visible light, as well as the lack of photoactivity of the photocatalyst Degussa P25 TiO_2. It is observed that N/TiO_2 materials synthesized at different reaction times, but at the same temperature, have similar photocatalytic activity. On the other hand, N/TiO_2 150_10 material shows a slightly better photocatalytic activity than other N/TiO_2 materials, probably due to the effect of the residual urea, which contributes to higher adsorption of CIP. However, the N/TiO_2 200_10 material also displays a good photoactivity under CVL, comparable to that one achieved by the N/TiO_2 150_10 material, as detailed in Table 7, where kinetic parameters for all materials under both radiation sources are compared. The enhanced photocatalytic activity of the N/TiO_2 materials under visible light is most likely attributed to the presence of nitrogen, which might either cause the narrowing of the bandgap of TiO_2 or introducing impurities states that do not modify the energy band gap but contribute shifting its photo-responses to the visible spectrum [31, 140]. In terms of CIP removal under both radiation sources, all synthesized materials show a synergistic effect of adsorption and photocatalysis, where N/TiO_2 materials synthesized at 200°C remove more than 25% of CIP by adsorption process.

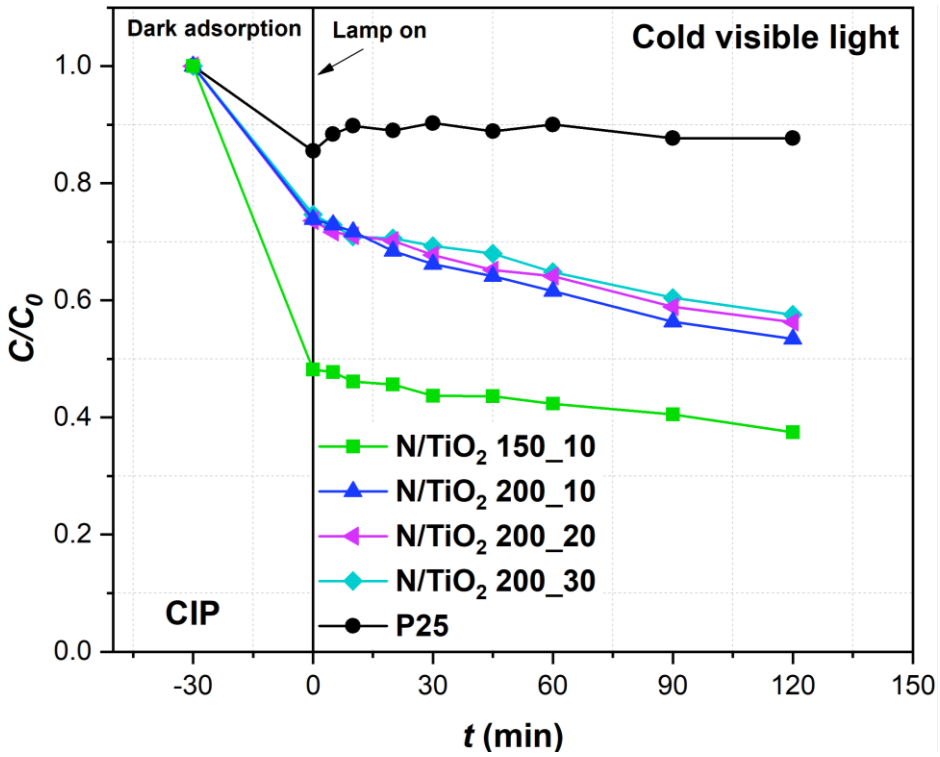

Figure 16. Photocatalytic degradation of ciprofloxacin (CIP) by Degussa P25 TiO_2 and N/TiO_2 materials under cold visible light (CVL).

For the photocatalytic tests under both radiation sources, the pollutant removal is analyzed using the pseudo-first order and second order models to identify which model better describes the degradation process. The pseudo-first order represents a degradation mechanism affected mainly by the changes in the pollutant concentration, while in the second order model, several factors, such as light intensity, pollutant concentration, byproducts formations, etc., play an important role in the degradation rate [141].

The linear form of the pseudo-first order kinetic model is [142]:

$$-\ln\left(\frac{C}{C_0}\right) = k_1 \cdot t \tag{10}$$

The linear form of the second order kinetic model is [141]:

$$\frac{1}{C_t} - \frac{1}{C_0} = k_2 \cdot t \tag{11}$$

where, where C (mg · L^{-1}) is the concentration of pollutant at time t (min), C_0 (mg · L^{-1}) is the initial pollutant concentration, k_1 (min^{-1}) and k_2 ($L \cdot mg^{-1} \cdot min^{-1}$) are the degradation rate constants.

The kinetic constant for the pseudo-first order is obtained by the slope of the plot –Ln (*C/Co*) versus the irradiation time [142]. For the second order, the kinetic constant is obtained by the slope of the plot (1/*C*–1/*Co*) versus the irradiation time [141]. Based on the fitted parameters, it can be determined which model better explains the degradation mechanism. Table 7 shows the pseudo-first order (k_1, min^{-1}) and second order (k_2, $L \cdot mg^{-1} \cdot min^{-1}$) kinetic constants, their determination coefficients (R^2), and efficiencies for the CIP removal by N/TiO_2 materials and commercial TiO_2 P25. Under UVA and CVL, it is noticed that the second order model fits the data better (higher R^2) compared to the pseudo-first order model. Thus, the CIP removal follows a second order model, where the CIP removal is defined by several factors, not just changes in its concentration.

Table 7. Pseudo-first order, second order kinetic parameters and efficiencies of CIP removal by N/TiO_2 materials and TiO_2 P25 under UVA and cold visible light (CVL).

Lamp	Material	Removal by adsorption	Removal Efficiency, %	Model			
				Pseudo-first order k_1, min^{-1}		Second order k_2, $L \cdot mg^{-1} \cdot min^{-1}$	
		(%)	η	k_1	R^2	k_2	R^2
UVA	N/TiO_2 150_10	50.30	97.09	0.0289	0.9213	0.2409	0.9962
	N/TiO_2 200_10	28.82	99.53	0.0523	0.9024	1.3530	0.9485
	N/TiO_2 200_20	28.13	99.38	0.0529	0.8692	1.2789	0.9856
	N/TiO_2 200_30	28.97	99.35	0.0507	0.8767	1.1332	0.9880
	P25	19.87	99.58	0.0589	0.8508	1.9217	0.9937
CVL	N/TiO_2 150_10	51.81	62.55	0.0021	0.9846	0.0046	0.9876
	N/TiO_2 200_10	26.14	46.57	0.0029	0.9933	0.0043	0.9974
	N/TiO_2 200_20	26.40	43.72	0.0024	0.9934	0.0035	0.9961
	N/TiO_2 200_30	25.35	42.43	0.0023	0.9903	0.0032	0.9930
	P25	12.63	*	*	*	*	*

*No photocatalytic degradation was observed

As expected, the photocatalytic activity of commercial TiO_2 P25 under UVA presents a higher degradation rate compared with the synthesized materials, but without photoactivity under visible light. On the other hand, the N/TiO_2 200_10 material has a good degradation rate under UVA irradiation, which is equivalent to 70% of the commercial one. Additionally, under CVL, this material also shows a good photocatalytic activity.

After evaluating the adsorption and photocatalytic tests, combined with the material characterization, it can be inferred that the temperature is the most relevant parameter in the microwave-assisted synthesis, and it is mainly affecting the crystallite size domains, which could determine the photoactivity. Based on these results, in this research, the optimal parameters identified for the microwave oven are at 200°C and 10 minutes.

4.2. Microwave-assisted synthesis of N/TiO_2 nanophotocatalysts: effect of nitrogen content

4.2.1. Characterization of nitrogen-doped materials

Once the optimal reaction time and temperature in the microwave oven were determined, N/TiO_2 materials were synthesized at different N/Ti molar ratio and subjected to broad structural, microstructural, and spectroscopic characterization in order to optimize the preparing procedure in terms of the N content in the N/TiO_2 materials. The specific surface area, pore-volume, and average pore diameter of Degussa P-25 and N/TiO_2 materials synthesized at different N/Ti molar ratios are presented in Table 8. It can be noticed that the specific surface areas of N/TiO_2 materials decrease with increasing N/Ti ratio. The sample without nitrogen (N/TiO_2 0) presents the highest specific surface area. A similar reduction in specific surface area with increasing nitrogen ratio was reported by Ma et al. [118]. This reduction could be attributed to interstitial doping, in which nitrogen atoms could be located in the interstitial voids instead of crystal lattice sites [29]. Moreover, the specific surface areas of N/TiO_2 materials are significantly higher than those of the photocatalyst Degussa P-25 (up to four times higher). Interestingly, it can be observed that the pore volume and the average pore diameter are not significantly affected by the N/Ti ratio.

Table 8. Specific surface area, pore-volume, and pore size of N/TiO_2 materials and Degussa P25.

Material	S_{BET}, $m^2 \cdot g^{-1}$	V_{pore}, $cm^3 \cdot g^{-1}$	Average Pore Diameter, nm
N/TiO_2 0	215.04	0.424	7.25
N/TiO_2 1	144.40	0.273	7.26
N/TiO_2 2	185.29	0.326	6.68
N/TiO_2 4	158.09	0.295	7.19
N/TiO_2 12	139.17	0.297	8.00
Degussa P25	48.14	0.196	13.69

Figure 17 shows the adsorption and desorption isotherms of commercial TiO_2 and N/TiO_2 materials synthesized at different N/Ti molar ratios, in which it is observed that N/TiO_2 materials display again a type IV nitrogen adsorption-desorption isotherms, as previously observed in the section of microwave parameters, with an H2 hysteresis type, indicating that the porosity is composed mainly of neck-like and wide body pores. On the contrary, the TiO_2 P25 exhibits an H4 hysteresis type, characteristic of slit-like pores. Additionally, it is noticed that synthesized materials have narrow pore distribution with a larger pore volume compared to the commercial one, which has a broad pore distribution but with smaller pore volume.

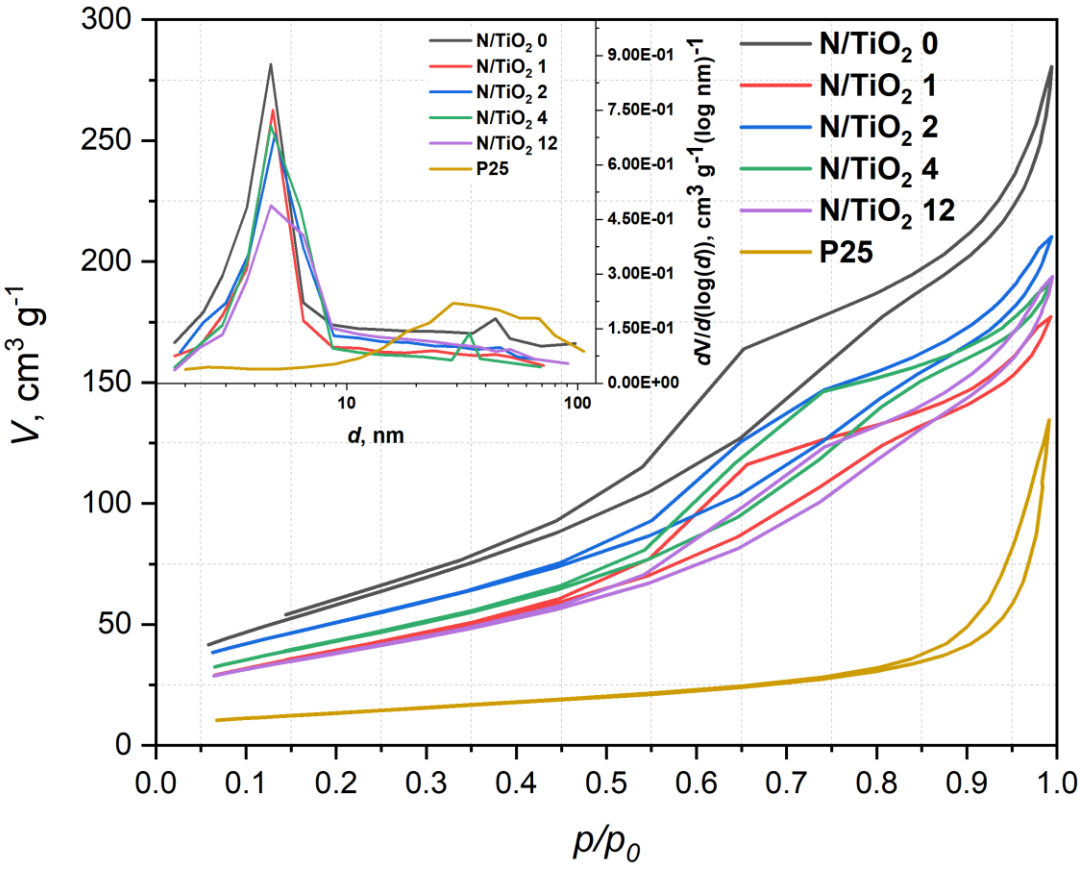

Figure 17. Adsorption-desorption isotherm, and pore size distribution of N/TiO_2 materials at different N/Ti molar ratios.

In Figure 18, the FTIR spectra of the N/TiO_2 materials and Degussa P25 are presented. A strong and wide band between 400 and 800 cm^{-1} is observed for all materials, which can be associated with the stretching vibrations of Ti–O–Ti bonds. Additionally, the wide band between 3,650 and 2,850 cm^{-1} and the peak at 1,632 cm^{-1} is correlated to stretching vibrations of the O–H group. Furthermore, in the N/TiO_2 materials containing a high N/Ti molar ratio (12

and 24), a small band around 1,457 cm^{-1} appears, which is attributed to the vibrations of the formed Ti-N bond [143]. Interestingly, all synthesized materials have a higher intensity of bands related to the O–H group than the P25 sample, which could be beneficial to produce hydroxyl radicals during photocatalytic reactions [144, 145]. Although the optimal N content cannot be determined from the FTIR scans, it could help to identify important material features such hydrophilicity and surface hydroxylation.

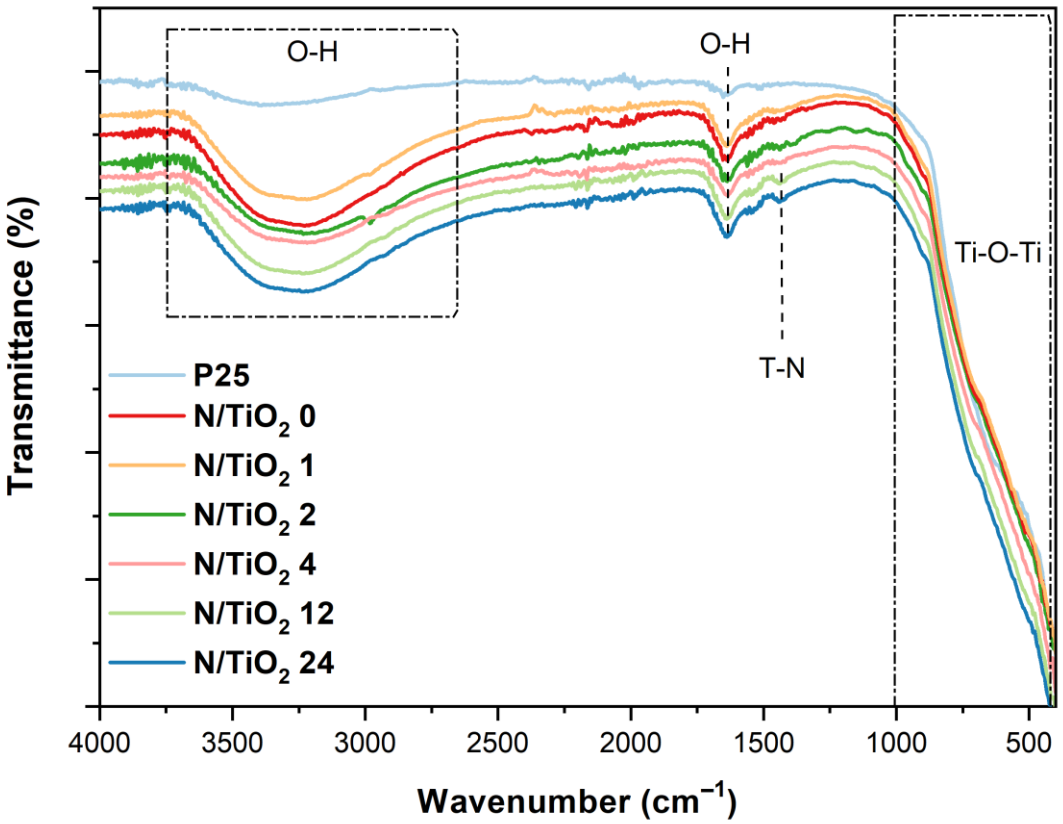

Figure 18. FTIR spectra of N/TiO_2 materials synthesized at different N/Ti ratio and Degussa P25.

The Raman spectra of the N/TiO_2 materials and commercial photocatalyst Degussa P25 are shown in Figure 19. In general, for all materials, five peaks can be identified which are associated with the A_{1g} (515 cm^{-1}), B_{1g} (396 cm^{-1}) and E_g (143, 396, and 637 cm^{-1}) Raman modes of TiO_2 anatase phase [30, 146], while, for the Degussa P25, an additional small peak at 444 cm^{-1}, which is characteristic for the TiO_2 rutile phase, is observed [147]. In all N/TiO_2 synthesized materials (with and without urea), a slight shifting of the Raman peaks of the B_{1g} and E_g to higher wavenumbers is detected (inset), and it could be attributed either to changes of surface oxygen vacancies or incorporation of nitrogen into the TiO_2 structure [86]. The Raman spectra indicate that nitrogen does not affect the crystallization of the TiO_2.

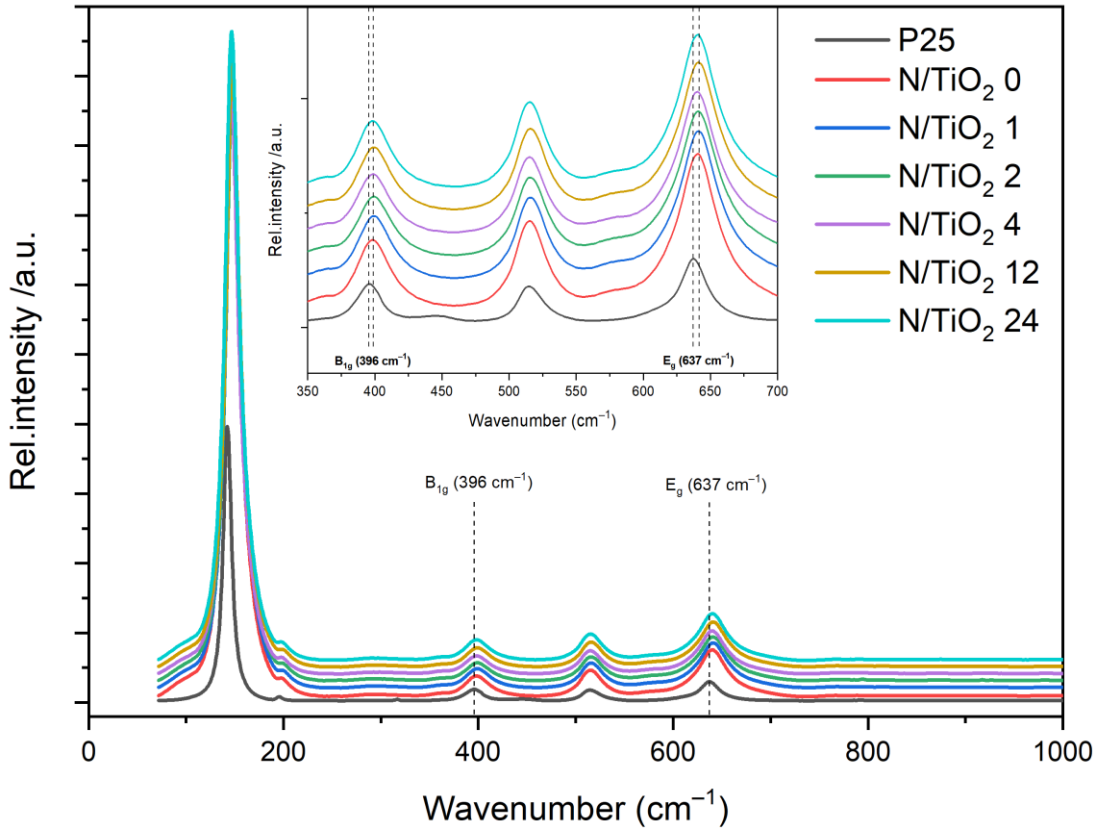

Figure 19. Raman spectra of N/TiO_2 materials synthesized at different N/Ti ratio and Degussa P25.

Figure 20 shows the X-ray diffraction patterns of N/TiO_2 materials and commercial photocatalyst Degussa P25. All synthesized N/TiO_2 materials display only diffraction peaks assigned to anatase (ICDD PDF#21–1272) [136], with crystallite size between 13 and 15 nm (determined by the Scherrer method); while the TiO_2 Degussa P25 exhibits diffraction peaks assigned to both anatase (ICDD PDF#21–1272) and rutile (ICDD PDF#21–1276) phases [119], with an average crystallite size of about 30 nm. In the materials containing urea, the anatase diffraction peak (101) is slightly shifted to a lower angle ($2\theta = 25.18°$) compared to the material without urea ($2\theta = 25.41°$), as shown in Figure 20 (inset), which could be associated with nitrogen doping [30]. Even though different N/Ti molar ratios were used, there are no observable changes in the phase composition nor the crystallite size of the N/TiO_2 materials. Apart from the slight shifting of the diffraction peak (101), no change is detected between materials with and without nitrogen, indicating that nitrogen doping has a negligible effect on the TiO_2 structure.

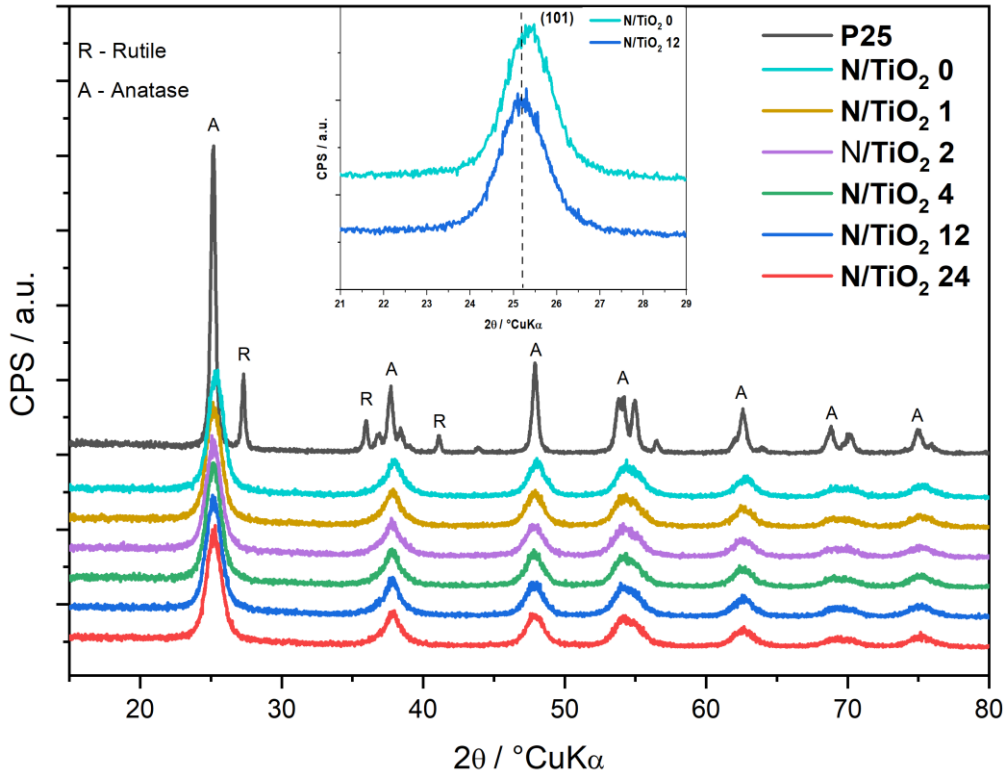

Figure 20. X-ray diffraction patterns of N/TiO_2 materials synthesized at different N/Ti ratio and Degussa P25.

The SEM analysis combined with EDS analysis was performed on the materials synthesized at 0 and 12 N/Ti molar ratios to determine the particle shape through a high-resolution imaging of the photocatalyst surface and to identify surface chemical composition and element distribution. From SEM images displayed in Figure 21, it is noticed that in both samples (0 and 12 N/Ti molar ratios), the particle shape is spherical, and they are agglomerated, indicating that nitrogen addition does not influence the morphology, shape, or size of the TiO_2 particles. Additionally, from the EDS analysis (Figure 22), the Ti and O signals, which are typical in TiO_2, are detected in both materials. Nitrogen traces are present even in the N/TiO_2 0, which can be due to an error on the EDS calibration assigning other signals to the nitrogen in this sample. In addition, it is well known that EDS is not a 100% quantitative method, therefore, the results obtained from this methodology are taken as indicators of the element composition. High-resolution EDS spectra were precisely acquired and fitted to allow more reliable quantitative results compared to conventional automated EDS analysis. From the high-resolution EDS spectra, it is observed that the material N/TiO_2 12 shows a stronger and more homogeneous presence of N throughout the material on the mapping than the material N/TiO_2 0.

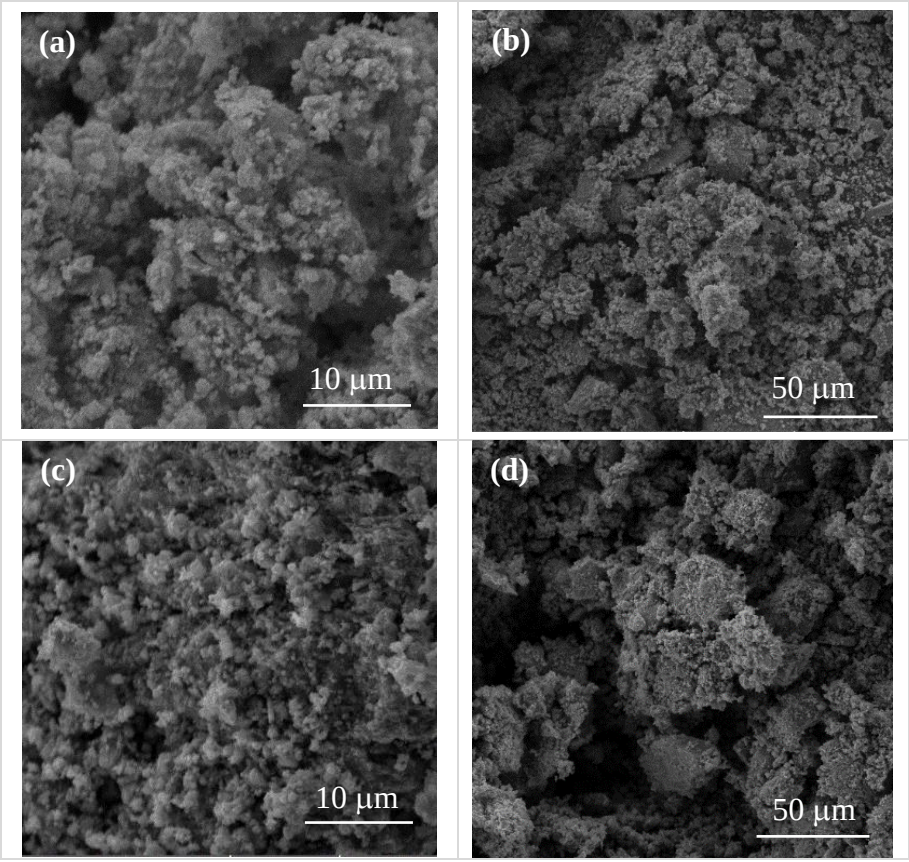

Figure 21. (a, b) SEM images of N/TiO_2 0; (c, d) SEM images of N/TiO_2 12 at different magnifications.

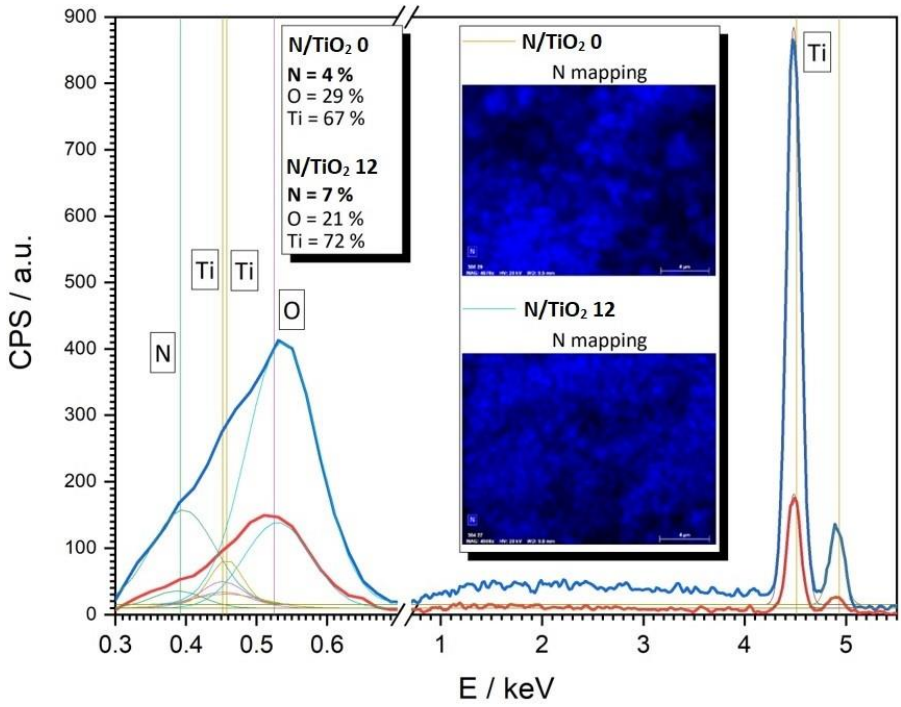

Figure 22. The fit of the EDS spectra for the N/TiO_2 0 (4 atomic % of N) and N/TiO_2 12 (7 atomic % of N). Inset: EDS mapping for the TiO_2 materials synthesized at 0 and 12 N/Ti molar ratios.

Figure 23 show the high-resolution spectra of Ti, O, and N obtained by XPS measurements, in which the chemical composition and oxidation states were determined, for N/TiO_2 0 and N/TiO_2 12. Figures 23a and c show the O 1s spectra of materials N/TiO_2 0 and N/TiO_2 12, respectively. In both materials, three different binding energy values are detected, where the main peak located around 530 eV could be assigned to oxygen bonded to titanium (O-Ti). The second peak located around 531.5 eV could be related to oxygen bonded to carbon, probably due to impurities from the synthesis (urea or acetylacetone). The third peak located around 533 eV could be attributed to adsorbed oxygen, probably for O-H bonds of chemisorbed water [118]. Additionally, it is noticed that the peak related to chemisorbed water is slightly more intense in the sample N/TiO_2 12 than the sample N/TiO_2 0, which could be beneficial for generating hydroxyl radicals, enhancing the photocatalytic activity. Figures 23b and d show the Ti 2p spectra of N/TiO_2 0 and N/TiO_2 12 materials, respectively. In both materials, the two peaks located around 458 eV and 464 eV correspond to Ti $2p^{1/2}$ and Ti $2p^{3/2}$, which indicates the formation of Ti^{4+}, typical of the anatase phase of TiO_2 [148–150]. On the other hand, Figure 23e displays N 1s spectrum recorded for N/TiO_2 12. The small peak with binding energy of 400.15 eV is attributed to nitrogen bonded to oxygen (N-O) [143, 151]. In general, it is assumed that the N 1s peak above 400 eV is related to interstitial doping [86]. The introduction of nitrogen in the TiO_2 lattice produces slight changes in the electronic densities of Ti and O. For the O 1s spectra, the main peak is shifted to lower binding energy from 530.1 to 529.95 eV; while for the Ti 2p spectra, the energy for the Ti $2p^{1/2}$ is shifted to lower binding energy from 458.8 to 458 eV. The binding energy shifting is higher for the O 1s spectra due to N-O bonding. Usually, N-O bonding in the interstitial sites is achieved under wet chemical processes, which is the applied method used in the present study [32]. Although there are several techniques that can help to determine the presence of a doping element such as nitrogen, the XPS analysis is the most suitable technique for confirming the success of the doping process as well as the type of doping (substitutional or interstitial) [29].

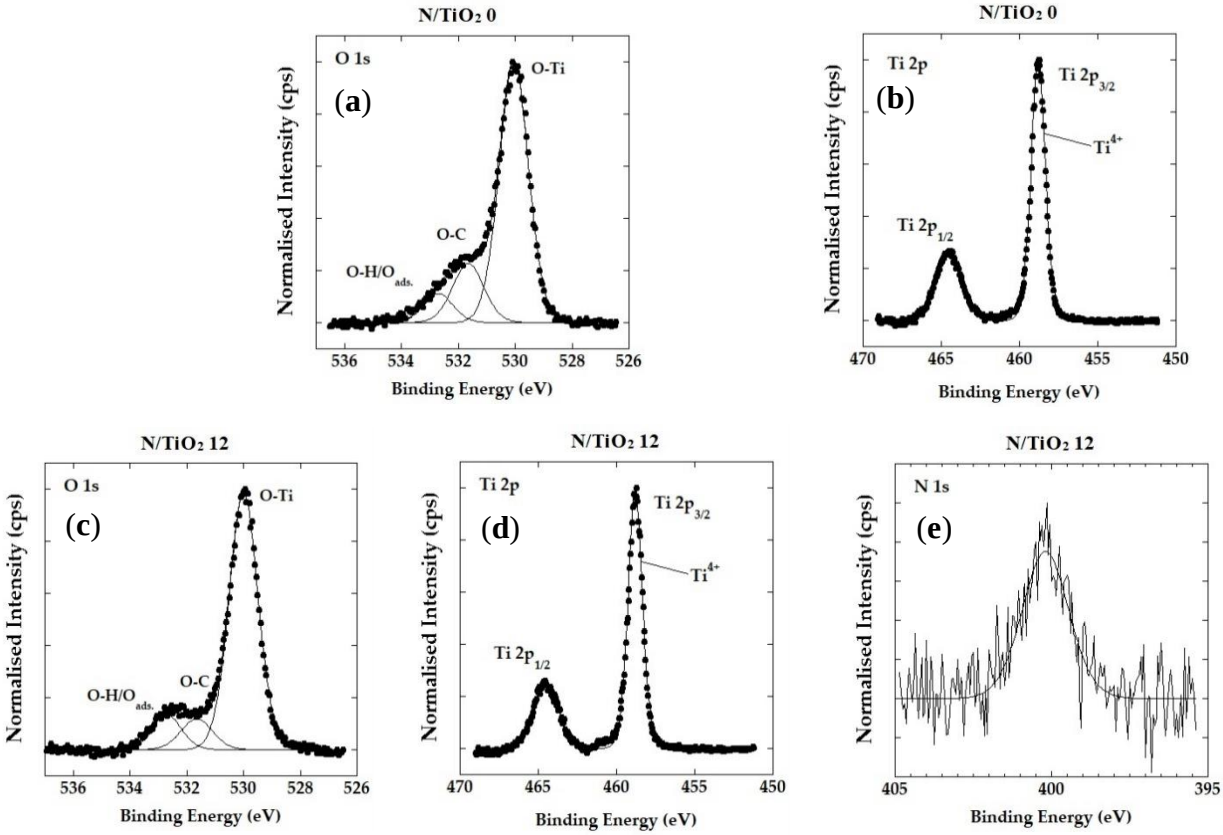

Figure 23. High-resolution XPS spectra: (a) O 1s spectrum and (b) Ti 2p spectrum of N/TiO_2 0; (c) O 1s spectrum, (d) Ti 2p spectrum, and (e) N 1s spectrum of N/TiO_2 12.

The DRS results and the Tauc plots are shown in Figure 24 and 25, respectively. From the DRS analysis (Figure 24), it is observed that there are no significant differences in the energy absorption between the N/TiO_2 materials and Degussa P25 in the UV region; however, in the region between 400 nm and 500 nm, the N/TiO_2 materials have some absorption in the visible region. Based on the DRS data, the Tauc plots can be obtained to determine the energy bandgap of all materials (Figure 25). It is noticed that all N/TiO_2 materials display a slightly lower energy bandgap in comparison to the Degussa P25, shifting the photon absorption to the visible region. Additionally, it is observed that the lowest energy bandgap is obtained for the material N/TiO_2 0, while the increment in the N/Ti molar ratio increases the energy bandgap. Similar results were reported by Suwannaruang et al. [152]. The lowest energy bandgap for the material N/TiO_2 0 indicates that the synthesis method also plays an important role on the material optical properties. On the other hand, the increment in the energy bandgap by the increment on the N/Ti molar ratio could be explained by the fact that, being the nitrogen introduced interstitially, as confirmed by XPS analysis, nitrogen is bonded to oxygen and could be acting as an impurity, creating a new energetic level that contributes to the absorption in the

visible light range without modifying the valence band (VB) or conduction band (CB) of TiO_2 [32, 33]. Kuo et al. confirmed, by density functional theory calculations, that band gap narrowing is achieved by substitutional nitrogen doping, while interstitial nitrogen doping produces localized impurities that do not reduce the energy band gap [33]. However, both types of doping contribute to the absorption of photons in the visible range. Previous studies have shown that a lower energy bandgap is not the only condition to achieve a higher photoactivity in the visible region. Other factors, such as oxygen vacancies and new energetic levels in the TiO_2 lattice, also play an important role in photocatalytic activity [32, 119, 152, 153].

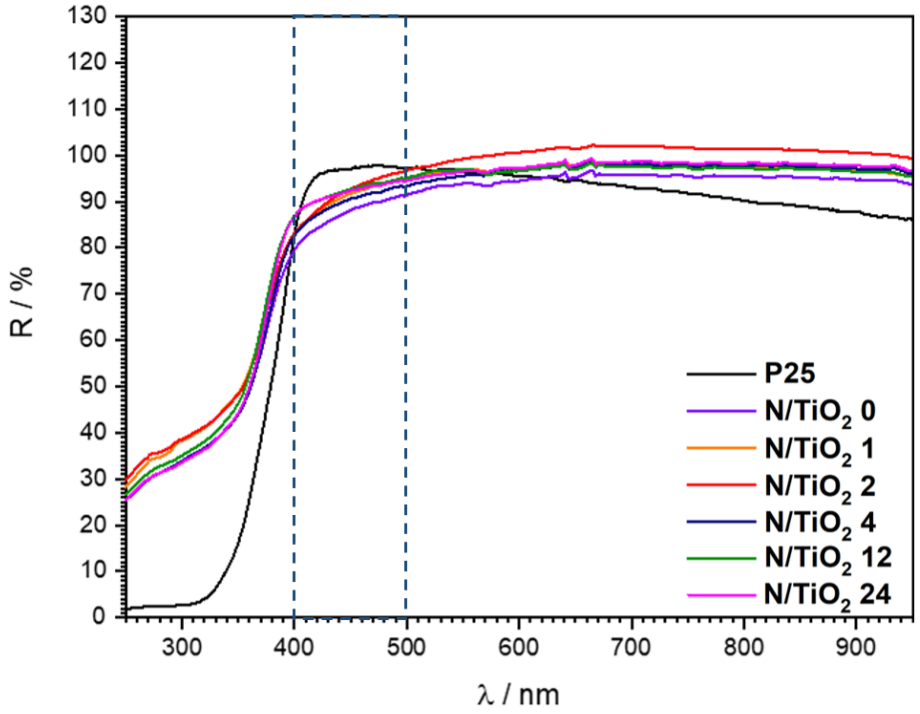

Figure 24. DRS spectra of N/TiO_2 materials synthesized at different N/Ti ratio and Degussa P25.

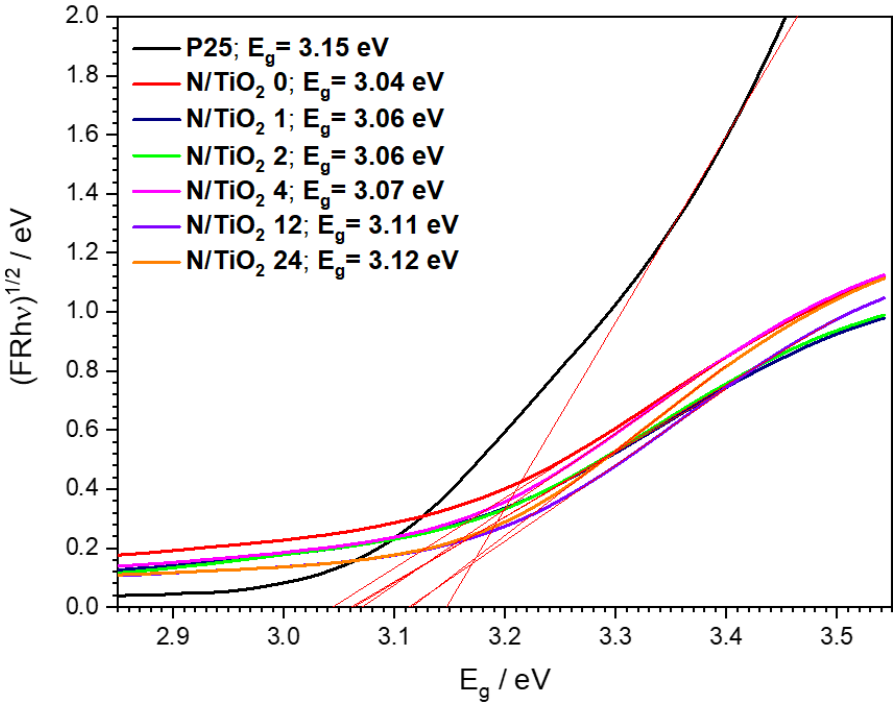

Figure 25. Tauc plot for energy bandgap determination of N/TiO_2 materials synthesized at different N/Ti ratio and Degussa P25.

4.2.2. Photocatalytic evaluation of nitrogen-doped materials

The photoactivity of the N/TiO_2 materials with the different N/Ti molar ratios, synthesized at 200°C for 10 min in the MW oven, were evaluated again through the degradation of CIP aqueous solution (10 $mg \cdot L^{-1}$ = 30 µM) under three different irradiation sources: UVA light (Figure 26), solar light simulator (Figure 27) and cold visible light (Figure 28). Before starting the degradation test, the initial pH value of the CIP solution was measured, ranging between 6.2 and 6.5. Evaluation under UVA irradiation shows that the photocatalyst Degussa P25 has the highest degradation rate, as expected, followed by the materials with a higher N/Ti molar ratio (12 and 24), which achieve up to 90% CIP removal in just 20 min of UVA irradiation. On the other hand, materials with a lower N/Ti molar ratio and without nitrogen doping (N/TiO_2 0) display a lower degradation rate within the first 20 minutes of irradiation, achieving less than 90% of the pollutant removal. After 60 minutes of UVA irradiation, all synthesized materials achieved more than 95% of pollutant removal, and no significant changes in the CIP concentration were detected. These results indicate that increasing the N/Ti molar ratio increases the degradation rate. After the photocatalytic experiments, the pH value was measured, and it remained unchanged. Although most of the CIP was degraded, the formed byproducts could probably still have the carboxylic acid group, contributing to keeping the pH.

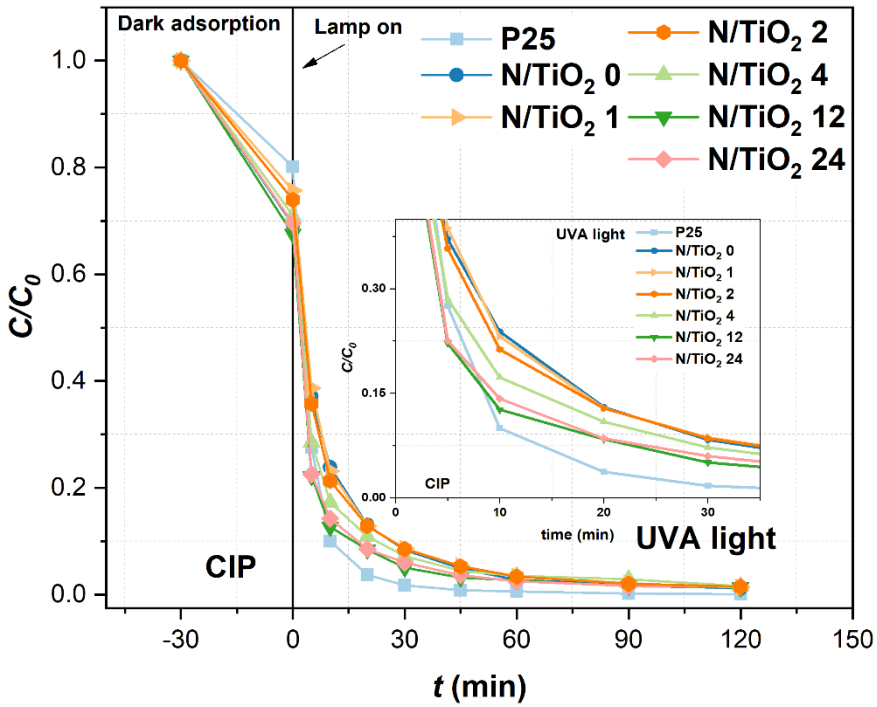

Figure 26. Photocatalytic degradation of ciprofloxacin by Degussa P25 TiO_2 and N/TiO_2 materials under UVA light

Under the solar light simulator (SLS), it is noticed that the degradation of CIP follows a trend like the one observed under the UVA radiation, where the photocatalyst Degussa P25 again displays the highest degradation rate, followed by the materials with a higher N/Ti molar ratio (12 and 24), achieving up to 90% CIP removal in just 20 minutes of solar irradiation. Also, it is observed a similar tendency for the materials with a lower N/Ti molar ratio and without nitrogen doping (N/TiO_2 0) like under UVA irradiation, where less than 90% of the pollutant removal is achieved within the first 20 minutes due to a lower degradation rate under SLS irradiation. After 60 minutes of SLS irradiation, all synthesized materials reached more than 95% of pollutant removal, and no significant changes in the CIP concentration were detected anymore.

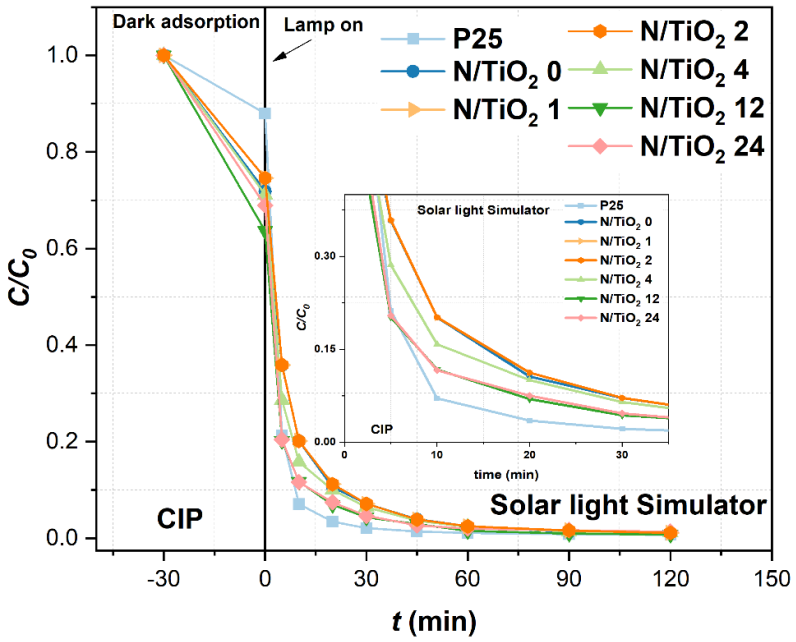

Figure 27. Photocatalytic degradation of ciprofloxacin by Degussa P25 TiO_2 and N/TiO_2 materials under SLS

Although the commercial photocatalyst exhibits the highest degradation rate for CIP removal, the kinetic constants calculated for each material, as shown in Table 9, reveal that commercial photocatalyst has a lower degradation rate under SLS than the degradation rate under UVA irradiation. On the contrary, all synthesized materials present a higher degradation rate under SLS than under UVA irradiation. The results indicate that nitrogen doping positively affects the photocatalytic activity across a broad irradiation spectrum. The improvement in the degradation rate for CIP removal under a broad irradiation spectrum such as SLS could be attributed to interstitial nitrogen doping, in which new energetic levels in the TiO_2 lattice are created instead of modifying the energy bandgap. These energetic levels probably shift the light absorption to the visible range or promote charge separation, enhancing the photocatalytic activity under the solar spectrum [29, 146]. Although there is an increase in the degradation rate with an increase in the N/Ti molar ratio, it was observed that at an N/Ti molar ratio of 12, the maximum degradation rate was achieved. For an N/Ti molar ratio of 24, the degradation rate is similar to that at an N/Ti molar ratio of 12, indicating that additional nitrogen beyond a certain threshold (12), does not contribute to the photocatalytic activity. Even an excess of nitrogen dopant could act as a recombination center that could reduce photocatalytic activity [118]. After the photocatalytic experiments, the pH value was measured, finding again that the pH remained invariable.

The photocatalytic experiments under cold visible light (CVL), displayed in Figure 28, show that all synthesized N/TiO_2 materials present photocatalytic activity under the visible

spectrum, whereas the commercial photocatalyst (Degussa P25) shows no photoactivity under visible irradiation source, as expected. Similar to observation under UVA and SLS, the degradation rate for CIP removal under CVL also increases with an increment in the N/Ti molar ratio. Nevertheless, under this less energetic irradiation, none of the tested N/TiO_2 materials achieved complete removal of CIP after 120 minutes of irradiation. This could be explained by the fact that the photons emitted by this lamp are mainly from the wavelength around 600 nm, with only a small portion emitted at 450 nm (Appendix, Figure S3d). Under this type of lamp, the degradation rates are 100 times lower than under the SLS, and a longer irradiation period could be required to achieve complete CIP removal. These results demonstrate that nitrogen doping effectively shifts photon absorption into the visible light range and shows that the synthesis method also plays an important role in the material properties (morphological, structural, optical, etc.). After the photocatalytic experiments, the pH value was measured, finding again that the pH remained invariable.

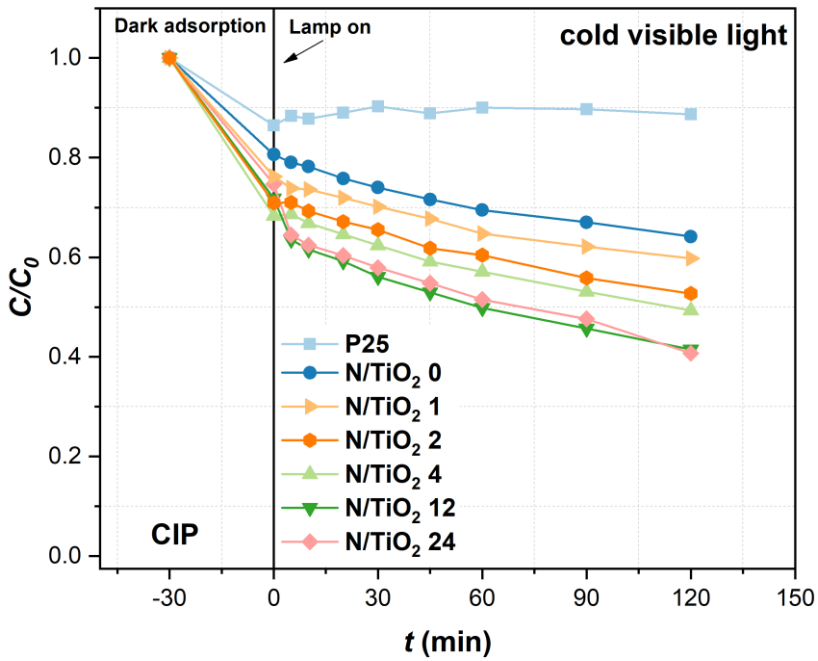

Figure 28. Photocatalytic degradation of ciprofloxacin by Degussa P25 TiO_2 and N/TiO_2 materials under CVL

The pseudo-first order and second order models were applied to determine the kinetic parameters for CIP degradation by each material under the three different irradiation sources, applying equations (10) and (11), previously described. By analyzing the fitting parameters for each model, the one that provides a better fit accurately describes the process and therefore indicates the reaction mechanism more effectively.

Table 9 shows the pseudo-first order (k_1, min^{-1}) and second order kinetic constants (k_2, L $mg^{-1} \cdot min^{-1}$) and removal efficiencies of N/TiO_2 materials. It can be observed that, for experiments conducted under UVA and SLS, the pseudo-first order model displays a determination coefficient (R^2) below 0.90 in most of the cases, indicating a poor accuracy of the model. However, for the experiments performed under CVL, the model shows a determination coefficient (R^2) above 0.90. On the other hand, for the second order model, the determination coefficient (R^2), for experiments under UVA and SLS is approximately 0.99 in most of the cases, suggesting a better fit of this model to the degradation process, which is influenced by various factors such as pollutant concentration, by-product formation, light intensity, etc. Although under CVL, both models have a determination coefficient (R^2) above 0.90, the second order model fits the experimental results better.

Table 9. Parameters obtained from the ciprofloxacin (CIP) degradation under UVA, Solar light simulator (SLS), and cold visible light (CVL) fitted to pseudo-first order kinetic model and to second order kinetic model for N/TiO_2 materials and TiO_2 P25.

pseudo-first order kinetic model						
	k_1, min^{-1}			**R^2**		
Lamp	**UVA**	**SLS**	**CVL**	**UVA**	**SLS**	**CVL**
N/TiO_2 0	0.0380	0.0432	0.0021	0.9001	0.9023	0.9796
N/TiO_2 4	0.0406	0.0443	0.0028	0.8893	0.8928	0.9957
N/TiO_2 12	0.0432	0.0477	0.0053	0.8635	0.8843	0.9432
N/TiO_2 24	0.0425	0.0464	0.0055	0.8621	0.8673	0.9392
Degussa P25	0.0588	0.0563	-	0.8562	0.8187	-

second order kinetic model									
	k_2, L $mg^{-1} \cdot min^{-1}$			**R^2**			**Removal Efficiency (η, %)**		
Lamp	**UVA**	**SLS**	**CVL**	**UVA**	**SLS**	**CVL**	**UVA**	**SLS**	**CVL**
N/TiO_2 0	0.39	0.58	0.0028	0.996	0.991	0.986	98.1	98.7	35.8
N/TiO_2 4	0.48	0.65	0.0044	0.995	0.989	0.998	98.5	98.8	50.6
N/TiO_2 12	0.59	0.98	0.0088	0.998	0.987	0.969	98.7	99.2	58.5
N/TiO_2 24	0.54	0.79	0.0091	0.987	0.997	0.966	98.4	99.0	59.3
Degussa P25	1.79	1.23	-	0.991	0.995	-	99.6	99.4	12.3*

***** By adsorption process.

Under the three different radiation sources, it was observed a synergistic effect between the adsorption and the photocatalytic processes for CIP removal, as shown in Figures 26, 27, and 28. Regardless of the N/Ti molar ratio, all N/TiO_2 materials demonstrated similar adsorption capacity, where the adsorption process contributes to approximately 30% of CIP

removal. This uniform adsorption capacity correlates with the high specific surface area of all N/TiO_2 materials and the affinity of the amine and carboxylic groups of CIP with the hydroxyl groups on the surface of the materials, favoring the adsorption of the pollutant on the photocatalyst surface. Considering this synergistic interaction between adsorption and photodegradation of CIP and based on the fitting analysis of the applied models, it could be deduced that the photocatalytic degradation of CIP by the N/TiO_2 materials under the three irradiation sources follows the second order kinetic model. Previously, Gabelica et al. reported similar results [41]. The pseudo-first order and second order kinetic plots of CIP photocatalytic degradation by Degussa P25 TiO_2 and N/TiO_2 materials are given in the Appendix (Figure S5 and S6).

After evaluating the adsorption and photocatalytic tests, combined with the material characterization, it can be inferred that the N/TiO_2 material with an N/Ti molar ratio of 12 exhibit the highest photoactivity based on nitrogen content; therefore, the N/Ti molar ratio of 12 was selected to continue further studies on material synthesis.

4.3. Microwave-Assisted synthesis of N/TiO_2/rGO nanocomposites: effect of rGO content

4.3.1. Graphene oxide reduction

Before incorporating rGO into the N/TiO_2 photocatalyst, a chemical reduction of graphene oxide (GO) combined with a thermal treatment was performed using ascorbic acid as a reducing agent under mild conditions in the microwave oven (125°C, 45 minutes). To verify the reduction of GO, XRD and Raman analyses were performed.

The X-ray diffraction pattern of GO has a singular diffraction peak at $2\theta = 10.4°$, corresponding to the (001) lattice plane, as shown in Figure 29, and it is attributed to oxygenated functional groups on the carbon [39]. Besides, the additional small and wide peak around $2\theta = 20.1°$ could indicate that GO is not completely connected by oxygen atoms [154]. On the contrary, the X-ray diffraction pattern of the rGO sample displays a diffraction peak at $2\theta = 24.3°$, corresponding to the (002) lattice plane. The absence of the diffraction peak related to the (001) plane and the appearance of the diffraction peak of the (002) lattice plane suggests the successful reduction of GO to rGO [123]. On the other hand, the additional diffraction peak

that appears at 2θ = 42.7° for the rGO sample could be attributed to stack disorder layers of rGO [155].

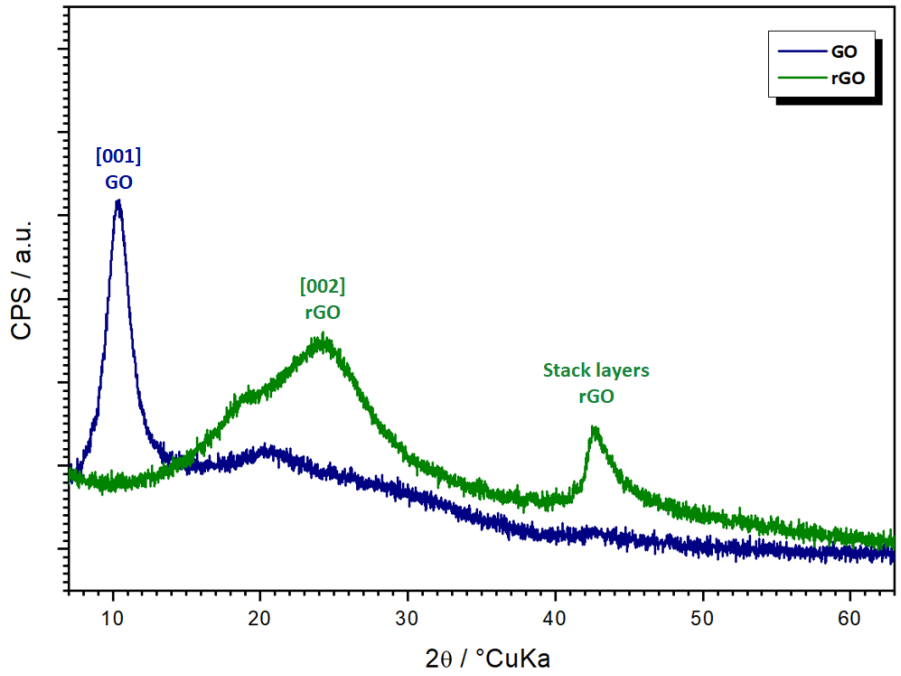

Figure 29. X-ray diffraction patterns of GO and rGO.

The Raman analysis shows that both samples (GO and rGO) have the characteristic D and G bands, around 1,350 and 1,590 cm^{-1}, respectively (Figure 30). The D and G bands are typical for all sp^2 carbon structures. Usually, the D band is associated with the breathing mode of sp^3 defects in the carbon structure. In contrast, the G band refers to stretching vibrations of ordered sp^2-bonded carbon atoms in a two-dimensional hexagonal lattice [156]. In the GO sample, the D band appears at 1,350 cm^{-1}, while for the rGO, this band was shifted to lower wavenumber (1,342 cm^{-1}); this shifting of the D band on the rGO is probably due to the reduction in the size of in-plane sp^2 domains by creating defects, vacancies, and distortions of the sp^2 domains after complete reduction [157]. On the other hand, the G band for the GO and rGO are found at 1,590 cm^{-1} and 1,591 cm^{-1}, respectively. The slight shifting to a higher wavenumber in the rGO could be due to oxygen moieties removal [155]. Based on the XRD and Raman analysis, it has been determined that the reduction of GO to rGO was successfully achieved under mild conditions and using non-hazardous chemicals.

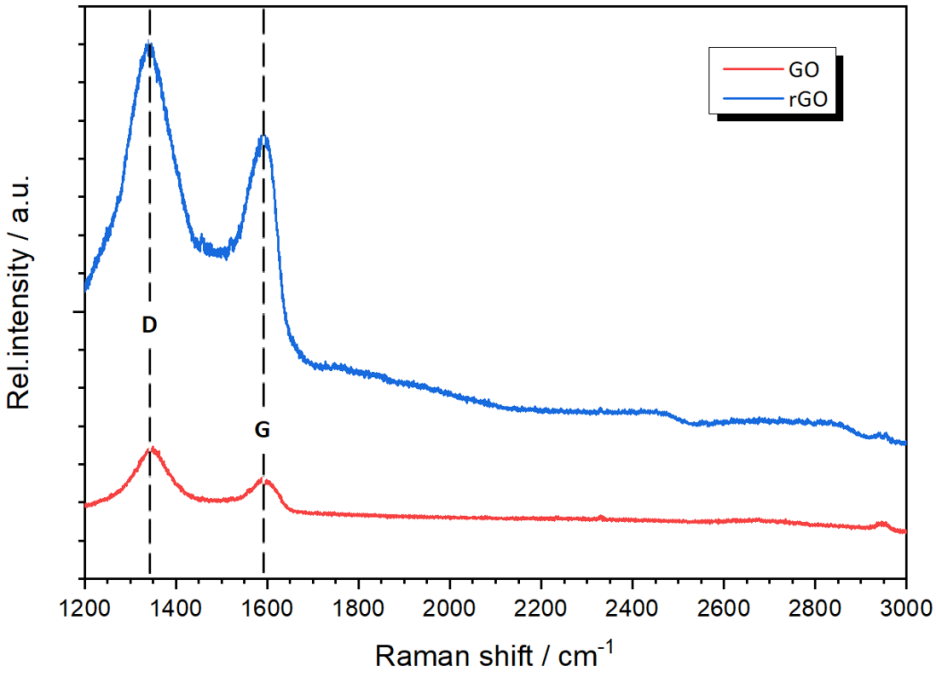

Figure 30. Raman spectra of GO and rGO.

4.3.2. Characterization of N/TiO_2/rGO nanocomposites

After determining the optimal N/Ti molar ratio and successfully obtaining rGO, N/TiO_2/rGO materials were synthesized, keeping the nitrogen content (N/Ti molar ratio = 12) and introducing different amounts of rGO (0.25 – 10 wt. %); the obtained materials were subjected to broad structural, microstructural, and spectroscopic characterization in order to optimize the preparation procedure in terms of the rGO content in the N/TiO_2/rGO materials.

Nitrogen adsorption/desorption isotherms were used to investigate the Brunauer, Emmett, and Teller (BET) specific surface area, while the pore size distribution was determined by the Barrett-Joyner-Halenda (BJH) method (Figure 31). A summary of the specific surface area, pore volume, and average pore diameter of N/TiO_2 12, N/TiO_2/rGO, P25 photocatalysts, and rGO material are presented in Table 10. It can be observed that the rGO sample has the largest surface area, and once it is incorporated into N/TiO_2/rGO, it contributes to the increment on the specific surface area, improving this property up to 27% in comparison to the N/TiO_2 material. Again, the synthesized materials display an outstanding specific surface area compared to the commercial photocatalysts Degussa P25 (48 $m^2 \cdot g^{-1}$).

Table 10. Specific surface area, pore volume, and pore size of P25, N/TiO_2, N/TiO_2/rGO photocatalysts, and rGO material.

Material	S_{BET}, $m^2 \cdot g^{-1}$	Vpore, $cm^3 \cdot g^{-1}$	**Average pore diameter, nm**
TiO_2 P25	48	0.196	13.7
rGO	192	0.323	6.5
N/TiO_2 12	139	0.297	8.0
N/TiO_2/rGO 0.25 wt. %	176	0.309	6.7
N/TiO_2/rGO 1 wt. %	171	0.303	6.7
N/TiO_2/rGO 3 wt. %	170	0.297	6.7
N/TiO_2/rGO 5 wt. %	176	0.303	6.6
N/TiO_2/rGO 10 wt. %	177	0.297	6.4

Figure 31 shows the nitrogen adsorption/desorption isotherms, in which it is observed that N/TiO_2/rGO and N/TiO_2 materials display type IV nitrogen adsorption-desorption isotherms, typical for mesoporous materials, with an H2 hysteresis type, indicating that the porosity is composed mainly of neck-like and wide body pores [158, 159]; while the TiO_2 Degussa P25 presents an H4 hysteresis type, characteristic of slit-like pores. Although the introduction of rGO reduced slightly the pore diameter in the N/TiO_2/rGO materials compared to N/TiO_2 photocatalyst, the pore volume remained similar in all synthesized materials. On the other hand, it is noticed that there are not significant changes of the material porosity regardless of rGO amount, which could indicate that the amount of rGO incorporated into the photocatalyst is limited, probably for the stacking layers of rGO that was observed from the XRD analysis.

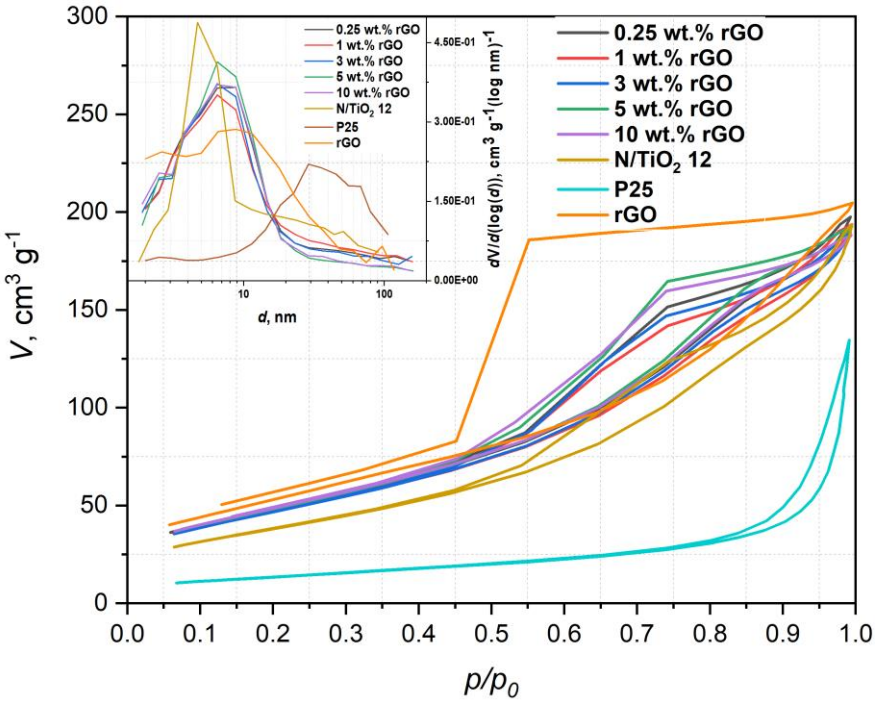

Figure 31. Adsorption-desorption isotherm, and pore size distribution of N/TiO_2 materials at different N/Ti molar ratios.

Following the methodology previously employed to identify alterations in the surface chemistry of N/TiO_2 materials via variations in nitrogen content, encompassing functional groups, chemical bonds, and the surface characteristics of the photocatalyst (hydrophilic/hydrophobic behavior), FTIR spectroscopy was utilized to observe changes in the N/TiO_2/rGO materials induced by the incorporation of rGO. FTIR spectra of N/TiO_2, N/TiO_2/rGO materials, and commercial photocatalyst (Degussa P25) are presented in Figure 32. The characteristic strong wide band associated with the stretching vibrations of Ti–O–Ti bonds is observed in all materials in the region between 400 and 800 cm^{-1}, without noticing changes by rGO addition [145]. Also, the signals related to the stretching vibrations of the O–H group for all materials are detected in the region between 3,670 and 2,800 cm^{-1}, as well as the peak linked to the stretching vibrations of the O–H group related to adsorbed water (1,638 cm^{-1}) [30]. However, it is noticed that the intensity of the O–H groups is reduced in all N/TiO_2/rGO materials compared to N/TiO_2 12, which could be associated with the incorporation of rGO due to the hydrophobic nature of rGO. Nevertheless, all N/TiO_2/rGO materials still have a higher intensity of bands related to the O–H group than the commercial photocatalyst P25, which could contribute to producing hydroxyl radicals during photocatalytic reactions [144, 145]. On the other hand, with N/TiO_2 12 and N/TiO_2/rGO photocatalysts

containing up to 3 wt. % rGO a small peak around 1455 cm^{-1} is observed, which could be attributed to the stretching vibrations of the N–H group [139].

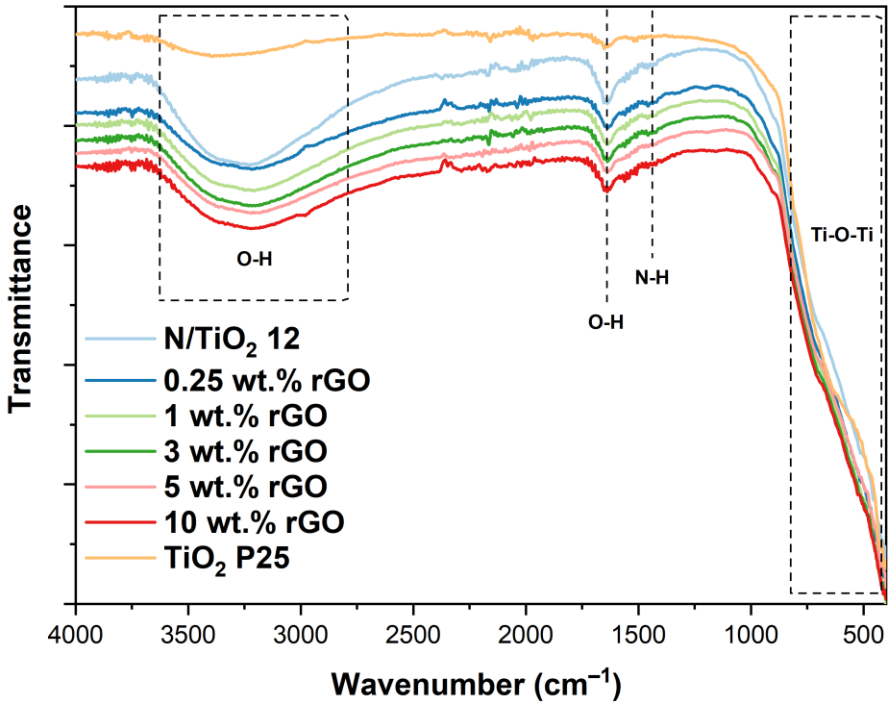

Figure 32. FTIR spectra of N/TiO_2, N/TiO_2/rGO photocatalysts with different amounts of rGO (0.25, 1, 3, 5 and 10 wt. %) and Degussa P25.

Raman analysis was performed for N/TiO_2 12 and N/TiO_2/rGO materials to observe the effect of rGO on the photocatalyst structure. The obtained Raman spectra of N/TiO_2 12 and N/TiO_2/rGO materials are displayed in Figure 33. In all analyzed materials, Raman modes associated to the anatase phase of TiO_2 are detected: 144 cm^{-1}(Eg), 398 cm^{-1}(B1g), 515 cm^{-1}(A1g), and 637 cm^{-1}(Eg) [160]. Additionally, Raman mode related to the rutile or brookite phase of TiO_2 are observed. On the other hand, two peaks located at 1,350 cm^{-1} and 1,618 cm^{-1} are associated with the stretching vibrations of ordered sp^2-bonded carbon atoms (G band) and with the breathing mode of sp^3 defects in the carbon structure (D band) of rGO, which are only observed in the N/TiO_2/rGO materials [142]. The absence of these two peaks on the N/TiO_2 12 could confirm the successful incorporation of rGO on the N/TiO_2/rGO materials. The Eg Raman mode at 144 cm^{-1} is shifted to a higher wavenumber (149 cm^{-1}) when rGO is incorporated, probably due to the surface defects created by the rGO, which could indicate a good interaction between the rGO and TiO_2 that could promote the charge separation during the photocatalytic process [98, 161].

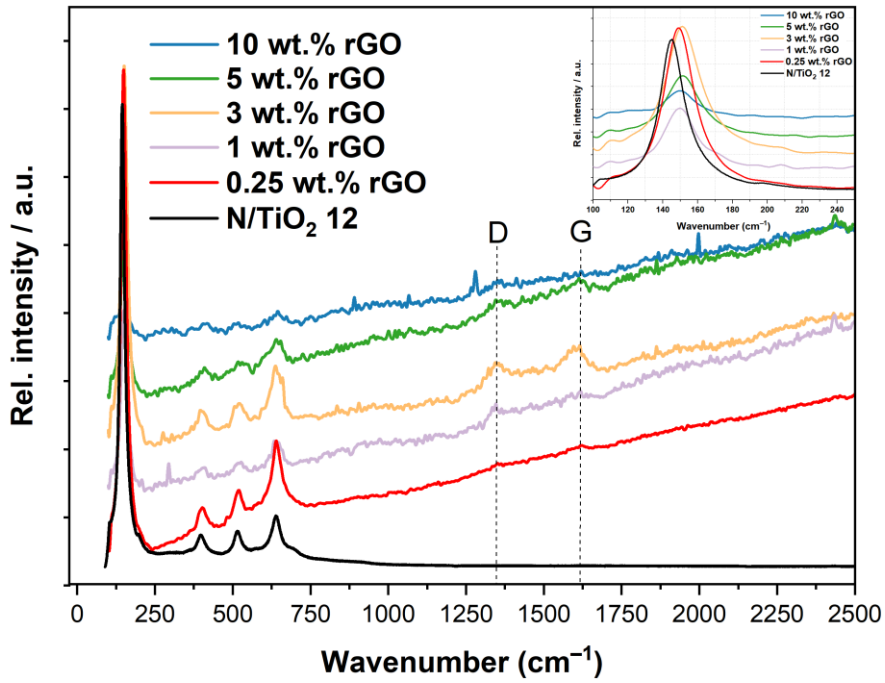

Figure 33. Raman spectra of N/TiO_2 and N/TiO_2/rGO photocatalysts with different amounts of rGO (0.25, 1, 3, 5 and 10 wt. %).

As a complement to the Raman analysis, X-ray diffraction (XRD) analysis allows the determination of crystalline phases and any changes resulting from the rGO addition. The X-ray diffraction (XRD) patterns of N/TiO_2 12 and N/TiO_2/rGO materials are presented in Figure 34. All materials display the characteristic diffraction peaks related to the anatase phase: 25.40° (101); 38.08° (112); 48.15° (200); 55.07° (211); 62.88° (204); 70.31° (220); 75.03° (215) (ICDD PDF#21-1272) [133]; which confirm the crystalline phase previously observed on the Raman analysis. Additionally, two diffraction peaks around 23° and 43° 2θ are observed on the N/TiO_2/rGO materials and are attributed to rGO and the stack disorder layers of rGO, respectively. These two peaks were previously identified in Figure 29. The absence of these two peaks in the N/TiO_2 12 material confirms the successful introduction of rGO into N/TiO_2/rGO materials.

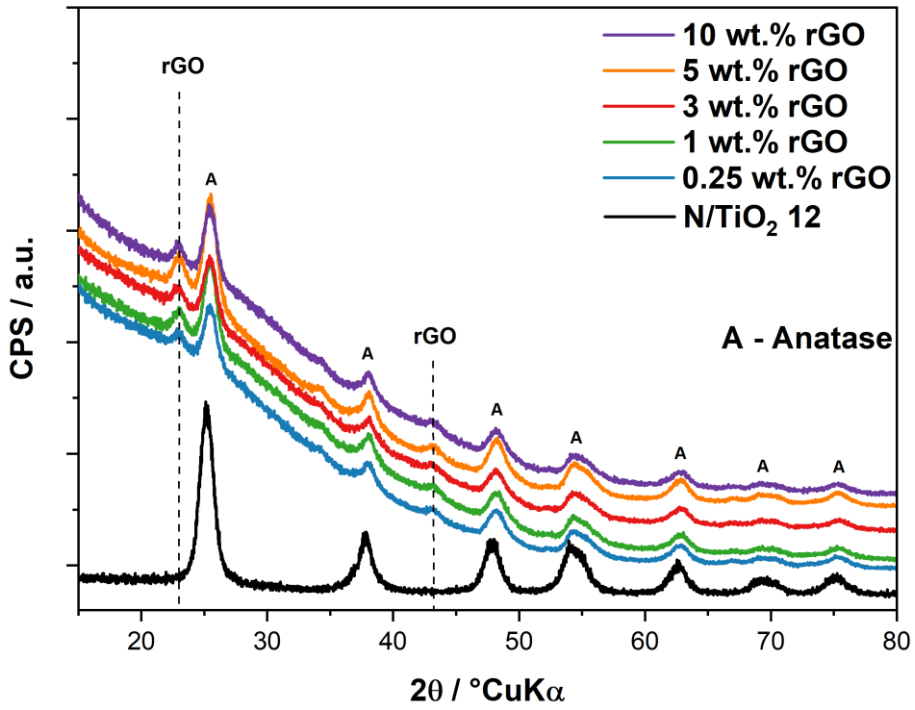

Figure 34. X-ray diffraction patterns of N/TiO_2 and N/TiO_2/rGO photocatalysts with different amounts of rGO (0.25, 1, 3, 5 and 10 wt. %).

Data obtained from the diffuse reflectance spectroscopy (DRS) analysis was used to calculate the energy bandgap using the Tauc plot for both synthesized N/TiO_2 12 and N/TiO_2/rGO materials (Figure 35). The results reveal that the incorporation of rGO leads to a reduction in the energy bandgap, with all N/TiO_2/rGO materials exhibiting lower energy bandgaps compared to the N/TiO_2 12 material and the commercial photocatalyst Degussa P25 (3.20 eV) [162]. Moreover, it is observed that the reduction in the energy bandgap is directly proportional to the amount of rGO; nevertheless, for loading values beyond 5 wt. % rGO, no additional changes in the energy bandgap are observed. The results observed from the Tauc plot could indicate that apart from the electron trap effect known in the rGO [163], it can also act as an energy bandgap narrower.

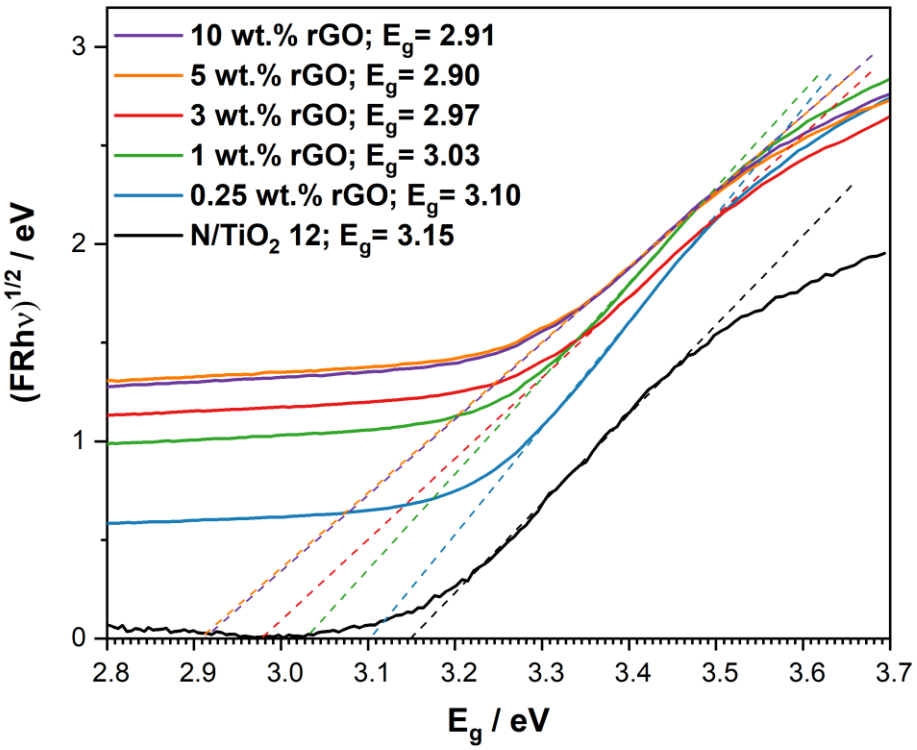

Figure 35. Tauc plot for energy bandgap determination of N/TiO_2 and N/TiO_2/rGO photocatalysts with different amounts of rGO (0.25, 1, 3, 5 and 10 wt. %).

For changes in chemical composition between the N/TiO_2 12 and N/TiO_2/rGO materials, the surface elemental composition of the materials was determined by SEM-EDS analysis, which is presented in Table 11. The compositional analysis reveals that carbon content is proportional to the rGO loading. In contrast, the oxygen composition is inversely proportional to the rGO amount, which is expected due to the reduction of oxygen functional groups (carbonyl, carboxylic acids, epoxy, etc.) in the rGO after the chemical and thermal reduction of GO. As expected, N/TiO_2 12 material shows no presence of carbon moieties. On the other hand, the nitrogen element detected on the N/TiO_2 12 material is not observed in the N/TiO_2/rGO materials. The lack of detection of nitrogen elements in the N/TiO_2/rGO materials could be due to the coverage of nitrogen fraction by carbon moieties. Additionally, it is known that SEM-EDS elemental analysis is more qualitative than quantitative method, and for light elements such as nitrogen and carbon, the method is not very precise [164].

Table 11. Elemental composition of N/TiO_2 and N/TiO_2/rGO photocatalysts determined by SEM-EDS analysis.

Material	Elemental composition, wt. %			
	Ti	O	C	N
N/TiO_2 12	72.0	21.0	–	7.0
N/TiO_2/rGO 0.25 wt. %	83.7	15.3	1.0	–
N/TiO_2/rGO 1 wt. %	83.1	15.2	1.7	–
N/TiO_2/rGO 3 wt. %	85.0	12.3	2.7	–
N/TiO_2/rGO 5 wt. %	85.1	12.2	2.7	–
N/TiO_2/rGO 10 wt. %	86.3	11.9	1.8	–

In order to have a more precise estimation of carbon, nitrogen, and oxygen composition, an additional technique, XPS analysis, was used to complement surface characterization. The bulk composition of the most relevant materials (N/TiO_2 12 and N/TiO_2/rGO with 0.25 wt. % photocatalysts) was determined by XPS analysis, and the results are summarized in Table 12. The XPS elemental composition analysis confirmed that, effectively, the oxygen content is lower in the N/TiO_2/rGO than in the N/TiO_2 due to the diminishing of oxygen functional groups in the rGO, as was observed previously in the SEM-EDS analysis. Also, it is confirmed that the carbon fraction is higher in the N/TiO_2/rGO than in the N/TiO_2 due to rGO content. Although SEM-EDS analysis did not show carbon content in the N/TiO_2 material, the XPS elemental composition reveals the presence of carbon impurities in this photocatalyst originating from the synthesis (urea or acetylacetone), as was previously identified in the subchapter 4.2.1 Characterization of nitrogen-doped materials (Figure 23). On the other hand, XPS analysis also allowed the detection of nitrogen elements in the N/TiO_2/rGO, even with double the amount of nitrogen compared to the N/TiO_2 material, which could indicate that rGO could favor the anchoring of nitrogen in the TiO_2.

Table 12. Bulk composition of N/TiO_2 and N/TiO_2/rGO photocatalysts determined by XPS analysis.

Material	Elemental composition, wt. %			
	Ti	O	C	N
N/TiO_2 12	21.5	66.5	11.5	0.5
N/TiO_2/rGO 0.25 wt. %	23.2	56.8	18.9	1.1

The chemical composition and oxidation states of the most relevant materials (N/TiO_2 12 and N/TiO_2/rGO with 0.25 wt. % photocatalysts) were determined through the XPS analysis, and the obtained high-resolution Ti, O, and N spectra are presented in Figure 36. The Ti 2p spectra for N/TiO_2 and N/TiO_2/rGO with 0.25 wt. % of rGO, which are shown in Figures 36a and 36d, respectively, display two signals at 458.7 eV and 464.5 eV that are related to Ti $2p_{1/2}$ and Ti $2p_{3/2}$, which are typical for Ti^{4+} oxidation states [149], indicating the formation of TiO_2 anatase phase, as was previously identified through the Raman and XRD analysis (Figures 32 and 33). Comparing the two photocatalysts (N/TiO_2 12 and N/TiO_2/rGO with 0.25 wt. %), no change is observed in the electronic densities, which probably indicates that rGO is not interacting directly with the Ti element.

The O 1s spectra for N/TiO_2 12 and N/TiO_2/rGO with 0.25 wt. % of rGO, shown in Figures 36b and 36e, present three binding energies. The main binding energy is located at 530.2 eV, associated with the bonding between oxygen and titanium (O-Ti). In contrast, the second binding energy at 531.6 eV is linked to the bonding between oxygen and carbon (O-C). In the case of N/TiO_2/rGO with 0.25 wt. % of rGO, this bonding could be attributed to the interaction between the carbon of rGO and the oxygen atom of the TiO_2 structure or due to oxygenated groups such as carbonyl, epoxy, carboxylic, etc. that were not completely removed during the reduction process [21]. On the contrary, the oxygen bonded to carbon (O-C) in the N/TiO_2 12 material and the binding energy presents lower intensity potentially associated with impurities from the synthesis (urea or acetylacetone). Additionally, a third signal, located at 532.8 eV, is related to the binding energy between oxygen and hydrogen (O-H) and could be attributed to the hydroxylated surface by chemisorbed water. For this third signal, N/TiO_2/rGO with 0.25 wt. % of rGO shows lower intensity compared to N/TiO_2 12 material, probably due to the hydrophobic nature of rGO [165]. Apart from the intensity changes observed for the O-C and O-H binding energies, there is a slight change in the electronic densities of oxygen, with a shifting of the main peak from 529.95 eV (N/TiO_2 12) to 530.25 eV (N/TiO_2/rGO with 0.25 wt. % of rGO), that could be attributed due to the interaction between carbon (rGO) and oxygen from TiO_2, and indicating that rGO was successfully incorporated into the TiO_2 structure.

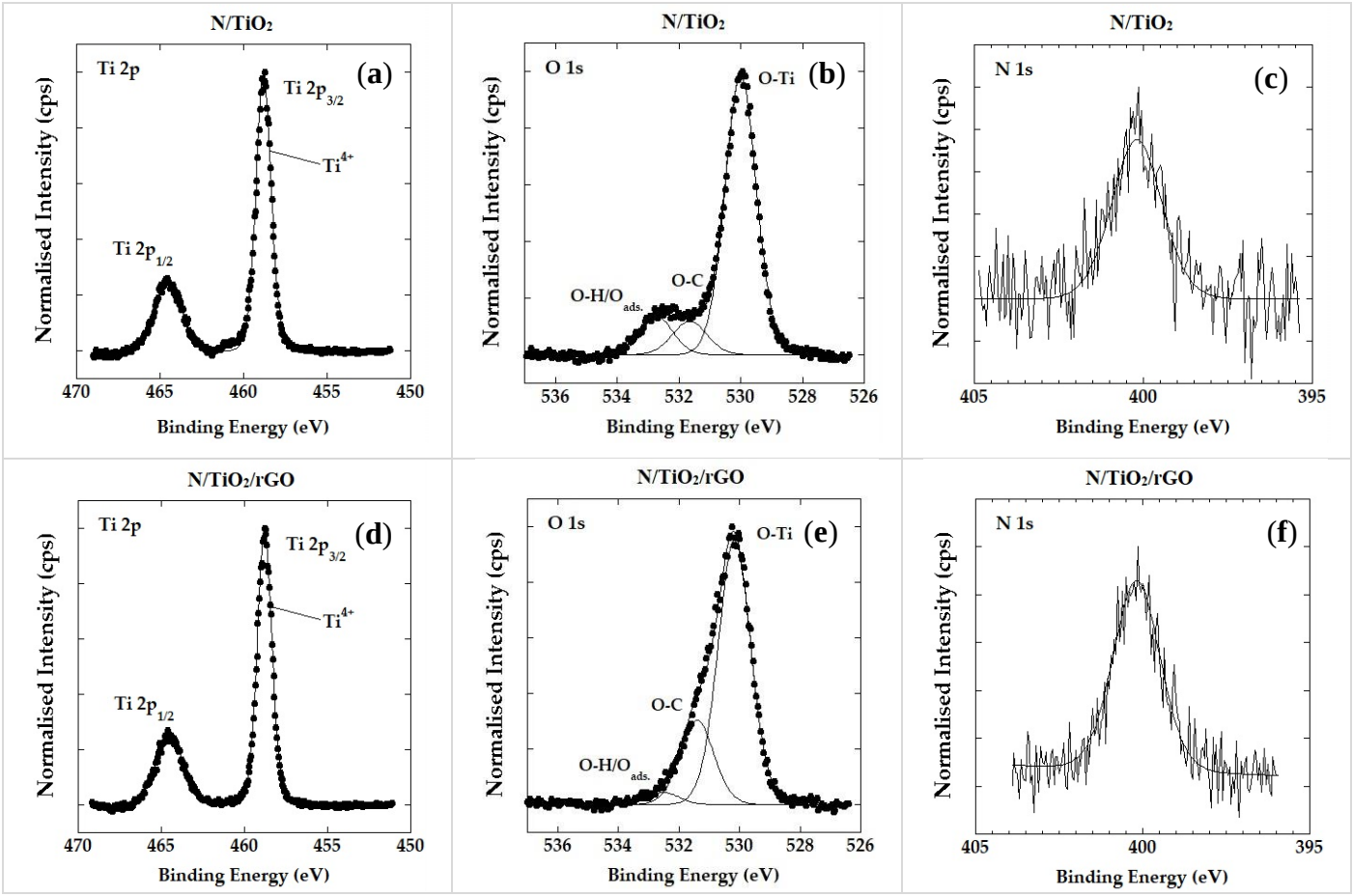

Figure 36. High-resolution XPS spectra of N/TiO_2 and N/TiO_2/rGO with 0.25 wt. % of rGO. (a), (b), and (c) are the Ti 2p spectrum, O 1s spectrum, and N 1s spectrum, respectively, for N/TiO_2. (d), (e) and (f) are the Ti 2p spectrum, O 1s spectrum, and N 1s spectrum, respectively, for N/TiO_2/rGO

On the other hand, the N 1s spectra for N/TiO_2 12 and N/TiO_2/rGO with 0.25 wt. % of rGO, shown in Figures 36c and 36f, show binding energy located at 400.15 eV that is related to the interstitial nitrogen doping assigned to the bonding between nitrogen and oxygen (N-O) [166], as was previously identified in subchapter 4.2.1. Characterization of nitrogen-doped materials (Figure 23e). Although this type of interstitial nitrogen doping (N-O) creates new energetic levels rather than modifying the energy bandgap, it contributes to absorption in the visible light range without modifying the energy bandgap [32, 33]. Additionally, there are no changes in the electronic densities around nitrogen elements between both photocatalysts (N/TiO_2 12 and N/TiO_2/rGO with 0.25 wt. %), reinforcing the theory that the only interaction of rGO with TiO_2 is through the O-C bonding.

4.3.3. Photocatalytic test of N/TiO_2/rGO nanocomposites

Before the photocatalytic evaluation of N/TiO_2 12, N/TiO_2/rGO materials, and commercial TiO_2 P25, the CIP adsorption-desorption equilibrium was determined, as shown in Figure 37. It can be seen that the pollutant has fast adsorption over the different photocatalysts, achieving most of the adsorption within the first five minutes, and the complete adsorption-desorption equilibrium is reached in 30 minutes. Additionally, it is noticed that N/TiO_2 12 and N/TiO_2/rGO materials adsorbed three times higher than the commercial photocatalyst (Degussa P25), which could be attributed to the larger specific surface area of the synthesized materials, as was previously observed (Table 10). Despite N/TiO_2/rGO materials having a higher specific surface area than N/TiO_2 12 material, there are no differences in the adsorption capacities. The fast adsorption of CIP on the synthesized materials and their similarity in the adsorption capacity could be related to the high affinity of the amine and carboxylic groups of CIP with the oxygen and nitrogen functional groups of materials that favor the adsorption by hydrogen bonds. The pH was measured at the beginning and end of the adsorption test, observing that pH did not change during the test, keeping it in the range of 6.2 – 6.5.

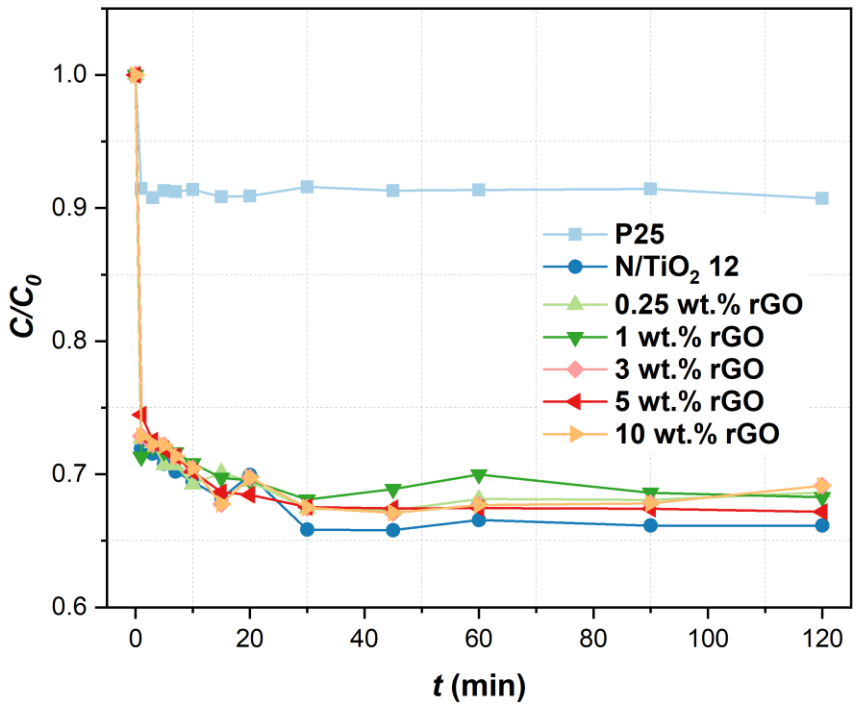

Figure 37. Adsorption-desorption equilibrium of ciprofloxacin CIP on P25, N/TiO_2 and N/TiO_2/rGO with different amounts of rGO.

Once the adsorption-desorption equilibrium for CIP was determined, the photoactivity of N/TiO_2 12, N/TiO_2/rGO materials with different amounts of rGO, and commercial TiO_2 P25 were evaluated again through the degradation of CIP aqueous solution (10 $mg \cdot L^{-1}$ = 30 µM) under three different irradiation source: UVA light (Figure 38), solar light simulator (Figure 39) and cold visible light (Figure 40). Before starting the degradation test, the initial pH value of the CIP solution was measured, ranging between 6.2 and 6.5. The photocatalytic test under UVA irradiation shows again that the Degussa P25 photocatalyst has the highest degradation rate, followed by the N/TiO_2/rGO 0.25 wt. %, N/TiO_2 12, and the other N/TiO_2/rGO materials, achieving up to 90% CIP removal in just 20 min of UVA irradiation, with the exception of N/TiO_2/rGO 5 wt. % that removed a little bit less than 90 % in the same period. After 60 minutes of UVA irradiation, all synthesized materials achieved more than 95% of pollutant removal, and no significant changes in the CIP concentration were detected afterwards. For the photocatalyst containing rGO, the highest photocatalytic activity is observed with the lowest amount used, and an increase in the rGO amount reduces the degradation rate. In this case, the only material that shows improvement compared to the N/TiO_2 12 is the N/TiO_2/rGO 0.25 wt. % material. After the photocatalytic experiments, the pH value was measured, finding that the pH remained invariable. Regarding the photolysis test, in which CIP is irradiated with UVA light without a photocatalyst, it is noticed that this pollutant is susceptible to degradation by the UVA irradiation alone; however, the degradation rate is relevant but slower compared to that observed when using any photocatalyst, and after 120 minutes of irradiation, a part of CIP remains in the solution (around 21%).

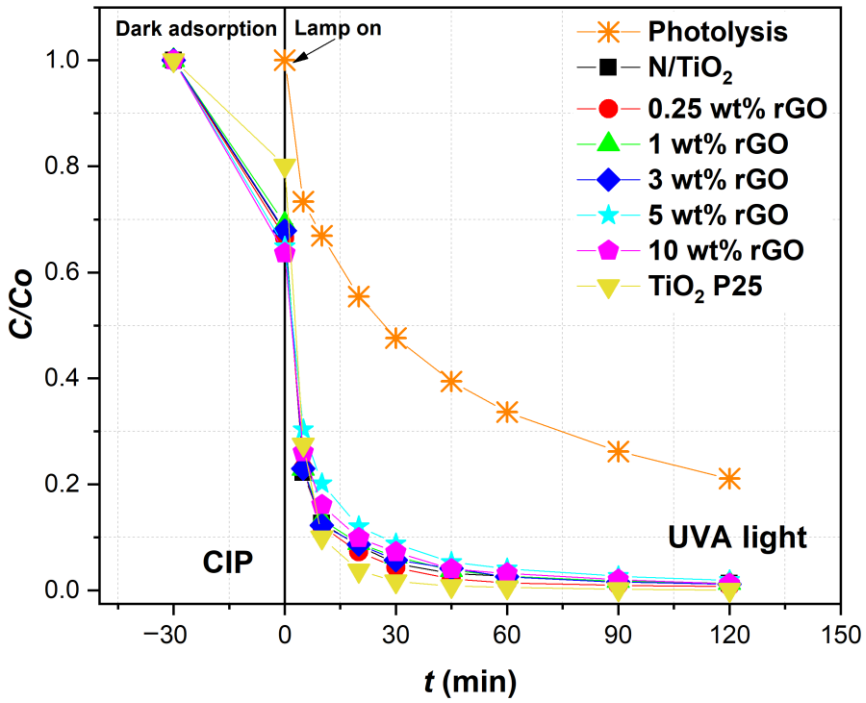

Figure 38. Photolytic and photocatalytic degradation of ciprofloxacin CIP by P25, N/TiO_2 and N/TiO_2/rGO with different amounts of rGO under UVA light.

Under the solar light simulator (SLS), it is noticed that the degradation of CIP follows a trend like the one observed under the UVA radiation, where the photocatalyst Degussa P25 again displays the highest degradation rate, followed by the N/TiO_2/rGO 0.25 wt. %, N/TiO_2 12, and the other N/TiO_2/rGO materials, achieving up to 90% CIP removal in just 20 minutes of solar irradiation. Similarly to the results observed under UVA irradiation, the photocatalytic activity also exhibits a trend where the lowest amount of rGO yields the highest activity, while an increase in the rGO amount leads to a reduction in the degradation rate. After 60 minutes of SLS irradiation, all synthesized materials reached more than 95% of pollutant removal, and no significant changes in the CIP concentration were detected. After the photocatalytic experiments, the pH value was measured, finding that the pH remained invariable. For the photolysis test, it is observed that the degradation rate is higher than under UVA, even achieving almost complete degradation of CIP (95%) after 120 minutes of irradiation.

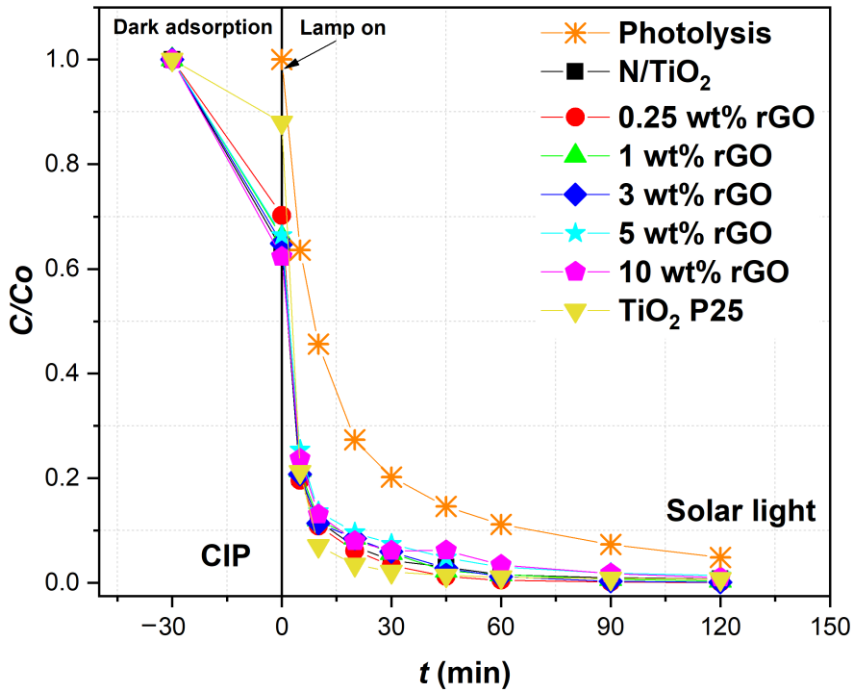

Figure 39. Photolytic and photocatalytic degradation of ciprofloxacin CIP by P25, N/TiO_2 and N/TiO_2/rGO with different amounts of rGO undersolar light simulator.

The photocatalytic experiments under cold visible light (CVL), displayed in Figure 40, show that all synthesized materials (N/TiO_2 12, N/TiO_2/rGO with different amounts of rGO) present photocatalytic activity under the visible spectrum, while the commercial photocatalyst (Degussa P25) does not show photoactivity under this irradiation source. Although N/TiO_2/rGO materials show lower photoactivity than N/TiO_2 12, they keep the trend in which an increment in the rGO content reduces the photocatalytic activity. Under this less energetic irradiation source, none of the tested materials achieved complete removal of CIP after 120 minutes of irradiation. On the other hand, the photolysis test shows that the photons in the wavelength range between 450 and 600 nm do not contain enough energy to break down the CIP molecule.

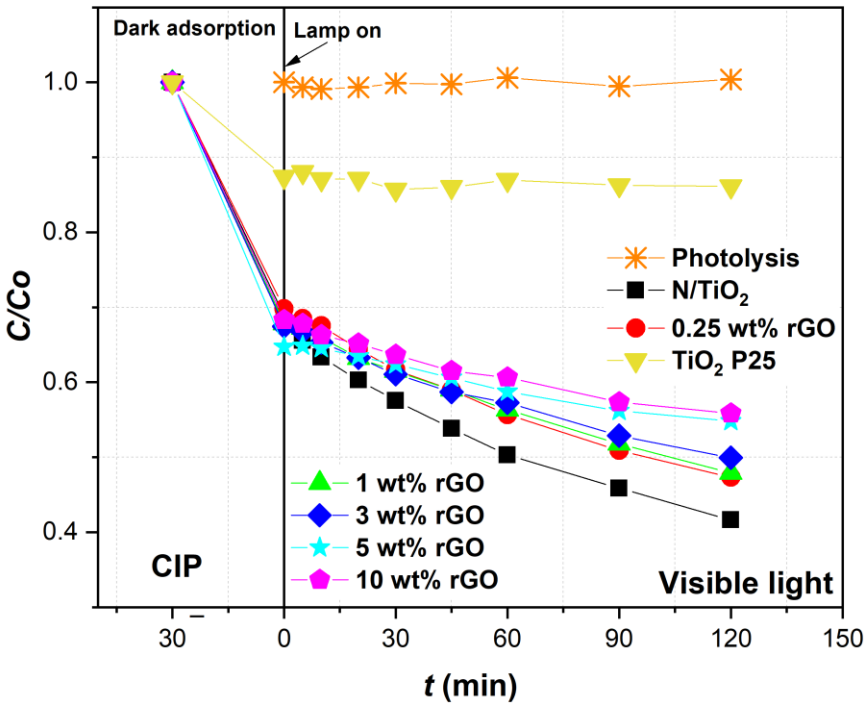

Figure 40. Photolytic and photocatalytic degradation of ciprofloxacin CIP by P25, N/TiO_2 and N/TiO_2/rGO with different amounts of rGO under cold visible light.

After evaluating all synthesized materials under the three different light sources, it was observed that for N/TiO_2/rGO materials, the degradation is reduced by the increment of rGO content, being the N/TiO_2/rGO 0.25 wt. % the most photoactive material, even better than the N/TiO_2 12, except under CVL. These findings could be explained by the fact that excess doping elements (N and rGO) could have a negative effect on the photocatalytic properties because they could act as recombination centers instead of preventing the recombination, thereby depleting the photoactivity [167–169]. Considering the material contains nitrogen dopant, the rGO amount required for dosing probably could be quite low. Additionally, as was observed in the XRD analysis (Figure 29), rGO contains some stack disorder layer that, in excess, could either block the light absorption, reducing the probability that TiO_2 could absorb photons, or act as an isolator that does not contribute to charge separation (h^+/e^-), depleting the photoactivity.

Apart from the synergistic effect of adsorption and photodegradation processes observed for all synthesized materials and analyzing N/TiO_2/rGO nanocomposite with 0.25 wt. % of rGO in more detail, it is noticed that the introduction of rGO improved the degradation rate under UVA and SLS irradiation compared to N/TiO_2 12, and its photoactivity under SLS is similar to the commercial TiO_2, as can be seen from the calculated kinetic constants summarized in Table 13. The improvement of photoactivity of N/TiO_2/rGO

nanocomposite with 0.25 wt. % of rGO could be attributed to the reduction in the recombination of photogenerated electron/hole charge pairs due to the role of rGO, which act as a sink for electrons in the composite [39]. On the other hand, comparing the degradation rate between UVA and SLS lamps and considering that SLS has 40 % lower UVA radiation intensity (59.2 $W \cdot m^{-2}$) than the UVA lamp (98.5 $W \cdot m^{-2}$) (more details about radiation intensity will be discussed in another subchapter), it is observed that under SLS, the degradation rate is increased around 30% compared to the experiment under UVA. This photocatalytic activity improvement under solar radiation could be attributed to the synergistic effect of nitrogen and rGO, where interstitial nitrogen doping creates new energetic levels that shift the light absorption to the visible range [31, 170]; meanwhile, rGO acts as a sink of electrons, avoiding the recombination phenomenon. On the contrary, the reduction in the photoactivity of N/TiO_2/rGO with 0.25 wt. % of rGO under CVL compared to N/TiO_2 12 could be explained by the fact that some part of interstitial nitrogen could be covered by the rGO, as was previously noticed in the SEM-EDS compositional analysis, preventing that nitrogen could absorb some photons.

For the photocatalytic tests, the degradation rate is analyzed using both the pseudo-first order and second order models to identify which model better describes the degradation process, as previously described in subsection 4.1.2. Adsorption and photocatalytic test (nitrogen-doped materials), equations (10) and (11). Also, based on fitting parameters analysis for each model, the one that offers a better parameter fitting is the one that describes the process more accurately and thus better points out the reaction mechanism.

Table 13. Pseudo-first order, second order kinetic parameters and efficiencies of CIP removal by N/TiO_2, TiO_2 P25, and N/TiO_2/rGO materials under UVA, Solar light simulator (SLS), and Cold visible light (CVL).

Lamp	Material	Removal by adsorption	Removal efficiency	Model			
				pseudo-first order k_1, min^{-1}		Second order k_2, L $mg^{-1} \cdot min^{-1}$	
		%	η, %	k_1	R^2	k_2	R^2
UVA	N/TiO_2	32.44	98.02	0.0432	0.8635	0.5881	0.9975
	TiO_2 P25	19.87	99.58	0.0589	0.8508	1.9217	0.9937
	N/TiO_2/rGO 0.25 wt. %	33.47	98.81	0.0489	0.8801	0.9388	0.9910
	N/TiO_2/rGO 1 wt. %	30.87	97.95	0.0425	0.8710	0.5652	0.9976
	N/TiO_2/rGO 3 wt. %	32.15	98.21	0.0433	0.8782	0.6245	0.9928
	N/TiO_2/rGO 5 wt. %	35.15	97.04	0.0379	0.9114	0.3992	0.9763
	N/TiO_2/rGO 10 wt. %	36.40	98.01	0.0407	0.8985	0.5093	0.9844
	Photolysis	*	78.92	0.0154	0.9404	0.0028	0.9953

SLS	N/TiO_2	36.32	98.77	0.0477	0.8843	0.9768	0.9869
	TiO_2 P25	12.04	99.26	0.0558	0.8122	1.2612	0.9839
	N/TiO_2/rGO 0.25 wt. %	29.75	99.90	0.0531	0.8645	1.2462	0.9866
	N/TiO_2/rGO 1 wt. %	33.96	99.42	0.0468	0.8773	0.8664	0.9873
	N/TiO_2/rGO 3 wt. %	35.12	99.82	0.0446	0.8869	0.7629	0.9861
	N/TiO_2/rGO 5 wt. %	33.59	97.88	0.0410	0.8879	0.4908	0.9921
	N/TiO_2/rGO 10 wt. %	37.70	98.34	0.0404	0.8870	0.5094	0.9771
	Photolysis	*	95.10	0.0304	0.9279	0.0140	0.9922
CVL	N/TiO_2	31.20	58.36	0.0046	0.9832	0.0079	0.9949
	TiO_2 P25	12.30	*	*	*	*	*
	N/TiO_2/rGO 0.25 wt. %	30.21	52.69	0.0035	0.995	0.0052	0.9991
	N/TiO_2/rGO 1 wt. %	32.15	52.10	0.003	0.9983	0.0050	0.9995
	N/TiO_2/rGO 3 wt. %	32.54	50.07	0.0027	0.9937	0.0044	0.9977
	N/TiO_2/rGO 5 wt. %	35.27	45.20	0.0015	0.9897	0.0021	0.9898
	N/TiO_2/rGO 10 wt. %	31.70	44.17	0.0019	0.9860	0.0026	0.9904
	Photolysis	*	*	*	*	*	*

*No photolytic or photocatalytic degradation was observed

The calculated kinetic constants are summarized in Table 13, where the pseudo-first order (k_1, min^{-1}) and second order (k_2, $L \cdot mg^{-1} \cdot min^{-1}$) kinetic constants, their determination coefficients (R^2), and efficiencies for the CIP removal by N/TiO_2, N/TiO_2/rGO materials, and commercial TiO_2 P25 under UVA, solar light simulator, and cold visible light are shown. As observed for nitrogen doped materials, under UVA and SLS, the pseudo-first order model displays a determination coefficient(R^2), in most of the cases, below 0.90, indicating that the model does not fit very well. Upon analyzing both irradiation sources by the second order model, it is observed that the determination coefficient(R^2) is above 0.98 in most cases. This indicates that the model accurately describes the degradation process, wherein degradation is affected by several aspects such as pollutant concentration, byproduct formation, light intensity, etc. In the case of CVL, both models show a determination coefficient(R^2) above 0.90; however, the second order model fits the data better.

Once all synthesized N/TiO_2/rGO materials were evaluated in the degradation of CIP under different irradiation sources, it was observed that the material with the lowest load amount of rGO (N/TiO_2/rGO with 0.25 wt. % of rGO) is the most photoactive nanocomposite. Therefore, this material was selected to continue with further photocatalytic tests, in which other pharmaceuticals are used as target pollutants: diclofenac (DCF, 10 $mg \cdot L^{-1}$ = 34 µM) and

salicylic acid (SA, 10 mg·L^{-1} = 72 µM). Additionally, apart from using the three irradiation sources (UVA, SLS, and CVL), another irradiation source is included in the photocatalytic test: blue visible light, which has a maximum energy emission at 405 nm, the transition zone between UVA and visible light.

To see the effect of the additional irradiation source (BVL), CIP removal was compared under different irradiation sources, including BVL, as shown in Figure 41. It can be seen that although the degradation rate under BVL is slower than under UVA and SLS, the N/TiO_2/rGO 0.25 wt.% photocatalyst achieves the same removal efficiency under this irradiation source as under UVA and SLS, after 60 minutes of irradiation. After that period, no significant changes in the CIP concentration were detected.

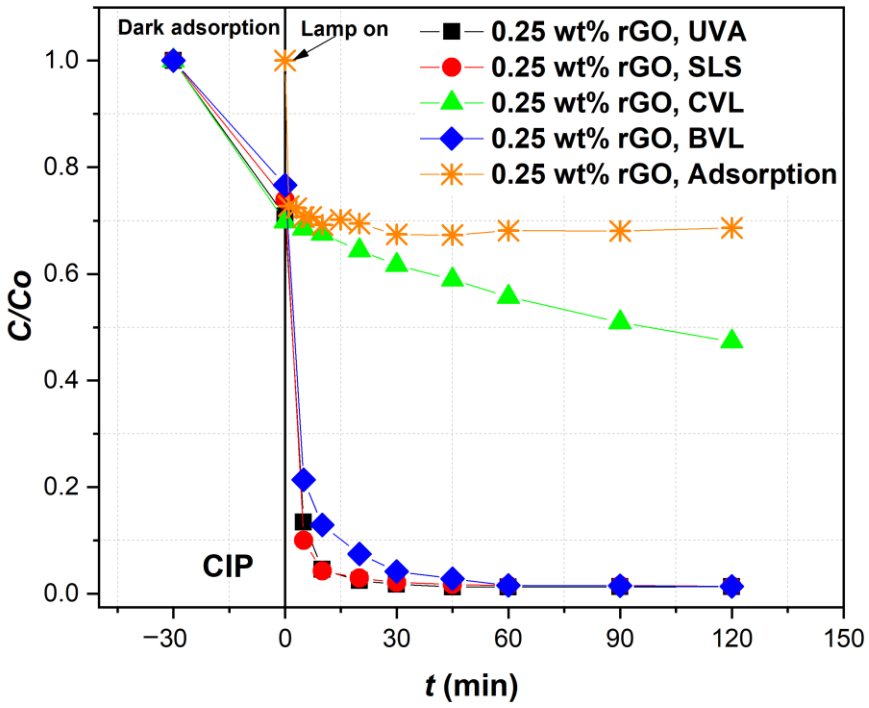

Figure 41. Adsorption and photocatalytic degradation of ciprofloxacin (CIP) by N/TiO_2/rGO with 0.25 wt. % of rGO material under UVA light, solar light simulator (SLS), cold visible light (CVL), and blue visible light (BVL).

On the other hand, before starting the degradation tests for the other pharmaceuticals, the DCF and SA adsorption-desorption equilibrium was determined. In the case of DCF, the adsorption process did not take place, as is displayed in Figure 42, while for SA, nearly 20 % of the pollutant is adsorbed, and within the first 5 minutes, the adsorption-desorption equilibrium is reached, as shown in Figure 43.

The initial pH value of the DCF and SA solutions were measured at the beginning of the degradation tests. For DCF, the solution pH was between 5.3 and 5.5, while for SA, the pH was 4.1– 4.2. DCF removal under different irradiation sources is shown in Figure 42. It can be seen that the DCF degradation rate under UVA and SLS is very fast compared to CVL, and no significant differences between these two irradiation sources are observed, where just 20 minutes of irradiation is needed to remove more than 90% of the pollutant. After 45 minutes of irradiation, almost 98% had been removed, after which no significant changes in the DCF concentration were detected. Under BVL, DCF presents a slower degradation compared to UVA and SLS irradiation sources, where 120 minutes of irradiation are required to accomplish more complete removal. On the contrary, no DFC removal is observed under CVL irradiation. After the photocatalytic experiments, the pH value was measured, finding that the pH remained invariable.

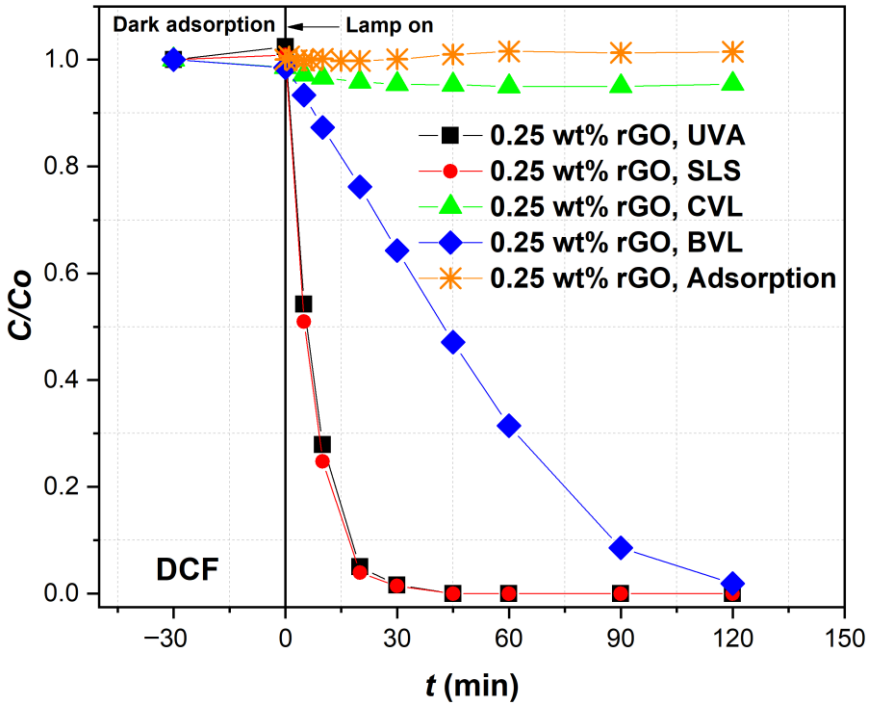

Figure 42. Adsorption and photocatalytic degradation of diclofenac (DCF) by N/TiO_2/rGO with 0.25 wt. % of rGO material under UVA light, solar light simulator (SLS), cold visible light (CVL), and blue visible light (BVL).

It is observed that for CIP and SA removal (Figures 41 and 43), a synergistic effect between adsorption and photocatalyst processes takes place, while for the DCF, the photocatalytic process is the only mechanism that is involved in pollutant removal. Also, it is noticed that for the pollutants that were adsorbed onto the photocatalyst (CIP and SA), the degradation rate under BVL was comparable to the UVA and SLS and presented some

degradation under CVL, indicating that the adsorption process plays an important role for pollutant removal under low energetic irradiation sources. Although DCF is present as a neutral molecule at the solution pH, SA being negatively charged, and CIP being positively and negatively charged (zwitterion form), the adsorption behavior is different for each pollutant, indicating that the adsorption process is probably governed by the molecule polarity rather than pollutant ionization state CIP and SA are polar molecules, while DCF is a non-polar molecule.

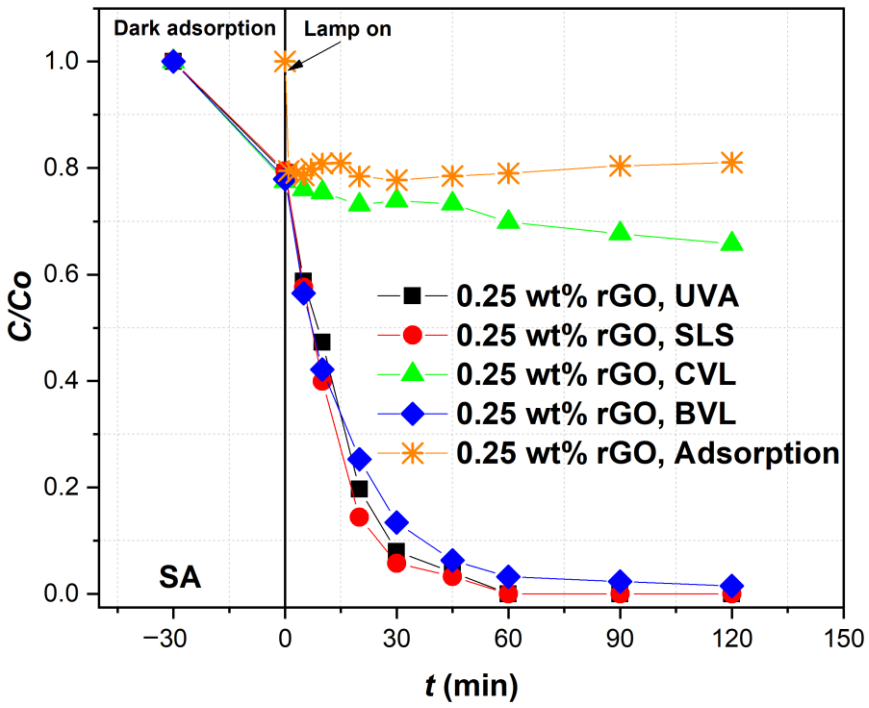

Figure 43. Adsorption and photocatalytic degradation of salicylic acid (SA) by N/TiO_2/rGO with 0.25 wt. % of rGO material under UVA light, solar light simulator (SLS), cold visible light (CVL), and blue visible light (BVL).

In addition to the photocatalytic tests, the three pharmaceuticals were subject to photolytic tests under different irradiation sources, as shown in Figure 44. It is noticed that CIP is the most susceptible molecule to photolytic degradation, being degraded under all irradiation sources except CVL. This pollutant is strongly degraded under SLS, being removed more than 90% after 120 minutes of irradiation, while under UVA and BVL, its removal achieves nearly 80% and 30%, respectively. On the other hand, DCF is susceptible to degradation only under SLS, probably by the most energetic fraction of solar radiation, being removed around 80%. On the contrary, the SA molecule is very resistant to degradation by the photolysis process, remaining invariable in its concentration under all irradiation sources applied.

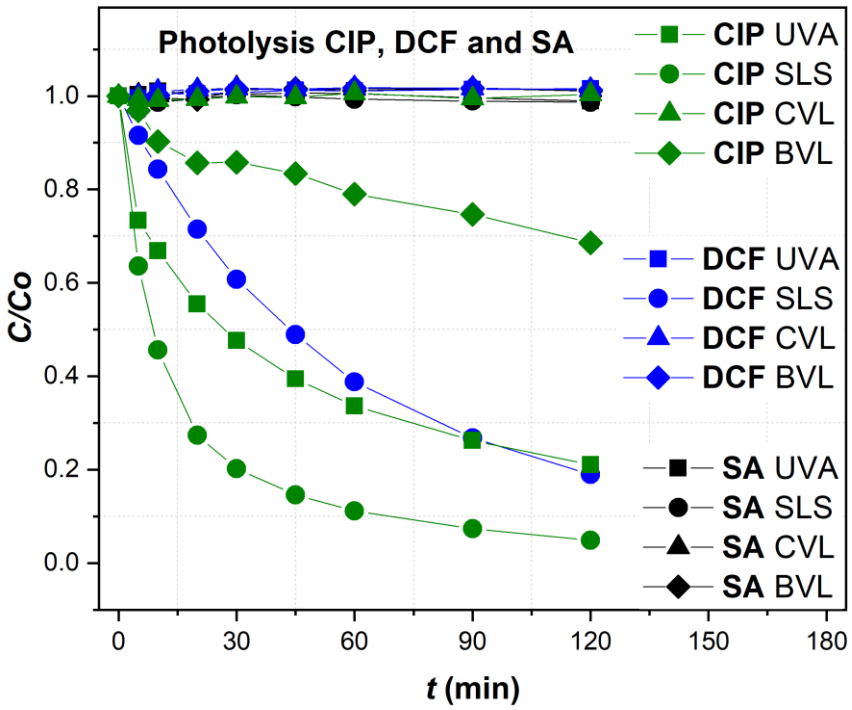

Figure 44. Photolysis of CIP, DCF, and SA under different irradiation sources.

The degradation rates for CIP, DCF, and SA, under different irradiation sources and using the N/TiO_2/rGO 0.25 wt.% as the photocatalyst, were analyzed using the pseudo-first order and second order models to identify which model better describes the degradation process. Table 14 summarizes the kinetic constants, determination coefficients (R^2), and removal efficiencies of each pollutant under different irradiation sources. Additionally, using the same models, the kinetic constants, determination coefficients (R^2), and removal efficiencies of CIP and DCF were determined for the photolysis process, and summarized in Table 15.

As previously observed for CIP degradation with N/TiO_2 and N/TiO_2/rGO materials, also under BVL, the pseudo-first order model displays a determination coefficient(R^2) below 0.90, while the second order model shows a determination coefficient(R^2) above 0.98, indicating that the second order model better describes the degradation process, in which the degradation is affected by several aspects such as pollutant concentration, byproduct formation, light intensity, etc. For DCF and SA pollutants, the determination coefficient(R^2) for both models is above 0.90; however, depending on the pollutant, one model fits better than the other. In the case of DCF, the degradation process fits better to the pseudo-first order model, in which the degradation rate depends mainly on the changes in pollutant concentration. On the contrary, the SA degradation process is better described by the second order model, similar to CIP

degradation. It is noticed that the pollutants that have adsorption onto the photocatalyst follow a second order model, indicating that the adsorption process plays an important role in the degradation process.

Table 14. Pseudo-first order, second order kinetic parameters, and CIP, DCF, and SA removal efficiencies by N/TiO_2/rGO 0.25 wt. % photocatalyst under UVA, solar light simulator (SLS), cold visible light (CVL), and blue visible light (BVL).

Pollutant	**Lamp**	**Removal efficiency**	**Model**			
			Pseudo-first order k_1, min^{-1}		**Second order k_2, $L \cdot mg^{-1} \cdot min^{-1}$**	
		***η*, %**	***k*1**	***R*²**	***k*2**	***R*²**
CIP	UVA	98.81	0.0489	0.8801	0.9388	0.9910
	SLS	99.90	0.0531	0.8645	1.2462	0.9866
	CVL	52.69	0.0035	0.9950	0.0052	0.9991
	BVL	98.51	0.0425	0.8228	0.4585	0.9936
DCF	UVA	98.29	0.0403	0.9632	1.3493	0.9516
	SLS	98.68	0.0430	0.9669	1.7313	0.9349
	CVL	*	*	*	*	*
	BVL	91.08	0.0276	0.9490	0.7612	0.6573
SA	UVA	99.46	0.0344	0.9333	1.1296	0.9725
	SLS	99.28	0.0432	0.9404	2.4893	0.9589
	CVL	34.24	0.0016	0.9700	0.0084	0.9748
	BVL	96.15	0.0304	0.9313	0.7479	0.9839

* No photocatalytic activity.

On the other hand, as was previously observed for CIP, it is also noticed that for DCF and SA removal, the N/TiO_2/rGO 0.25 wt.% photocatalyst presents a better degradation rate under SLS than under UVA irradiation source, despite that SLS has 40 % lower UV-A radiation intensity. These findings suggest a synergistic effect between nitrogen and rGO, wherein rGO serves as an electron sink, preventing recombination phenomena, while nitrogen doping introduces new energetic levels that enhance light absorption into the visible range. Given that UVA light is commonly used to activate TiO_2 photocatalytic processes, it was used as a reference to compare the effectiveness of photocatalytic processes under different lamps. On one side, it is observed that for pollutants removal in which adsorption takes place (CIP and SA), the degradation rate under SLS increases by 1.3 and 2.2 times, for CIP and SA,

respectively. On the contrary, for the DCF removal, in which adsorption does not occur, no difference in the degradation rate is noticed under SLS compared to the process under UVA.

In the case of the photocatalytic process under less energetic irradiation sources such as BVL and CVL, the degradation rates for the three evaluated pharmaceuticals present a reduction compared to the degradation rate under UVA light. For the photocatalytic process using energy from the transition zone between UVA and visible spectra (BVL), the pollutants DCF and SA present a reduction in the degradation rate 1.5 times compared to UVA irradiation. In contrast, the decrease in the degradation rate for CIP is around 2 times lower than under UVA irradiation. In the case of CVL, for the target pollutants removed by type of irradiation source, the degradation rates were significantly reduced when compared to UVA irradiation, around 180 times for CIP and 134 times for SA. This strong reduction in the degradation rates could be due to the low radiation energy of this lamp (450 and 660 nm), indicating that a longer period of irradiation is probably required to achieve complete pollutant removal.

Table 15. Pseudo-first order, second order kinetic parameters, and efficiencies CIP and DCF removal by photolysis under UVA, solar light simulator (SLS), and blue visible light (BVL).

Pollutant	**Lamp**	**Removal efficiency**	**Model**			
			Pseudo-first order k_1, min^{-1}		**Second order k_2, $L \cdot mg^{-1} \cdot min^{-1}$**	
		***η*, %**	***k*$_1$**	***R*^{2}**	***k*$_2$**	***R*^{2}**
CIP	UVA	78.92	0.0154	0.9402	0.0028	0.9953
	SLS	95.10	0.0304	0.9279	0.0140	0.9922
	BVL	31.41	0.0035	0.9167	0.0004	0.9367
DCF	SLS	80.99	0.0146	0.9964	0.0032	0.9784

Although it is observed that the kinetic model that describes the degradation rate depends primarily on the type of pollutant rather than the type of used irradiation source, it is perceived that the changes in the values of the kinetic constants (degradation rates) under different irradiation sources observed in each pollutant somehow could be determined by the energy emitted by the lamp (wavelength) and by the fact that the adsorption process takes place. For the more energetic wavelengths such as UVA and SLS irradiation, N/TiO_2/rGO 0.25 wt.% photocatalyst probably generates a higher amount of ROS by absorbing photons from the UVA spectrum and from the spectrum nearby to the UVA region. Additionally, if the adsorption process occurs, it is highly probable that pollutant removal proceeds by a combination of

degradation by ROS and surface charges (h^+/e^-). On the contrary, for the less energetic irradiation sources such as BVL and CVL, the adsorption process could define the degradation rate; even under CVL, adsorption appears necessary for the photocatalytic process to occur (CIP and SA). Under BVL and CVL, it could be probable that the ROS are not as energetic as ROS produced by UVA irradiation, and therefore, the pollutant removal is achieved by a redox process on the surface (h^+/e^-) rather than ROS.

4.3.4. Photocatalytic mechanisms of N/TiO_2/rGO nanocomposite

After evaluating N/TiO_2/rGO 0.25 wt.% photocatalyst for the degradation of the three different OMPs (CIP, DCF, and SA) under different irradiation sources (UVA, SLS, BVL, and CVL) and observing that kinetic model relies more on the type of pollutant rather than irradiation source, the following step on this research was to determine the degradation mechanisms that are involved in the degradation of the three pollutants and also study if there is any effect of the type of irradiation over degradation mechanism. Therefore, to identify the mechanism that takes place in the photocatalytic removal of CIP, DCF, and SA and, understand ROS and/or surface charges (h^+/e^-) role, each pollutant was subject to a photocatalytic test similar to the one performed previously but adding scavenger species. Methanol, *p*-benzoquinone, and formic acid were used as hydroxyl radical ($^{\bullet}OH$), superoxide radical ($O_2^{\bullet -}$), and hole (h^+) scavenger/interfering agents, respectively. The molar ratio pollutant:scavenger was 1:100, except for *p*-benzoquinone, which was 1:10 due to its limitations on the analytical determination.

Photocatalytic tests for CIP removal by N/TiO_2/rGO with 0.25 wt. % of rGO material in the presence of several scavenger agents under different irradiation sources is shown in Figure 45. First of all, it is noticed that in the experiments in which formic acid is added, there is a substantial reduction of CIP adsorption onto the photocatalyst surface, indicating probably that formic acid has stronger adsorption on the photocatalyst than CIP. Regarding photocatalytic CIP degradation, it is observed that the addition of formic acid has a considerable impact on the degradation rate compared to the addition of the other two scavenger agents, indicating that CIP oxidation is done mainly by the superficial holes (h^+); this similar behavior is observed under the four irradiation sources, indicating that the degradation mechanism also depends more in the type of pollutant rather than the irradiation source. Except for the photocatalytic test under the SLS, the addition of formic acid hinders the complete removal of CIP. On the other hand, the addition of p-benzoquinone and methanol slightly impacts the CIP

degradation rate; nevertheless, with a less energetic irradiation source, such as CVL, the role of these two scavenger agents takes more relevance.

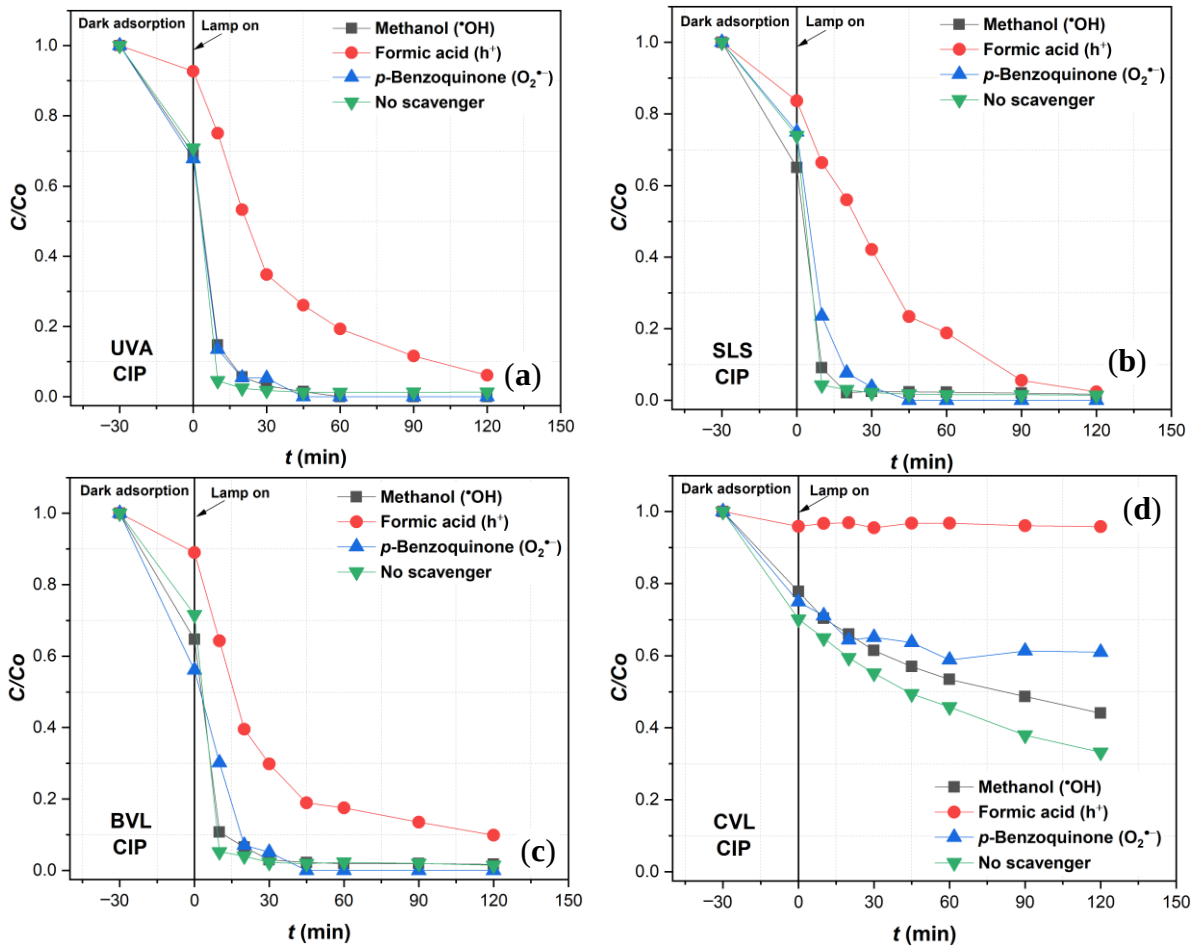

Figure 45. Photocatalytic degradation of ciprofloxacin (CIP) by N/TiO_2/rGO with 0.25 wt. % of rGO material in the presence of different scavenger agents under (a) UVA light, (b) solar light simulator (SLS), (c) blue visible light (BVL), and (d) cold visible light (CVL).

Figure 46 presents the results from the photocatalytic tests for DCF removal by N/TiO_2/rGO with 0.25 wt. % of rGO material in the presence of scavenger agents under different irradiation sources. For DFC, the photocatalytic tests with scavengers were not carried out under CVL because of the absence of photoactivity under this irradiation source. It is noticed that with the addition of any of the scavenger agents, the lack of adsorption of this pollutant onto the photocatalyst remains. Also, as was observed for CIP removal, the degradation rate for DFC removal is significantly reduced in the presence of formic acid, indicating that DCF degradation is performed mainly by the superficial holes (h^+). The addition of this scavenger hindered the complete removal of DCF under the three irradiation sources evaluated (UVA, SLS, and BVL).

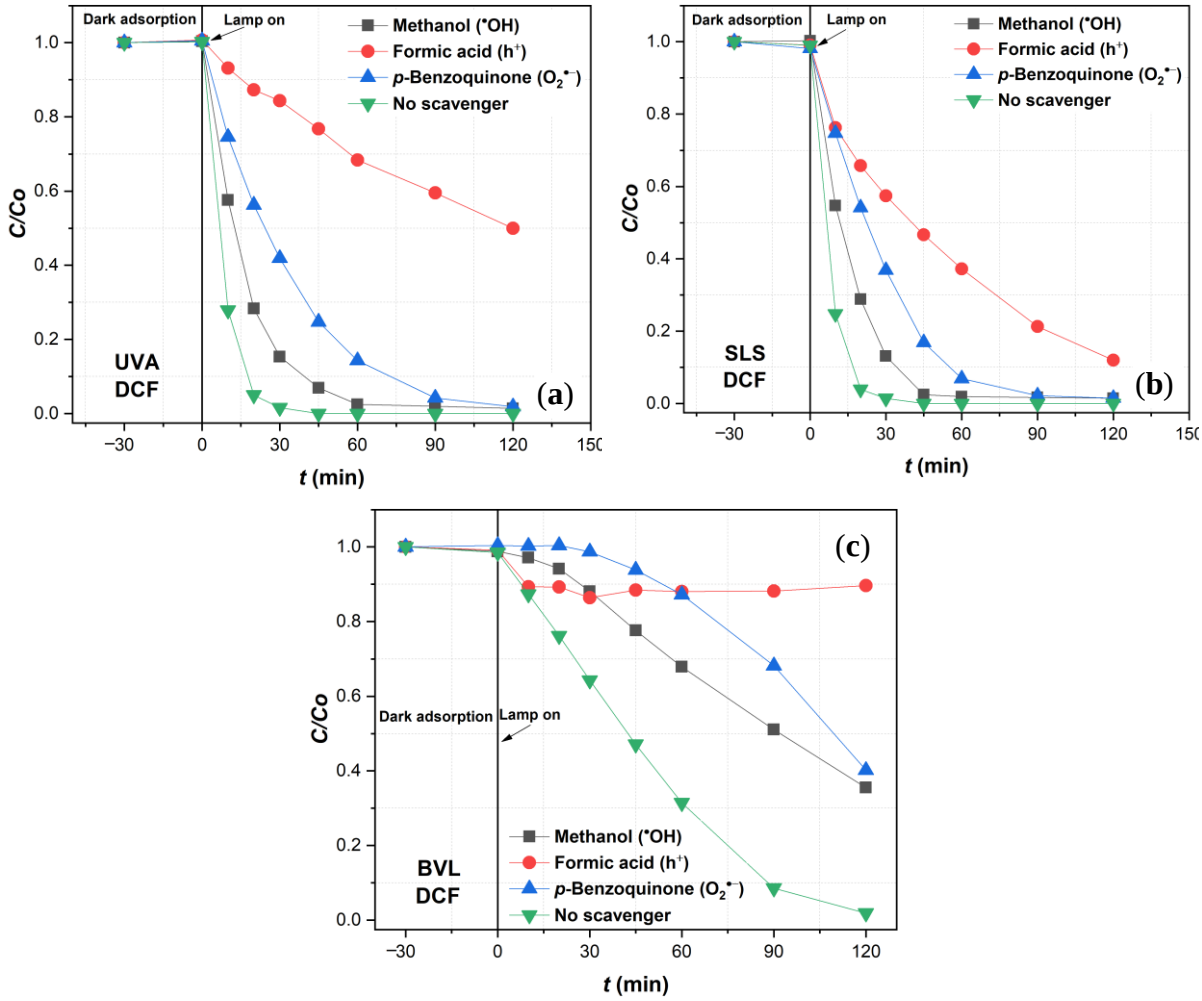

Figure 46. Photocatalytic degradation of diclofenac (DCF) by N/TiO_2/rGO with 0.25 wt. % of rGO material in the presence of different scavenger agents under (a) UVA light, (b) solar light simulator (SLS), and (c) blue visible light (BVL). Tests with scavengers were not carried out under CVL because of the absence of photoactivity under this irradiation source.

Contrary to what was observed with CIP, the addition of p-benzoquinone also reduces the DCF degradation rate; meanwhile, the addition of methanol also contributes to the reduction of the DCF degradation rate but to a lesser extent, which indicates that the superoxide radical ($O_2^{\bullet-}$) and hydroxyl radical ($^{\bullet}OH$) also play an important role in the degradation mechanism. Despite the addition of p-benzoquinone and methanol, the DCF removal under the UVA and SLS is completely achieved, while under BVL, the presence of any scavenging agent hinders the DCF removal, indicating that under this irradiation source, all ROS play an important role in pollutant removal. On the other hand, for DCF removal, a similar behavior is observed under the three irradiation sources, confirming that the degradation mechanism relies more on the type of pollutant than the irradiation source.

For the SA removal by N/TiO_2/rGO with 0.25 wt. % of rGO material in the presence of scavenger agents under different irradiation sources, the photocatalytic test results are displayed in Figure 47. Similar to DFC, the photocatalytic tests with scavengers were not carried out under CVL for SA due to the minimal photoactivity observed under this irradiation source. Although the addition of formic acid for SA removal also diminishes the degradation rate as observed for CIP and DCF, especially under UVA and SLS irradiation sources, the superficial holes (h^+) are not the main species involved in the SA removal. The superoxide radical ($O_2^{\bullet-}$) is the ROS responsible for the SA oxidation. Under the three irradiation sources evaluated (UVA, SLS, and BVL), the addition of methanol does not have any impact on the SA degradation rate, suggesting that the hydroxyl radical ($^{\bullet}OH$) does not play any role in the removal of this pollutant. On the other hand, although the superficial holes (h^+) play an important role under UVA and SLS irradiation sources for SA removal, under the BVL, the effect of the superficial holes (h^+) is neglectable, being the pollutant removed solely by the superoxide radical ($O_2^{\bullet-}$). This behavior differs from the previously observed for CIP and DCF removal under a less energetic irradiation source, in which the secondary oxidizing species took more relevance under this kind of irradiation source.

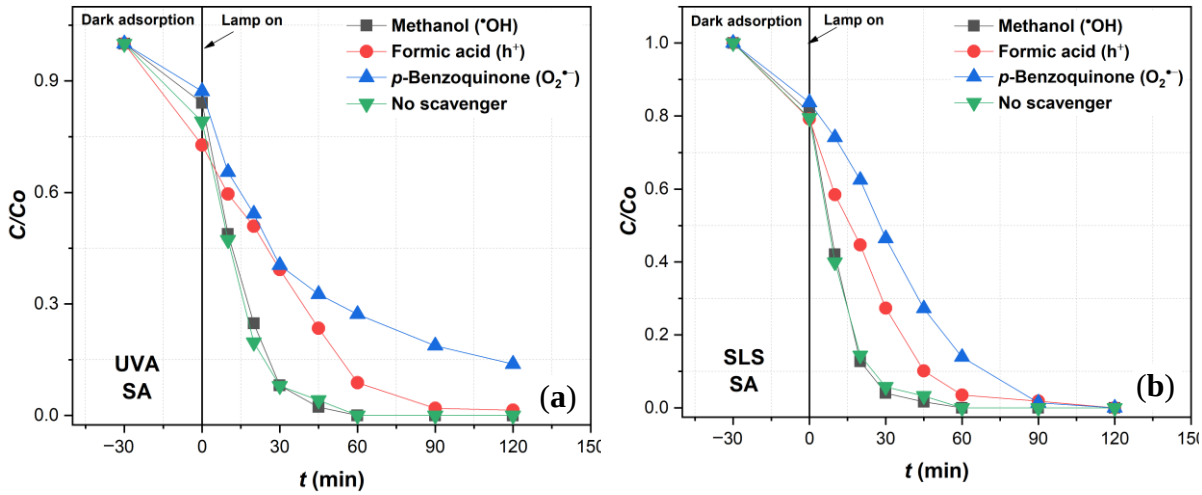

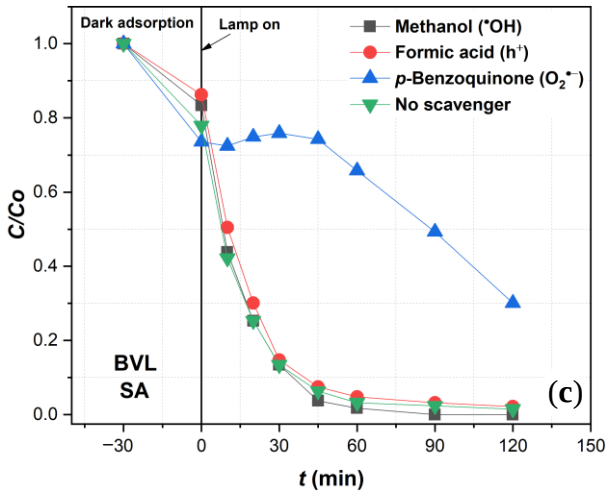

Figure 47. Photocatalytic salicylic acid (SA) degradation by N/TiO_2/rGO with 0.25 wt. % of rGO material in the presence of different scavenger agents under (a) UVA light, (b) solar light simulator (SLS), and (c) blue visible light (BVL). Tests with scavengers were not carried out under CVL for SA due to the minimal photoactivity observed under this irradiation source.

4.4.Irradiation intensity effect

After performing experiments for pollutant removal under different irradiation sources and using scavenger agents, the results suggested that the photocatalytic mechanism and kinetic model rely mainly on the type of pollutant rather than the irradiation source. However, it was also observed that the degradation rate is directly affected by the type of irradiation source, having, in all the cases, the highest degradation rates under the SLS and UVA irradiation sources. Additionally, it is important to remark that the light intensity used on the previous photocatalytic tests for SLS and UVA were quite high compared to natural conditions and were kept like that to be able to compare the different photocatalyst developed during this research (lamps located 20 cm away for the photocatalytic reactor). Once it was determined that N/TiO_2/rGO 0.25 wt.% photocatalyst is the most photoactive material, and after evaluating this material for pollutant removal (CIP, DCF, and SA) under different irradiations (UVA, SLS, BVL, and CVL), the next step on this research is to identify the feasibility of pollutant removal using natural solar irradiation. Based on a Global Solar Atlas, it was estimated for the City of Zagreb (Croatia) the average irradiation during the spring-summer-autumn season, which is calculated based on the direct normal irradiation (global irradiation), taking the average hourly profiles between February and October [171]. The average UVA irradiation was estimated to be 16.5 $W \cdot m^{-2}$, while the global irradiation was 290 $W \cdot m^{-2}$.

Having these values as a reference point for comparison, the distance between the photocatalytic reactor and the different lamps used in this research was adjusted to achieve the

average UVA or global irradiation. Based on the irradiation chart measured for each lamp at different height from the sensors (pyranometer in the range 285-2800 nm and UV-A sensor in the range 315 – 400 nm) (Appendix, Figure S2), the UVA lamp was relocated at 50 cm away from the reactor to achieve UVA natural irradiation, while the SLS lamp was relocated at 60 cm away from the reactor to achieve UVA and global irradiation.

On the contrary, the BVL and CVL lamps were relocated closer (15 cm from the reactor in spite of 20 cm) to achieve global irradiation. The average UVA and global irradiation value of each lamp at two different distances from the reactor and the ratio between UVA and global irradiation are presented in Table 16.

Table 16. UV and global irradiation values of each lamp at two distances to the reactor.

Lamp_distance	**Same distance to the reactor**		
	UV-A irradiation, $W \cdot m^{-2}$	**Total irradiation, $W \cdot m^{-2}$**	**UV-A/T ratio, %**
UVA_20 cm	98.5	118.6	83.05
SLS_20 cm	59.2	1266.6	4.67
CVL_20 cm	0	241.1	0
BVL_20 cm	3.6	176.6	2.04
Lamp_distance	**Same global irradiation**		
	UV-A irradiation, $W \cdot m^{-2}$	**Total irradiation, $W \cdot m^{-2}$**	**UV-A/T ratio, %**
UVA_50 cm	18.1	20.4	88.73
SLS_60 cm	15.2	291.7	5.21
CVL_15 cm	0	288.9	0
BVL_15 cm	5.8	289.1	2.01

Due to CIP being the most susceptible target pollutant to degradation by photolysis from the three OMPs evaluated and its significant photodegradation under CVL, this pharmaceutical was selected to evaluate the feasibility of pollutant removal by photocatalysis and photolysis using irradiation intensities similar to the natural solar irradiation. The results of photocatalytic degradation of CIP by N/TiO_2/rGO 0.25 wt.% under the four different irradiation sources at the two different irradiation intensities are shown in Figure 48. From the results, it is noticed that there were no significant differences in the degradation rate for each lamp when the height of the lamp was modified. However, there are some facts that are important to remark. On one

side, under UVA and SLS irradiation sources, although there is a significant reduction in energy emitted by the lamps, up to 80 %, the degradation rate only slightly decreases, achieving the complete removal of the pollutant within the first hour. On the other hand, under BVL, despite the increase in energy emitted by the lamp, up to 60%, there is a slight increase in the degradation rate, achieving complete CIP removal within the first 30 minutes. This improvement in the degradation rate could be attributed to the increase in UVA irradiation emitted by this lamp, which rises by 60 %. Finally, under CVL, there is no change in the degradation rate despite an increase in the energy emitted by the lamp, which goes up to 20%, probably because this lamp does not emit UVA irradiation.

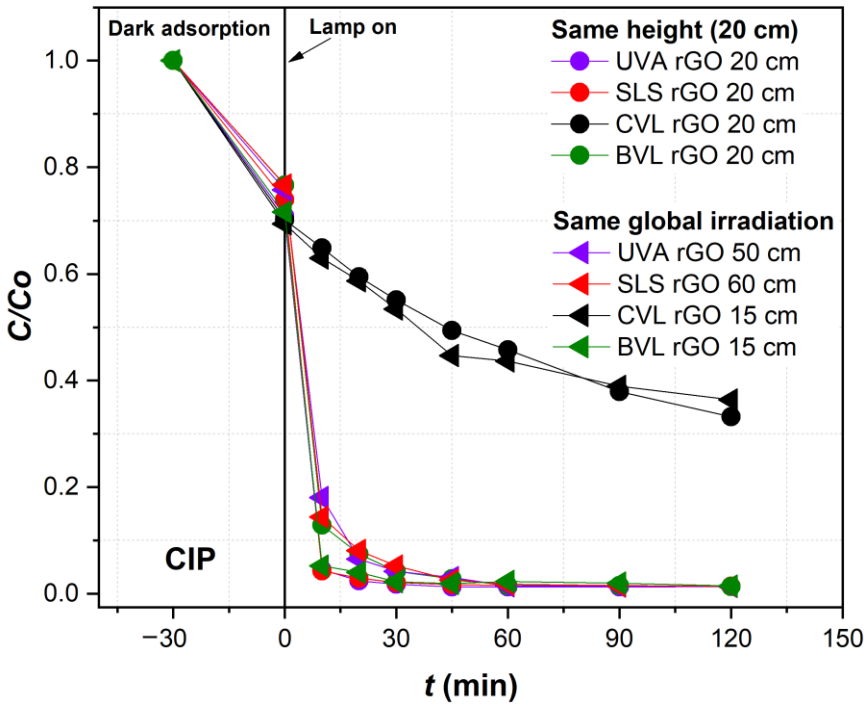

Figure 48. CIP removal by photocatalyst N/TiO_2/rGO with 0.25 wt. % of rGO with lamps located at two different distances from the reactor.

The results of CIP degradation by photolysis under the four different irradiation sources at the two different irradiation intensities are shown in Figure 49. On the contrary to the observed for the photocatalytic process, the changes in the irradiation intensities significantly impact the degradation rate in the photolysis process. In the case of the UVA lamp, in which the irradiation intensity is reduced from 98.5 $W \cdot m^{-2}$ to 18.1 $W \cdot m^{-2}$, the degradation rate is strongly reduced, changing the removal efficiency from 80% to just 30 %. From the experiment

under the SLS lamp, a significant reduction of the degradation rate is noticed when the global irradiation intensity is reduced from 1266.6 $W \cdot m^{-2}$ to 291.7 $W \cdot m^{-2}$. Although the irradiation intensity is reduced by around 77%, the removal efficiency is reduced by only 30%, shifting the removal efficiency from 95% to 65%, probably because part of the energy emitted by some wavelengths near the UVA could photolyze the pollutant. On the other hand, although the global irradiation intensity increased from 176.6 $W \cdot m^{-2}$ to 289.1 $W \cdot m^{-2}$ and the UVA irradiation intensity increased by around 60%, the removal efficiency barely changed from 75% to 70%. In the case of CVL, it is observed that there is no evidence of photolytic activity despite the increment of the global irradiation intensity from 241.1 $W \cdot m^{-2}$ to 288.9 $W \cdot m^{-2}$. Comparing the results from both processes, photocatalytic and photolytic, it can be seen that photocatalysis is barely affected by the changes in the irradiation intensities, and therefore, application of this process under natural solar irradiation is highly feasible.

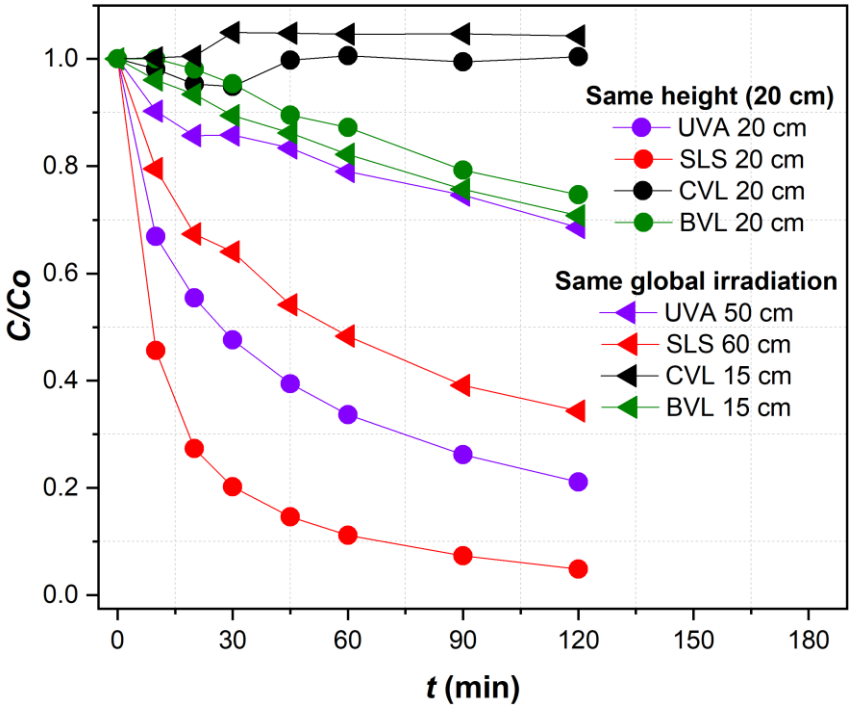

Figure 49. CIP removal by photolysis with lamps located at two different distances from the reactor.

4.5. Immobilization of N/TiO_2/rGO on Al_2O_3 foam

After selecting the N/TiO_2/rGO photocatalyst with 0.25 wt. % of rGO as the most photoactive material for removal of OMPs under different irradiation sources, and confirming

the feasibility of photocatalysis under natural solar irradiation, the next step in this research involves immobilization of the photocatalyst over a ceramic substrate like the alumina ceramic foam due to excellent chemical inertness, high UV light resistance, mechanical stability, and a large specific surface area of the substrate.

4.5.1. Characterization

One layer of N/TiO_2/rGO with 0.25 wt. % of rGO photocatalyst was immobilized over alumina ceramic foam combining the dip-coating method and mild thermal treatment, using SiO_2 as a binder for enhancing the stability and reusability. Figure 50 shows the visual appearance of Al_2O_3 foam substrate before coating (Figure 50a) and N/TiO_2/rGO-coated Al_2O_3 foam (N/TiO_2/rGO@ Al_2O_3) (Figure 50b). The coated ceramic foam got a grey color due to the 0.25 wt. % of rGO content in N/TiO_2/rGO photocatalyst. This visual inspection at first glance gives an idea of a successful coating of the photocatalyst over the ceramic foam.

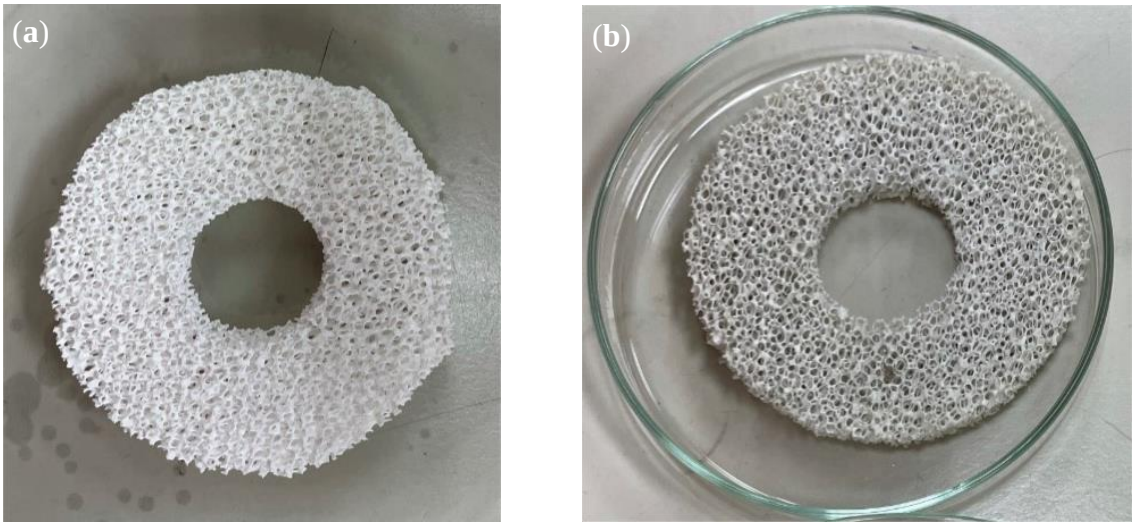

Figure 50. Al_2O_3 foam substrate and (b) N/TiO_2/rGO@Al_2O_3 foam.

The SEM images of the Al_2O_3 foam substrate before coating and the N/TiO_2/rGO-coated Al_2O_3 foam (N/TiO_2/rGO@Al_2O_3) are presented in Figure 51. Figures 51a and 51c show the surface of the Al_2O_3 ceramic foam surface at two different magnifications, where a smooth and homogeneous surface is clearly observed. Meanwhile, the N/TiO_2/rGO@Al_2O_3 ceramic foam displays a rough surface but with homogeneous photocatalyst distribution, as seen in Figures 51b and 51d. In the coated surface, some holes in the ceramic surface can be noticed (Figure 51b), which are defects of the Al_2O_3 itself, formed during the sintering process.

Although the photocatalyst has a homogeneous distribution, some large particles can be perceived as agglomerates that were not completely disaggregated during the sonication step before coating. Figure 51e shows an overview of the Al_2O_3@N/TiO_2/rGO ceramic foam, where a well-formed open structure with well-defined and interconnected walls can be seen. The photocatalyst immobilization in this kind of open structure could allow better irradiation of the inner immobilized photocatalyst.

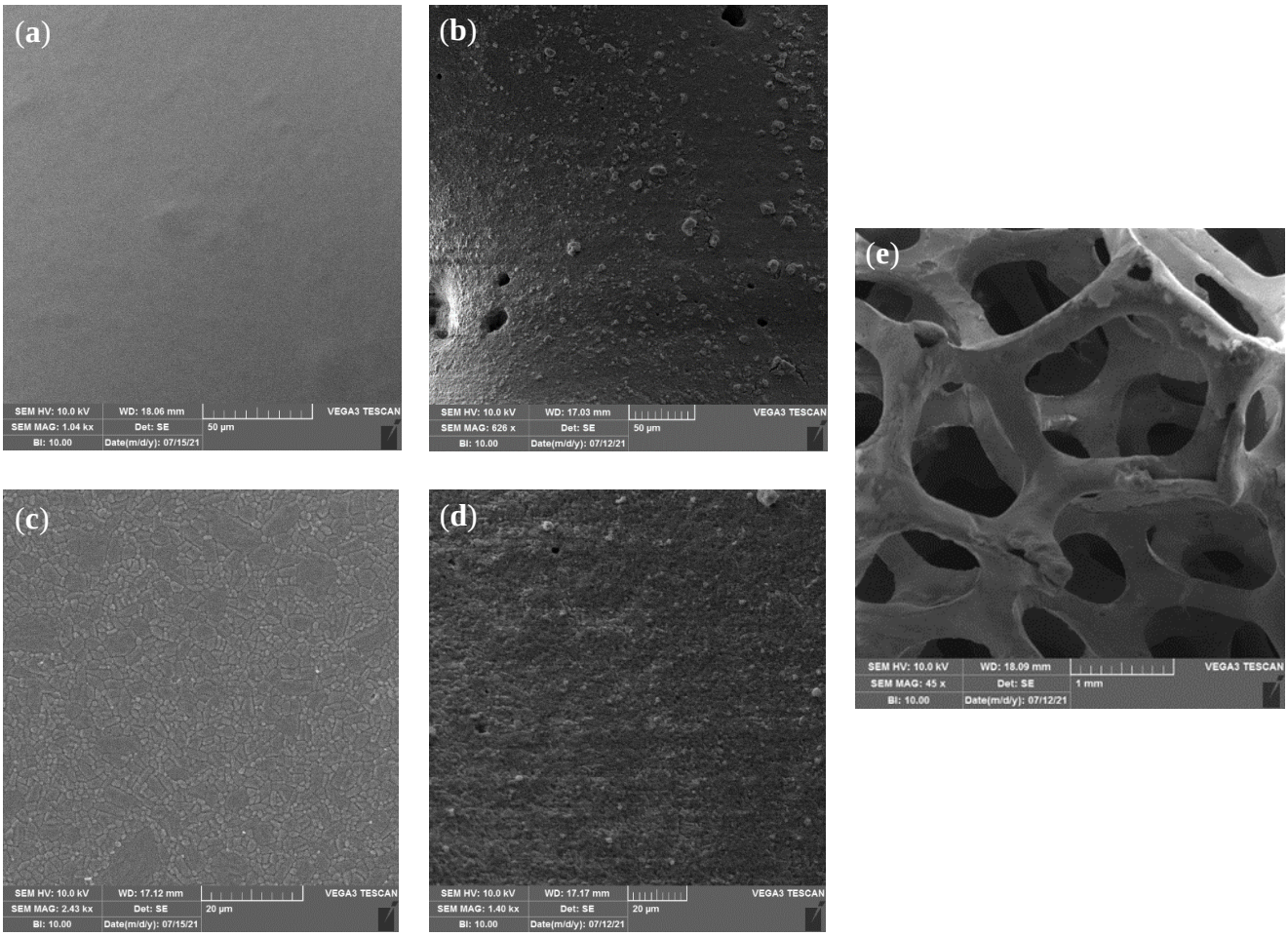

Figure 51. (a) and (c) SEM images of Al_2O_3 foam substrate; (b), (d) and (e) SEM images of N/TiO_2/rGO@Al_2O_3 foam.

4.5.2. Adsorption and photocatalytic test

Before the photocatalytic tests, an adsorption test for the N/TiO_2/rGO@Al_2O_3 and Al_2O_3 foam substrate was performed for two hours to determine the adsorption-desorption equilibrium for each pollutant, as shown in Figure 52. It is observed that CIP is the only pollutant that has some adsorption on the Al_2O_3 foam substrate (around 15 %), reaching the adsorption-desorption equilibrium within the first 20 minutes. On the other hand, CIP and SA have strong adsorption

over $N/TiO_2/rGO@Al_2O_3$ foam, also achieving the adsorption-desorption equilibrium during the first 20 minutes. On the contrary, DCF presents neglectable adsorption over the $N/TiO_2/rGO@Al_2O_3$ foam. These adsorption results are similar to those previously observed for the photocatalyst in suspension. However, the higher adsorption of target pollutants is probably due to the larger amount of the photocatalyst immobilized over the ceramic foam. Based on the ceramic ring weight before and after coating, it is estimated that approximately 150 mg of photocatalyst has been immobilized.

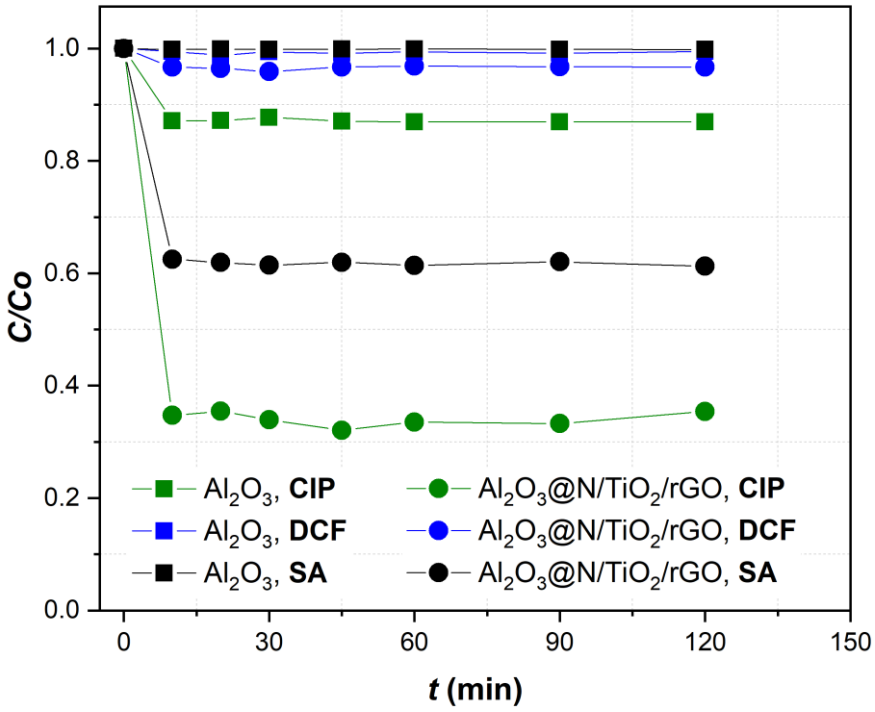

Figure 52. Adsorption-desorption equilibrium of CIP, DCF and SA over Al_2O_3 foam substrate and $N/TiO_2/rGO@Al_2O_3$ foam.

Photocatalytic tests for the CIP degradation by $N/TiO_2/rGO@Al_2O_3$ under UVA light, solar light simulator, cold visible light, and blue visible light are shown in Figure 53. Additionally, five consecutive photocatalytic degradation cycles for CIP, DCF and SA by $N/TiO_2/rGO@Al_2O_3$ under UVA light and its comparative degradation by Al_2O_3 foam substrate and by $N/TiO_2/rGO$ 0.25 wt. % in suspension under the same radiation source (UVA) are presented in Figures 54, 55, and 56, respectively. Meanwhile, the photocatalytic stability and reusability were assessed over 19 consecutive cycles, as summarized in Figure 57. It is important to remark that after every photocatalytic experiment, $N/TiO_2/rGO@Al_2O_3$ was washed thoroughly with deionized water, followed by UVA irradiation for 20 minutes to

remove the adsorbed remaining pollutant, ensuring the same conditions at the beginning of each experiment, and thus, the reproducibility between photocatalytic tests.

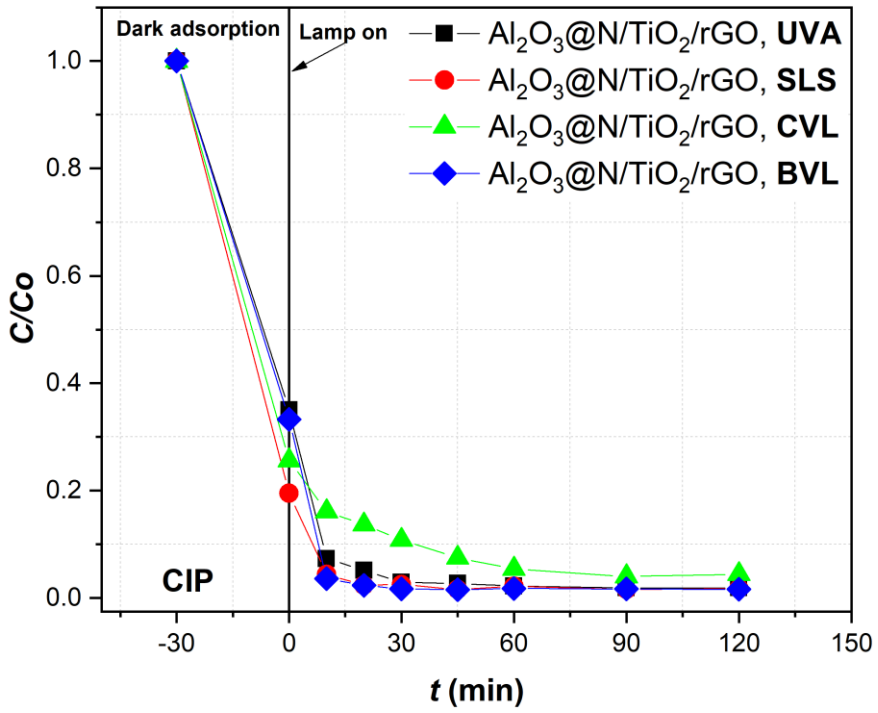

Figure 53. Photocatalytic degradation of ciprofloxacin (CIP) by N/TiO_2/rGO@Al_2O_3 foam under UVA, solar light simulator (SLS), cold visible light (CVL), and blue visible light (BVL).

In the case of degradation of CIP by N/TiO_2/rGO@Al_2O_3 under different radiation sources (Figure 53), it can be noticed that the adsorption process plays the main role in pollutant removal, where around 65% of pollutant is being removed by this mechanism, while the remaining 35% is degraded by photocatalysis. Under UVA, SLS, and BVL, no significant differences regarding pollutant removal are observed, achieving CIP removal efficiencies by around 98%. On the other hand, although under CVL, the removal efficiency is slightly lower compared to the other irradiation sources, it is noticed that the immobilized photocatalyst removes more than 95% of CIP by a synergistic effect of adsorption and photocatalysis, showing an improvement in comparison with the material in suspension that only achieved 50% of removal (Figure 41). Consecutive photocatalytic tests of N/TiO_2/rGO@Al_2O_3 ceramic foam for CIP, DCF, and SA removal under UVA light were performed to observe its stability and reusability. For CIP removal (Figure 54), it is observed also a synergistic effect of adsorption and photocatalytic mechanisms achieving more than 98% removal efficiency in the five consecutive cycles performed. Although the degradation rate of N/TiO_2/rGO@Al_2O_3 is lower

compared to N/TiO_2/rGO with 0.25 wt. % of rGO in suspension, after 30 minutes of UVA irradiation, the same removal efficiency was achieved.

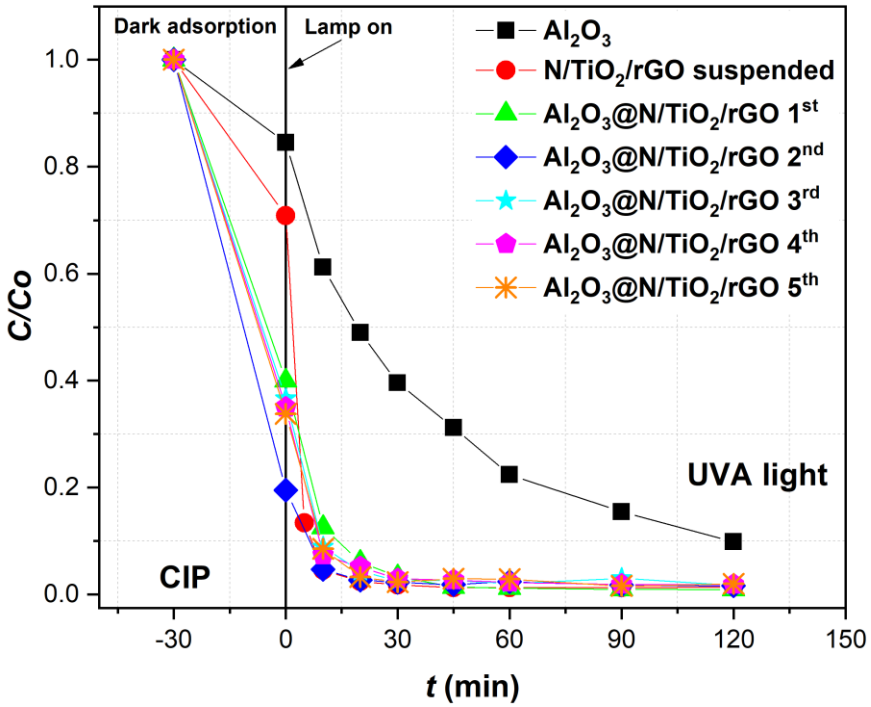

Figure 54. Photocatalytic degradation of ciprofloxacin (CIP) by Al_2O_3 ceramic foam substrate, N/TiO_2/rGO, and N/TiO_2/rGO@Al_2O_3 foam under UVA light.

In the case of DCF removal (Figure 55), the adsorption process has a neglectable impact, as was observed in previous photocatalytic experiments (Figure 42). Moreover, as expected, the degradation rate for N/TiO_2/rGO@Al_2O_3 is lower compared to N/TiO_2/rGO with 0.25 wt. % of rGO in suspension because of the mass transfer limitation. However, just 45 minutes of irradiation is needed to achieve more than 90% pollutant removal, and after 60 minutes of irradiation, no significant changes in the degradation are observed. Additionally, it is observed that between each photocatalytic test, the results are very similar, which suggests that the experiments are reproducible and, most importantly, the N/TiO_2/rGO@Al_2O_3 is stable after every photocatalytic test and does not lose photoactivity.

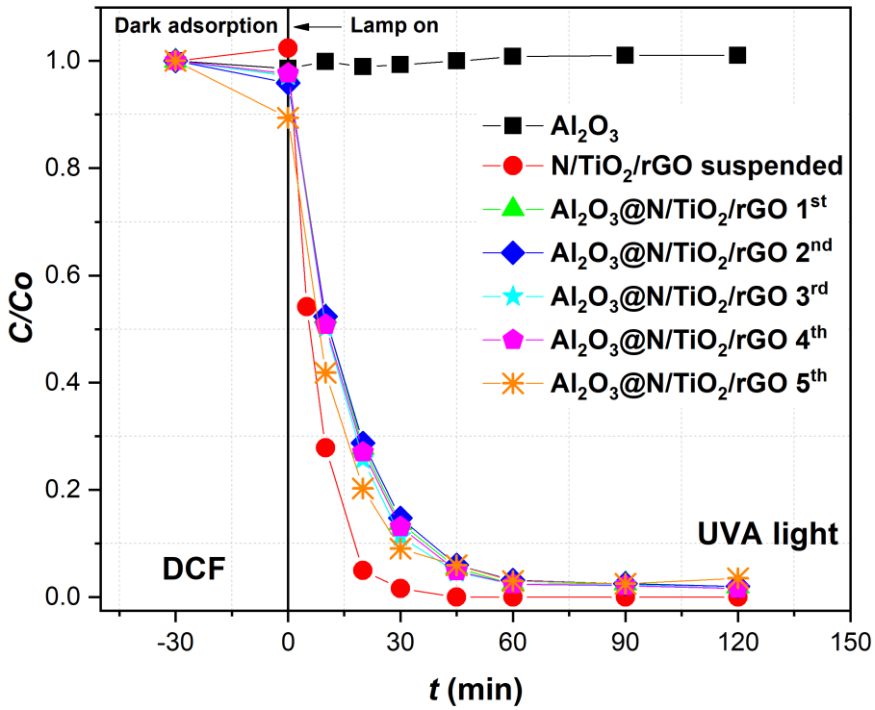

Figure 55. Photocatalytic degradation of diclofenac (DCF) by Al_2O_3 ceramic foam substrate, N/TiO_2/rGO, and N/TiO_2/rGO@Al_2O_3 foam under UVA light.

For SA removal (Figure 56), a synergistic effect of adsorption and photocatalysis is also involved in the pollutant removal mechanism. However, while adsorption plays a secondary role in pollutant removal, photocatalysis remains the primary mechanism responsible for the degradation of SA, requiring only 30 minutes of irradiation to achieve 90% degradation. On the other hand, although CIP degradation was observed in the presence of Al_2O_3 foam substrate under UVA irradiation, this is attributed to the CIP photolytic degradation, as was previously observed (Figure 44). The lack of Al_2O_3 foam photocatalytic activity is confirmed by the absence of DCF (Figure 55) and SA (Figure 56) degradations under the same irradiation.

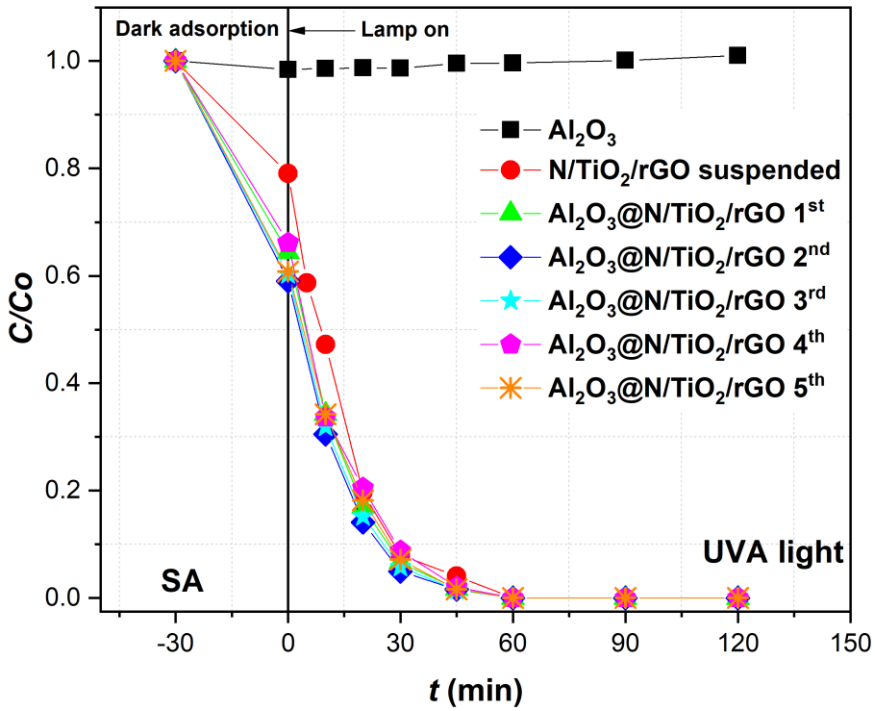

Figure 56. Photocatalytic degradation of salicylic acid (SA) by Al_2O_3 ceramic foam substrate, $N/TiO_2/rGO$, and $N/TiO_2/rGO@Al_2O_3$ foam under UVA light.

Figure 57 was built by combining the results of adsorption-desorption equilibrium and the results from the photocatalytic tests to determine the contribution effect of each mechanism, as well as to show the stability and reusability of the $N/TiO_2/rGO@Al_2O_3$ ceramic foam after several consecutive cycles. Based on these results, it is noticed that photocatalysis does not lose photoactivity during the 19 consecutive photocatalytic cycles, achieving more than 95 % of pollutant removal in all experiments performed. These results could prove that $N/TiO_2/rGO$ with 0.25 wt. % of rGO itself is stable, and the use of SiO_2 as a binder provides good adhesion of the photocatalyst over the ceramic substrate, improving the reusability of the $N/TiO_2/rGO@Al_2O_3$ ceramic foam. Although some authors suggest that SiO_2 could improve the photocatalytic activity [172, 173], in this case, SiO_2 in the $N/TiO_2/rGO@Al_2O_3$ ceramic foam could help in the adsorption process rather than in the photoactivity due to the lack of calcination during the coating process. The presence of SiO_2 could also be the reason for the higher adsorption of CIP and SA. However, the differences in the adsorption onto the material could be more related to the polarity of each molecule, being adsorbed polar substances such as CIP and SA, while non-polar structures such as DCF are not adsorbed.

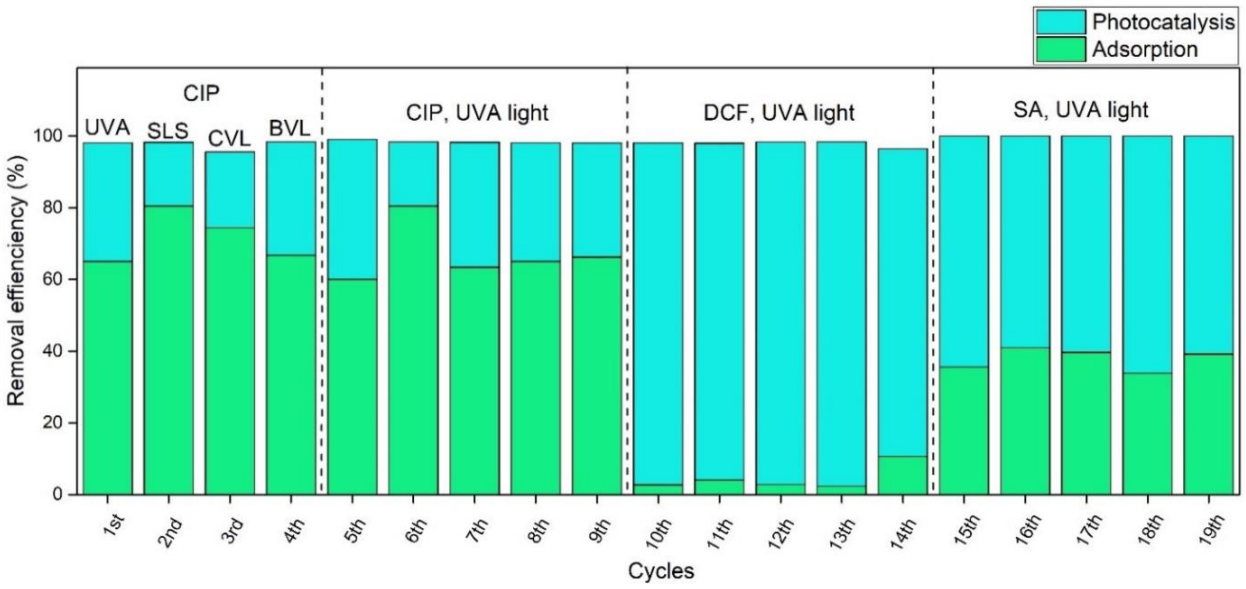

Figure 57. Reusability and stability tests for 19 consecutive cycles. Photocatalytic degradation of ciprofloxacin (CIP) by N/TiO_2/rGO@Al_2O_3 foam under UVA light, Solar light simulator (SLS), cold visible light (CVL) and blue visible light (BVL). Photocatalytic degradation of ciprofloxacin (CIP), diclofenac (DCF), and salicylic acid (SA) by N/TiO_2/rGO@Al_2O_3 foam under UVA light.

4.6.Transformation products and degradation pathways of CIP and DCF

CIP and DCF degradations by N/TiO_2/rGO@Al_2O_3 ceramic foam under different irradiation sources were studied using LC-HRMS. Due to the lack of analytical standards for the newly identified products, TPs were identified through several databases and spectral libraries that are linked to the Compound Discoverer software (Thermo Fisher Scientific). The results obtained by the Orbitrap Exploris 120 HRMS, displayed in Tables 17 and 18, were screened and matched by applying a mass error less than 5 ppm. Therefore, all the TPs identified for both parent compounds are tentative structures. Besides the identification of TPs, qualitative profiles of each TPs are displayed in Figures 58 and 60, showing how those compounds appear and disappear during the photocatalytic oxidation process. Due to lack of analytical standards, these profiles are qualitative and are obtained by normalizing the chromatographic peak area of each product to the initial chromatographic peak area (at time 0) of the parent compounds (CIP or DCF).

Table 17. CIP byproducts transformation based on the database and spectral libraries.

Compound	Formula	Calc. MW	*m/z*	ΔMass [ppm]	RT [min]
CIP	C17H18FN3O3	331.1328	332.1401	-1.1297	1.6519
TPC1	C17H19N3O4	329.1371	330.1444	-1.2726	1.4997
TPC2	C17H19N3O5	345.1321	346.1394	-1.1051	1.5943
TPC3	C17H16FN3O5	361.1070	362.1143	-1.2189	1.9474
TPC4	C14H11FN2O4	290.0699	291.0772	-1.2122	2.1572
TPC5	C17H18FN3O4	347.1278	348.1351	-0.9302	1.9929
TPC6	C17H20FN3O5	365.1382	366.1455	-1.2409	1.5775
TPC7	C17H16FN3O3	329.1172	330.1245	-1.1872	1.5823
TPC8	C17H18FN3O4	347.1276	348.1348	-1.6559	1.6721
TPC9	C17H18FN3O5	363.1226	364.1299	-1.1577	1.8076
TPC10	C17H16FN3O4	345.1122	346.1195	-0.8712	1.4476
TPC11	C17H16FN3O5	361.1072	362.1144	-0.6446	1.3139
TPC12	C17H14FN3O4	343.0965	344.1037	-1.0556	1.8219

In total, 12 probable TPs derived from the CIP photocatalytic degradation process were identified through several databases and spectral libraries linked to the Compound Discoverer software (Thermo Fisher Scientific), displayed in Table 17. On the other hand, after analyzing the qualitative profiles of each TP, presented in Figure 58, it is noticed that most of the identified TPs are formed during the photocatalytic test under cold visible light (450 nm and 600 nm, 100 W). However, two main TPs commonly appear in the photocatalytic degradation test under all irradiation sources, TPC3 and TPC4. These two TPs are formed by the attack of CIP's piperazine ring. TPC3 (*m/z* 362) is a dialdehyde derivative that rapidly appears after the oxidation and further cleavage of the piperazine ring, and its subsequent loss of two CO molecules and additional oxidation gives TCP4 (*m/z* 291) [63, 174]. Under UVA, SLS, and BVL, TPC3 (*m/z* 362) starts to appear during the first minutes of the photocatalytic process, and simultaneously, TPC4 (*m/z* 291) also begins to form, achieving their maximum concentration during the first 20-30 minutes of irradiation, followed by a decay in the TPs concentration until they disappear completely after one hour under UVA and SLS irradiation, while for BVL irradiation takes at least hour and half. In the case of the photocatalytic test under CVL, these two TPs are also formed during the first 30 minutes of photocatalytic degradation; however, after two hours of irradiation, these two molecules remain in the solution, even without reaching the maximum concentration as observed under the other irradiation sources.

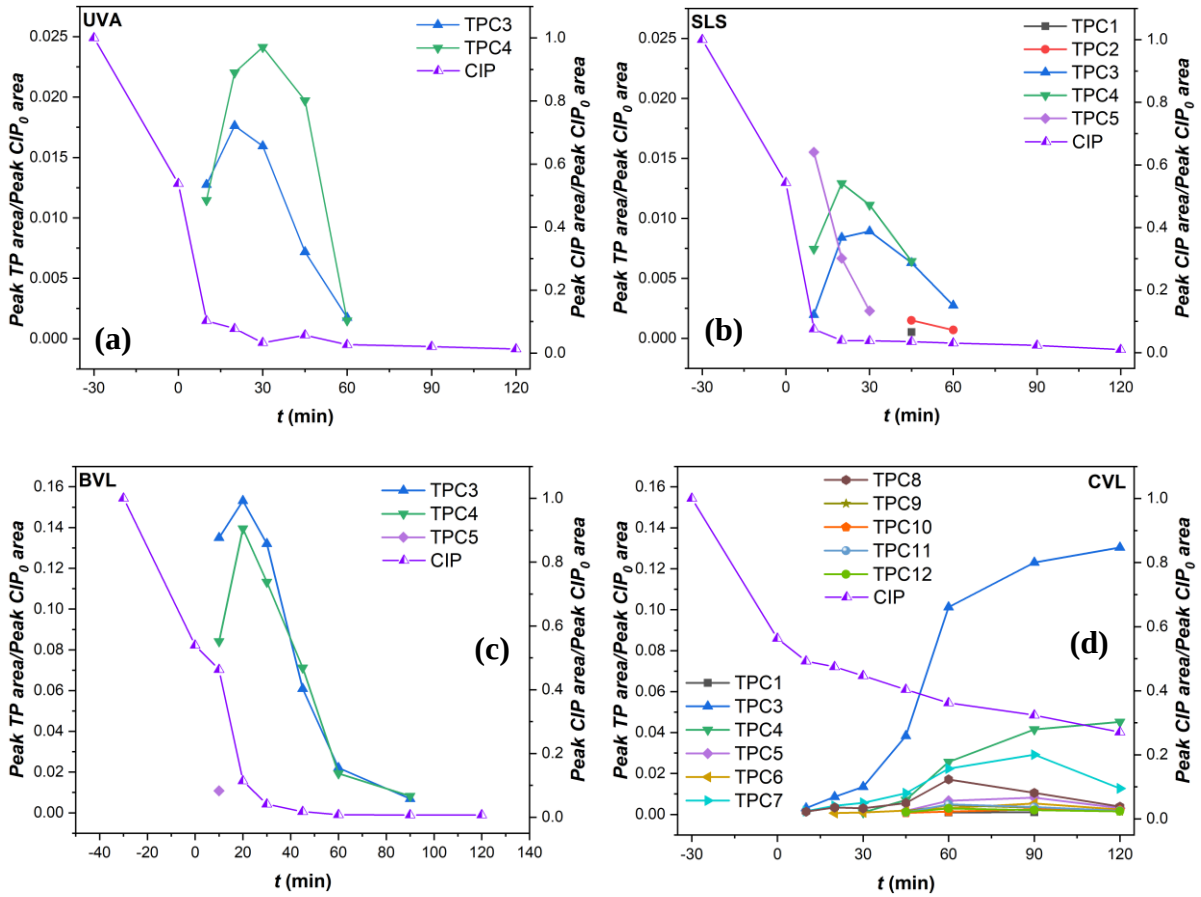

Figure 58. TPs profile generated during the photocatalytic degradation of ciprofloxacin (CIP) by N/TiO_2/rGO@Al_2O_3 foam under UVA light (a), solar light simulator (SLS)(b), blue visible light (BVL)(c) and cold visible light (CVL) (d).

Under SLS, in addition to TPC3 and TPC4, some other TPs were shortly detected, like TPC1, TPC2 and TPC5. TPC1 (*m/z* 330) briefly appears after 30 minutes of solar irradiation, where the fluoride atom is substituted by hydroxyl, and then TPC2 (*m/z* 346) is formed after further addition of hydroxyl group in the quinolone ring structure [175]. In the case of CIP photocatalytic degradation under CVL, 12 probable TPs were detected, and after 120 minutes of irradiation, all molecules remained in the solution. The probable degradation pathways are proposed in Figure 59, while the formation of these byproducts probably occurred as follows. During the formation of TPC5 (*m/z* 348) by the hydroxylation of the quinolone ring [175], the piperazine ring is also oxidized (TPC7, *m/z* 330) and hydroxylated in the amine group (TPC8, *m/z* 348) at the same time [176]. After some minutes, TPC5 (*m/z* 348) is further oxidized, cleaving the quinolone ring to produce TPC6 (*m/z* 366) [177]. After 45 minutes of irradiation, additional four byproducts are detected, with TPC7 (*m/z* 330) further oxidized to produce TPC9 (*m/z* 364), followed by the formation of a ketone derivative (TPC10, *m/z* 346), as suggested by Salma et al. [176]. Additionally, Hu et al. [175] proposed that TPC10 (*m/z* 346) could be further

hydroxylated in the piperazine ring without cleaving it, producing TPC11 (*m/z* 362). On the other hand, TPC12 (*m/z* 344) was previously reported as a CIP transformation byproduct under visible light irradiation but using graphitized carbon nitride nanosheets as a photocatalyst [178].

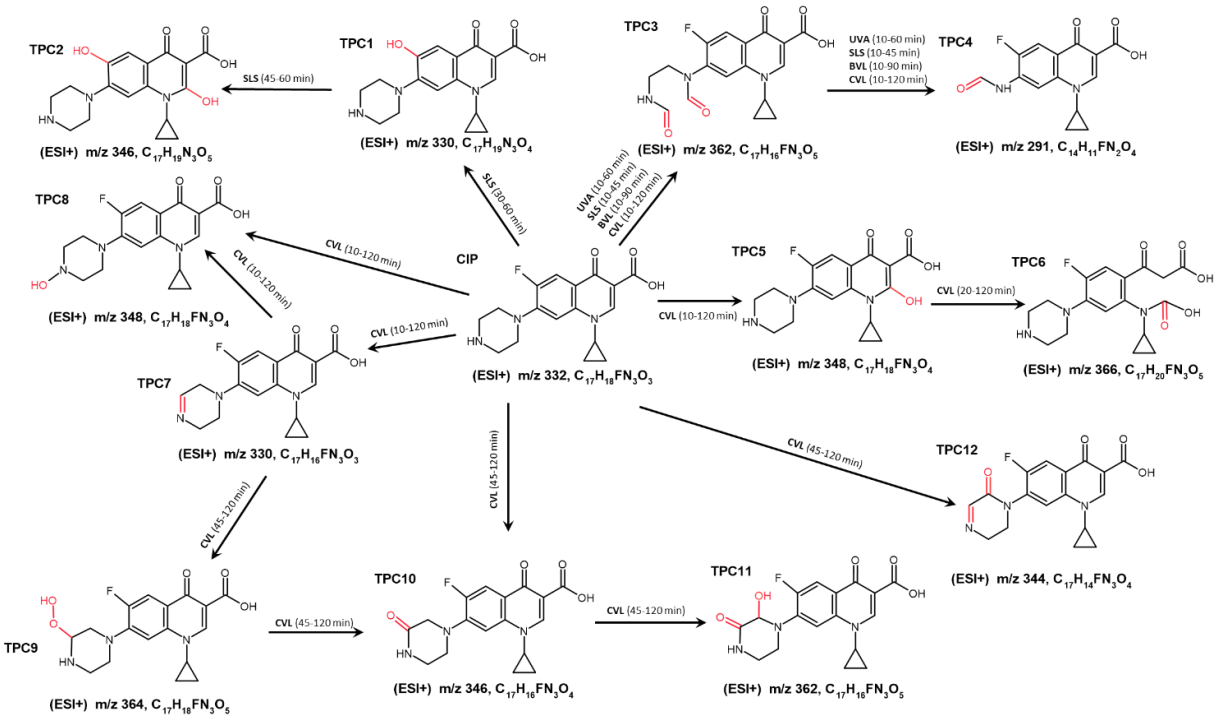

Figure 59. Ciprofloxacin pathways degradation by N/TiO_2/rGO@Al_2O_3 foam under UVA light (UVA), solar light simulator (SLS), blue visible light (BVL), and cold visible light (CVL).

In the case of DCF, 10 different TPs are identified through several databases and spectral libraries linked to the Compound Discoverer software (Thermo Fisher Scientific), displayed in Table 18. The qualitative profiles of each TP, presented in Figure 60, show that all TPs are detected under all irradiation sources but appear at different times depending on the irradiation source. After 120 minutes of irradiation, the parent compound and most of the byproducts were decomposed under UVA and SLS. Under the less energetic irradiation source (BVL), all TPs remain in the solution after 120 minutes of the photocatalytic process. No dechlorination stage occurs in any probable degradation pathways proposed in Figure 61. DCF degradation under CVL was not studied using LC-HRMS due to the lack of pollutant removal under this irradiation (previously observed in Figure 42).

Table 18. DCF byproducts transformation based on the database and spectral libraries.

Compound	Formula	Calc. MW	*m/z*, (ESI)	ΔMass [ppm]	RT [min]
DCF	C14H11Cl2NO2	295.0165	294.0092 (-)	-0.5965	3.6503
TPD1	C14H11Cl2NO3	311.0116	310.0043 (-)	-0.0356	3.1203
TPD2	C14H11Cl2NO3	311.0114	310.0041 (-)	-0.6118	3.2658
TPD3	C14H9Cl2NO3	308.9956	310.0028 (+)	-1.2531	3.5483
TPD4	C14H9Cl2NO4	324.9908	323.9835 (-)	-0.1516	2.7562
TPD5	C14H9Cl2NO3	308.9956	310.0029 (+)	-1.0024	3.7607
TPD6	C14H11Cl2NO4	327.0064	325.9991 (-)	-0.3199	4.2854
TPD7	C14H9Cl2NO3	308.9956	310.0029 (+)	-1.1049	4.8279
TPD8	C14H9Cl2NO	277.0057	278.0130 (+)	-1.3983	3.7522
TPD9	C6H5Cl2N	160.9798	159.9726 (-)	-0.3865	2.1663
TPD10	C6H5Cl2NO	176.9748	175.9675 (-)	-0.1593	2.8009

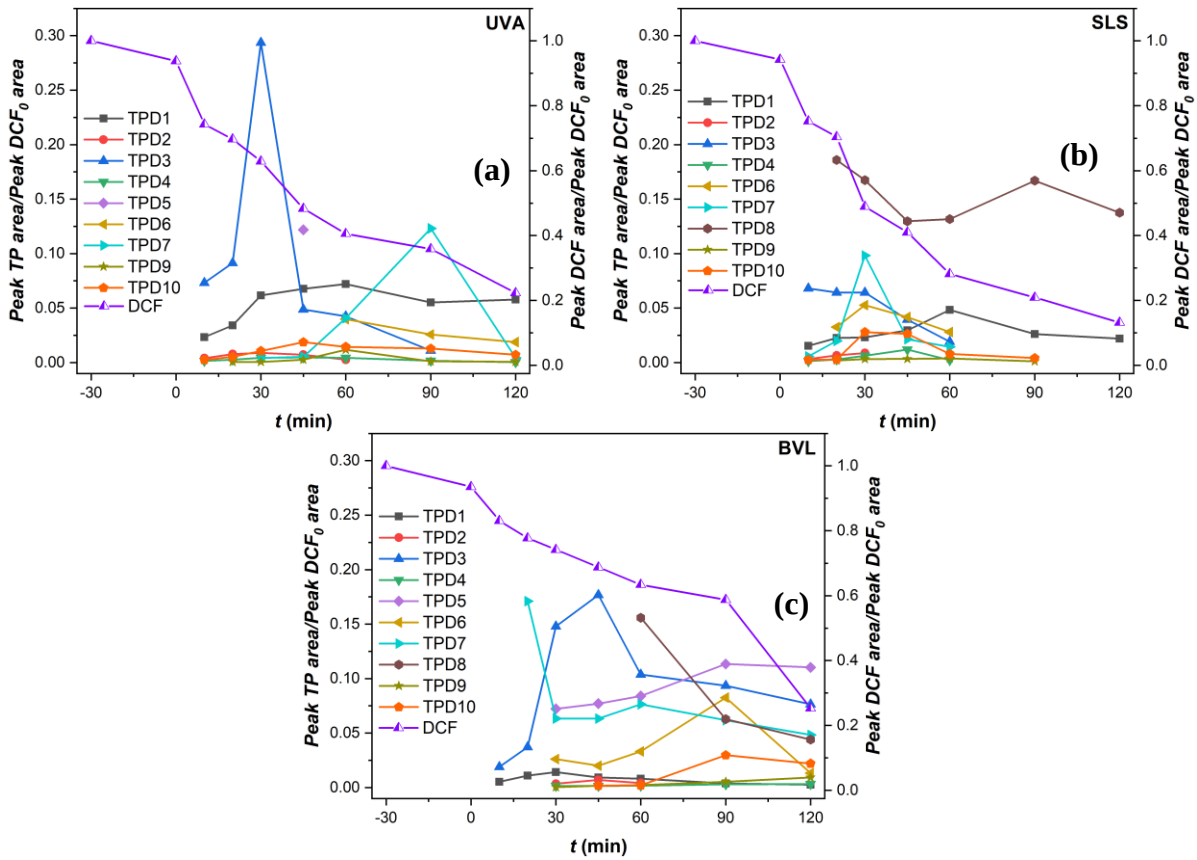

Figure 60. TPs profile generated during the photocatalytic degradation of diclofenac (DCF) by N/TiO_2/rGO@Al_2O_3 foam under (a) UVA light, (b) solar light simulator (SLS), and (c) blue visible light (BVL).

During the first minutes of photocatalytic degradation of DCF, several byproducts are formed. On one hand, a mono-hydroxylation of DCF occurs on both aromatic rings at the same time, being formed TPD1 (*m/z* 310) and TPD2 (*m/z* 310) [66], followed by further oxidation that gives the formation of the respective quinone imine structures (TPD3, *m/z* 310 and TPD5, *m/z* 310) [67, 179]. Apart from the quinone imines formation, the di-hydroxylation could take place to give the formation of TPD6 (*m/z* 324), as suggested by Michael et al. [65]. From the qualitative profiles, it can be observed that TPD1 rapidly forming, and its concentration remains stable over time, while TPD2 is shortly appearing, indicating that hydroxylation occurs mainly in the ring where the carboxylic acid is located (TPD1). On the other hand, during the first hour of the photocatalytic test, TPD1 is further oxidized to form TPD3, which appears rapidly within 45 minutes, and then drops quickly. TPD3 is completely removed under UVA and SLS but remains under BVL. Also, it is found that TPD3 (*m/z* 310) could be further hydroxylated in the chlorinated ring, forming TPD4 (*m/z* 324), as was reported by Murgolo et al. [180].

Although TPD4 (*m/z* 324) is formed under the three evaluated irradiation sources, it is noticed that under BVL takes a longer time to appear, and it is completely removed only by SLS irradiation. On the other hand, TPD7 (*m/z* 310), an epoxide-based compound, is detected. Although this compound is a precursor of dimer formation [181, 182], those large molecules were not found during the photocatalytic process. Additionally, the cleavage C-N bond of DCF could occur, forming TPD8 (*m/z* 160), as is detected under SLS and BVL irradiation sources; this compound is one of the few molecules that remain in the solution under SLS. TPD8 is further oxidized by hydroxylation to produce TPD9 (*m/z* 176) [67, 94]. Like TPD8, TPD10 (*m/z* 278) is a byproduct formed only under SLS and BVL, taking a longer time to appear under BVL. TPD10 (*m/z* 278) is an indole derivative that is yielded by a cyclization process [94, 183].

In general, it is observed that DCF has several TPs, and their appearance and disappearance depend on the irradiation source, being the SLS irradiation the most effective irradiation source for the removal of DCF and most of its TPs.

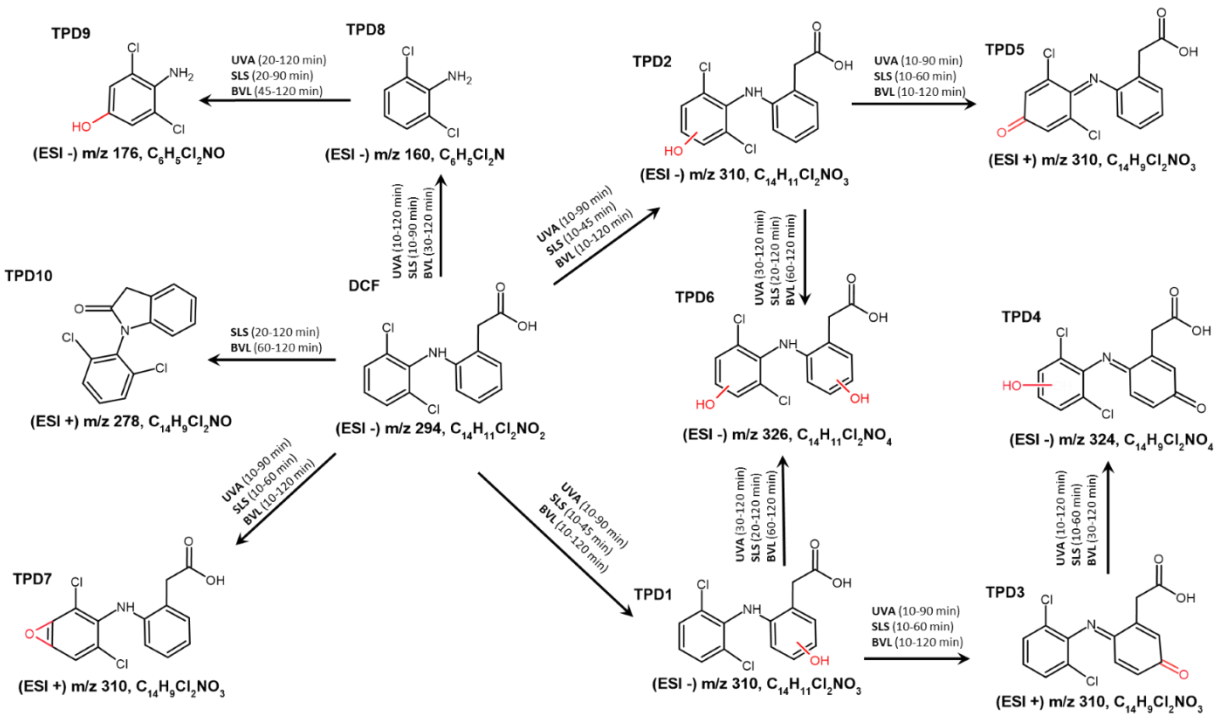

Figure 61. Diclofenac pathways degradation by N/TiO_2/rGO@Al_2O_3 foam under UVA light (UVA), solar light simulator (SLS), and blue visible light (BVL). (ESI+) Positive ionization mode, (ESI-) negative ionization mode.

5. CONCLUSIONS

From obtained results of microwave-assisted synthesis for determination of critical parameters of MW oven for N/TiO_2, it was demonstrated that it is possible to synthesize TiO_2 nanoparticles in a short period and at a low temperature as 150°C, giving as a result crystalline material without the need for further thermal treatment process. The microwave-assisted method demonstrated that it could be an alternative and environmentally friendly synthesis technique due to reduced energy consumption during material processing compared to the conventional wet-synthesis techniques such as sol-gel and hydrothermal methods. It was found that the temperature is the most relevant parameter that defines the morphological properties of TiO_2 which ultimately define the photocatalytic activity. Higher temperature promotes crystal growth and gives a material with higher crystallinity, while the reaction time hardly affects these morphological parameters. Also, it was identified that regardless of the temperature or reaction time, the microwave-assisted method produced materials with high purity, and all materials synthesized always obtained anatase crystalline, the most photoactive polyform of titania. Regarding the photocatalytic performance, it was noticed that materials with a higher crystallinity, obtained by higher MW temperature, presented a higher photocatalytic activity in the removal of CIP under different irradiation sources. Based on the morphological, photocatalytic activity, and energy saving, the optimal conditions for the synthesis of TiO_2-based materials were 200°C and 10 minutes.

Regarding the nitrogen content in TiO_2, it was noticed that changes in the N/Ti molar ratio barely influenced the morphological and optical properties. Although the material porosity was somehow affected by the increment in the N/Ti molar ratio, it was compensated by the large surface area and pore volume in the obtained materials compared to the commercial TiO_2 Degussa P25. On the contrary, the variation in the nitrogen content had a relevant impact on the photocatalytic performance, especially under visible irradiation sources. This positive effect, principally under visible irradiation, was attributed to the new energetic levels rather than the reduction of the energy bandgap, which contributed to the photon adsorption in the visible spectrum. Additionally, it was noticed that with a higher N/Ti molar ratio, the photocatalytic activity on the CIP removal under different irradiation sources was improved. However, after some nitrogen concentration, it could have an unfavorable effect on the degradation rate because nitrogen could act as a recombination center that favors the charges recombination. Based on the photocatalytic activity, this research found that the optimal N/Ti

molar ratio for the synthesis of N/TiO_2 materials was 12. In future research, based on this N/Ti molar ratio, evaluating different nitrogen precursors to compare their effects on the morphological, optical, and photocatalytic properties is recommended.

From obtained results of rGO amount in N/TiO_2/rGO microwave-assisted synthesis, it was found that the material porosity is improved by adding rGO compared to the N/TiO_2 material. Although the optical property of the material is modified by the addition of rGO, where the energy bandgap is reduced, the increment in the amount of rGO did not have a positive impact on the photocatalytic performance, especially under visible irradiation sources due to an excess of rGO with a shielding effect for light absorption and that could act as a recombination center that hinders the photoactivity of TiO_2. The photocatalytic performance revealed that a lower rGO content achieves better photoactivity. Additionally, it was determined that the main contribution of rGO on the photocatalyst was to reduce the recombination effect, showing that a combination of nitrogen doping and rGO incorporation could be a good strategy to overcome the limitation of TiO_2 photocatalysis. The optimal loading of rGO for N/TiO_2/rGO composite was 0.25 wt.%. In future research, it is recommended to evaluate the reduction degree of GO or to use commercial rGO, as well as evaluate different dispersion mechanisms for better incorporation of rGO to exploit the full potential of this carbon source (high electrical and thermal conductivity).

Regarding pollutant removal (CIP, DCF, and SA) under different irradiation sources, it was realized that the kinetic model and degradation mechanism rely mainly on the type of pollutant rather than the irradiation source. Also, it was found that the adsorption process plays an important role during the photocatalytic process, especially when the main irradiation source is the visible light. On the other hand, although the irradiation source, i.e., irradiation intensity, does not determine the degradation mechanism, it significantly impacts the degradation rate for pollutant removal.

Regarding photocatalyst immobilization, it was demonstrated that the use of Al_2O_3 ceramic foam combined with the use of a binder agent provided adhesion of the photocatalyst on surface of alumina foam (stability) and reusability of the N/TiO_2/rGO nanocomposite under several uses without losing photoactivity. The open-cell ceramic foam proved to be an alternative for photocatalyst immobilization due to the reduction of the mass transfer limitation while giving a good area for irradiation. The ceramic foam support combined with the visible irradiation and adsorbed in the N/TiO_2/rGO composites could have the potential for pollutant

removal under solar natural irradiation, especially in decentralized wastewater treatment plants. Finally, but no less important, the TPs detection and possible pathways identified suggested that some byproducts formed could be potentially more toxic than the parent compounds. Additionally, under real situations, the byproducts could react with each other, producing other compounds that make detecting them more difficult. Therefore, apart from the byproduct's detection, the use of toxicity tests could be more effective in evaluating tertiary treatments (advanced oxidation processes) and that is a suggestion for further investigations in this area.

6. REFERENCES

1. Mekonnen, M.M.; Hoekstra, A.Y. Sustainability: Four Billion People Facing Severe Water Scarcity. *Sci Adv* **2016**, *2*, 1–7, doi:10.1126/sciadv.1500323.
2. Programme Division *United Nations Children's Fund, Reimagining WASH: Water Security for All*; New York, 2021;
3. Zhang, H.; Sun, H.; Liu, Y. Water Reclamation and Reuse. *Water Environment Research* **2020**, *92*, 1701–1710, doi:10.1002/wer.1425.
4. FAO *The State of Food and Agriculture: Overcoming Water Challenges in Agriculture*; 2020; ISBN 9789251334416.
5. Sivaranjanee, R.; Kumar, P.S. A Review on Remedial Measures for Effective Separation of Emerging Contaminants from Wastewater. *Environ Technol Innov* **2021**, *23*, 101741, doi:10.1016/j.eti.2021.101741.
6. Wang, J.; Wang, S. Removal of Pharmaceuticals and Personal Care Products (PPCPs) from Wastewater: A Review. *J Environ Manage* **2016**, *182*, 620–640, doi:10.1016/j.jenvman.2016.07.049.
7. Wilkinson, J.L.; Boxall, A.B.A.; Kolpin, D.W.; Leung, K.M.Y.; Lai, R.W.S.; Wong, D.; Ntchantcho, R.; Pizarro, J.; Mart, J.; Echeverr, S.; et al. Pharmaceutical Pollution of the World ' s Rivers. **2022**, *119*, 1–10, doi:10.1073/pnas.2113947119/-/DCSupplemental.Published.
8. Wilkinson, J.; Hooda, P.S.; Barker, J.; Barton, S.; Swinden, J. Occurrence, Fate and Transformation of Emerging Contaminants in Water: An Overarching Review of the Field. *Environmental Pollution* **2017**, *231*, 954–970, doi:10.1016/j.envpol.2017.08.032.
9. Rout, P.R.; Zhang, T.C.; Bhunia, P.; Surampalli, R.Y. Treatment Technologies for Emerging Contaminants in Wastewater Treatment Plants: A Review. *Science of the Total Environment* **2021**, *753*, 141990, doi:10.1016/j.scitotenv.2020.141990.
10. Mezzelani, M.; Gorbi, S.; Regoli, F. Pharmaceuticals in the Aquatic Environments: Evidence of Emerged Threat and Future Challenges for Marine Organisms. *Mar Environ Res* **2018**, *140*, 41–60, doi:10.1016/j.marenvres.2018.05.001.
11. Dhangar, K.; Kumar, M. Tricks and Tracks in Removal of Emerging Contaminants from the Wastewater through Hybrid Treatment Systems: A Review. *Science of the Total Environment* **2020**, *738*, 140320, doi:10.1016/j.scitotenv.2020.140320.
12. Rizzo, L.; Malato, S.; Antakyali, D.; Beretsou, V.G.; Đolić, M.B.; Gernjak, W.; Heath, E.; Ivancev-Tumbas, I.; Karaolia, P.; Lado Ribeiro, A.R.; et al. Consolidated vs New Advanced Treatment Methods for the Removal of Contaminants of Emerging Concern from Urban Wastewater. *Science of the Total Environment* **2019**, *655*, 986–1008, doi:10.1016/j.scitotenv.2018.11.265.

13. Liang, S.; Maceiko, S.M.; Takeguchi, W.A.; Yates, R.S. Bench-Scale Ozonation for Removing Constituents of Emerging Concern. *J Am Water Works Assoc* **2014**, *106*, 89–90, doi:10.5942/jawwa.2014.106.0063.

14. Lofrano, G.; Faiella, M.; Carotenuto, M.; Murgolo, S.; Mascolo, G.; Pucci, L.; Rizzo, L. Thirty Contaminants of Emerging Concern Identified in Secondary Treated Hospital Wastewater and Their Removal by Solar Fenton (like) and Sulphate Radicals-Based Advanced Oxidation Processes. *J Environ Chem Eng* **2021**, *9*, 106614, doi:10.1016/j.jece.2021.106614.

15. Arfanis, M.K.; Adamou, P.; Moustakas, N.G.; Triantis, T.M.; Kontos, A.G.; Falaras, P. Photocatalytic Degradation of Salicylic Acid and Caffeine Emerging Contaminants Using Titania Nanotubes. *Chemical Engineering Journal* **2017**, *310*, 525–536, doi:10.1016/j.cej.2016.06.098.

16. McMichael, S.; Fernández-Ibáñez, P.; Byrne, J.A. A Review of Photoelectrocatalytic Reactors for Water and Wastewater Treatment. *Water (Switzerland)* **2021**, *13*, doi:10.3390/w13091198.

17. Serna-Galvis, E.A.; Lee, J.; Hernández, F.; Botero-Coy, A.M.; Torres-Palma, R.A. Sonochemical Advanced Oxidation Processes for the Removal of Pharmaceuticals in Wastewater Effluents. In *Handbook of Environmental Chemistry*; Springer Science and Business Media Deutschland GmbH, 2021; Vol. 108, pp. 349–381.

18. Ma, D.; Yi, H.; Lai, C.; Liu, X.; Huo, X.; An, Z.; Li, L.; Fu, Y.; Li, B.; Zhang, M.; et al. Critical Review of Advanced Oxidation Processes in Organic Wastewater Treatment. *Chemosphere* **2021**, *275*, 130104, doi:10.1016/j.chemosphere.2021.130104.

19. Gomes, J.; Lincho, J.; Domingues, E.; Quinta-Ferreira, R.; Martins, R. N–TiO_2 Photocatalysts: A Review of Their Characteristics and Capacity for Emerging Contaminants Removal. *Water (Basel)* **2019**, *11*, 373, doi:10.3390/w11020373.

20. Shayegan, Z.; Lee, C.S.; Haghighat, F. TiO_2 Photocatalyst for Removal of Volatile Organic Compounds in Gas Phase – A Review. *Chemical Engineering Journal* **2018**, *334*, 2408–2439, doi:10.1016/j.cej.2017.09.153.

21. Li, W.; Yang, X.; Fu, H.; An, X.; Zhao, H. Synthesis of TiO_2-Reduced Graphene Oxide Nanocomposites Offering Highly Enhanced Photocatalytic Activity. *J Nanosci Nanotechnol* **2019**, *19*, 7089–7096, doi:10.1166/jnn.2019.16624.

22. Gillespie, P.N.O.; Martsinovich, N. Origin of Charge Trapping in TiO_2/Reduced Graphene Oxide Photocatalytic Composites: Insights from Theory. *ACS Appl Mater Interfaces* **2019**, *11*, 31909–31922, doi:10.1021/acsami.9b09235.

23. Nasirian, M.; Mehrvar, M. Photocatalytic Degradation of Aqueous Methyl Orange Using Nitrogen-Doped TiO_2 Photocatalyst Prepared by Novel Method of Ultraviolet-Assisted Thermal Synthesis. *Desalination Water Treat* **2019**, *137*, 371–380, doi:10.5004/dwt.2019.23192.

24. Fagan, R.; McCormack, D.E.; Dionysiou, D.D.; Pillai, S.C. A Review of Solar and Visible Light Active TiO_2 Photocatalysis for Treating Bacteria, Cyanotoxins and

Contaminants of Emerging Concern. *Mater Sci Semicond Process* **2016**, *42*, 2–14, doi:10.1016/j.mssp.2015.07.052.

25. Dong, H.; Zeng, G.; Tang, L.; Fan, C.; Zhang, C.; He, X.; He, Y. An Overview on Limitations of TiO_2-Based Particles for Photocatalytic Degradation of Organic Pollutants and the Corresponding Countermeasures. *Water Res* **2015**, *79*, 128–146, doi:10.1016/j.watres.2015.04.038.

26. Schneider, J.; Matsuoka, M.; Takeuchi, M.; Zhang, J.; Horiuchi, Y.; Anpo, M.; Bahnemann, D.W. Understanding TiO_2 Photocatalysis: Mechanisms and Materials. *Chem Rev* **2014**, *114*, 9919–9986, doi:10.1021/cr5001892.

27. Ansari, S.A.; Khan, M.M.; Ansari, M.O.; Cho, M.H. Nitrogen-Doped Titanium Dioxide (N-Doped TiO_2) for Visible Light Photocatalysis. *New Journal of Chemistry* **2016**, *40*, 3000–3009, doi:10.1039/c5nj03478g.

28. Piątkowska, A.; Janus, M.; Szymański, K.; Mozia, S. C-,N- and S-Doped TiO_2 Photocatalysts: A Review. *Catalysts* **2021**, *11*, doi:10.3390/catal11010144.

29. Ding, W.; Li, W. A First Principles Study of the Energetics and Core Level Shifts of Anion-Doped TiO_2 Photocatalysts. *Chinese Journal of Catalysis* **2014**, *36*, 181–187, doi:10.1016/S1872-2067(14)60165-0.

30. Brindha, A.; Sivakumar, T. Visible Active N, S Co-Doped TiO_2/Graphene Photocatalysts for the Degradation of Hazardous Dyes. *J Photochem Photobiol A Chem* **2017**, *340*, 146–156, doi:10.1016/j.jphotochem.2017.03.010.

31. Natarajan, T.S.; Mozhiarasi, V.; Tayade, R.J. Nitrogen Doped Titanium Dioxide (N-TiO_2): Synopsis of Synthesis Methodologies, Doping Mechanisms, Property Evaluation and Visible Light Photocatalytic Applications. *Photochem* **2021**, *1*, 371–410, doi:10.3390/photochem1030024.

32. Asahi, R.; Morikawa, T.; Irie, H.; Ohwaki, T. Nitrogen-Doped Titanium Dioxide as Visible-Light-Sensitive Photocatalyst: Designs, Developments, and Prospects. *Chem Rev* **2014**, *114*, 9824–9852, doi:10.1021/cr5000738.

33. Kuo, C.L.; Chen, W.G.; Chen, T.Y. The Electronic Structure Changes and the Origin of the Enhanced Optical Properties in N-Doped Anatase TiO_2 - A Theoretical Revisit. *J Appl Phys* **2014**, *116*, doi:10.1063/1.4894444.

34. Suwannaruang, T.; Hildebrand, J.P.; Taffa, D.H.; Wark, M.; Kamonsuangkasem, K.; Chirawatkul, P.; Wantala, K. Visible Light-Induced Degradation of Antibiotic Ciprofloxacin over Fe–N–TiO_2 Mesoporous Photocatalyst with Anatase/Rutile/Brookite Nanocrystal Mixture. *J Photochem Photobiol A Chem* **2020**, *391*, 112371, doi:10.1016/j.jphotochem.2020.112371.

35. Singh, R.K.; Kumar, R.; Singh, D.P. Graphene Oxide: Strategies for Synthesis, Reduction and Frontier Applications. *RSC Adv* **2016**, *6*, 64993–65011, doi:10.1039/c6ra07626b.

36. Alam, S.N.; Sharma, N.; Kumar, L. Synthesis of Graphene Oxide (GO) by Modified Hummers Method and Its Thermal Reduction to Obtain Reduced Graphene Oxide (RGO)*. *Graphene* **2017**, *06*, 1–18, doi:10.4236/graphene.2017.61001.

37. Tang, B.; Chen, H.; Peng, H.; Wang, Z.; Huang, W. Graphene Modified TiO_2 Composite Photocatalysts: Mechanism, Progress and Perspective. *Nanomaterials* **2018**, *8*, 27–30, doi:10.3390/nano8020105.

38. Wang, Y.; Wang, X.; Zhang, M.; Fang, L.; Jin, L.; Gao, J.; Zhang, Y.; Yang, B.; He, G.; Sun, Z. TiO_2 Nanorod Array Film Decorated with RGO Nanosheets for Enhancing Photocatalytic and Photoelectrochemical Properties. *J Alloys Compd* **2019**, *770*, 243–251, doi:10.1016/j.jallcom.2018.08.098.

39. El-Shafai, N.M.; El-Khouly, M.E.; El-Kemary, M.; Ramadan, M.S.; Derbalah, A.S.; Masoud, M.S. Fabrication and Characterization of Graphene Oxide–Titanium Dioxide Nanocomposite for Degradation of Some Toxic Insecticides. *Journal of Industrial and Engineering Chemistry* **2019**, *69*, 315–323, doi:10.1016/j.jiec.2018.09.045.

40. Catauro, M.; Tranquillo, E.; Dal Poggetto, G.; Pasquali, M.; Dell'Era, A.; Ciprioti, S.V. Influence of the Heat Treatment on the Particles Size and on the Crystalline Phase of TiO_2 Synthesized by the Sol-Gel Method. *Materials* **2018**, *11*, doi:10.3390/ma11122364.

41. Gabelica, I.; Ćurković, L.; Mandić, V.; Panžić, I.; Ljubas, D.; Zadro, K. Rapid Microwave-Assisted Synthesis of $Fe_3O_4/SiO_2/TiO_2$ Core-2-Layer-Shell Nanocomposite for Photocatalytic Degradation of Ciprofloxacin. *Catalysts* **2021**, *11*, doi:10.3390/catal11101136.

42. Kadam, A.N.; Dhabbe, R.S.; Kokate, M.R.; Gaikwad, Y.B.; Garadkar, K.M. Preparation of N Doped TiO_2 via Microwave-Assisted Method and Its Photocatalytic Activity for Degradation of Malathion. *Spectrochim Acta A Mol Biomol Spectrosc* **2014**, *133*, 669–676, doi:10.1016/j.saa.2014.06.020.

43. Kremsner, J.M.; Stadler, A. *A Chemist's Guide to Microwave Synthesis*; 3rd Editio.; Anton Paar GmbH: Graz, 2018;

44. Blanco-Vega, M.P.; Guzmán-Mar, J.L.; Villanueva-Rodríguez, M.; Maya-Treviño, L.; Garza-Tovar, L.L.; Hernández-Ramírez, A.; Hinojosa-Reyes, L. Photocatalytic Elimination of Bisphenol A under Visible Light Using Ni-Doped TiO_2 Synthesized by Microwave Assisted Sol-Gel Method. *Mater Sci Semicond Process* **2017**, *71*, 275–282, doi:10.1016/j.mssp.2017.08.013.

45. Cunha, D.L.; Kuznetsov, A.; Achete, C.A.; Eduardo, A.; Marques, M. Immobilized TiO_2 on Glass Spheres Applied to Heterogeneous Photocatalysis : Photoactivity , Leaching and Regeneration Process. **2018**, 1–19, doi:10.7717/peerj.4464.

46. Alvear-daza, J.J.; Pais-ospina, D.; Marín-silva, D.A.; Pinotti, A.; Damonte, L.; Pizzio, L.R.; Osorio-vargas, P.; Rengifo-herrera, J.A. Facile Photocatalytic Immobilization Strategy for P-25 TiO_2 Nanoparticles on Low Density Polyethylene Films and Their UV-A Photo-Induced Super Hydrophilicity and Photocatalytic Activity. *Catal Today* **2020**, 1–9, doi:10.1016/j.cattod.2020.07.029.

47. Kiwi, J.; Rtimi, S. Applied Catalysis B : Environmental Insight into the Interaction of Magnetic Photocatalysts with the Incoming Light Accelerating Bacterial Inactivation and Environmental Cleaning. *Appl Catal B* **2021**, *281*, 119420, doi:10.1016/j.apcatb.2020.119420.

48. Ramone, A.; Scharnberg, D.A.; Carvalho, A.; Loreto, D.; Bender, T.; Kopp, A.; Arcaro, S.; Andréa, P.; Assis, A. De; Rodriguez, L. Porous Ceramic Supported TiO_2 Nanoparticles : Enhanced Photocatalytic Activity for Rhodamine B Degradation. *Boletín de la Sociedad Española de Cerámica y Vidrio* **2020**, *59*, 230–238, doi:10.1016/j.bsecv.2019.12.001.

49. Magnone, E.; Kim, M.K.; Lee, H.J.; Park, J.H. Facile Synthesis of TiO_2-Supported Al_2O_3 Ceramic Hollow Fiber Substrates with Extremely High Photocatalytic Activity and Reusability. *Ceram Int* **2021**, *47*, 7764–7775, doi:10.1016/j.ceramint.2020.11.121.

50. Yildiz, T.; Yatmaz, H.C.; Öztürk, K. Anatase TiO_2 Powder Immobilized on Reticulated Al_2O_3 Ceramics as a Photocatalyst for Degradation of RO16 Azo Dye. *Ceram Int* **2020**, *46*, 8651–8657, doi:10.1016/j.ceramint.2019.12.098.

51. 2015/495, C.I.D. (Eu); 2015, of 20 M. COMMISSION IMPLEMENTING DECISION (EU) 2015/495 of 20 March 2015 Establishing a Watch List of Substances for Union-Wide Monitoring in the Field of Water Policy Pursuant to Directive 2008/105/EC of the European Parliament and of the Council. *Official Journal of the European Union* **2015**, *L78/40*, 20–30.

52. 2018/840/EC *Commission Implementing Decision (EU) 2018/840 of 5 June 2018 Establishing a Watch List of Substances for Union-Wide Monitoring in the Field of Water Policy*; 2018; Vol. L 141;

53. IDMC Grid 2022. **2022**.

54. UN Summary Progress Update 2021 : SDG 6 — Water and Sanitation for All. *UN-Water integrated monitoring initiative* **2021**, 1–58.

55. Fekadu, S.; Alemayehu, E.; Dewil, R.; Van der Bruggen, B. Pharmaceuticals in Freshwater Aquatic Environments: A Comparison of the African and European Challenge. *Science of the Total Environment* **2019**, *654*, 324–337, doi:10.1016/j.scitotenv.2018.11.072.

56. Morin-Crini, N.; Lichtfouse, E.; Liu, G.; Balaram, V.; Ribeiro, A.R.L.; Lu, Z.; Stock, F.; Carmona, E.; Teixeira, M.R.; Picos-Corrales, L.A.; et al. Emerging Contaminants: Analysis, Aquatic Compartments and Water Pollution. In; 2021; pp. 1–111.

57. Patel, M.; Kumar, R.; Kishor, K.; Mlsna, T.; Pittman, C.U.; Mohan, D. Pharmaceuticals of Emerging Concern in Aquatic Systems: Chemistry, Occurrence, Effects, and Removal Methods. *Chem Rev* **2019**, *119*, 3510–3673, doi:10.1021/acs.chemrev.8b00299.

58. Morin-Crini, N.; Lichtfouse, E.; Fourmentin, M.; Ribeiro, A.R.L.; Noutsopoulos, C.; Mapelli, F.; Fenyvesi, É.; Vieira, M.G.A.; Picos-Corrales, L.A.; Moreno-Piraján, J.C.; et al. Remediation of Emerging Contaminants. In; Morin-Crini, N., Lichtfouse, E., Crini, G., Eds.; Springer, Cham, 2021; pp. 1–106.

59. Cui, N.; Zada, A.; Song, J.; Yang, Y.; Liu, M.; Wang, Y.; Wu, Y.; Qi, K.; Selvaraj, R.; Liu, S.Y.; et al. Plasmon-Induced ZnO-Ag/AgCl Photocatalyst for Degradation of Tetracycline Hydrochloride. *Desalination Water Treat* **2022**, *245*, 247–254, doi:10.5004/dwt.2022.27976.

60. Zhang, Z.; Zada, A.; Cui, N.; Liu, N.; Liu, M.; Yang, Y.; Jiang, D.; Jiang, J.; Liu, S. Synthesis of Ag Loaded ZnO/BiOCl with High Photocatalytic Performance for the Removal of Antibiotic Pollutants. *Crystals (Basel)* **2021**, *11*, 1–12, doi:10.3390/cryst11080981.

61. European Commission Establishing a Watch List of Substances for Union-Wide Monitoring in the Field of Water Policy Pursuant to Directive 2008/105/EC of the European Parliament and of the Council. *Official Journal of the European Union* **2020**, *L 257*, 32–35.

62. European Commission Commision Implementing Decision (EU) 2022/1307-22 July 2022-Establishing a Watch List of Substances for Union-Wide Monitoring in the Field of Water Policy Pursuant to Directive 2008/105/EC of the European Parliament and of the Council. **2022**, *2016*, 48–119.

63. Jiang, C.; Ji, Y.; Shi, Y.; Chen, J.; Cai, T. Sulfate Radical-Based Oxidation of Fluoroquinolone Antibiotics: Kinetics, Mechanisms and Effects of Natural Water Matrices. *Water Res* **2016**, *106*, 507–517, doi:10.1016/j.watres.2016.10.025.

64. Kutuzova, A.; Dontsova, T.; Kwapinski, W. Application of TiO_2-based Photocatalysts to Antibiotics Degradation: Cases of Sulfamethoxazole, Trimethoprim and Ciprofloxacin. *Catalysts* **2021**, *11*, 728, doi:10.3390/catal11060728.

65. Michael, I.; Achilleos, A.; Lambropoulou, D.; Torrens, V.O.; Pérez, S.; Petrović, M.; Barceló, D.; Fatta-Kassinos, D. Proposed Transformation Pathway and Evolution Profile of Diclofenac and Ibuprofen Transformation Products during (Sono)Photocatalysis. *Appl Catal B* **2014**, *147*, 1015–1027, doi:10.1016/j.apcatb.2013.10.035.

66. Li, W.; Yu, R.; Li, M.; Guo, N.; Yu, H.; Yu, Y. Photocatalytical Degradation of Diclofenac by Ag-BiOI-RGO: Kinetics, Mechanisms and Pathways. *Chemosphere* **2019**, *218*, 966–973, doi:10.1016/j.chemosphere.2018.11.185.

67. Liu, F.; Liang, J.; Chen, L.; Tong, M.; Liu, W. Photocatalytic Removal of Diclofenac by Ti Doped BiOI Microspheres under Visible Light Irradiation: Kinetics, Mechanism, and Pathways. *J Mol Liq* **2019**, *275*, 807–814, doi:10.1016/j.molliq.2018.11.119.

68. Hu, Z.; Cai, X.; Wang, Z.; Li, S.; Wang, Z.; Xie, X. Construction of Carbon-Doped Supramolecule-Based g-C_3N_4/TiO_2 Composites for Removal of Diclofenac and Carbamazepine: A Comparative Study of Operating Parameters, Mechanisms, Degradation Pathways. *J Hazard Mater* **2019**, *380*, 120812, doi:10.1016/j.jhazmat.2019.120812.

69. Martínez, C.; Canle L., M.; Fernández, M.I.; Santaballa, J.A.; Faria, J. Aqueous Degradation of Diclofenac by Heterogeneous Photocatalysis Using Nanostructured Materials. *Appl Catal B* **2011**, *107*, 110–118, doi:10.1016/j.apcatb.2011.07.003.

70. Mugunthan, E.; Saidutta, M.B.; Jagadeeshbabu, P.E. Visible Light Assisted Photocatalytic Degradation of Diclofenac Using TiO_2-WO_3 Mixed Oxide Catalysts. *Environ Nanotechnol Monit Manag* **2018**, *10*, 322–330, doi:10.1016/j.enmm.2018.07.012.

71. Chen, X.; Zhang, W.; Zhang, L.; Feng, L.; Wen, J.; Yang, J.; Zhang, C.; Jiang, J.; Wang, H. Effective Photocatalytic Salicylic Acid Removal under Visible Light Irradiation Using Ag_2S/AgI-Bi_2S_3/BiOI with Z-Scheme Heterojunctions. *Appl Surf Sci* **2019**, *481*, 1335–1343, doi:10.1016/j.apsusc.2019.03.214.

72. Goi, A.; Veressinina, Y.; Trapido, M. Degradation of Salicylic Acid by Fenton and Modified Fenton Treatment. *Chemical Engineering Journal* **2008**, *143*, 1–9, doi:10.1016/j.cej.2008.01.018.

73. Hu, R.; Zhang, L.; Hu, J. Study on the Kinetics and Transformation Products of Salicylic Acid in Water via Ozonation. *Chemosphere* **2016**, *153*, 394–404, doi:10.1016/j.chemosphere.2016.03.074.

74. Stamatis, N.K.; Konstantinou, I.K. Occurrence and Removal of Emerging Pharmaceutical, Personal Care Compounds and Caffeine Tracer in Municipal Sewage Treatment Plant in Western Greece. *J Environ Sci Health B* **2013**, *48*, 800–813, doi:10.1080/03601234.2013.781359.

75. Pronk, G.J.; Stofberg, S.F.; Van Dooren, T.C.G.W.; Dingemans, M.M.L.; Frijns, J.; Koeman-Stein, N.E.; Smeets, P.W.M.H.; Bartholomeus, R.P. Increasing Water System Robustness in the Netherlands: Potential of Cross-Sectoral Water Reuse. *Water Resources Management* **2021**, *35*, 3721–3735, doi:10.1007/s11269-021-02912-5.

76. Bauer, S.; Behnisch, J.; Dell, A.; Gahr, A.; Leinhos, M.; Linke, H.J.; Shen, W.; Tolksdorf, J.; Wagner, M. Water Reuse Fit for Purpose by a Sustainable Industrial Wastewater Management Concept. *Chem Ing Tech* **2019**, *91*, 1472–1479, doi:10.1002/cite.201900024.

77. Yang, J.; Monnot, M.; Ercolei, L.; Moulin, P. Membrane-Based Processes Used in Municipal Wastewater Treatment for Water Reuse: State-of-the-Art and Performance Analysis. *Membranes (Basel)* **2020**, *10*, 1–56, doi:10.3390/membranes10060131.

78. EC, E.C. REGULATION (EU) 2020/741 OF THE EUROPEAN PARLIAMENT AND OF THE COUNCIL of 25 May 2020 on Minimum Requirements for Water Reuse (Text with EEA Relevance). *Official Journal of the European Union* **2020**, *L*, *177 (63*, 32–55.

79. Kanakaraju, D.; Glass, B.D.; Oelgemöller, M. Advanced Oxidation Process-Mediated Removal of Pharmaceuticals from Water: A Review. *J Environ Manage* **2018**, *219*, 189–207, doi:10.1016/j.jenvman.2018.04.103.

80. Taoufik, N.; Boumya, W.; Achak, M.; Sillanpää, M.; Barka, N. Comparative Overview of Advanced Oxidation Processes and Biological Approaches for the Removal Pharmaceuticals. *J Environ Manage* **2021**, *288*, doi:10.1016/j.jenvman.2021.112404.

81. Khan, N.A.; Khan, S.U.; Ahmed, S.; Farooqi, I.H.; Yousefi, M.; Mohammadi, A.A.; Changani, F. Recent Trends in Disposal and Treatment Technologies of Emerging-

Pollutants- A Critical Review. *TrAC - Trends in Analytical Chemistry* **2020**, *122*, doi:10.1016/j.trac.2019.115744.

82. Bethi, B.; Sonawane, S.H.; Bhanvase, B.A.; Gumfekar, S.P. Nanomaterials-Based Advanced Oxidation Processes for Wastewater Treatment: A Review. *Chemical Engineering and Processing: Process Intensification* 2016, *109*, 178–189.

83. Arzate, S.; Pfister, S.; Oberschelp, C.; Sánchez-Pérez, J.A. Environmental Impacts of an Advanced Oxidation Process as Tertiary Treatment in a Wastewater Treatment Plant. *Science of the Total Environment* **2019**, *694*, doi:10.1016/j.scitotenv.2019.07.378.

84. Radović Vučić, M.; Baošić, R.; Mitrović, J.; Petrović, M.; Velinov, N.; Kostić, M.; Bojić, A. Comparison of the Advanced Oxidation Processes in the Degradation of Pharmaceuticals and Pesticides in Simulated Urban Wastewater: Principal Component Analysis and Energy Requirements. *Process Safety and Environmental Protection* **2021**, *149*, 786–793, doi:10.1016/j.psep.2021.03.039.

85. Monteagudo, J.M.; El-taliawy, H.; Durán, A.; Caro, G.; Bester, K. Sono-Activated Persulfate Oxidation of Diclofenac: Degradation, Kinetics, Pathway and Contribution of the Different Radicals Involved. *J Hazard Mater* **2018**, *357*, 457–465, doi:10.1016/j.jhazmat.2018.06.031.

86. Gomes, J.; Lincho, J.; Domingues, E.; Quinta-Ferreira, R.; Martins, R. N–TiO_2 Photocatalysts: A Review of Their Characteristics and Capacity for Emerging Contaminants Removal. *Water (Basel)* **2019**, *11*, 373, doi:10.3390/w11020373.

87. Ma, D.; Yi, H.; Lai, C.; Liu, X.; Huo, X.; An, Z.; Li, L.; Fu, Y.; Li, B.; Zhang, M.; et al. Critical Review of Advanced Oxidation Processes in Organic Wastewater Treatment. *Chemosphere* **2021**, *275*, 130104, doi:10.1016/j.chemosphere.2021.130104.

88. Čizmić, M.; Ljubas, D.; Škorić, I.; Rožman, M.; Ašperger, D.; Ćurković, L.; Petrović, M.; Babić, S. Photolytic and Photocatalytic Degradation of Febantel in Aqueous Media. *Desalination Water Treat* **2018**, *104*, 294–303, doi:10.5004/dwt.2018.21915.

89. Brienza, M.; Katsoyiannis, I.A. Sulfate Radical Technologies as Tertiary Treatment for the Removal of Emerging Contaminants from Wastewater. *Sustainability (Switzerland)* **2017**, *9*, doi:10.3390/su9091604.

90. Vimal, G.; Shah, K.J. *Advances in Wastewater Treatment I Edited by Introduction to Conventional Wastewater Treatment Technologies: Limitations and Recent Advances*; 2021;

91. Ćurković, L.; Ljubas, D.; Šegota, S.; Bačić, I. Photocatalytic Degradation of Lissamine Green B Dye by Using Nanostructured Sol-Gel TiO2 Films. *J Alloys Compd* **2014**, *604*, 309–316, doi:10.1016/j.jallcom.2014.03.148.

92. Wen, J.; Li, X.; Liu, W.; Fang, Y.; Xie, J.; Xu, Y. Photocatalysis Fundamentals and Surface Modification of TiO_2 Nanomaterials. *Cuihua Xuebao/Chinese Journal of Catalysis* **2015**, *36*, 2049–2070, doi:10.1016/S1872-2067(15)60999-8.

93. Khaki, M.R.D.; Shafeeyan, M.S.; Raman, A.A.A.; Daud, W.M.A.W. Application of Doped Photocatalysts for Organic Pollutant Degradation - A Review. *J Environ Manage* **2017**, *198*, 78–94, doi:10.1016/j.jenvman.2017.04.099.

94. Salaeh, S.; Juretic Perisic, D.; Biosic, M.; Kusic, H.; Babic, S.; Lavrencic Stangar, U.; Dionysiou, D.D.; Loncaric Bozic, A. Diclofenac Removal by Simulated Solar Assisted Photocatalysis Using TiO_2-Based Zeolite Catalyst; Mechanisms, Pathways and Environmental Aspects. *Chemical Engineering Journal* **2016**, *304*, 289–302, doi:10.1016/j.cej.2016.06.083.

95. Xi, J.; Zhang, Y.; Chen, X.; Hu, Y. A Simple Sol–Gel Hydrothermal Method for the Synthesis of Defective TiO_2 Nanocrystals with Excellent Visible-Light Photocatalytic Activity. *Research on Chemical Intermediates* **2020**, *46*, 2205–2214, doi:10.1007/s11164-020-04087-x.

96. Gupta, S.M.; Tripathi, M. A Review on the Synthesis of TiO_2 Nanoparticles by Solution Route. *Central European Journal of Chemistry* **2012**, *10*, 279–294, doi:10.2478/s11532-011-0155-y.

97. Drunka, R.; Grabis, J.; Jankovica, D.; Rasmane, D.A.; Krumina, A. Photocatalytic Properties of TiO_2 Nanostructures of Different Morphology Modified with Various Modifiers. *Proceedings of the Estonian Academy of Sciences* **2019**, *68*, 168–177, doi:10.3176/proc.2019.2.08.

98. Sharavath, V.; Sarkar, S.; Ghosh, S. One-Pot Hydrothermal Synthesis of TiO_2/Graphene Nanocomposite with Simultaneous Nitrogen-Doping for Energy Storage Application. *Journal of Electroanalytical Chemistry* **2018**, *829*, 208–216, doi:10.1016/j.jelechem.2018.09.056.

99. Hua, L.; Yin, Z.; Cao, S. Recent Advances in Synthesis and Applications of Carbon-Doped TiO_2 Nanomaterials. *Catalysts* **2020**, *10*, 1–16, doi:10.3390/catal10121431.

100. Faraldos, M.; Bahamonde, A. Environmental Applications of Titania-Graphene Photocatalysts. *Catal Today* **2017**, *285*, 13–28, doi:10.1016/j.cattod.2017.01.029.

101. Cabello, G.; Davoglio, R.A.; Cuadrado, L.G. The Role of Small Nanoparticles on the Formation of Hot Spots under Microwave-Assisted Hydrothermal Heating. *Inorg Chem* **2018**, *57*, 7252–7258, doi:10.1021/acs.inorgchem.8b00911.

102. Mendiola-Alvarez, S.Y.; Guzmán-Mar, J.L.; Turnes-Palomino, G.; Maya-Alejandro, F.; Hernández-Ramírez, A.; Hinojosa-Reyes, L. UV and Visible Activation of Cr(III)-Doped TiO_2 Catalyst Prepared by a Microwave-Assisted Sol–Gel Method during MCPA Degradation. *Environmental Science and Pollution Research* **2017**, *24*, 12673–12682, doi:10.1007/s11356-016-8034-x.

103. Myasoedova, T.N.; Kalusulingam, R.; Mikhailova, T.S. Sol-Gel Materials for Electrochemical Applications: Recent Advances. *Coatings* **2022**, *12*, doi:10.3390/coatings12111625.

104. Navas, D.; Fuentes, S.; Castro-Alvarez, A.; Chavez-Angel, E. Review on Sol-Gel Synthesis of Perovskite and Oxide Nanomaterials. *Gels* **2021**, *7*, doi:10.3390/gels7040275.

105. Fu, R.; Yin, Q.; Guo, X.; Tong, X.; Wang, X. Evolution of Mesoporous TiO_2 during Fast Sol–Gel Synthesis. *Research on Chemical Intermediates* **2017**, *43*, 6433–6445, doi:10.1007/s11164-017-2999-z.

106. Crisan, M. A Short History of the Sol-Gel Processes Initiated in Institute of Physical Chemistry. *Revue Roumaine de Chimie* **2018**, *63*, 385–392.

107. MODAN, E.M.; PLĂIAȘU, A.G. Advantages and Disadvantages of Chemical Methods in the Elaboration of Nanomaterials. *The Annals of "Dunarea de Jos" University of Galati. Fascicle IX, Metallurgy and Materials Science* **2020**, *43*, 53–60, doi:10.35219/mms.2020.1.08.

108. Nikam, A. V.; Prasad, B.L.V.; Kulkarni, A.A. Wet Chemical Synthesis of Metal Oxide Nanoparticles: A Review. *CrystEngComm* **2018**, *20*, 5091–5107, doi:10.1039/C8CE00487K.

109. Hashim, N.; Muda, Z.; Hussein, M.Z.; Isa, I.M.; Mohamed, A.; Kamari, A.; Bakar, S.A.; Mamat, M.; Jaafar, A.M. A Brief Review on Recent Graphene Oxide-Based Material Nanocomposites: Synthesis and Applications. *Journal of Materials and Environmental Science* **2016**, *7*, 3225–3243.

110. Zhang, R.; Santangelo, S.; Fazio, E.; Neri, F.; D'Arienzo, M.; Morazzoni, F.; Zhang, Y.; Pinna, N.; Russo, P.A. Stabilization of Titanium Dioxide Nanoparticles at the Surface of Carbon Nanomaterials Promoted by Microwave Heating. *Chemistry - A European Journal* **2015**, *21*, 14901–14910, doi:10.1002/chem.201502433.

111. Zhu, Y.J.; Chen, F. Microwave-Assisted Preparation of Inorganic Nanostructures in Liquid Phase. *Chem Rev* **2014**, *114*, 6462–6555, doi:10.1021/cr400366s.

112. Bregadiolli, B.A.; Fernandes, S.L.; De Oliveira Graeff, C.F. Easy and Fast Preparation of TiO_2-Based Nanostructures Using Microwave Assisted Hydrothermal Synthesis. *Materials Research* **2017**, *20*, 912–919, doi:10.1590/1980-5373-MR-2016-0684.

113. Bora, L. V.; Mewada, R.K. Visible/Solar Light Active Photocatalysts for Organic Effluent Treatment: Fundamentals, Mechanisms and Parametric Review. *Renewable and Sustainable Energy Reviews* **2017**, *76*, 1393–1421, doi:10.1016/j.rser.2017.01.130.

114. Belver, C.; Bedia, J.; Rodriguez, J.J.; Gómez-Avilés, A.; Peñas-Garzón, M. *Semiconductor Photocatalysis for Water Purification*; 2019; ISBN 9780128139264.

115. Fang, W.; Xing, M.; Zhang, J. Modifications on Reduced Titanium Dioxide Photocatalysts: A Review. *Journal of Photochemistry and Photobiology C: Photochemistry Reviews* **2017**, *32*, 21–39, doi:10.1016/j.jphotochemrev.2017.05.003.

116. Mehta, A.; Sharma, M.; Kumar, A.; Basu, S. Effect of Au Content on the Enhanced Photocatalytic Efficiency of Mesoporous Au/TiO_2 Nanocomposites in UV and Sunlight. *Gold Bull* **2017**, *50*, 33–41, doi:10.1007/s13404-016-0191-7.

117. Ansari, S.A.; Khan, M.M.; Ansari, M.O.; Cho, M.H. Nitrogen-Doped Titanium Dioxide (N-Doped TiO_2) for Visible Light Photocatalysis. *New Journal of Chemistry* **2016**, *40*, 3000–3009, doi:10.1039/C5NJ03478G.

118. Ma, X.; Hao, K.; Dai, Y.; Song, L.; Yu, Q.; Yin, X.; Wang, Z. Enhanced Visible-Light Photocatalytic Activity by the Comprehensive Effects of Mesoporous and N-Doping at the Meso-N-TiO_2 Nanocatalysts. *ChemistrySelect* **2021**, *6*, 6029–6036, doi:10.1002/slct.202101243.

119. Bakre, P. V.; Tilve, S.G.; Shirsat, R.N. Influence of N Sources on the Photocatalytic Activity of N-Doped TiO_2. *Arabian Journal of Chemistry* **2020**, *13*, 7637–7651, doi:10.1016/j.arabjc.2020.09.001.

120. Kusiak-Nejman, E.; Morawski, A.W. TiO_2/Graphene-Based Nanocomposites for Water Treatment: A Brief Overview of Charge Carrier Transfer, Antimicrobial and Photocatalytic Performance. *Appl Catal B* **2019**, *253*, 179–186, doi:10.1016/j.apcatb.2019.04.055.

121. Khalid, N.R.; Majid, A.; Tahir, M.B.; Niaz, N.A.; Khalid, S. Carbonaceous-TiO_2 Nanomaterials for Photocatalytic Degradation of Pollutants: A Review. *Ceram Int* **2017**, *43*, 14552–14571, doi:10.1016/j.ceramint.2017.08.143.

122. Marcano, D.C.; Kosynkin, D. V.; Berlin, J.M.; Sinitskii, A.; Sun, Z.; Slesarev, A.; Alemany, L.B.; Lu, W.; Tour, J.M. Improved Synthesis of Graphene Oxide. *ACS Nano* **2010**, *4*, 4806–4814, doi:10.1021/nn1006368.

123. Coros, M.; Pogacean, F.; Turza, A.; Dan, M.; Berghian-Grosan, C.; Pana, I.O.; Pruneanu, S. Green Synthesis, Characterization and Potential Application of Reduced Graphene Oxide. *Physica E Low Dimens Syst Nanostruct* **2020**, *119*, 113971, doi:10.1016/j.physe.2020.113971.

124. Ismail, Z. Green Reduction of Graphene Oxide by Plant Extracts: A Short Review. *Ceram Int* **2019**, *45*, 23857–23868, doi:10.1016/j.ceramint.2019.08.114.

125. Giovannetti, R.; Rommozzi, E.; Zannotti, M.; D'Amato, C.A. Recent Advances in Graphene Based TiO_2 Nanocomposites ($GTiO_2Ns$) for Photocatalytic Degradation of Synthetic Dyes. *Catalysts* **2017**, *7*, doi:10.3390/catal7100305.

126. Tolosana-Moranchel, Á.; Manassero, A.; Satuf, M.L.; Alfano, O.M.; Casas, J.A.; Bahamonde, A. Influence of TiO_2-RGO Optical Properties on the Photocatalytic Activity and Efficiency to Photodegrade an Emerging Pollutant. *Appl Catal B* **2019**, *246*, 1–11, doi:10.1016/j.apcatb.2019.01.054.

127. Srikanth, B.; Goutham, R.; Badri Narayan, R.; Ramprasath, A.; Gopinath, K.P.; Sankaranarayanan, A.R. Recent Advancements in Supporting Materials for Immobilised Photocatalytic Applications in Waste Water Treatment. *J Environ Manage* **2017**, *200*, 60–78, doi:10.1016/j.jenvman.2017.05.063.

128. Čizmić, M.; Ljubas, D.; Rožman, M.; Ašperger, D.; Ćurković, L.; Babíc, S. Photocatalytic Degradation of Azithromycin by Nanostructured TiO_2 Film: Kinetics, Degradation Products, and Toxicity. *Materials* **2019**, *16*, doi:10.3390/ma12060873.

129. Aguas, Y.; Hincapié, M.; Sánchez, C.; Botero, L.; Fernández-Ibañez, P. Photocatalytic Inactivation of Enterobacter Cloacae and Escherichia Coli Using Titanium Dioxide Supported on Two Substrates. *Processes* **2018**, *6*, doi:10.3390/pr6090137.

130. Kete, M.; Pavlica, E.; Fresno, F.; Bratina, G.; Štangar, U.L. Highly Active Photocatalytic Coatings Prepared by a Low-Temperature Method. *Environmental Science and Pollution Research* **2014**, *21*, 11238–11249, doi:10.1007/s11356-014-3077-3.

131. Hussein, F.H.; Hassan Hussein, F. *Photochemical Treatments of Textile Industries Wastewater*;

132. Bloh, J.Z. A Holistic Approach to Model the Kinetics of Photocatalytic Reactions. *Front Chem* **2019**, *7*, doi:10.3389/fchem.2019.00128.

133. Sanchez Tobon, C.; Ljubas, D.; Mandić, V.; Panžić, I.; Matijašić, G.; Ćurković, L. Microwave-Assisted Synthesis of N/TiO_2 Nanoparticles for Photocatalysis under Different Irradiation Spectra. *Nanomaterials* **2022**, *12*, doi:10.3390/nano12091473.

134. Sanchez Tobon, C.; Panžić, I.; Bafti, A.; Matijašić, G.; Ljubas, D.; Ćurković, L. Rapid Microwave-Assisted Synthesis of N/TiO_2/RGO Nanoparticles for the Photocatalytic Degradation of Pharmaceuticals. *Nanomaterials* **2022**, *12*, doi:10.3390/nano12223975.

135. Schwartzwalder, K.; Somers, A.W. Method of Making Porous Ceramic Articles. *U.S. Patent* **1963**, 4.

136. Švagelj, Z.; Mandić, V.; Ćurković, L.; Biošić, M.; Žmak, I.; Gaborardi, M. Titania-Coated Alumina Foam Photocatalyst for Memantine Degradation Derived by Replica Method and Sol-Gel Reaction. *Materials* **2020**, *13*, doi:10.3390/ma13010227.

137. Cheng, X.; Yu, X.; Xing, Z.; Yang, L. Synthesis and Characterization of N-Doped TiO_2 and Its Enhanced Visible-Light Photocatalytic Activity. *Arabian Journal of Chemistry* **2016**, *9*, S1706–S1711, doi:10.1016/j.arabjc.2012.04.052.

138. Sher Shah, M.S.A.; Park, A.R.; Zhang, K.; Park, J.H.; Yoo, P.J. Green Synthesis of Biphasic TiO_2-Reduced Graphene Oxide Nanocomposites with Highly Enhanced Photocatalytic Activity. *ACS Appl Mater Interfaces* **2012**, *4*, 3893–3901, doi:10.1021/am301287m.

139. Factorovich, M.; Guz, L.; Candal, R. N-TiO_2: Chemical Synthesis and Photocatalysis. *Advances in Physical Chemistry* **2011**, *2011*, doi:10.1155/2011/821204.

140. Cheng, X.; Yu, X.; Xing, Z.; Yang, L. Synthesis and Characterization of N-Doped TiO_2 and Its Enhanced Visible-Light Photocatalytic Activity. *Arabian Journal of Chemistry* **2016**, *9*, S1706–S1711, doi:10.1016/j.arabjc.2012.04.052.

141. Rizzo, L.; Meric, S.; Kassinos, D.; Guida, M.; Russo, F.; Belgiorno, V. Degradation of Diclofenac by TiO_2 Photocatalysis: UV Absorbance Kinetics and Process Evaluation through a Set of Toxicity Bioassays. *Water Res* **2009**, *43*, 979–988, doi:10.1016/j.watres.2008.11.040.

142. Tang, X.; Wang, Z.; Wang, Y. Visible Active N-Doped TiO_2/Reduced Graphene Oxide for the Degradation of Tetracycline Hydrochloride. *Chem Phys Lett* **2018**, *691*, 408–414, doi:10.1016/j.cplett.2017.11.037.

143. Yang, G.; Jiang, Z.; Shi, H.; Xiao, T.; Yan, Z. Preparation of Highly Visible-Light Active N-Doped TiO_2 Photocatalyst. *J Mater Chem* **2010**, *20*, 5301–5309, doi:10.1039/c0jm00376j.

144. Barkul, R.P.; Koli, V.B.; Shewale, V.B.; Patil, M.K.; Delekar, S.D. Visible Active Nanocrystalline N-Doped Anatase TiO_2 Particles for Photocatalytic Mineralization Studies. *Mater Chem Phys* **2016**, *173*, 42–51, doi:10.1016/j.matchemphys.2016.01.035.

145. Chung, K.H.; Kim, B.J.; Park, Y.K.; Kim, S.C.; Jung, S.C. Photocatalytic Properties of Amorphous N-Doped TiO_2 Photocatalyst under Visible Light Irradiation. *Catalysts* **2021**, *11*, doi:10.3390/catal11081010.

146. Madurai Ramakrishnan, V.; Sandberg, S.; Muthukumarasamy, N.; Kvamme, K.; Balraju, P.; Agilan, S.; Velauthapillai, D. Microwave-Assisted Solvothermal Synthesis of Worms-like TiO_2 Nanostructures in Submicron Regime as Light Scattering Layers for Dye-Sensitized Solar Cells. *Mater Lett* **2019**, *236*, 747–751, doi:10.1016/j.matlet.2018.11.049.

147. Russo, P.; Liang, R.; He, R.X.; Zhou, Y.N. Phase Transformation of TiO_2 Nanoparticles by Femtosecond Laser Ablation in Aqueous Solutions and Deposition on Conductive Substrates. *Nanoscale* **2017**, *9*, 6167–6177, doi:10.1039/c7nr00201g.

148. Kadam, A.N.; Dhabbe, R.S.; Kokate, M.R.; Gaikwad, Y.B.; Garadkar, K.M. Preparation of N Doped TiO_2 via Microwave-Assisted Method and Its Photocatalytic Activity for Degradation of Malathion. *Spectrochim Acta A Mol Biomol Spectrosc* **2014**, *133*, 669–676, doi:10.1016/j.saa.2014.06.020.

149. Kocijan, M.; Ćurković, L.; Radošević, T.; Podlogar, M. Enhanced Photocatalytic Activity of Hybrid RGO@TiO_2/CN Nanocomposite for Organic Pollutant Degradation under Solar Light Irradiation. *Catalysts* **2021**, *11*, doi:10.3390/catal11091023.

150. Atuchin, V. V.; Kesler, V.G.; Pervukhina, N. V.; Zhang, Z. Ti 2p and O 1s Core Levels and Chemical Bonding in Titanium-Bearing Oxides. *J Electron Spectros Relat Phenomena* **2006**, *152*, 18–24, doi:10.1016/j.elspec.2006.02.004.

151. Nolan, N.T.; Synnott, D.W.; Seery, M.K.; Hinder, S.J.; Van Wassenhoven, A.; Pillai, S.C. Effect of N-Doping on the Photocatalytic Activity of Sol-Gel TiO_2. *J Hazard Mater* **2012**, *211–212*, 88–94, doi:10.1016/j.jhazmat.2011.08.074.

152. Suwannaruang, T.; Kidkhunthod, P.; Chanlek, N.; Soontaranon, S.; Wantala, K. High Anatase Purity of Nitrogen-Doped TiO_2 Nanorice Particles for the Photocatalytic Treatment Activity of Pharmaceutical Wastewater. *Appl Surf Sci* **2019**, *478*, 1–14, doi:10.1016/j.apsusc.2019.01.158.

153. Hu, S.; Wang, A.; Li, X.; Löwe, H. Hydrothermal Synthesis of Well-Dispersed Ultrafine N-Doped TiO_2 Nanoparticles with Enhanced Photocatalytic Activity under Visible Light. *Journal of Physics and Chemistry of Solids* **2010**, *71*, 156–162, doi:10.1016/j.jpcs.2009.10.012.

154. Siburian, R.; Sihotang, H.; Lumban Raja, S.; Supeno, M.; Simanjuntak, C. New Route to Synthesize of Graphene Nano Sheets. *Oriental Journal of Chemistry* **2018**, *34*, 182–187, doi:10.13005/ojc/340120.

155. Low, F.W.; Lai, C.W.; Abd Hamid, S.B. Easy Preparation of Ultrathin Reduced Graphene Oxide Sheets at a High Stirring Speed. *Ceram Int* **2015**, *41*, 5798–5806, doi:10.1016/j.ceramint.2015.01.008.

156. Rani, V.; Das, R.K.; Golder, A.K. Fabrication of Reduced Graphene Oxide-Graphite Paste Electrode for H_2O_2 Formation and Its Implication for Ciprofloxacin Degradation. *Surfaces and Interfaces* **2017**, *7*, 99–105, doi:10.1016/j.surfin.2017.03.003.

157. Baraket, M.; Walton, S.G.; Wei, Z.; Lock, E.H.; Robinson, J.T.; Sheehan, P. Reduction of Graphene Oxide by Electron Beam Generated Plasmas Produced in Methane/Argon Mixtures. *Carbon N Y* **2010**, *48*, 3382–3390, doi:10.1016/j.carbon.2010.05.031.

158. Cychosz, K.A.; Thommes, M. Progress in the Physisorption Characterization of Nanoporous Gas Storage Materials. *Engineering* **2018**, *4*, 559–566, doi:10.1016/j.eng.2018.06.001.

159. Singh, I.; Birajdar, B. Synthesis, Characterization and Photocatalytic Activity of Mesoporous Na-Doped TiO_2 Nano-Powder Prepared via a Solvent-Controlled Non-Aqueous Sol-Gel Route. *RSC Adv* **2017**, *7*, 54053–54062, doi:10.1039/c7ra10108b.

160. John, D.; Rajalakshmi, A.S.; Lopez, R.M.; Achari, V.S. TiO_2-Reduced Graphene Oxide Nanocomposites for the Trace Removal of Diclofenac. *SN Appl Sci* **2020**, *2*, doi:10.1007/s42452-020-2662-y.

161. Appavu, B.; Kannan, K.; Thiripuranthagan, S. Enhanced Visible Light Photocatalytic Activities of Template Free Mesoporous Nitrogen Doped Reduced Graphene Oxide/Titania Composite Catalysts. *Journal of Industrial and Engineering Chemistry* **2016**, *36*, 184–193, doi:10.1016/j.jiec.2016.01.042.

162. Sheshmani, S.; Nayebi, M. Modification of TiO_2 with Graphene Oxide and Reduced Graphene Oxide; Enhancing Photocatalytic Activity of TiO_2 for Removal of Remazol Black B. *Polym Compos* **2019**, *40*, 210–216, doi:10.1002/pc.24630.

163. Zhang, Y.; Yang, H.M.; Park, S.J. Synthesis and Characterization of Nitrogen-Doped TiO_2 Coatings on Reduced Graphene Oxide for Enhancing the Visible Light Photocatalytic Activity. *Current Applied Physics* **2018**, *18*, 163–169, doi:10.1016/j.cap.2017.12.001.

164. Wolfgong, W.J. Chemical Analysis Techniques for Failure Analysis: Part 1, Common Instrumental Methods. In *Handbook of Materials Failure Analysis with Case Studies from the Aerospace and Automotive Industries*; Elsevier Inc., 2016; pp. 279–307 ISBN 9780128011775.

165. Tian, H.; Wan, C.; Xue, X.; Hu, X.; Wang, X. Effective Electron Transfer Pathway of the Ternary TiO_2/RGO/Ag Nanocomposite with Enhanced Photocatalytic Activity under Visible Light. *Catalysts* **2017**, *7*, 20–24, doi:10.3390/catal7050156.

166. Wen, X.; Zhao, S.; Asuha, S. Preparation of Nitrogen-Doped Mesoporous TiO_2/RGO Composites and Its Application to Visible Light-Assisted Photocatalytic Degradation. *J Nanomater* **2019**, *2019*, doi:10.1155/2019/6467107.

167. Yadav, H.M.; Kim, J.S. Solvothermal Synthesis of Anatase TiO_2-Graphene Oxide Nanocomposites and Their Photocatalytic Performance. *J Alloys Compd* **2016**, *688*, 123–129, doi:10.1016/j.jallcom.2016.07.133.

168. Suave, J.; Amorim, S.M.; Ângelo, J.; Andrade, L.; Mendes, A.; Moreira, R.F.P.M. TiO_2/Reduced Graphene Oxide Composites for Photocatalytic Degradation in Aqueous and Gaseous Medium. *J Photochem Photobiol A Chem* **2017**, *348*, 326–336, doi:10.1016/j.jphotochem.2017.08.064.

169. Tang, R.; Jiang, Q.; Liu, Y. Preparation and Study on Photocatalytic Activity of N-Doped TiO_2 Decorated N-Doped Graphene. *Procedia Eng* **2017**, *205*, 573–580, doi:10.1016/j.proeng.2017.10.423.

170. Ananpattarachai, J.; Kajitvichyanukul, P.; Seraphin, S. Visible Light Absorption Ability and Photocatalytic Oxidation Activity of Various Interstitial N-Doped TiO_2 Prepared from Different Nitrogen Dopants. *J Hazard Mater* **2009**, *168*, 253–261, doi:10.1016/j.jhazmat.2009.02.036.

171. World Bank Group Global Solar Atlas Available online: https://globalsolaratlas.info/detail?c=42.642041,16.062012,6&m=site&s=45.79817,15.952148.

172. Huynh, N.D.T.; Vo, K.D.; Nguyen, T.V.; Le, M.V. Enhancing the Photoactivity of TiO_2/SiO_2 Monolithic Catalyst and Its Reusability for Wastewater Treatment. *MATEC Web of Conferences* **2019**, *268*, 07005, doi:10.1051/matecconf/201926807005.

173. Yang, Z.Y.; Shen, G.Y.; He, Y.P.; Liu, X.X.; Yang, S.J. Preparation of TiO_2/SiO_2 Composite Oxide and Its Photocatalytic Degradation of Rhodamine B. *Journal of Porous Materials* **2016**, *23*, 589–599, doi:10.1007/s10934-015-0114-7.

174. Sun, Z.; Zhang, X.; Zhu, R.; Dong, X.; Xu, J.; Wang, B. Facile Synthesis of Visible Light-Induced g-C_3N_4/Rectorite Composite for Efficient Photodegradation of Ciprofloxacin. *Materials* **2018**, *11*, doi:10.3390/ma11122452.

175. Hu, H.; Chen, Y.; Ye, J.; Zhuang, L.; Zhang, H.; Ou, H. Degradation of Ciprofloxacin by 185/254 Nm Vacuum Ultraviolet: Kinetics, Mechanism and Toxicology. *Environ Sci (Camb)* **2019**, *5*, 564–576, doi:10.1039/c8ew00738a.

176. Salma, A.; Thoröe-Boveleth, S.; Schmidt, T.C.; Tuerk, J. Dependence of Transformation Product Formation on PH during Photolytic and Photocatalytic Degradation of Ciprofloxacin. *J Hazard Mater* **2016**, *313*, 49–59, doi:10.1016/j.jhazmat.2016.03.010.

177. Wang, Y.; Shen, C.; Zhang, M.; Zhang, B.T.; Yu, Y.G. The Electrochemical Degradation of Ciprofloxacin Using a SnO_2-Sb/Ti Anode: Influencing Factors, Reaction Pathways and Energy Demand. *Chemical Engineering Journal* **2016**, *296*, 79–89, doi:10.1016/j.cej.2016.03.093.

178. Jiménez-Salcedo, M.; Monge, M.; Tena, M.T. Study of Intermediate By-Products and Mechanism of the Photocatalytic Degradation of Ciprofloxacin in Water Using Graphitized Carbon Nitride Nanosheets. *Chemosphere* **2020**, *247*, doi:10.1016/j.chemosphere.2020.125910.

179. Coelho, A.D.; Sans, C.; Agüera, A.; Gómez, M.J.; Esplugas, S.; Dezotti, M. Effects of Ozone Pre-Treatment on Diclofenac: Intermediates, Biodegradability and Toxicity Assessment. *Science of the Total Environment* **2009**, *407*, 3572–3578, doi:10.1016/j.scitotenv.2009.01.013.

180. Murgolo, S.; Moreira, I.S.; Piccirillo, C.; Castro, P.M.L.; Ventrella, G.; Cocozza, C.; Mascolo, G. Photocatalytic Degradation of Diclofenac by Hydroxyapatite-TiO_2 Composite Material: Identification of Transformation Products and Assessment of Toxicity. *Materials* **2018**, *11*, doi:10.3390/ma11091779.

181. Keen, O.S.; Thurman, E.M.; Ferrer, I.; Dotson, A.D.; Linden, K.G. Dimer Formation during UV Photolysis of Diclofenac. *Chemosphere* **2013**, *93*, 1948–1956, doi:10.1016/j.chemosphere.2013.06.079.

182. Iovino, P.; Chianese, S.; Canzano, S.; Prisciandaro, M.; Musmarra, D. Photodegradation of Diclofenac in Wastewaters. *Desalination Water Treat* **2017**, *61*, 293–297, doi:10.5004/dwt.2016.11063.

183. Dadban Shahamat, Y.; Zazouli, M.A.; Zare, M.R.; Mengelizadeh, N. Catalytic Degradation of Diclofenac from Aqueous Solutions Using Peroxymonosulfate Activated by Magnetic MWCNTs-$CoFe_3O_4$ Nanoparticles. *RSC Adv* **2019**, *9*, 16496–16508, doi:10.1039/c9ra02757b.

7. APPENDIX

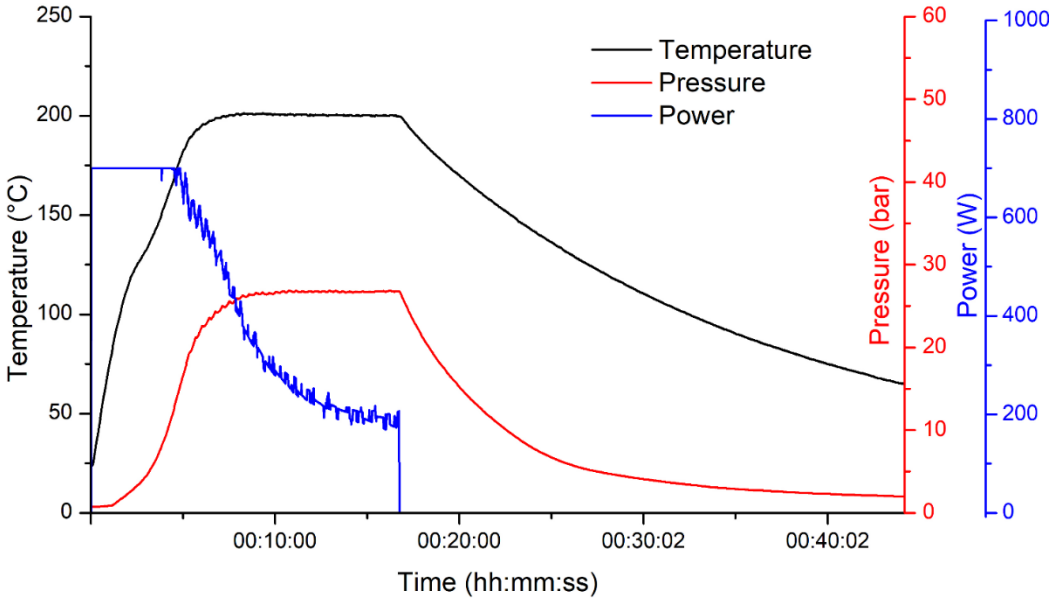

Figure S1. Inner pressure, temperature, and power supplied by the Microwave oven during the synthesis of nanocomposite N/TiO_2/rGO with 0.25 wt. % of rGO.

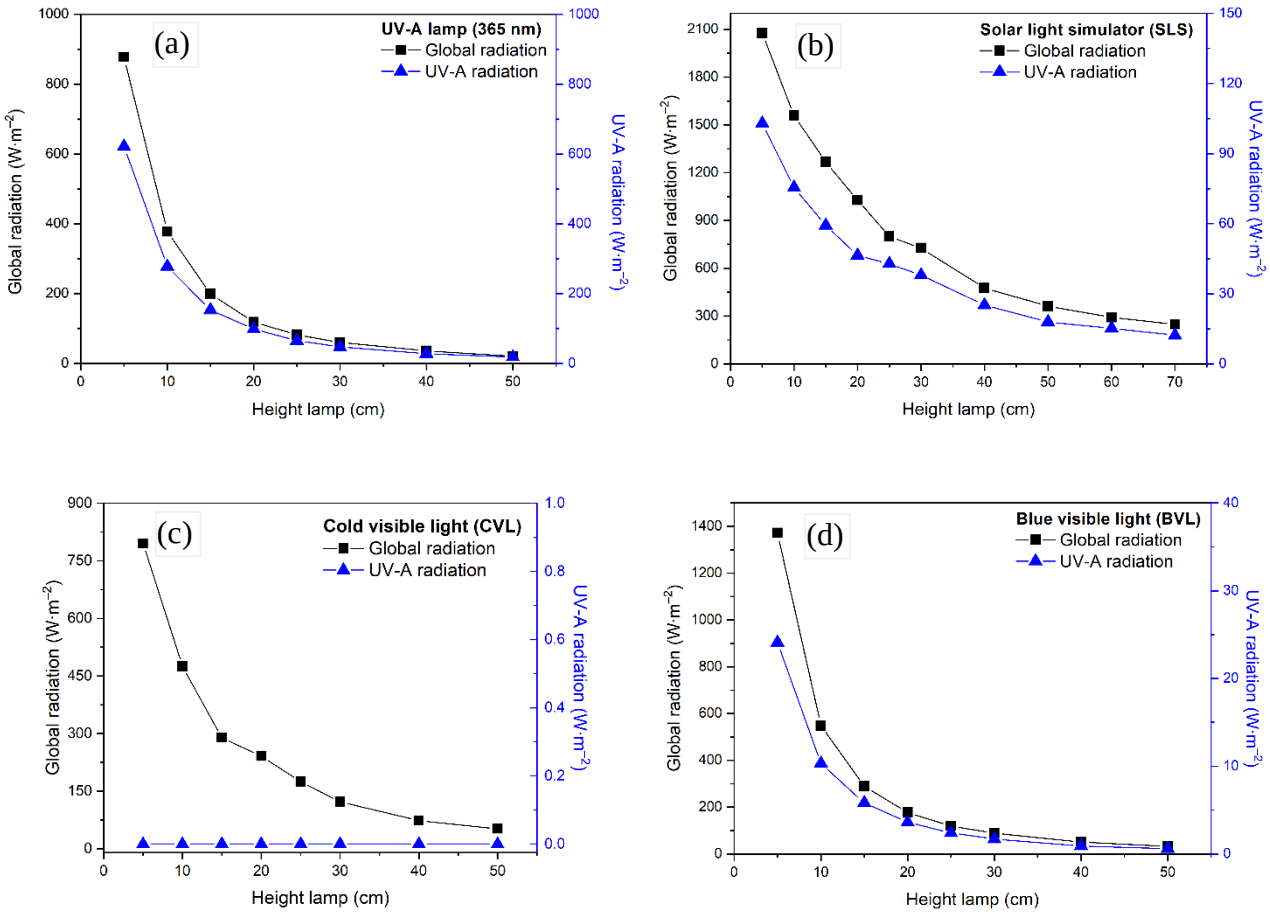

Figure S2. Global and UV-A radiation measurement of (a) UV-A lamp, (b) solar light simulator (SLS) lamp, (c) cold visible light (CVL) lamp, and (d) blue visible light (BVL) lamp.

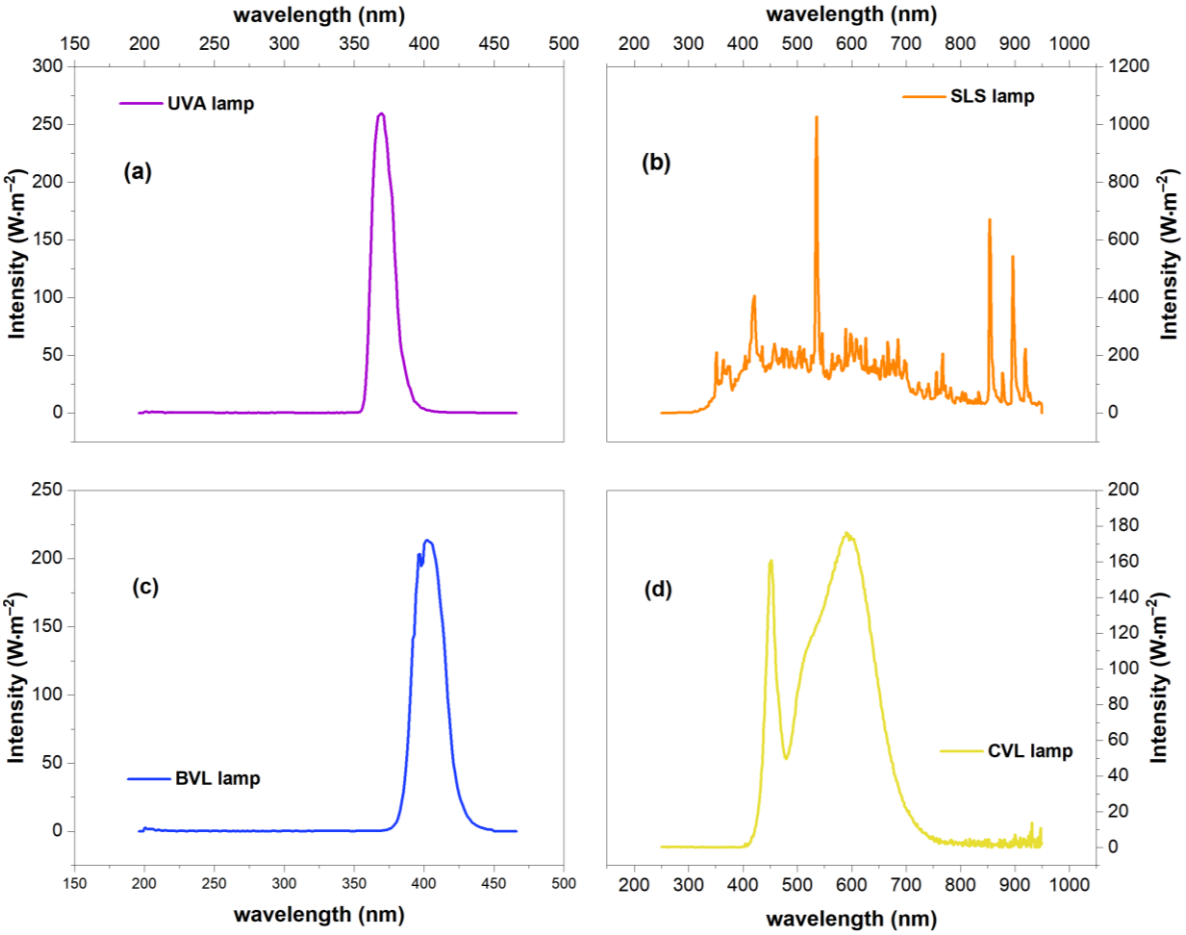

Figure S3. Radiation spectra of the different lamps at 20 cm height: (a) UVA light (UVA), (b) solar light simulator (SLS), (c) Blue visible light (BVL), and (d) Cold visible light (CVL).

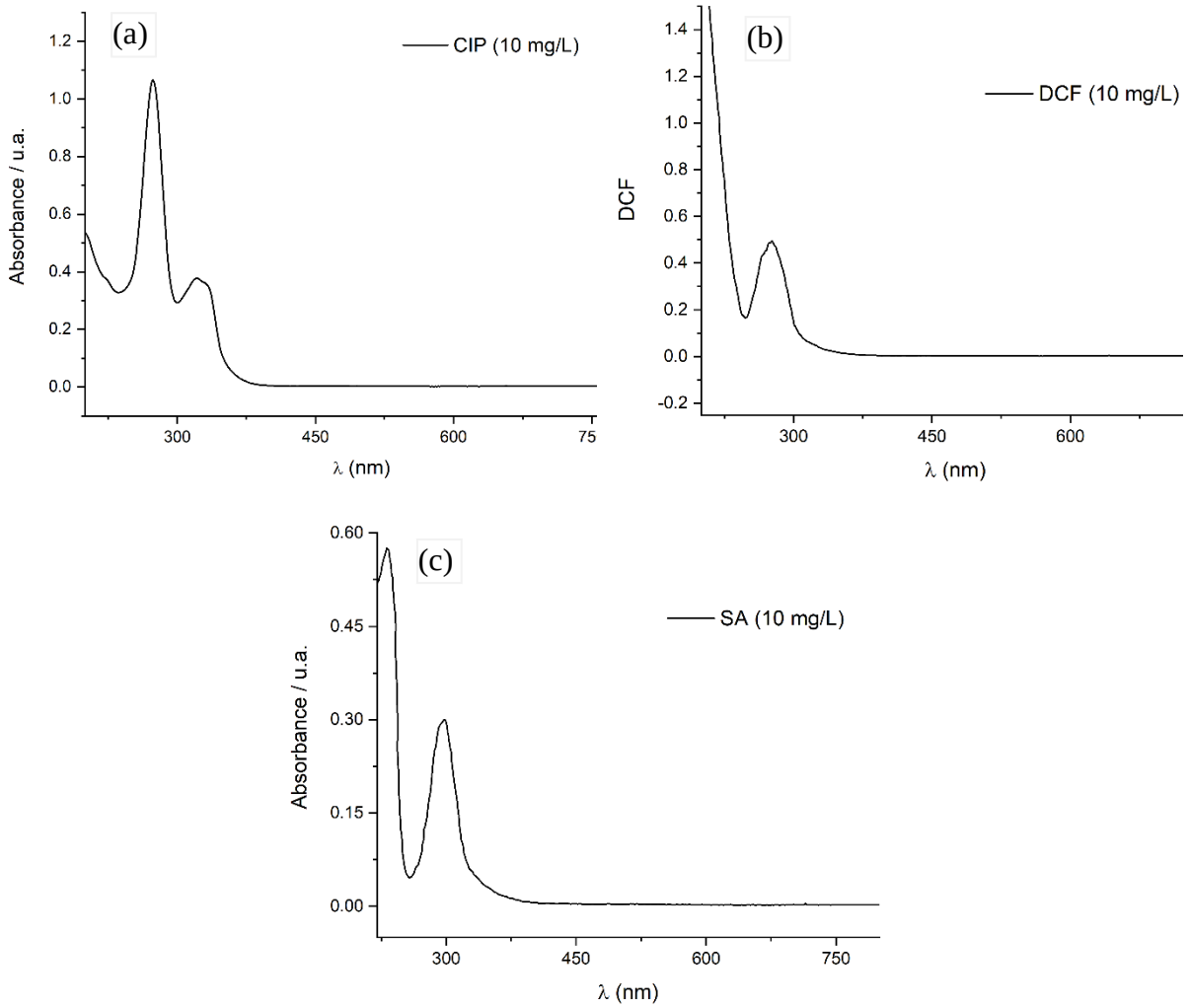

Figure S4. UV/Vis Absorbance spectra of (a) ciprofloxacin (CIP), (b) diclofenac (DCF), and (c) salicylic acid (SA).

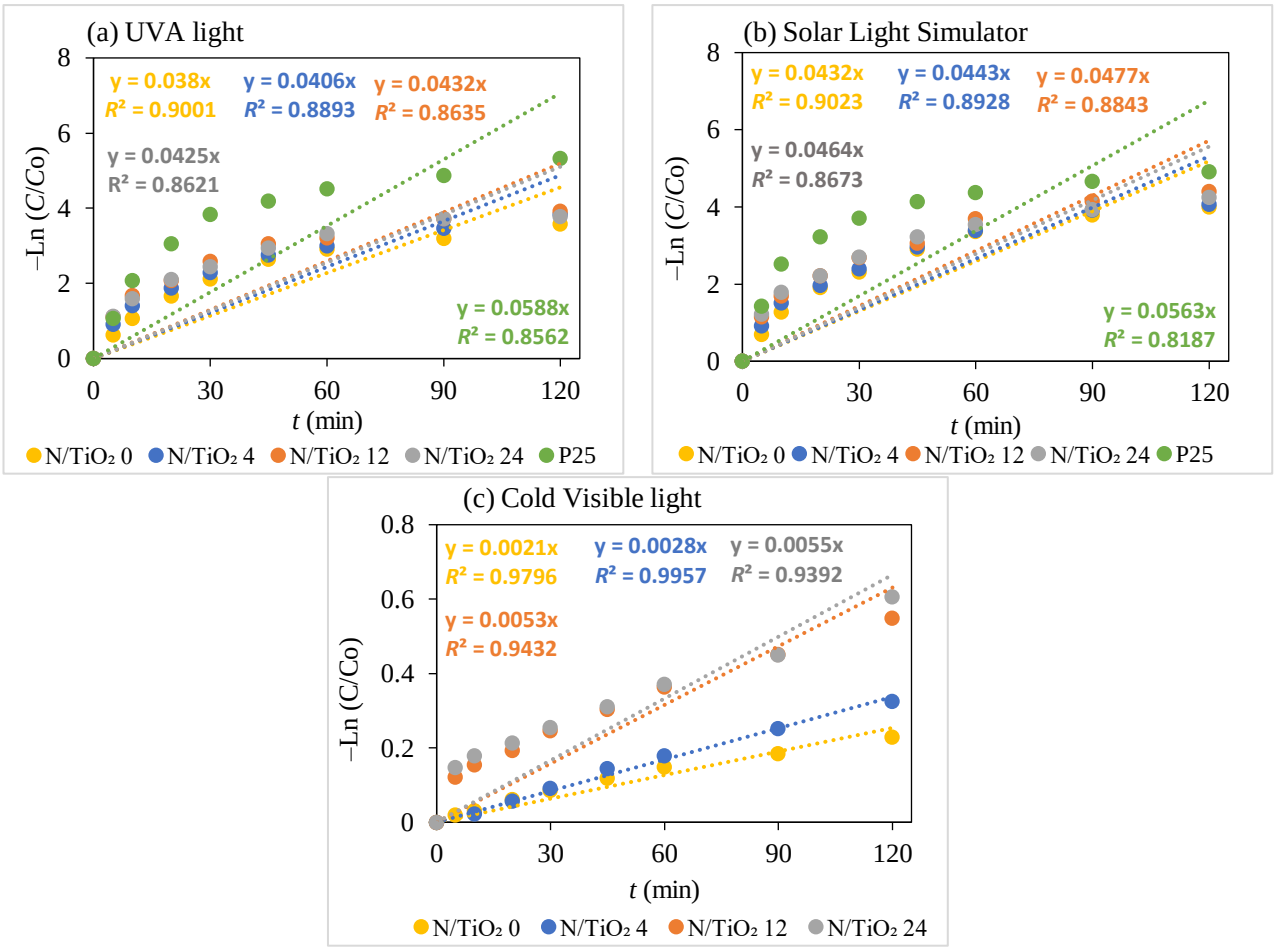

Figure S5. Pseudo-first order kinetic rate of the photocatalytic degradation of ciprofloxacin by Degussa P25 TiO_2 and N/TiO_2 samples under (a) UVA light (lamp I), (b) solar light simulator lamp (II), and (c) cold visible light (lamp III).

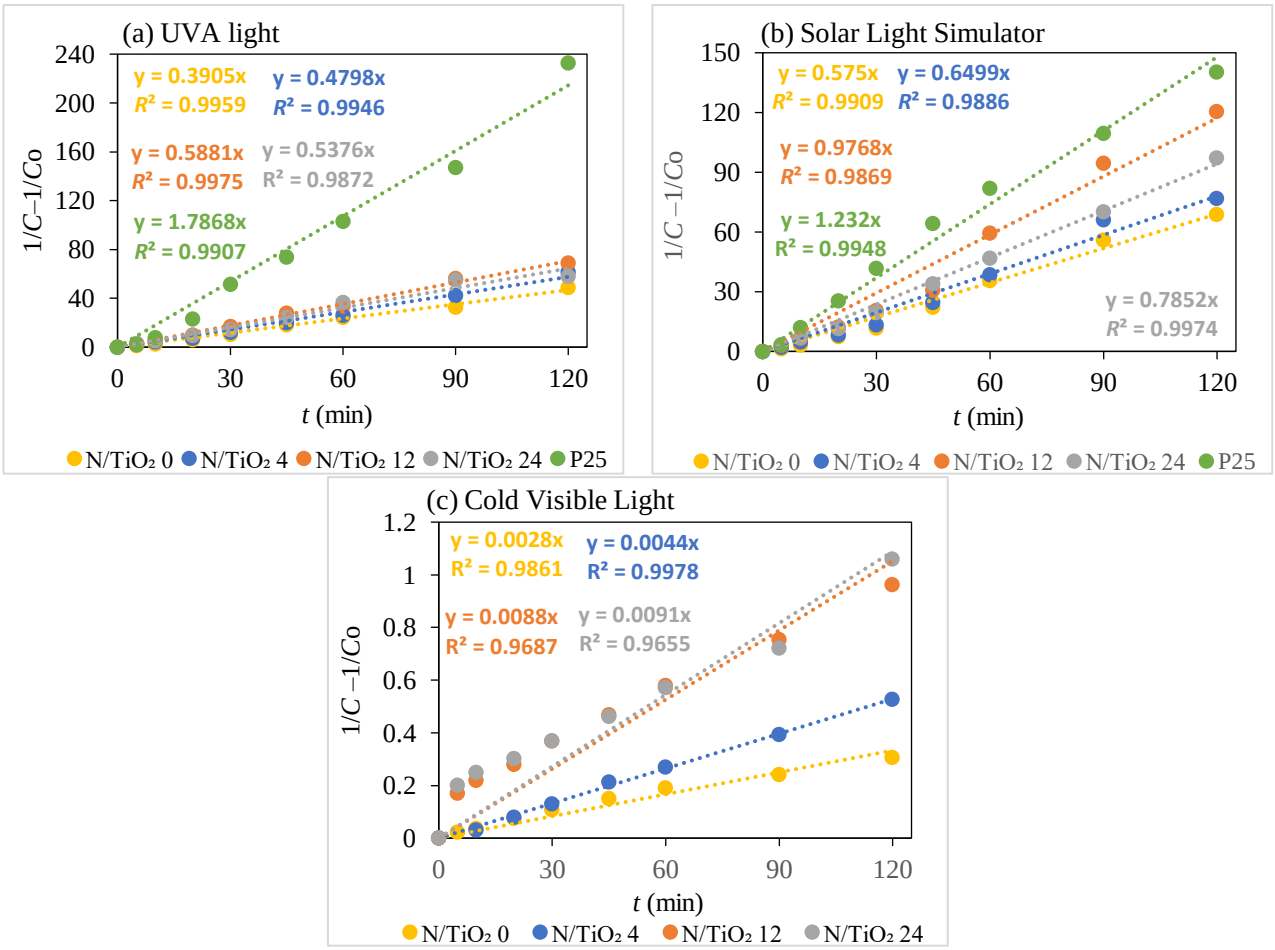

Figure S6. Second order kinetic rate of the photocatalytic degradation of ciprofloxacin by Degussa P25 TiO_2 and N/TiO_2 samples under (a) UVA light (lamp I), (b) solar light simulator lamp (II), and (c) Cold visible light (lamp III).

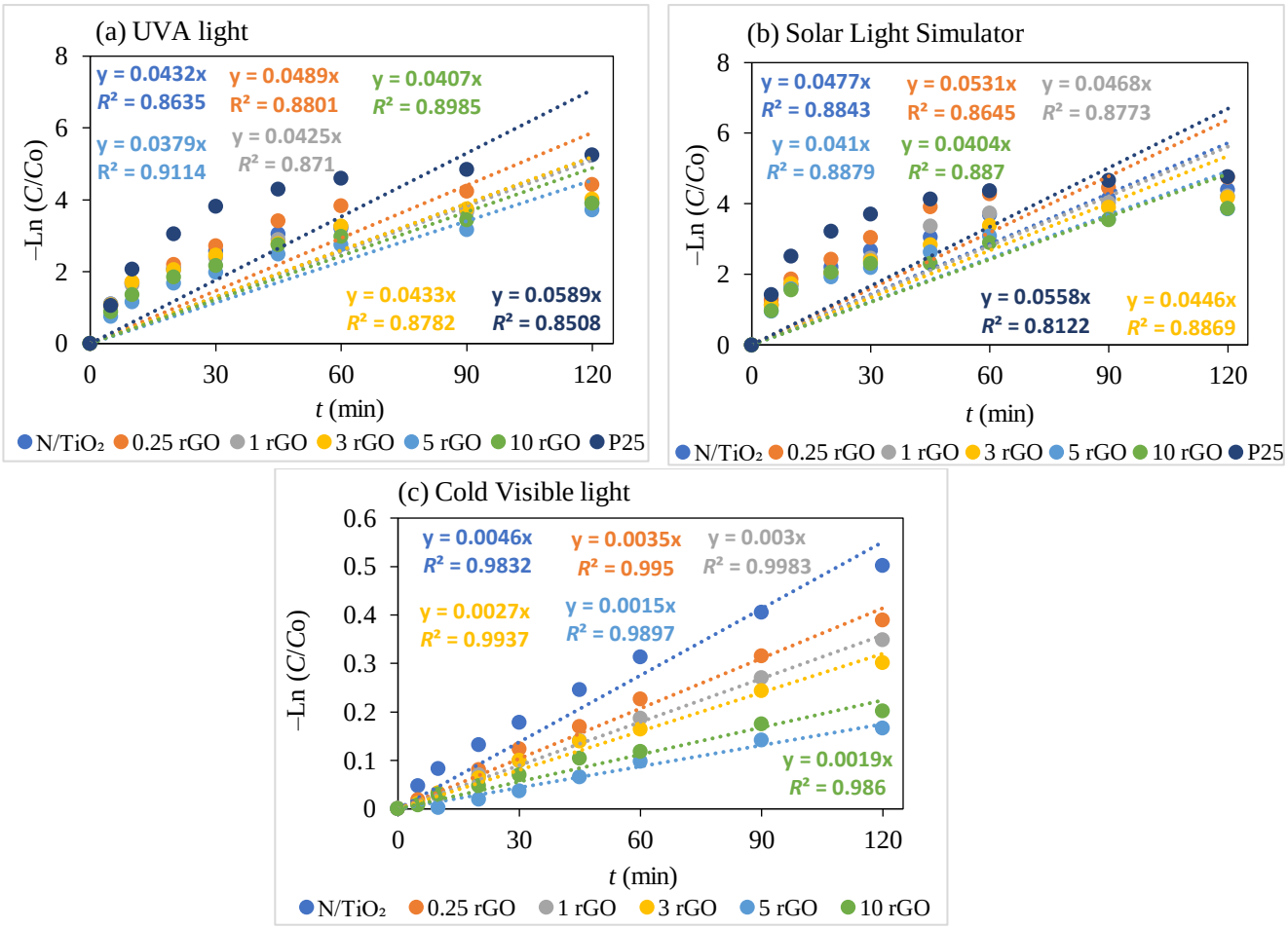

Figure S7. Pseudo-first order kinetic rate of the photocatalytic degradation of ciprofloxacin by Degussa P25 N/TiO_2 and N/TiO_2/rGO samples under (a) UVA light (lamp I), (b) solar light simulator lamp (II), and (c) cold visible light (lamp III).

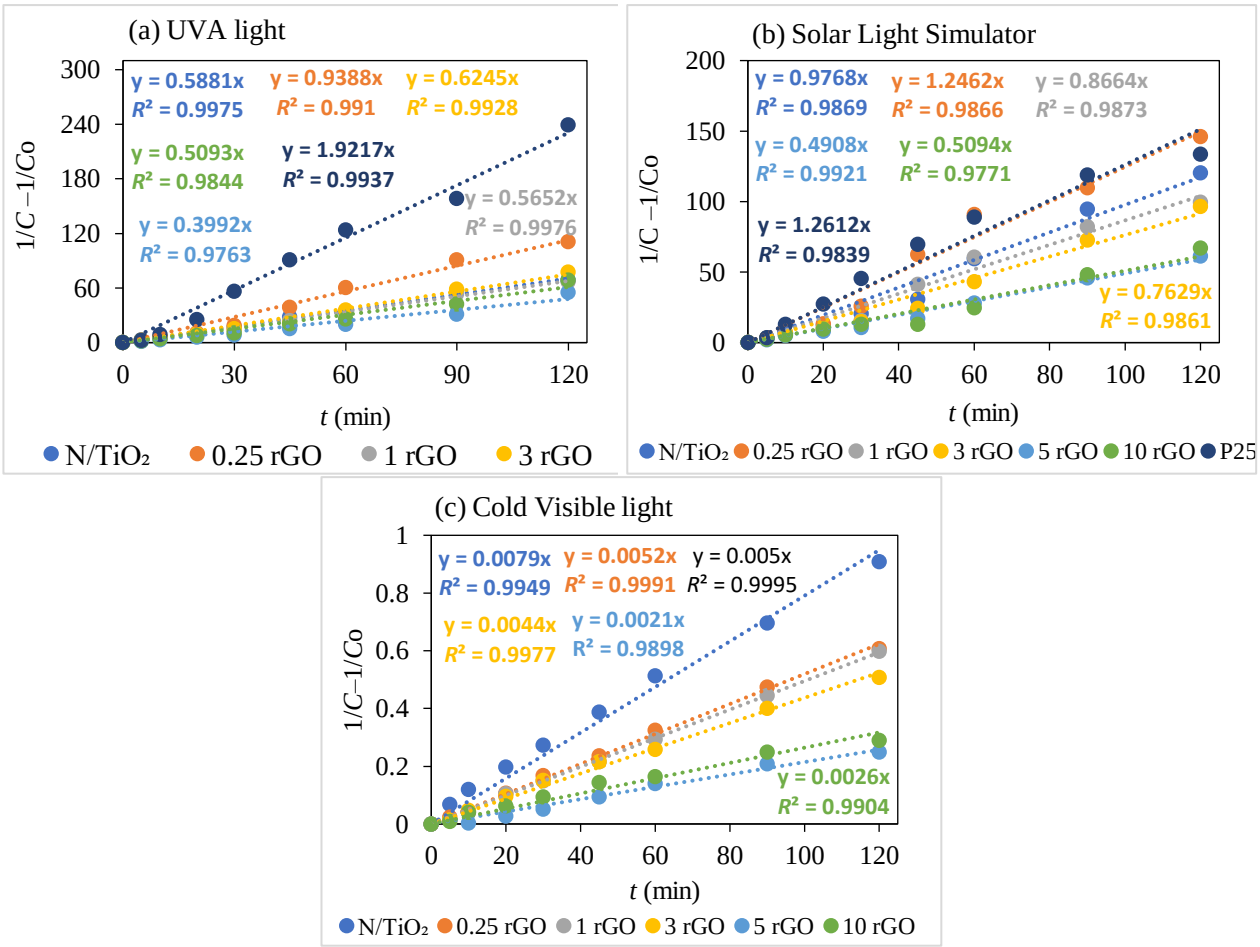

Figure S8. Second order kinetic rate of the photocatalytic degradation of ciprofloxacin by Degussa P25 N/TiO_2 and N/TiO_2/rGO samples under (a) UVA light (lamp I), (b) solar light simulator lamp (II), and (c) Cold visible light (lamp III).

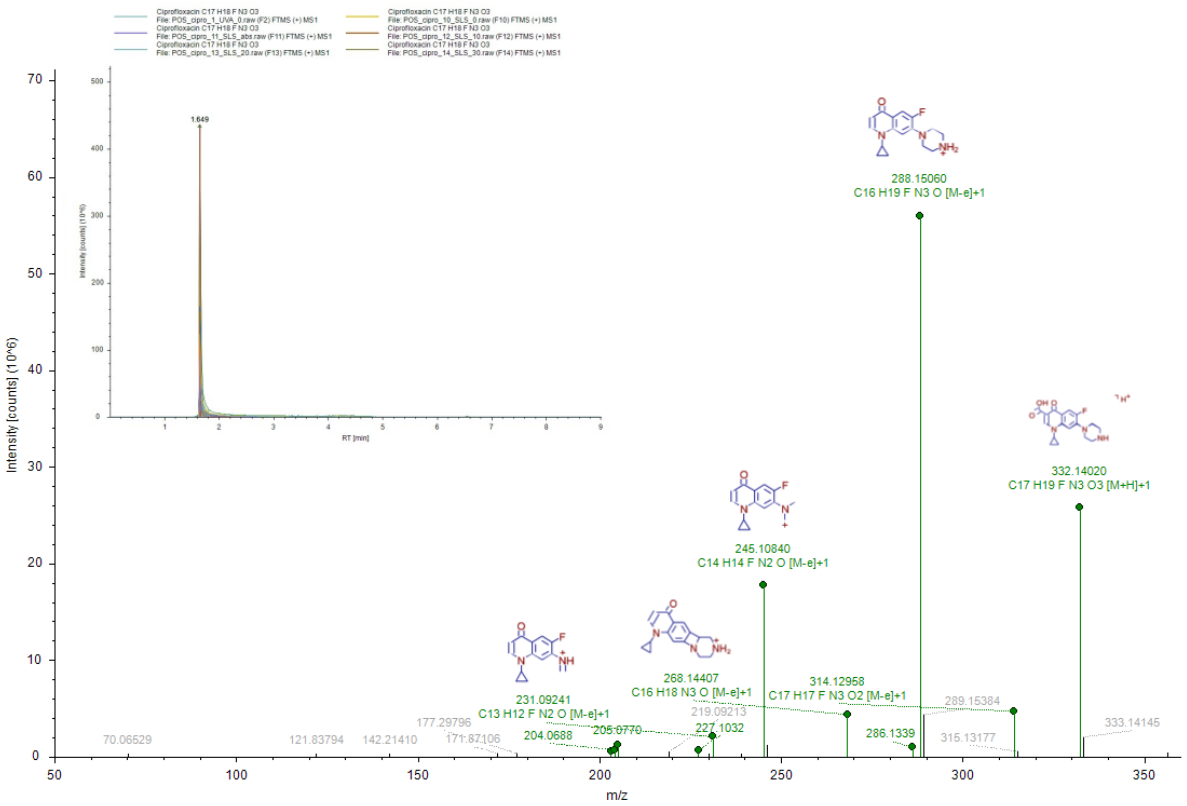

Figure S9. MS^2 mass spectra fragment ions of ciprofloxacin; inset, peak retention time.

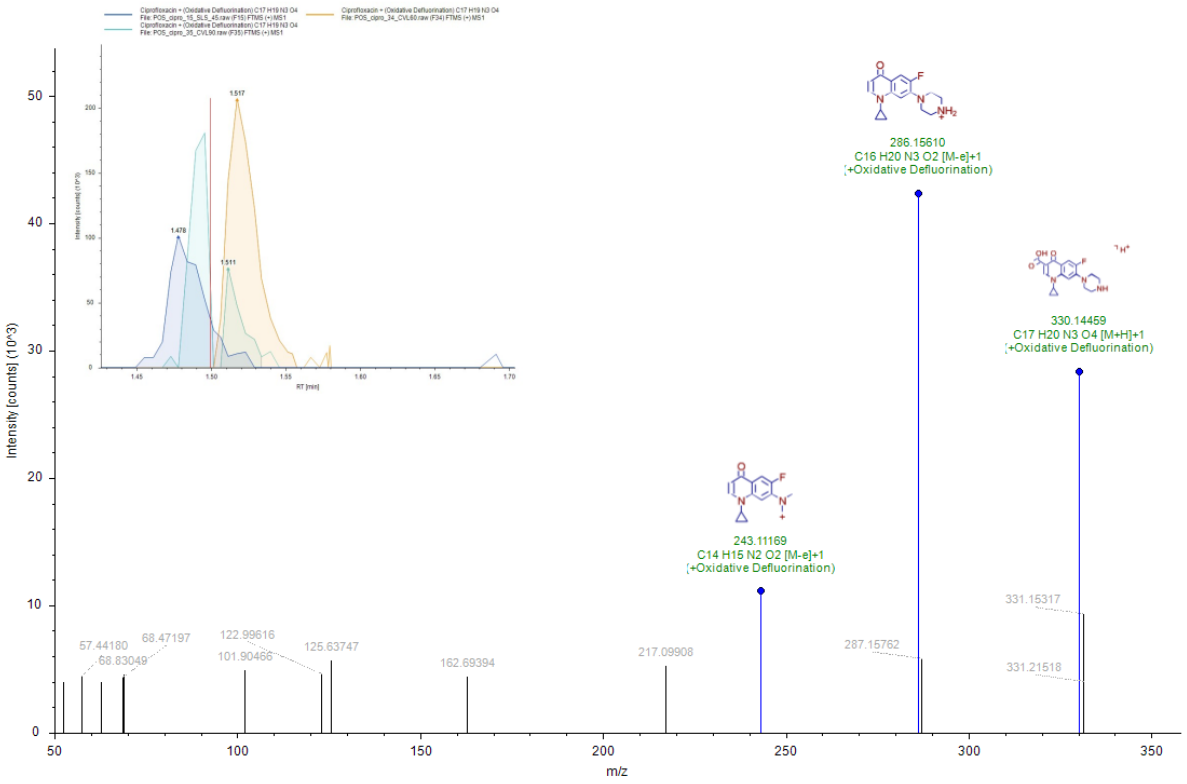

Figure S10. MS^2 mass spectra fragment ions of TPC1; inset, peak retention time.

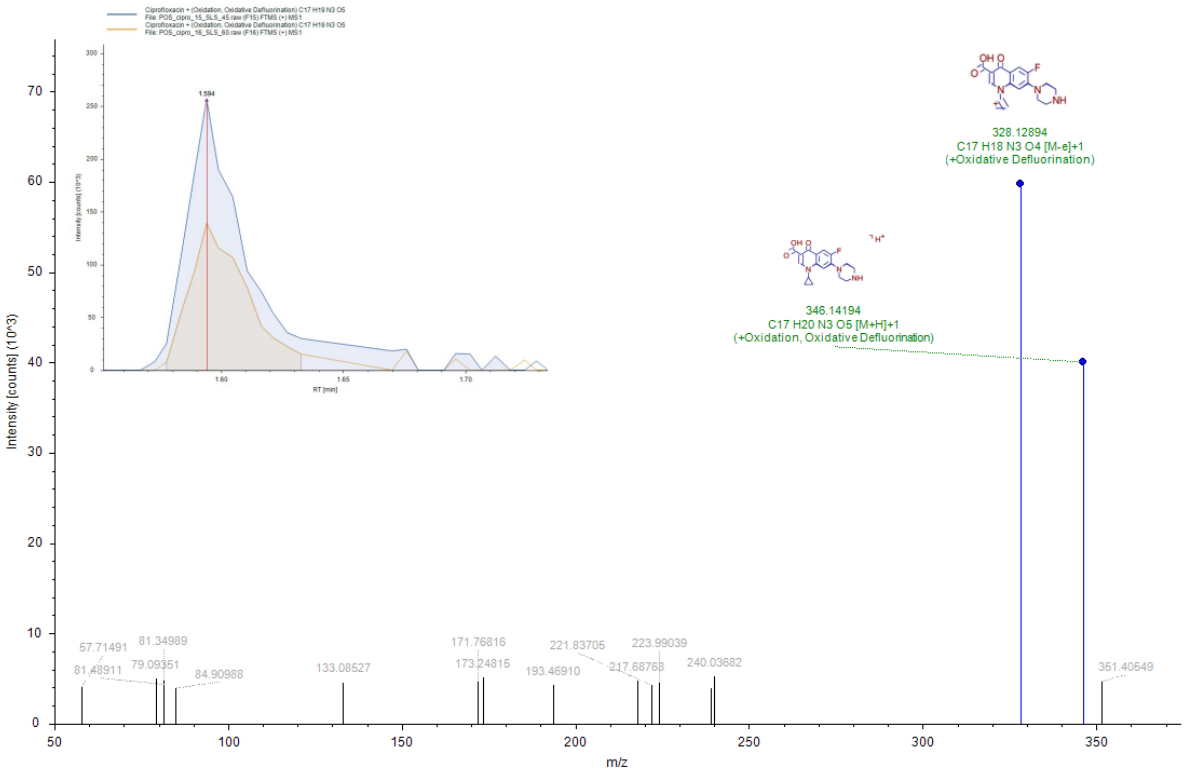

Figure S11. MS^2 mass spectra fragment ions of TPC2; inset, peak retention time.

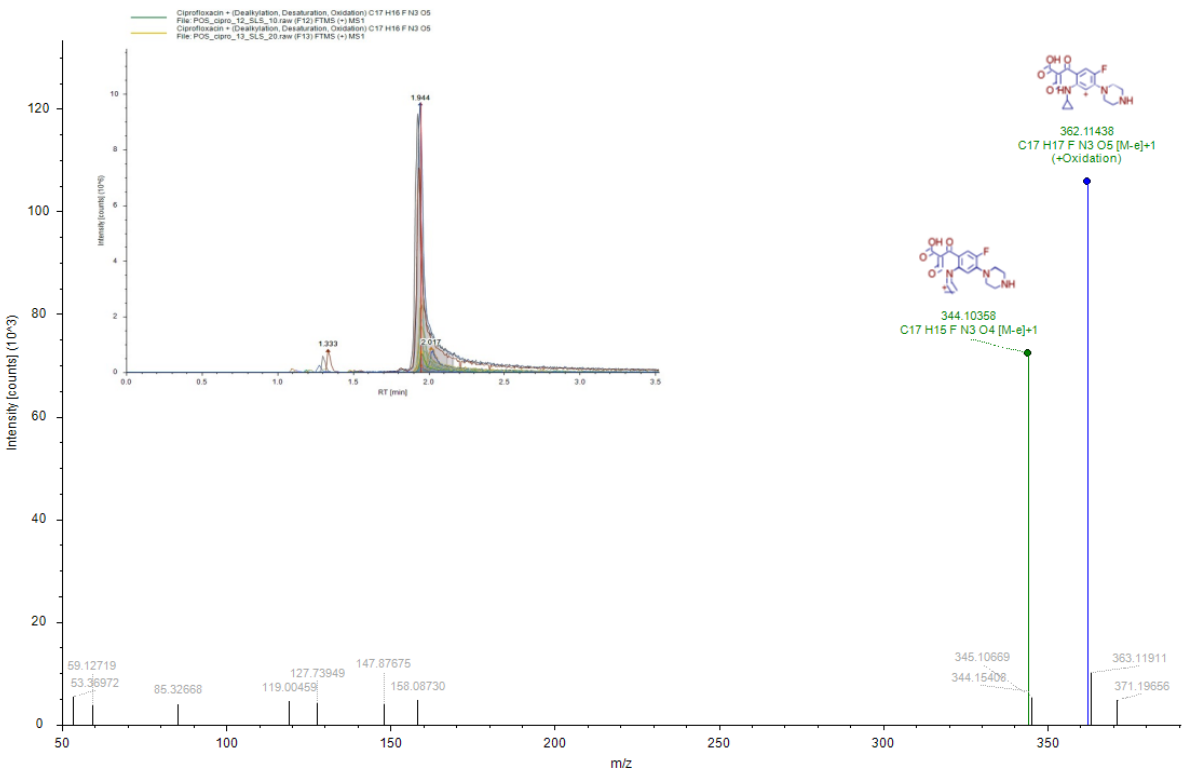

Figure S12. MS^2 mass spectra fragment ions of TPC3; inset, peak retention time.

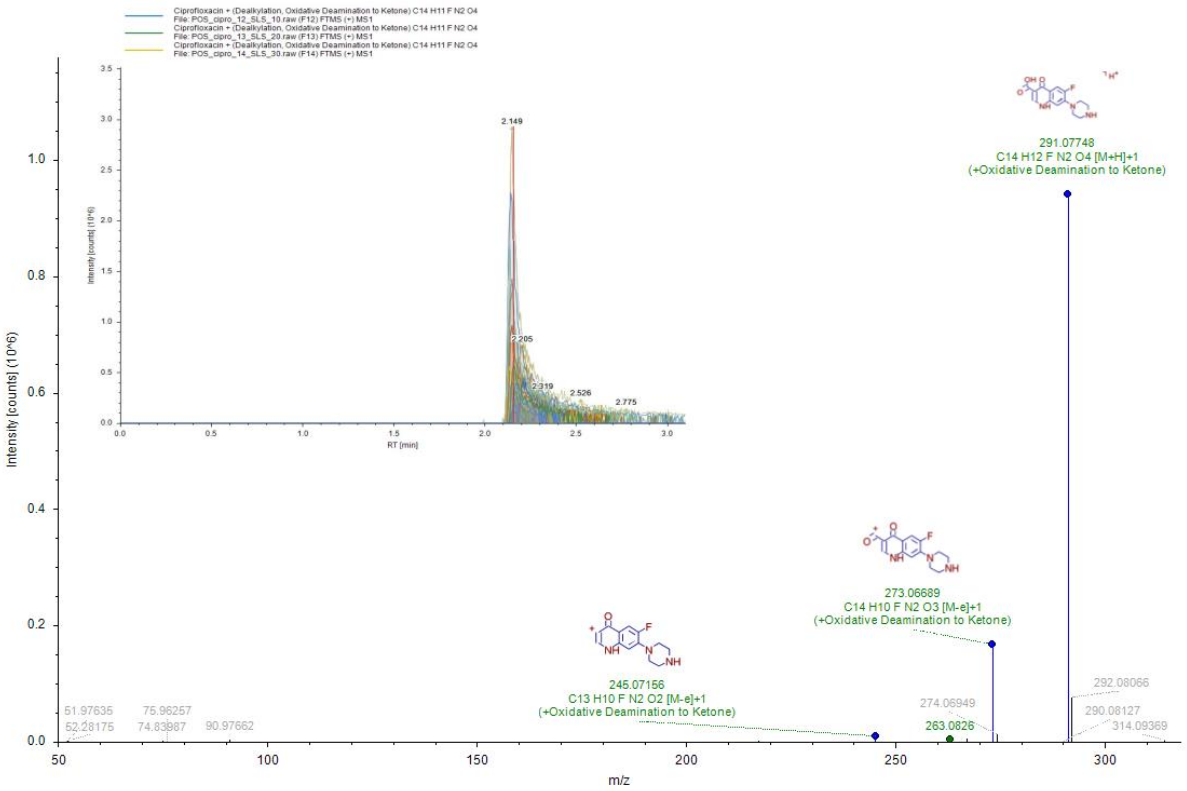

Figure S13. MS^2 mass spectra fragment ions of TPC4; inset, peak retention time.

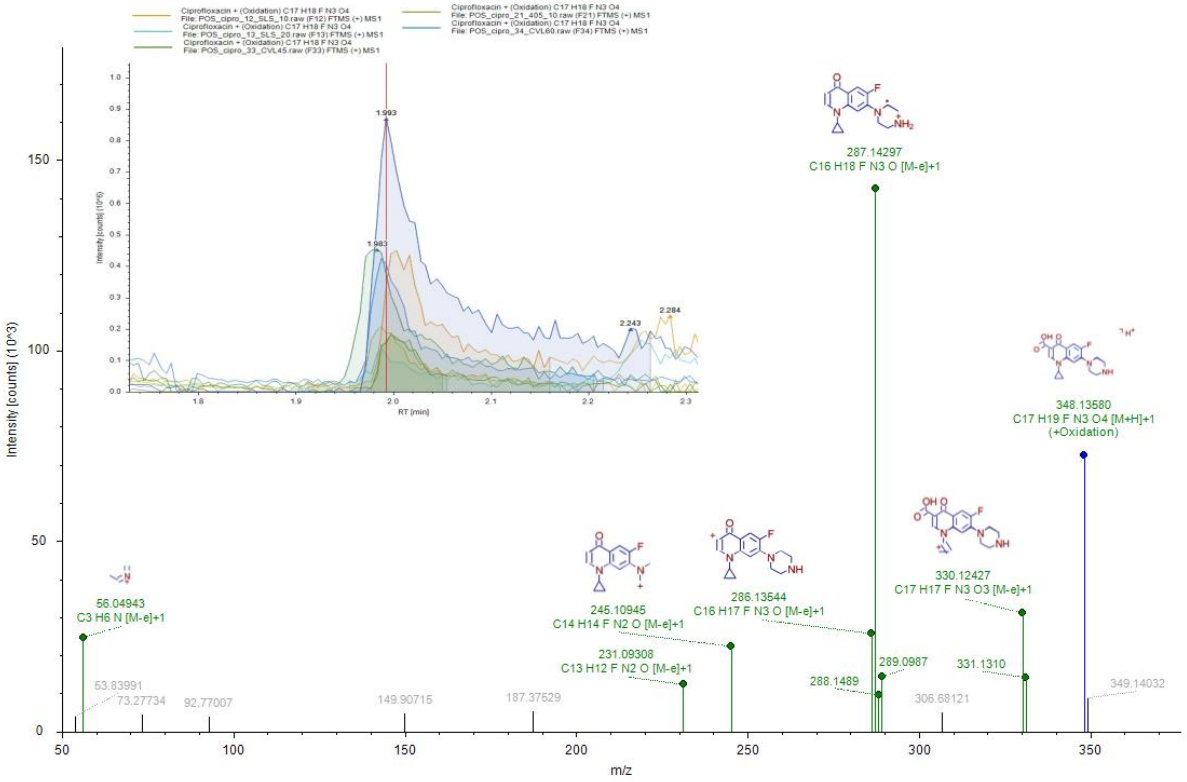

Figure S14. MS^2 mass spectra fragment ions of TPC5; inset, peak retention time.

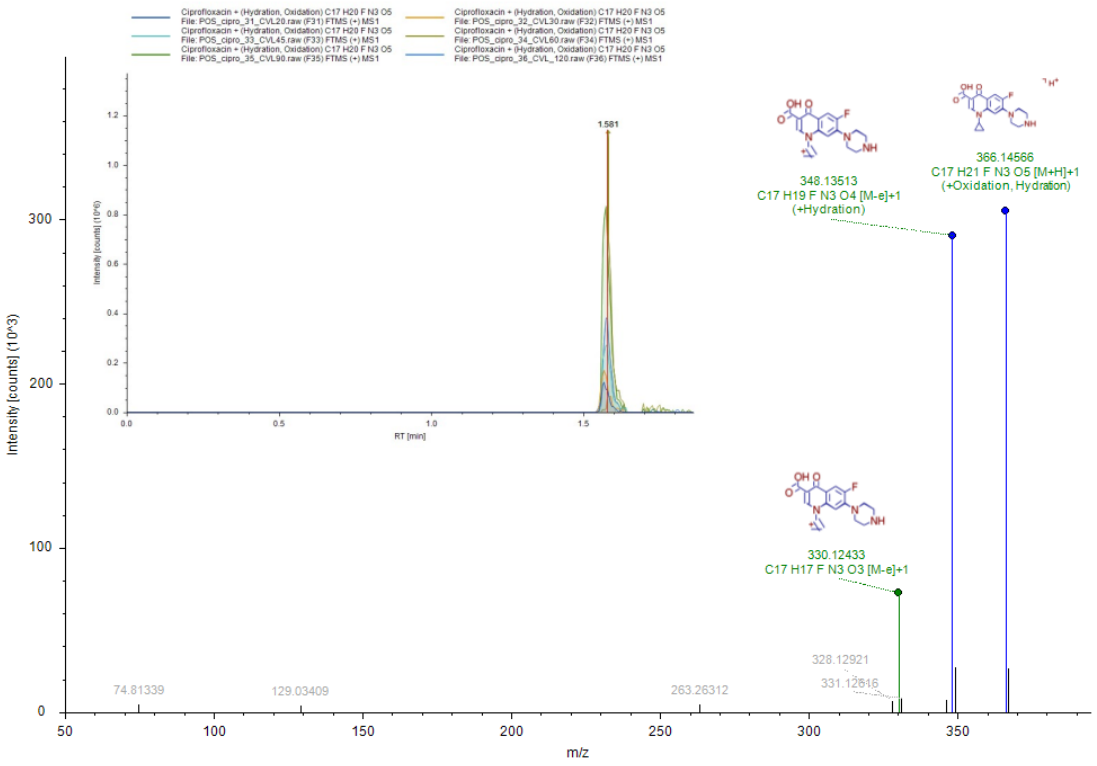

Figure S15. MS^2 mass spectra fragment ions of TPC6; inset, peak retention time.

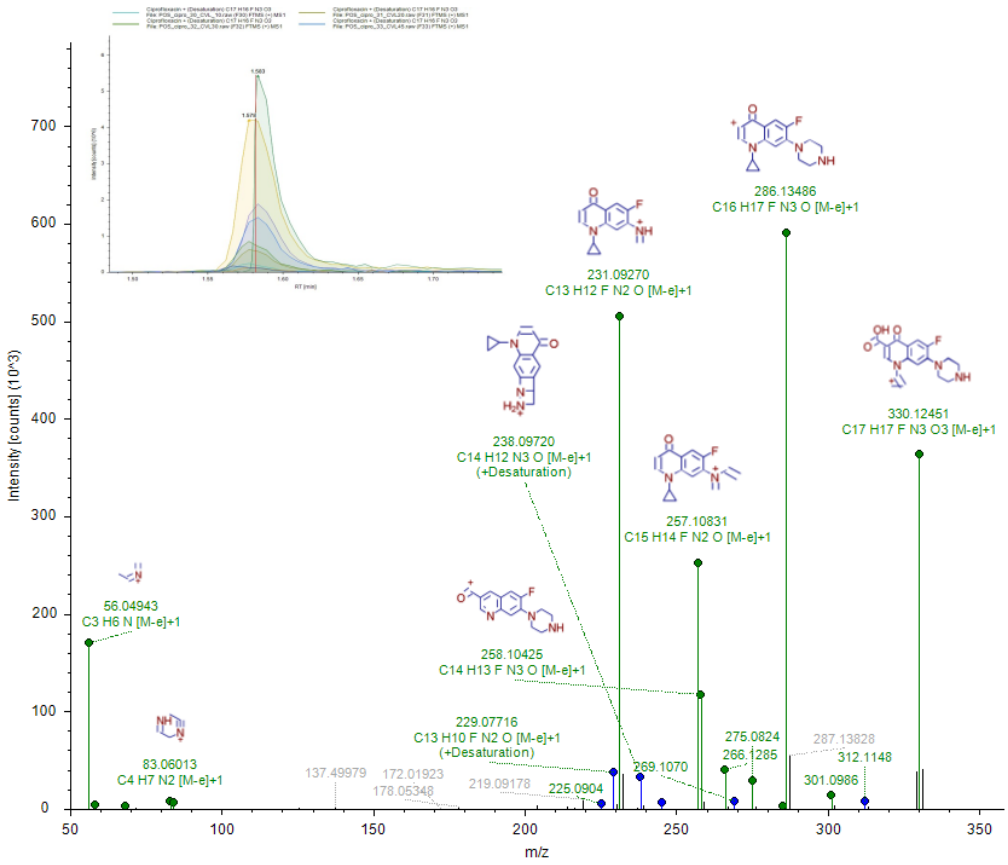

Figure S16. MS^2 mass spectra fragment ions of TPC7; inset, peak retention time.

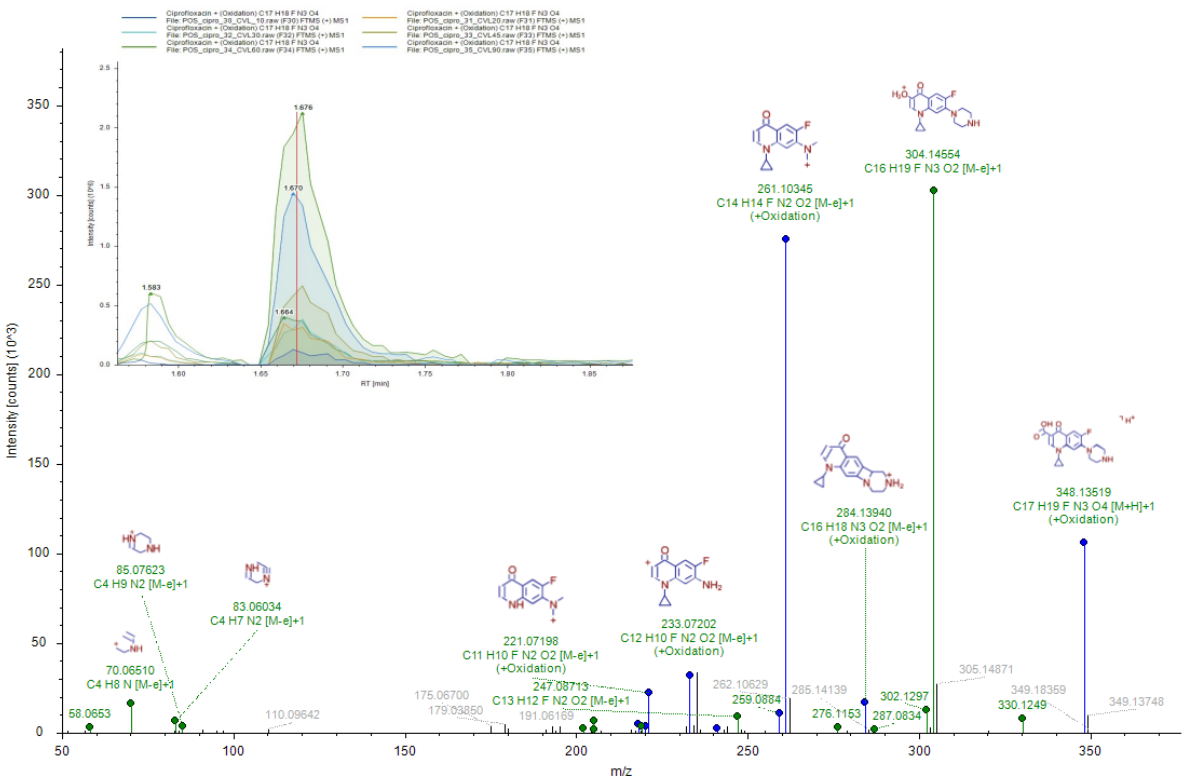

Figure S17. MS^2 mass spectra fragment ions of TPC8; inset, peak retention time.

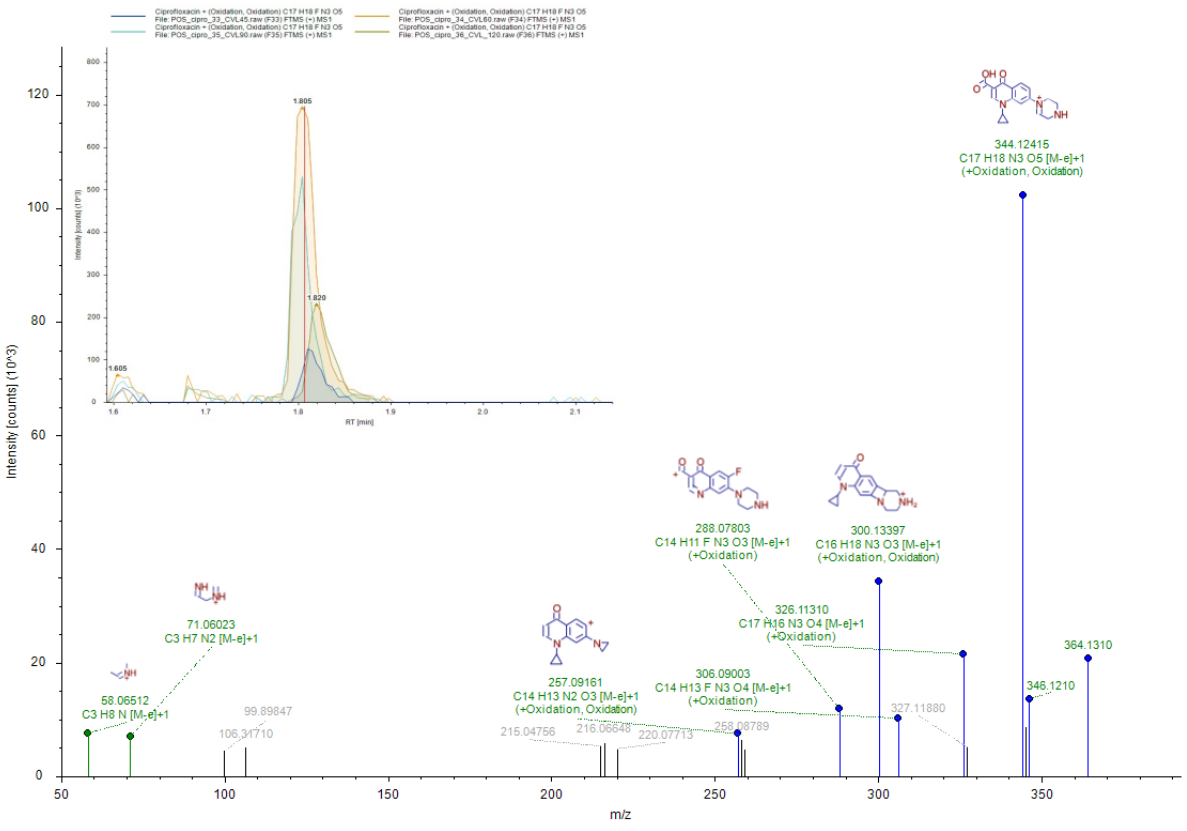

Figure S18. MS^2 mass spectra fragment ions of TPC9; inset, peak retention time.

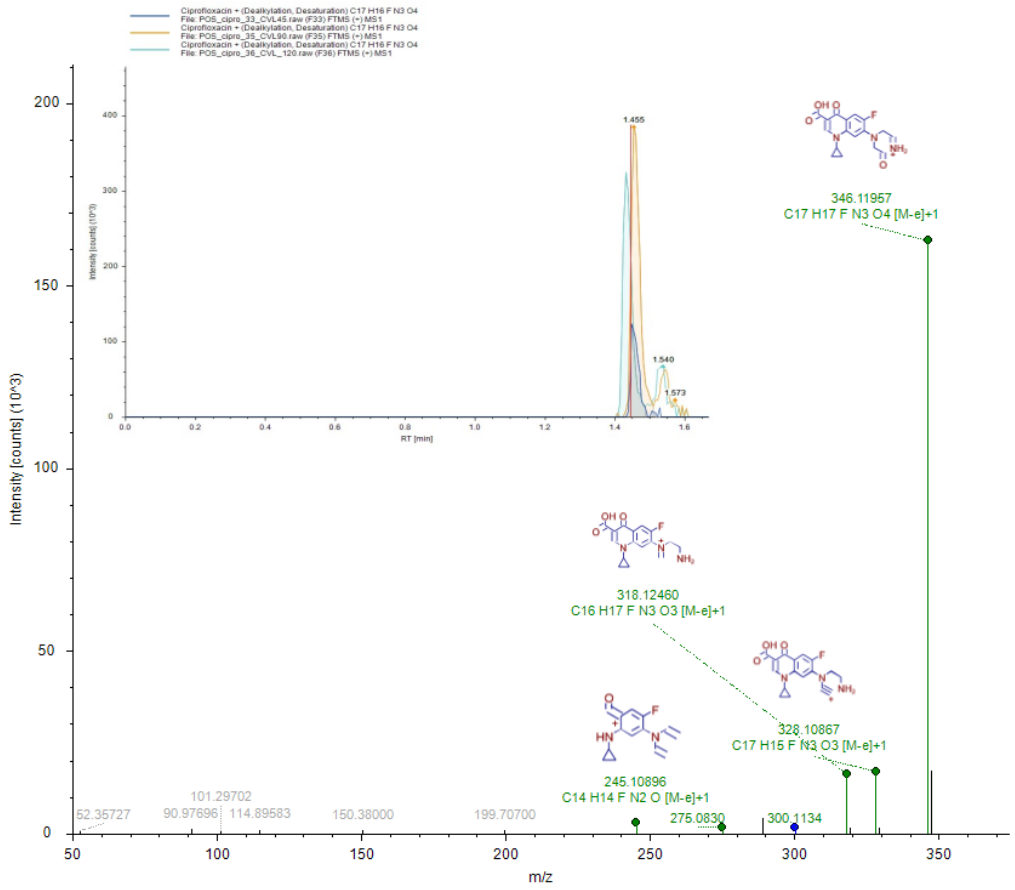

Figure S19. MS^2 mass spectra fragment ions of TPC10; inset, peak retention time.

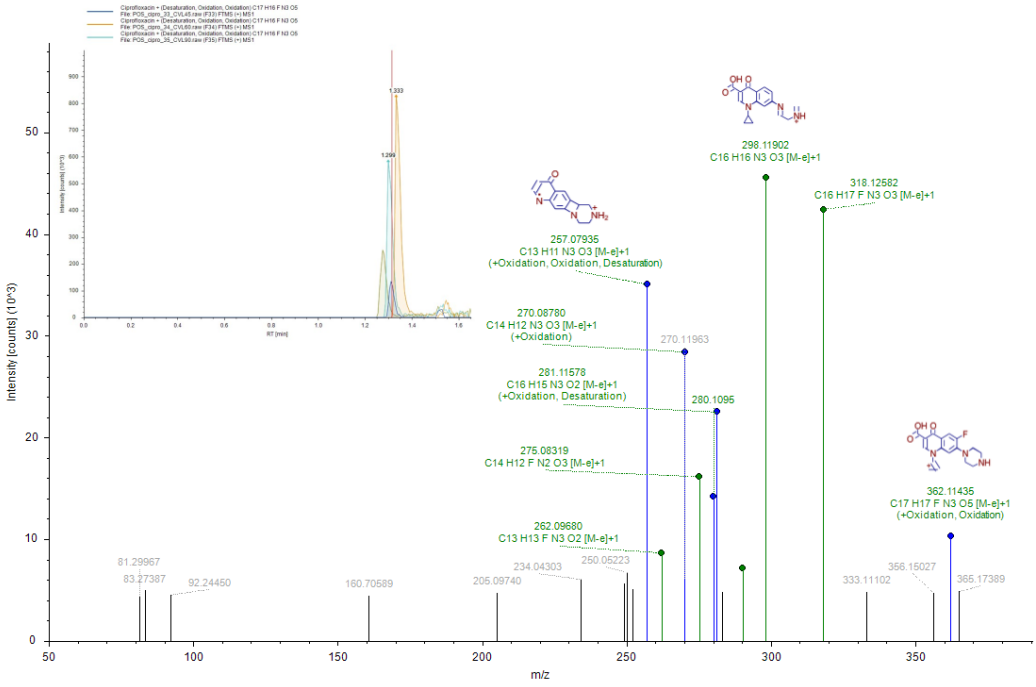

Figure S20. MS^2 mass spectra fragment ions of TPC11; inset, peak retention time.

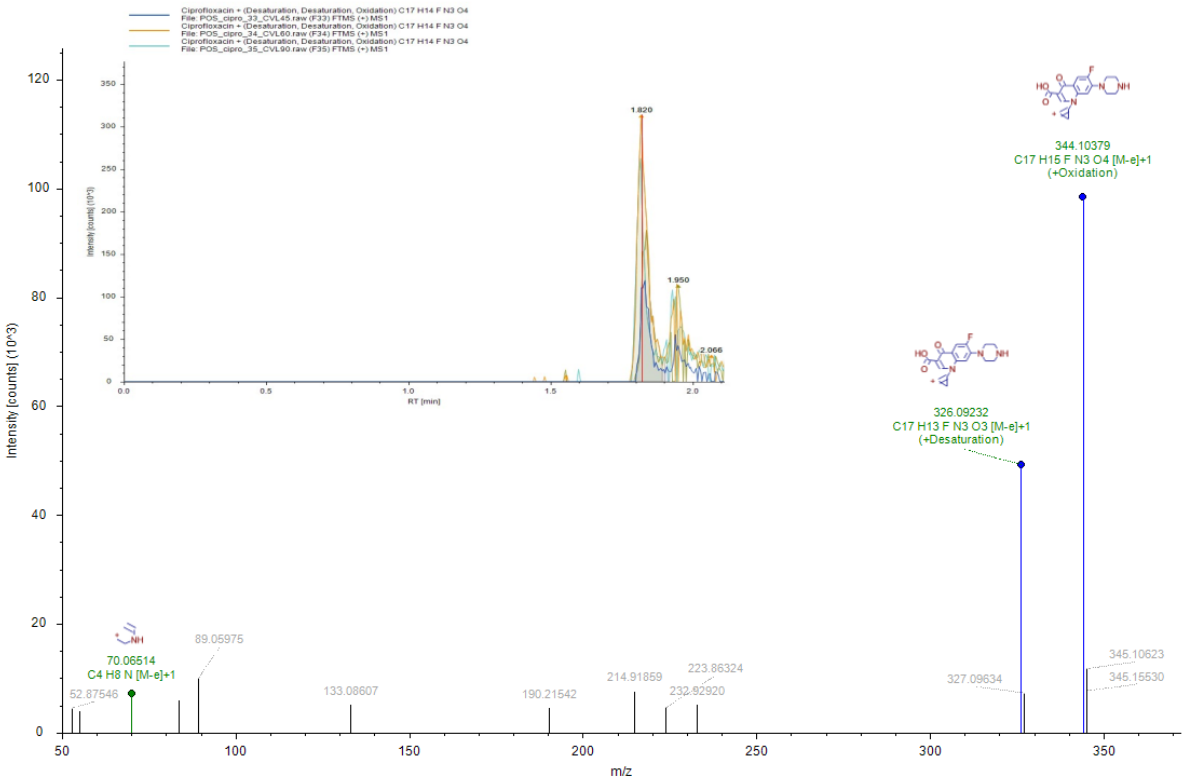

Figure S21. MS^2 mass spectra fragment ions of TPC12; inset, peak retention time.

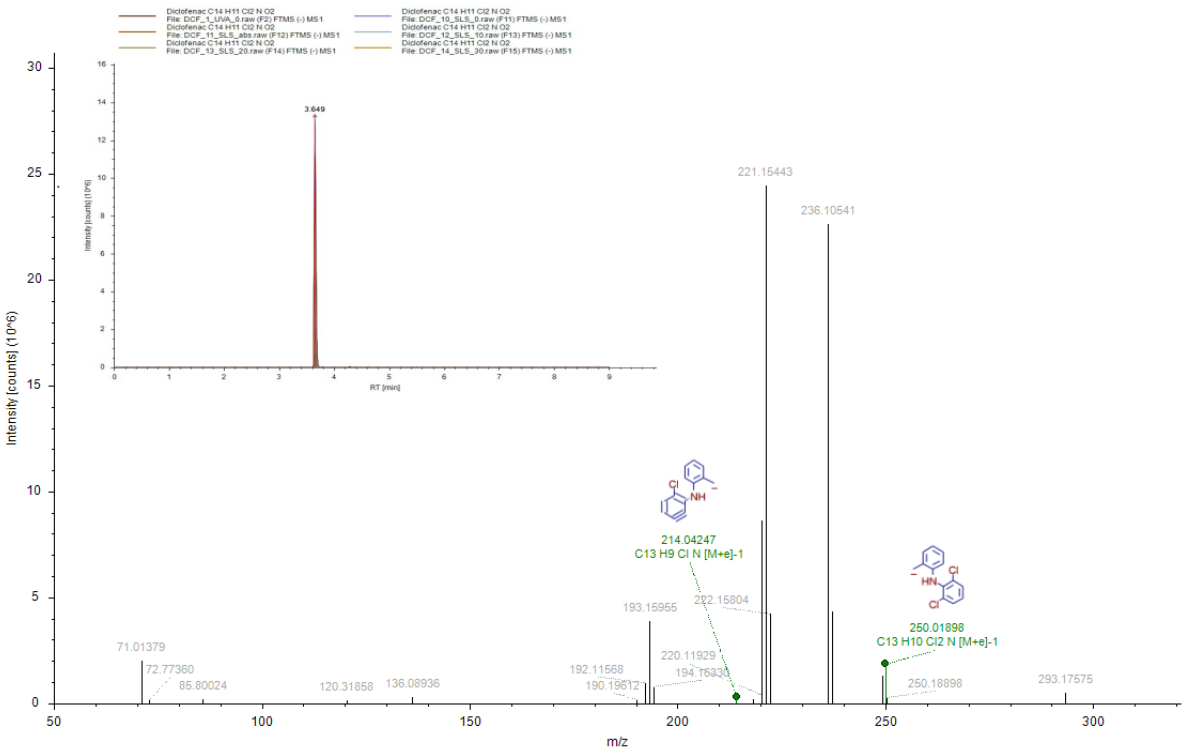

Figure S22. MS^2 mass spectra fragment ions of diclofenac; inset, peak retention time.

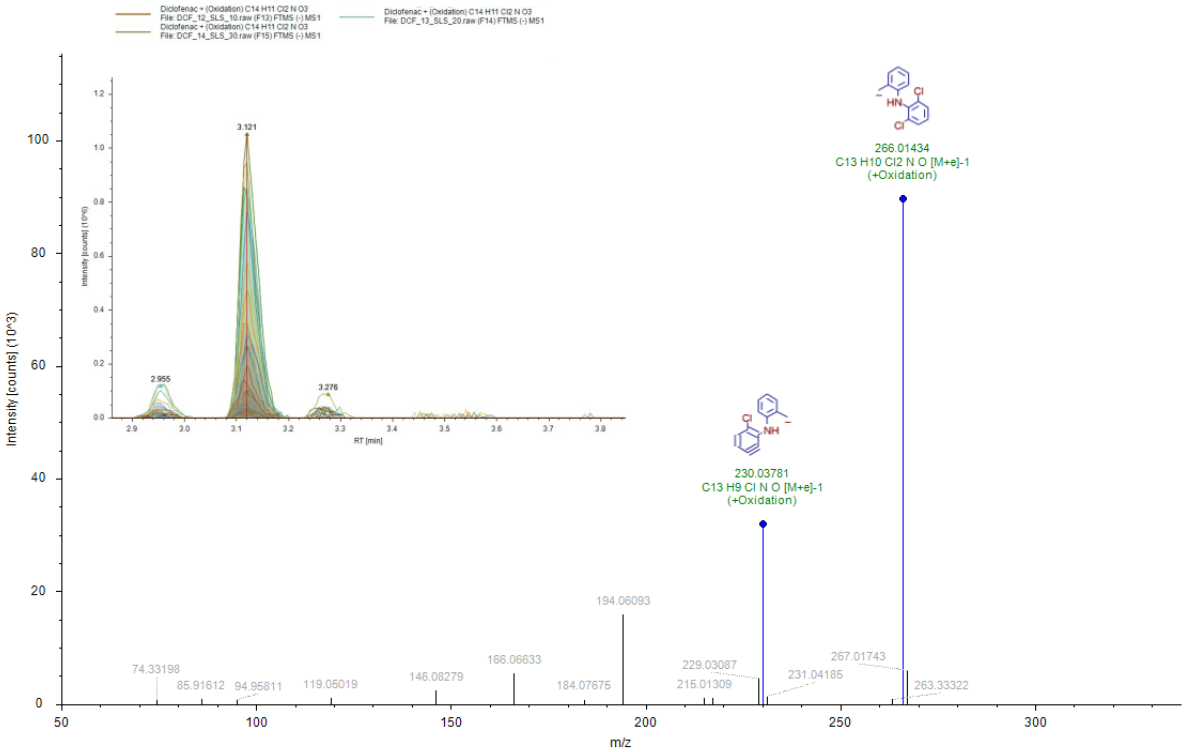

Figure S23. MS^2 mass spectra fragment ions of TPD1; inset, peak retention time.

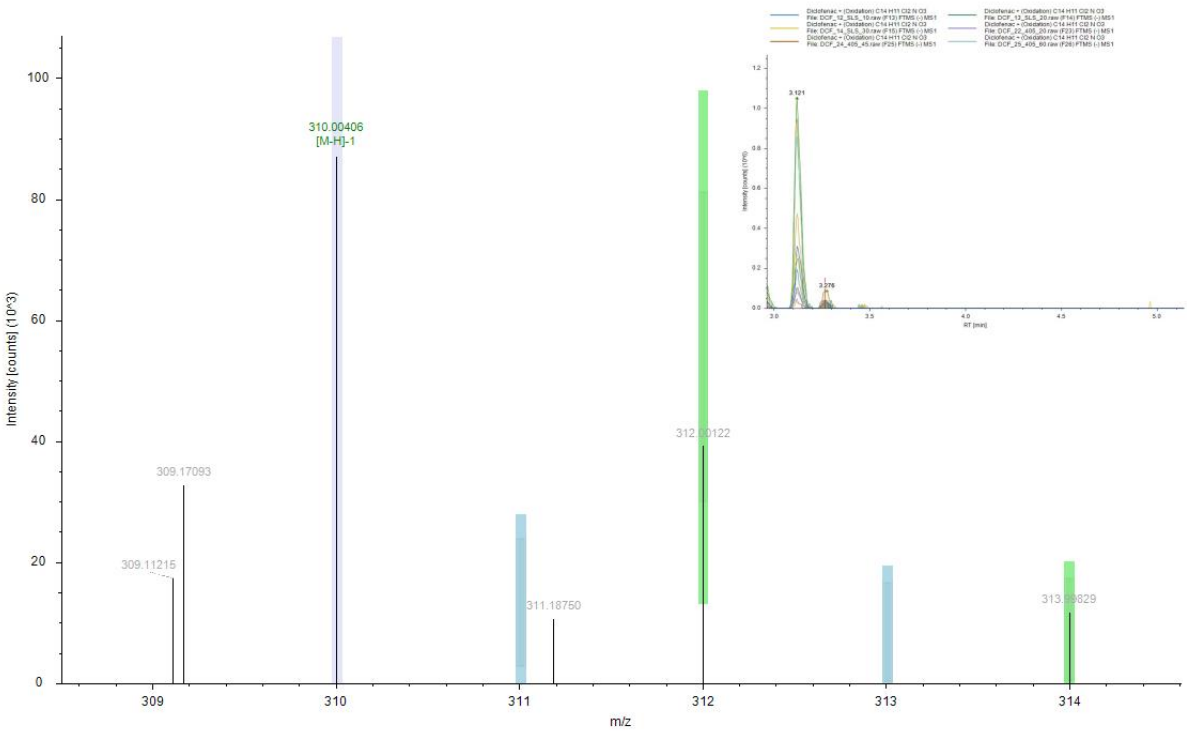

Figure S24. MS^1 mass spectra fragment ions of TPD2; inset, peak retention time.

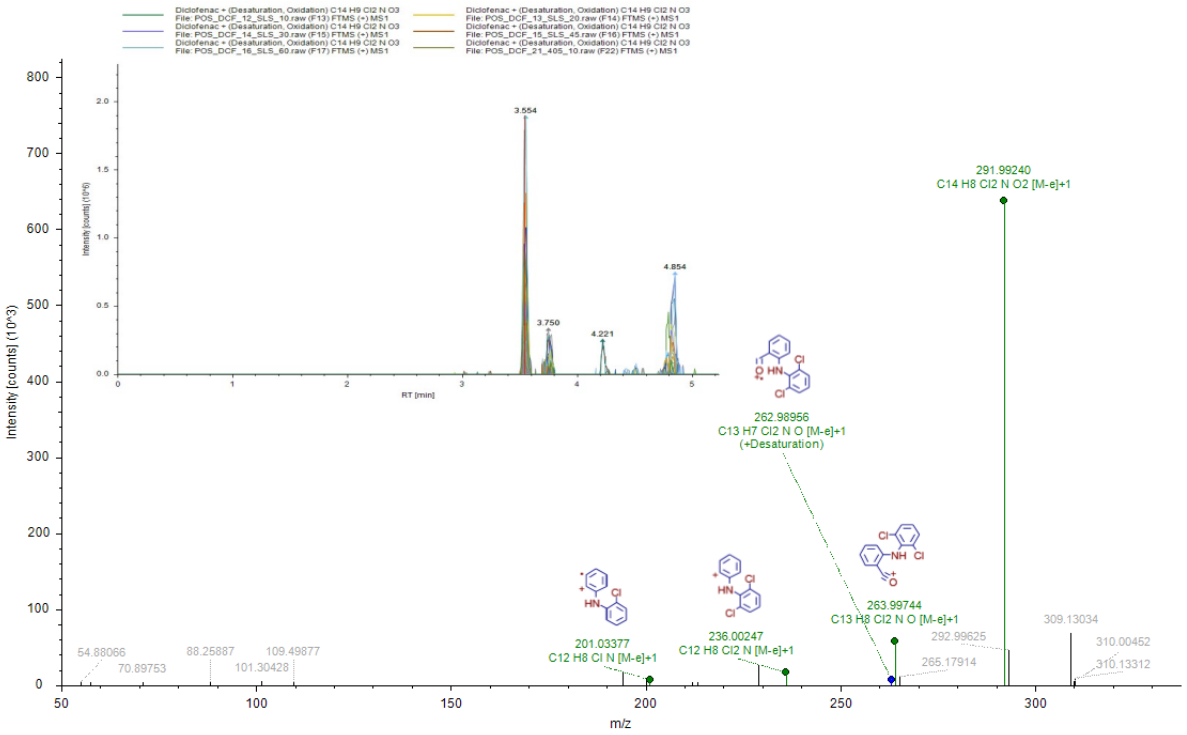

Figure S25. MS^2 mass spectra fragment ions of TPD3; inset, peak retention time.

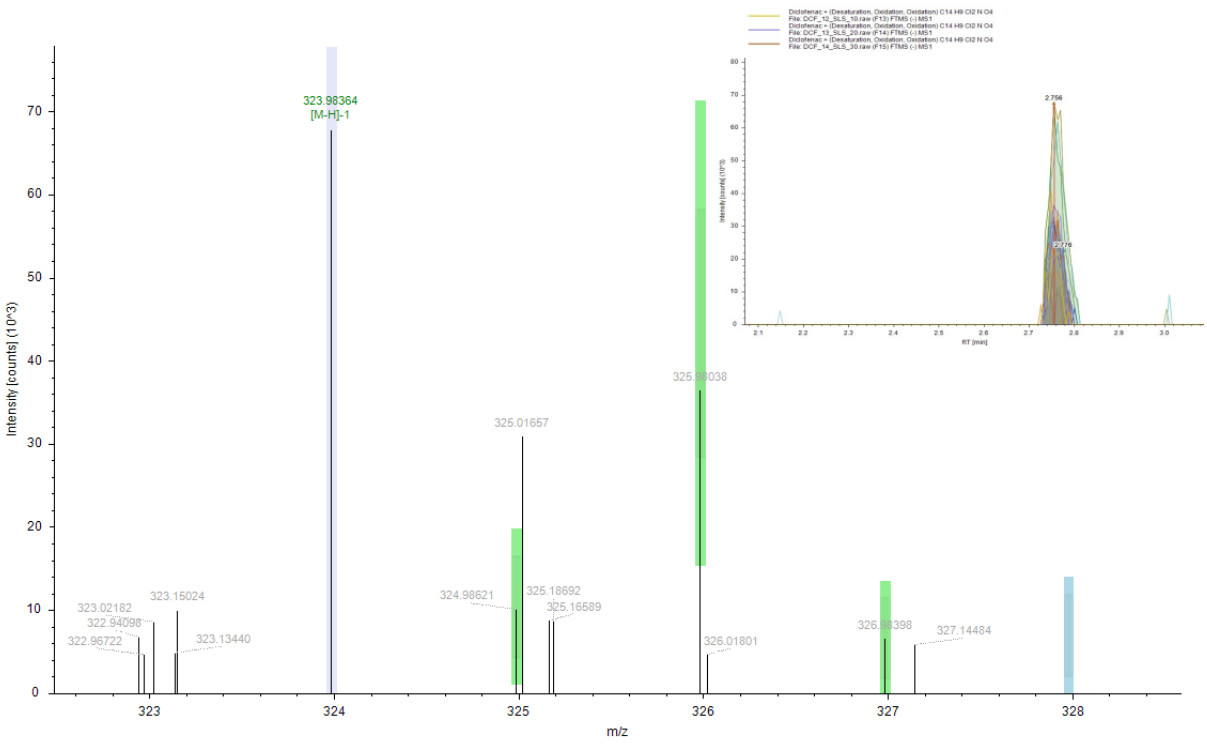

Figure S26. MS^1 mass spectra fragment ions of TPD4; inset, peak retention time.

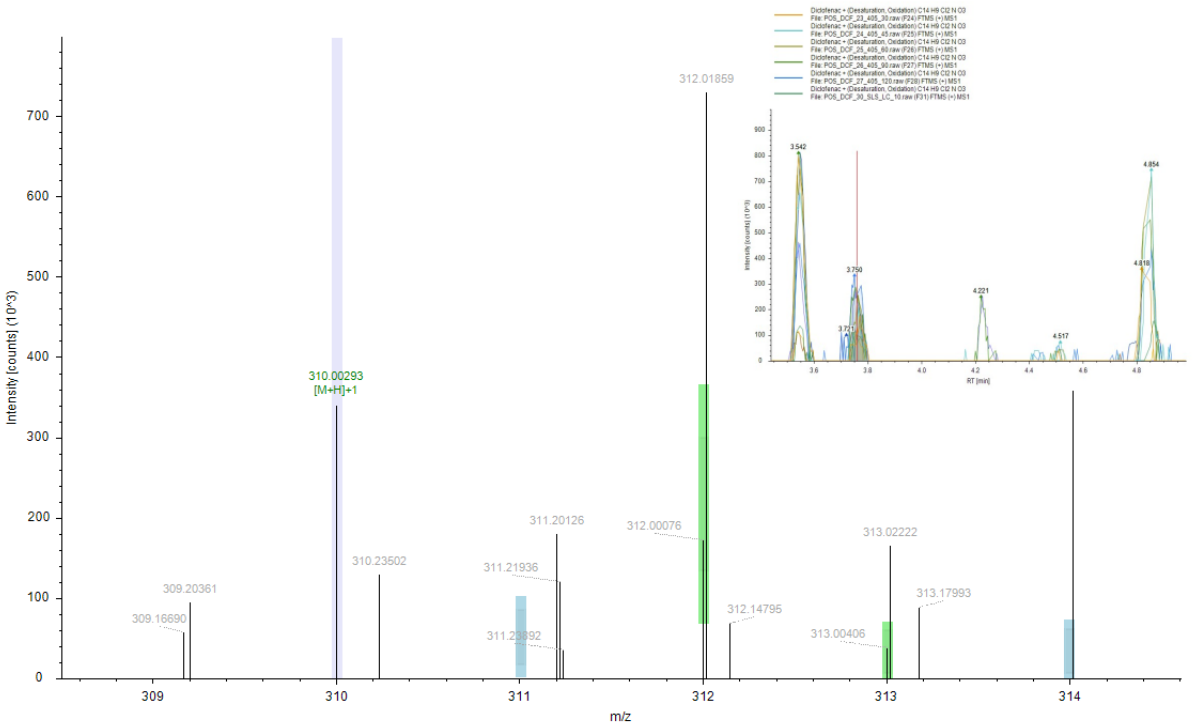

Figure S27. MS[1] mass spectra fragment ions of TPD5; inset, peak retention time.

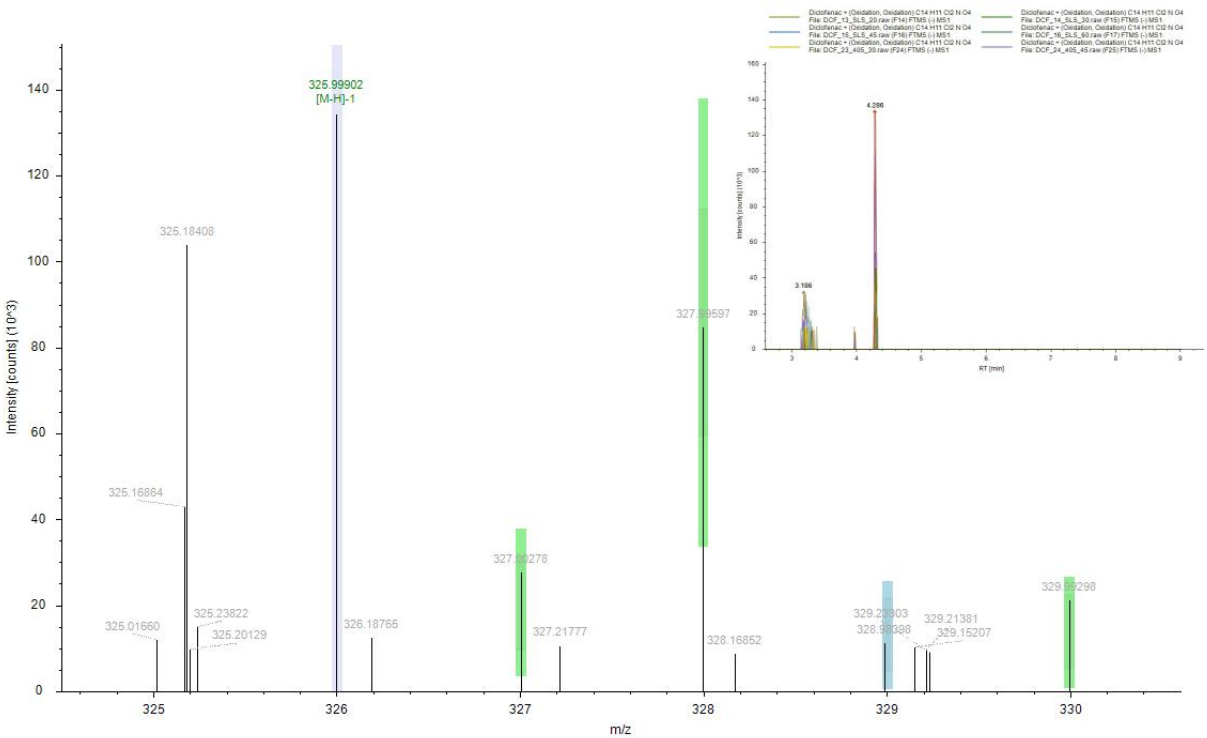

Figure S28. MS[1] mass spectra fragment ions of TPD6; inset, peak retention time.

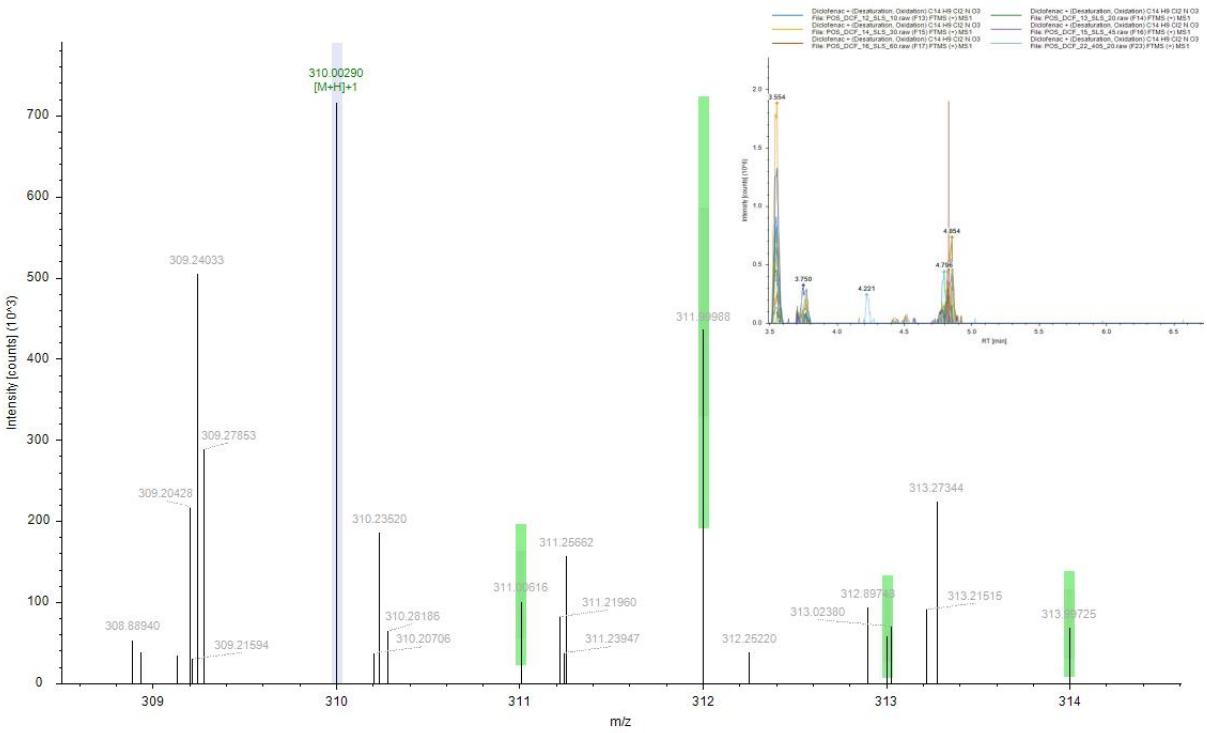

Figure S29. MS[1] mass spectra fragment ions of TPD7; inset, peak retention time.

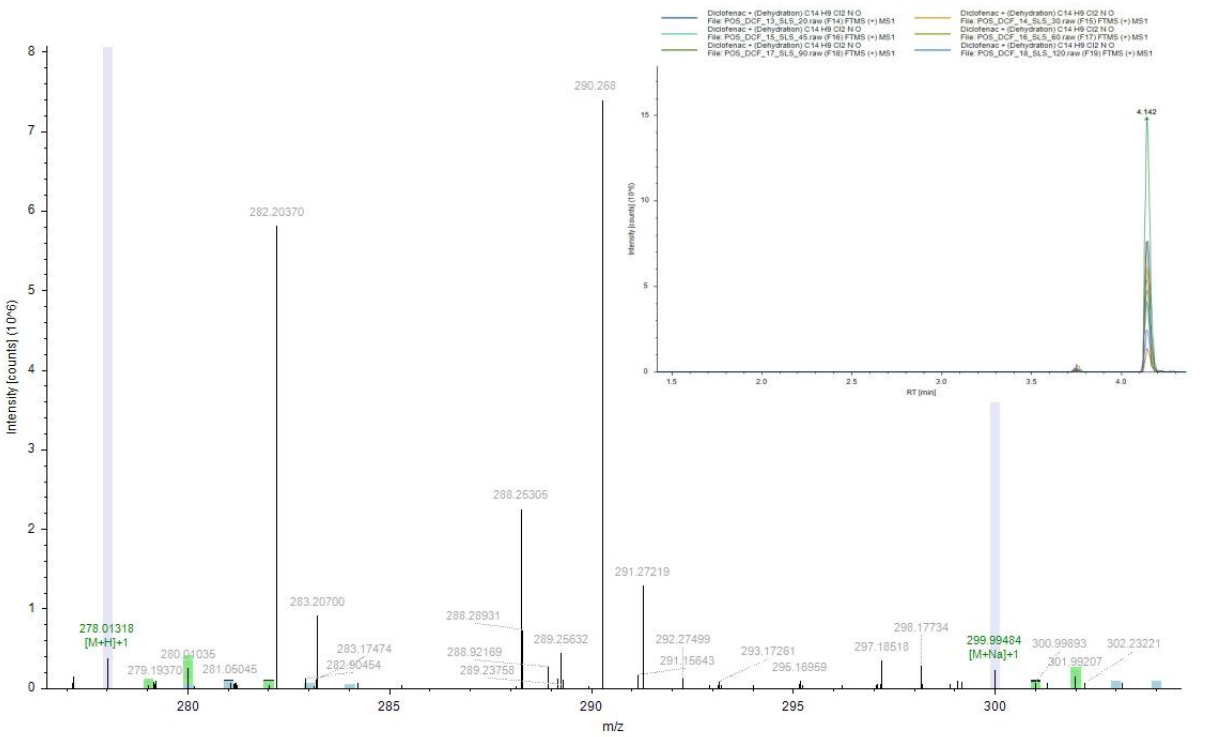

Figure S30. MS[1] mass spectra fragment ions of TPD8; inset, peak retention time.

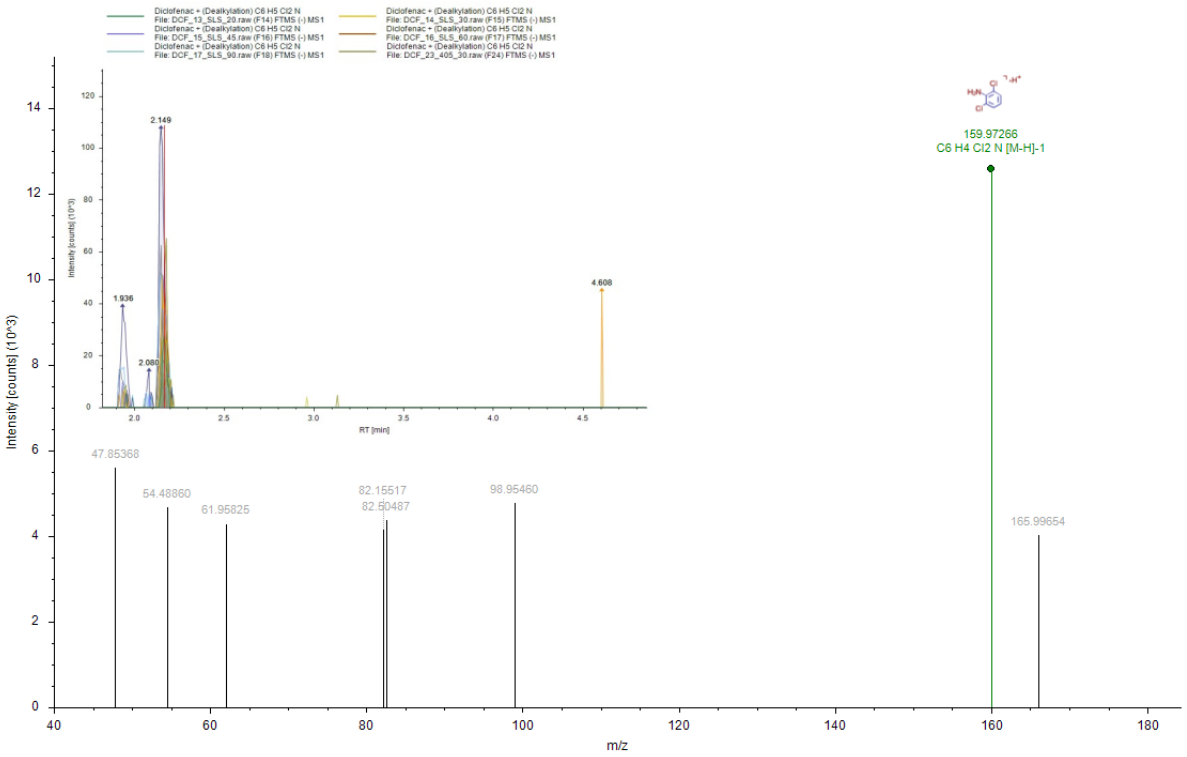

Figure S31. MS^2 mass spectra fragment ions of TPD9; inset, peak retention time.

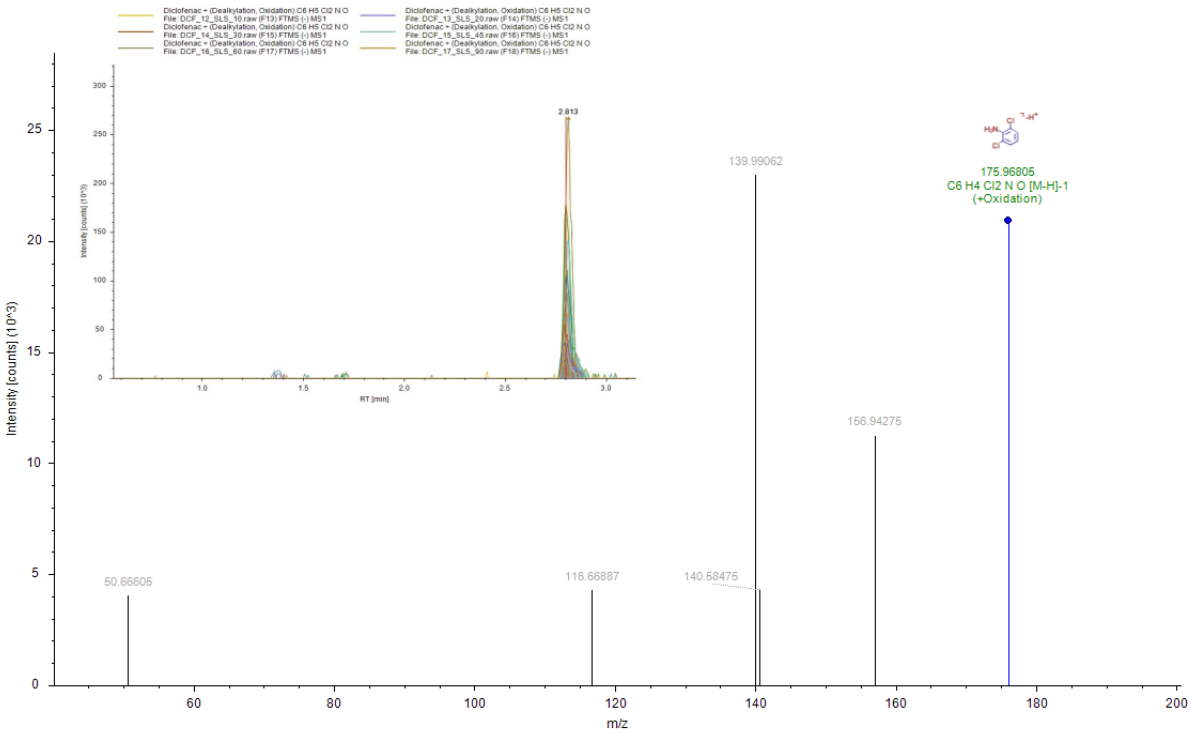

Figure S32. MS^2 mass spectra fragment ions of TPD10; inset, peak retention time.

Author's biography

Camilo Sánchez Tobón was born in 1986 in Medellin, Colombia. In 2012, he graduated in Chemical Engineering from the University of Antioquia (Colombia). He joined the research group Applied Physicochemical Processes during his bachelor's. During that time, he participated in several projects related to Advanced Oxidation Processes for water treatment applications using solar energy. His bachelor thesis titled: "*Synthesis of photoactive TiO_2, modified with N, Se, and Si; from $TiOSO_4$ by the sol-gel method and the solvothermal technique*" was granted Honorable Mention by the Chemical Engineering Professional Board of Colombia.

In 2016, he obtained his M.Sc. in Process Engineering (MPE) from Offenburg University of Applied Sciences (Germany) and the University of Warmia and Mazury (Poland) with an emphasis on renewable energy and wastewater treatment. His master's thesis at Fraunhofer ISE focused on synthesizing mesoporous materials for dehumidification processes.

He was an operations engineer, managing an industrial wastewater treatment plant – WWTP for the PepsiCo Industry. He had the opportunity to start up and operate the first Zero Liquid Discharge – ZLD plant in Colombia.

Camilo was hired in 2019 as an early-stage researcher (ESR) by the NOWELTIES project, an Innovative Training Network part of the framework of EU Horizon 2020's Marie Skłodowska-Curie Actions. His research focused on the microwave-assisted synthesis of nanocomposites based on nitrogen-doped TiO_2/graphene oxide for the removal of organic micropollutants present in water, applying different irradiation sources. He did his research at the Faculty of Mechanical Engineering and Naval Architecture (FSB), University of Zagreb (Croatia), and at the Doctoral Programme in Water Science and Technology, University of Girona (Girona, Spain), in collaboration with the Catalan Institute for Water Research (Girona, Spain).

At an international conference "ICSDWE2021: International Conference on Sustainable Development of Water and Environment", he won the best oral presentation award entitled *"N/TiO_2 nanocomposites: microwave-assisted synthesis, characterization and photocatalytic activity"*.

Author's published works

Sanchez Tobon, C.; Panžić, I.; Bafti, A.; Matijašić, G.; Ljubas, D.; Ćurković, L. Rapid Microwave-Assisted Synthesis of N/TiO_2/rGO Nanoparticles for the Photocatalytic Degradation of Pharmaceuticals. *Nanomaterials* 2022, 12, 3975. https://doi.org/10.3390/nano12223975.

Sanchez Tobon, C.; Ljubas, D.; Mandić, V.; Panžić, I.; Matijašić, G.; Ćurković, L. Microwave-Assisted Synthesis of N/TiO_2 Nanoparticles for Photocatalysis under Different Irradiation Spectra. *Nanomaterials* 2022, 12, 1473. https://doi.org/10.3390/nano12091473.

Aguas, Y.; Hincapié, M.; **Sánchez Tobon, C**.; Botero, L.; Fernández-Ibañez, P. Photocatalytic Inactivation of Enterobacter cloacae and Escherichia coli Using Titanium Dioxide Supported on Two Substrates. *Processes* 2018, *6*, 137. https://doi.org/10.3390/pr6090137.

Sanchez Tobon, **C.**; Jeremias, F.; Ernst, S. J.; Henninger, S. K. Synthesis, functionalization and evaluation of ethylene-bridged PMOs as adsorbents for sorption dehumidification and cooling systems, *Microporous and Mesoporous Materials* 2017, 244, 151, https://doi.org/10.1016/j.micromeso.2017.02.058.